

Alma Mater Studiorum – Università di Bologna

DOTTORATO DI RICERCA

Geofisica

Ciclo XXII

Settore/i scientifico disciplinari di afferenza: **GEO/10 Geofisica della terra solida**

The polarization of horizontal ground motion: an analysis of possible causes.

Presentata da: **Marta Pischiutta**

Coordinatore Dottorato

Prof. Michele Dragoni

Relatore

Dott. Antonio Rovelli

Esame finale anno 2009

to Giordano and Gabriele,

*hoping they will find wonderful
“polarization directions” in
their journeys*

Contents

1	Introduction	1
2	Methods of analysis	2
	2.1 Spectral Methods : rotated SSR and RF.....	4
	2.2 Covariance Analysis Method	5
3	The occurrence of polarization on permanent seismological stations	12
	3.1 Stations and analysis method	12
	3.2 Results	17
	3.3 The relation with topography	18
	3.4 An hypothesis about a correlation with lineament domains.....	19
4	Topographic amplification and polarization effects	27
	4.1 The amplification due to topography	27
	4.2 The influence of topography on polarization.....	29
	4.3 Nocera Umbra hill case study.....	30
	4.3.1 <i>The damage observed after 1997 earthquakes</i>	31
	4.3.2 <i>Geological setting</i>	33
	4.3.3 <i>Analysis method & results</i>	34
	4.3.4 <i>2D numerical models</i>	40
	4.3.5 <i>Comparison with 3D Numerical models</i>	45
	4.3.6 <i>Nocera Umbra hill case conclusions</i>	48

4.4 Cerreto Laziale hill case study	50
4.4.1 <i>Geological setting</i>	51
4.4.2 <i>Polarization at CERT station</i>	56
4.4.3 <i>Array polarization analysis</i>	58
4.4.3.1 Seismic events polarization analysis results	59
4.4.3.2 Ambient noise polarization analysis results	60
4.4.4 <i>Backazimuth and apparent velocity</i>	62
4.4.4.1 Frankel method ambient noise results.	63
4.4.4.2 Frankel method seismic events results.	65
4.4.4.3 Discussion of results.	66
4.4.5 <i>Conclusions</i>	70
5 Polarization across faults	71
5.1 Introduction	71
5.2 The Hayward fault experiment.	75
5.2.1 <i>Geological setting</i>	76
5.2.2 <i>Site and station deployment</i>	82
5.2.3 <i>Seismic events analysis & results</i>	84
5.2.4 <i>Ambient noise recordings data : analysis & results</i>	90
5.2.5 <i>Brittle deformation models</i>	96
5.2.6 <i>Discussion</i>	98
5.3 Agri valley case study	100
5.3.1 <i>Geological setting</i>	101
5.3.2 <i>Data analysis & results</i>	104
5.3.3 <i>Comparison with s-waves splitting fast velocity</i>	110

	5.2.4 Brittle deformation models	114
	5.2.5 Discussion.	116
6	Numerical simulations involving fractured media	117
	6.1 Method	118
	6.1.1 Fracture distributions..	118
	6.1.1.1 Models with one set of fractures homogeneously distributed across the half space.	121
	6.1.1.2 Models with faults	123
	6.1.1.3 Models with a fractal distribution of fractures	127
	6.1.2 TFEM method..	127
	6.1.3 Simulation parameters	129
	6.2 Results	131
	6.2.1 Models with one set of fractures	131
	6.2.1.2 SH simulations	131
	6.2.2.2 SH and PSV simulations	136
	6.2.3 Models with several set of fractures: SH and PSV simulations	138
	6.3 Conclusions	146
7	Conclusions	147
	References	152

Chapter 1

Introduction

This study is addressed to find a systematic explanation for a frequent seismological observation, i.e. strongly polarized ground motion. So far, polarization has been mostly seen as an effect of the seismic source, depending on radiation pattern of double couple mechanism, and therefore on the source backazimuth where ground motion is recorded. But in the seismological practice, strongly polarized motions are more frequent at specific sites, even recording ambient vibrations that are expected to be chaotic in nature, consequently their polarization should be randomly distributed. Here the attention is focused on study cases where topography and fluid-filled fractures in fault zones play a major role on the observed polarizations.

In Chapter 2 the methods of analysis are illustrated, consisting in both spectral analyses and diagonalization of the covariance matrix. One innovative issue is the definition of a hierarchical criterion to establish an objective degree of waveform polarization.

Chapter 3 is devoted to a statistical analysis of the occurrence of polarization, through an investigation using noise signals from Italian Seismic Network (run by INGV). The statistical distribution found from random noise surprisingly results in a not random pattern. It emerges a major role of the seismic station geomorphology. This analysis indicate that the strongest effects are found when stations are characterized at a local scale by significant topographic irregularities, mostly elongated ridges. At a different scale, polarization results are also compared to the distribution of lineament domains along the Italian territory, that are the expression of the main structural features at the regional scale. Unexpectedly, also at this scale a statistically significant influence of lineaments on the distribution of polarizations is found.

The effects of topography on ground motion polarization during earthquakes are investigated in detail in Chapter 4, with two study cases: Nocera Umbra and Cerreto Laziale hill. On the hill of Nocera Umbra the experiment was performed from May to June 1998, during the Umbria-Marche seismic sequence through a seismic array deployed by INGV researchers. To study the effect of topography, ground motion waveforms are analyzed here through spectral methods and the polarization analysis. Moreover 2D numerical simulations of the hill seismic response are also performed, and compared with 3D models simultaneously run by INGV researchers at the Prague University.

Cerreto Laziale hill was recognized as an interesting site to be thoroughly studied while performing the polarization study on the Italian National Seismic Network stations data. In order to better understand the nature of the recorded noise wavefield, we deployed a temporary array of six stations near the hill top to record ambient noise. The analysis of covariance is carried out and backazimuth and apparent velocity of the incoming wavefields are estimated with conventional array techniques.

Following many results recently found by INGV researchers on fault zones of Mount Etna, the possible causes of ground motion polarization in fault zones are investigated in Chapter 5. In this chapter we illustrate the results found on two faults, namely the Hayward fault, in the San Francisco bay area, and the Agri Valley fault in southern Italy. In the Hayward fault an experiment was carried out during a 3-months stage at the US Geological Survey, Menlo Park, thanks to an agreement between INGV and USGS. A temporary array of 6 seismic stations were installed to record the ambient noise. Joe Fletcher cooperated in the field and kindly provided previously recorded earthquake data on that fault. For the other fault we analyzed the ground motion polarization using seismometric data collected during a previous experiment in the Agri Valley to study local seismicity (Valoroso et al., 2009). Using the same data, Pastori et al. (2009) estimated the S-wave splitting directions: their results are used in Chapter 5 to investigate

the relation between polarization, crack orientations and active stress field searching for an interpretation in terms of fluid-filled cracks. For both the Hayward fault and Agri valley, the deformation pattern produced in the fault damage zone was modeled using the package FRAP (courtesy by Francesco Salvini).

In order to understand the possible role of fluid-filled fractures on the experimental results of Chapter 5, 2D numerical methods were used in Chapter 6 simulating realistic distributions of fractures in the uppermost crust. Modeling of wave propagation in fractured media was developed in a partnership with Prof. A. John Haines during a one month stage at Department of Earth Sciences, University of Cambridge, UK. The method to create fracture distributions is implemented here using the triangular finite element method developed by John Haines (presented in Elena Klien's, PhD thesis). In this approach, the normal components of traction and velocity along the fracture are continuous while the tangential traction is null. Fracture distributions were created in such a way to properly reproduce the systematic variability and chaos of nature. Models were constructed both using one single set of fractures oriented along different orientations and adding two sets of fractures, where length and spacing are constrained to have a fractal relation.

Chapter 2

Methods of analysis

2.1 Spectral Methods : rotated SSR and RF

The spectral methods used in the study of polarization include the calculation of standard spectral ratios (SSRs) and receiver functions (RFs) after rotating the horizontal components by steps of 10° , from 0° to 180° . This approach is very powerful in enhancing, if any, the occurrence of site-specific directional resonances with a significant polarization in the horizontal plane.

The use of the rotated horizontal components in spectral ratios (SSRs) was firstly introduced by Spudich *et al.* (1996) to study the directional resonance due to topography irregularity at Tarzana, California, where ground acceleration reached 1.78 g during the 1989 Northridge earthquake. Using the same procedure, Cultrera *et al.* (2003) found a directional resonance in the fault zone of Nocera Umbra, where accelerations were anomalously large repeatedly exceeding 0.5 g for moderate-magnitude normal-faulting earthquakes. It was subsequently exploited by Rigano *et al.* (2008) and by Di Giulio *et al.* (2009), to study polarization across Etna faults.

The first step to rotate the pair of horizontal components, is dividing the horizontal plane into a set of directions spaced by 10° bins from 0° (N) to 180° (S). For each direction, the spectrum of the rotated horizontal components is calculated through fast Fourier transform and a smoothing function is applied. Then SSRs are calculated using as denominator the spectrum of the reference station where the horizontal components are rotated by the same angle. When a reference station is not available, RFs are computed using the vertical component spectrum as denominator. Before the spectral computation, seismic signals are detrended, the mean is removed, and a cosine window taper is applied.

In this way the spectral ratios become a function of frequency and direction of motion. They are drawn as contour maps of amplitude, where the rotation angles are plotted versus frequency (Figure 2.1). Analogues plots with the standard deviation are represented and all the spectra of the 18 rotated components are plotted too.

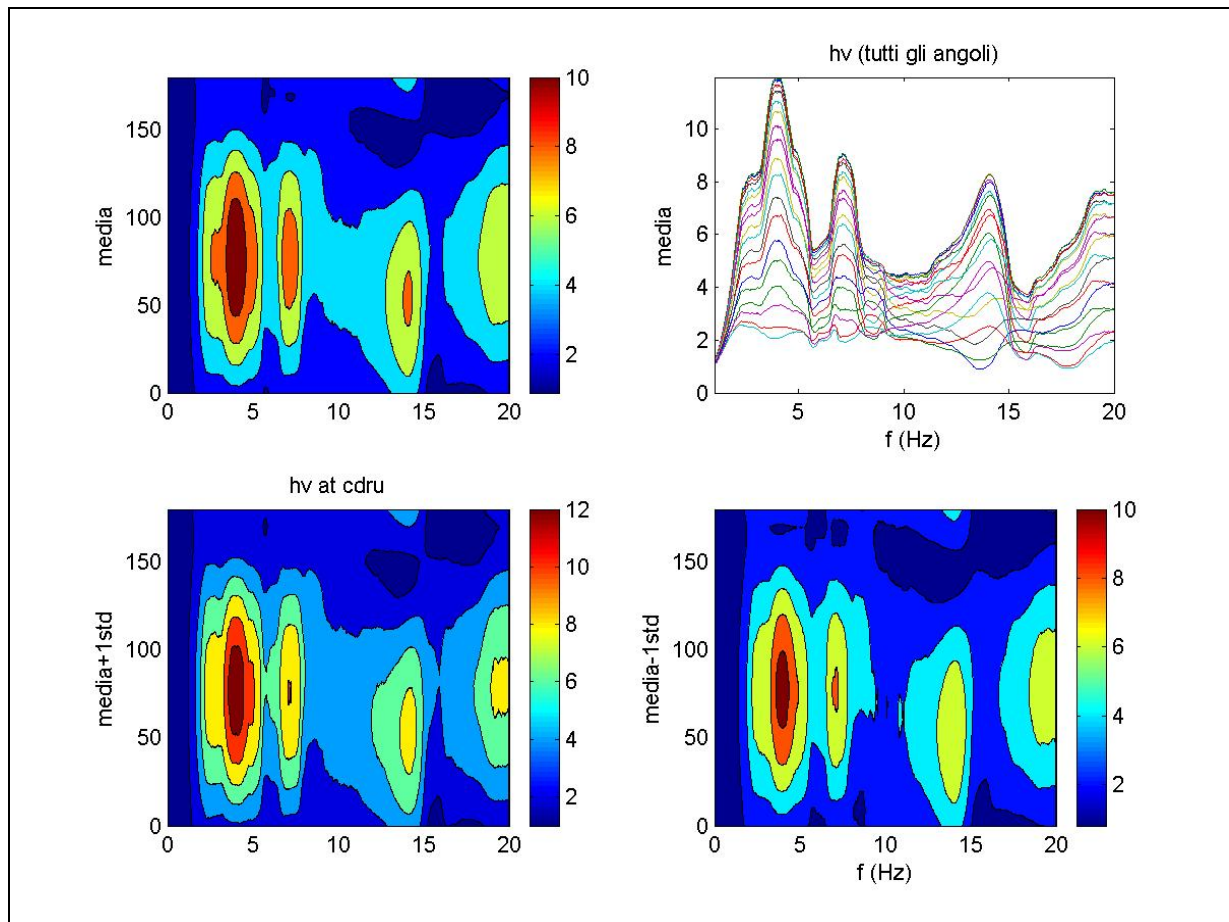


Figure 2.1 – Example of rotated receiver functions (RFs) calculated for station CDRU (Italian Seismic Network run by INGV). Spectra calculated for all the angles of rotation (right top panel) and the contours of the geometric mean (top left panel) of spectral ratios as a function of frequency (x axis) and direction of motion (y axis). The geometric mean and the ± 1 standard deviation patterns (bottom), are shown too.

2.2 Covariance Analysis Method

Spectral methods are a powerful tool to recognize directional amplifications even though this approach provides a relative estimate and may thus be biased by the denominator spectrum. A direct estimate of the polarization angle can be achieved by the covariance matrix method (Jurkevics, 1988), providing a more direct visual inspection of the predominant direction of horizontal ground motion. This analysis involves the computation of eigenvectors and eigenvalues of the covariance matrix obtained from three component seismograms and is carried out in the time domain.

At first the signals are detrended and the mean is removed; then they are bandpass filtered considering the frequency bands where the previous spectral analysis revealed some interesting and relevant amplification pattern. To estimate the covariance matrix \bar{S} , the code POLARSAC (La Rocca *et al.*, 2004) is applied to the three component of motion in the time domain, using an

overlapping moving window which width is tailored depending on the case. This program can be applied to earthquakes and ambient noise, by varying the threshold of RMS. This value is calculated for each moving window through the amplitudes of the three components: only windows with RMS over the threshold chosen by the user are analyzed.

The polarization is estimated separately in each window with the basic assumption that each window shows only one defined (or null) polarization, because the motion is assumed to be purely polarized over the window duration. The data matrix in each window is written as

$$2.1 \quad \vec{X} = [x_{ij}]$$

where $i = 1, \dots, N$, $j = 1, \dots, 3$, x_{ij} is the i th sample of component j and N is the number of samples (i.e. of windows). The mean of each component of \vec{X} is removed over the window duration.

The covariance matrix is calculated as:

$$2.2 \quad S_{jk} = \frac{XX^T}{N} = \frac{1}{N} \sum_{i=1}^N x_{ij}x_{ik}$$

It is a 3x3 matrix, real and symmetric whose terms represent the auto and cross variance of the three components of signals ($z=1$, $n-s=2$, $e-w=3$).

$$2.3 \quad \vec{S} = \begin{bmatrix} S_{zz} & S_{zn} & S_{ze} \\ S_{nz} & S_{nn} & S_{ne} \\ S_{ez} & S_{en} & S_{ee} \end{bmatrix}$$

Eigenvalues $\lambda_1 \succ \lambda_2 \succ \lambda_3$ and eigenvectors \vec{u}_i are found by solving the algebraic eigenproblem for \vec{S} :

$$2.4 \quad (\vec{S} - \lambda^2 \vec{I})\vec{u} = 0$$

The covariance matrix is positive and semidefinite therefore the eigenvalues are real and positive. They respectively correspond to the axis length and to the axis orientation of polarization ellipsoid (Figure 2.2), and describe the particle motion in the data window.

The polarization vector, PV, is defined through the vectorial sum

$$2.5 \quad PV = \sum_{i=1}^3 \lambda_i \vec{u}_i$$

For each time window the code POLARSAC yields four values related the polarization ellipsoid:

- **I - APPARENT INCIDENCE ANGLE OF RECTILINEAR MOTION** - the angle between the eigenvector associated to the higher eigenvalue and z-axis;

$$2.6 \quad I = \arccos(\vec{u}_1)$$

- **R - RECTILINEARITY** - It indicates to what extent the three axes differ. It takes values between 0 (spherical motion) and 1 (rectilinear motion).

$$2.7 \quad R = 1 - \frac{\lambda_2 + \lambda_3}{2\lambda_1}$$

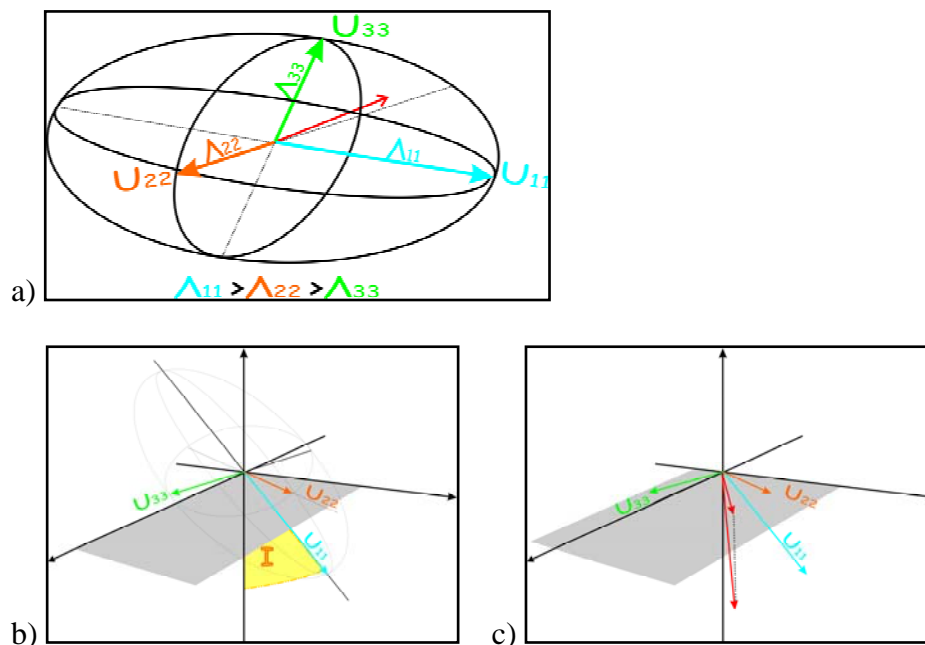


Figure 2.2 – a) The polarization ellipsoid; b) Incidence; c) the PV (red) and its projection of horizontal plane.

- **AZ - POLARIZATION AZIMUTH** – the angle between the horizontal component of the PV and North.

$$2.8 \quad AZ = \arctg \left[\frac{u_{21}(\text{sign}(u_{11}))}{u_{31}(\text{sign}(u_{11}))} \right]$$

where $u_{j1} = 1, \dots, 3$ are the three direction cosines of eigenvector \bar{u}_1 . The sign function has been introduced to take positive vertical component of \bar{u}_1 resolving the 180° ambiguity (Jurkevics, 1988).

- **P - PLANARITY** – Is representative of the flatness of the polarization ellipsoid indicating how much the motion is confined to a plane.

$$2.9 \quad P = 1 - \frac{2\lambda_3}{\lambda_1 + \lambda_2}$$

Among these values, the **AZ** is the one which is used to represent polarization and that is plotted through a circular histogram (rose diagram) computed at bins of 10° . Bins that differ by 180° are cumulated together as having the same polarization direction, their separation having no physical meaning.

In order to take into account the other three values, enhancing results from time windows with rectilinear and horizontal particle motion, a criterion has been thought to weigh the azimuths coming from the analyzed sliding windows. In fact, if the polarization ellipsoid is semi-spherical or is rectilinear-near-vertical, the PV has in any cases an horizontal component that provides a value of AZ. In this case it is plotted with the same importance of other azimuths belonging to horizontal rectilinear, more representative ellipsoids.

The *hierarchical criterion* establishes to exclude from statistics values of AZ associated to $R < 0.5$ and $I < 45^\circ$, while the rest of values of R (between 0.5 and 1) and I (between 45° and 90°) are transformed to a range between 0 and 1. They are then multiplied providing a weight factor **WH=R*I**. This factor represents the measure which each value of azimuth (belonging to the same time window of R and I) enters in the statistics. The final circular histogram is therefore performed from 0 to 360° (at bins of 10°).

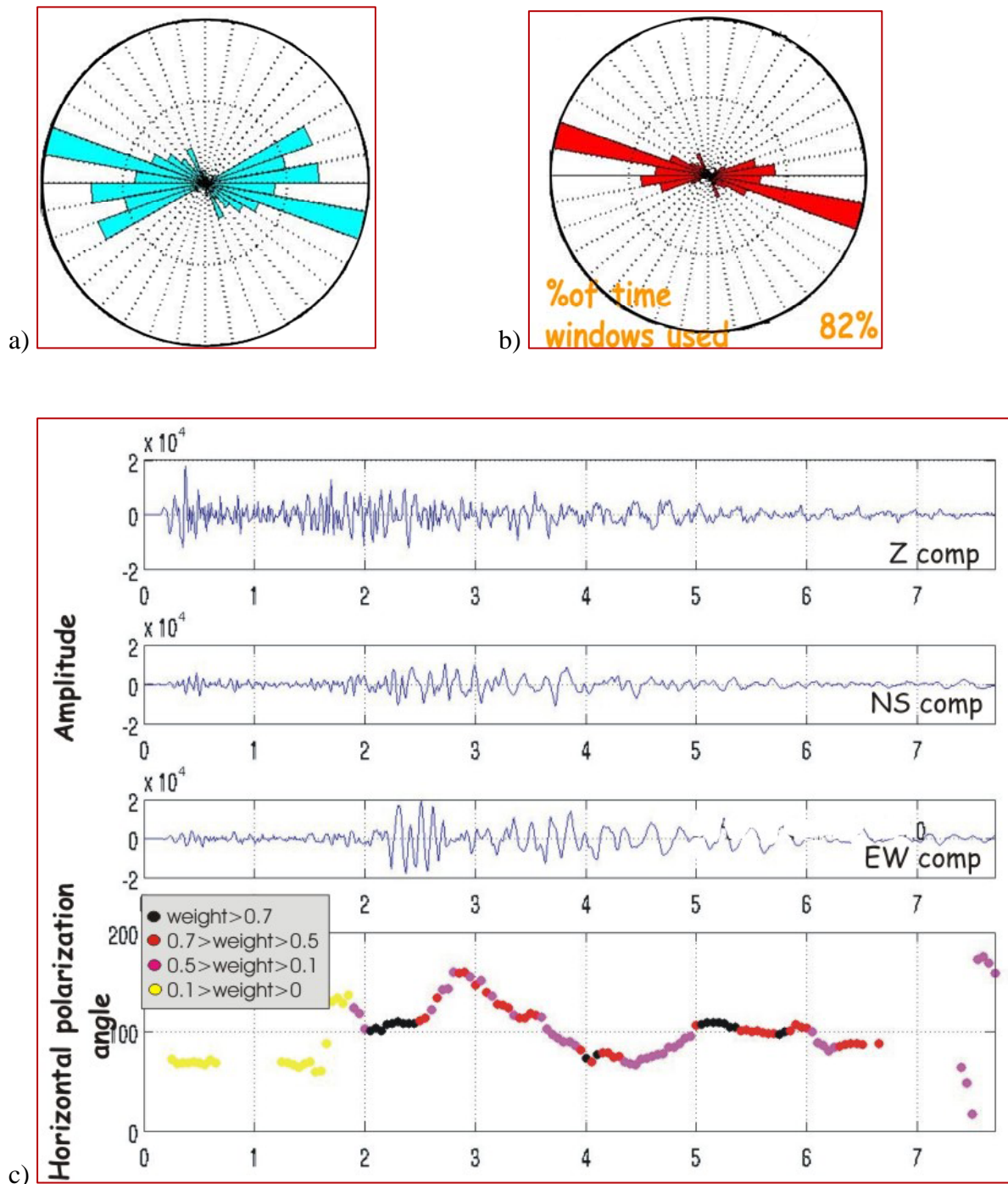


Figure 2.3 – Example of covariance matrix analysis results and hierarchical chosen criterion. a) Rose diagram produced by plotting the polarization azimuths (AZ) from the whole set of analyzed time windows. Bins that differ by 180° are cumulated together as having the same polarization direction; b) Rose diagram produced by plotting the weighted polarization azimuths (AZ). The percentage of time windows used is reported; c) polarization angles plotted versus time. The weights associated to each angle are represented through a colour scale (see legend).

To ensure that the statistics is representative of the whole time windows analyzed along the signals, the percentage of rejected time windows is calculated, with the constrain of being less than 25%.

An example of two rose diagrams calculated applying and not applying the weight criterion is shown in Figure 2.3, top panels.

Moreover the values of **AZ** are plotted versus time and along signals to detect any changes with the different seismic phases, or simply with time when studying ambient noise. The associated weights are represented through a colour scale, as shown in Figure 2.3, bottom panel.

Chapter 3

The occurrence of polarization on permanent seismological stations



Figure III – Stations of the Italian seismic network

With the aim of achieving an indication about the statistical occurrence of polarization, a systematical analysis is carried out using 212 stations of the Italian Seismic Network (run by INGV). The horizontal polarization is estimated on 30 minutes of ambient noise (day & night) using the Covariance matrix method and the rotated receiver functions.

Results are compared to the lineament domains distribution along Italian territory, that are the expression of the main structural features at the regional scale.

3.1 Stations and analysis method

The location of stations of the permanent Italian Seismic Network is shown in Figure III. Their distribution is not homogeneous because they were installed close to seismogenic areas, being mostly concentrated across the Alps and Apennines mountain chains and near active volcanic areas. From their continuous recordings, 30 minutes of ambient noise were selected during night and day times when wind velocity was on average lower than 5m/s and in absence of rain precipitation. This selection was performed using the meteorological website of Italian Air Force (www.meteoam.it). In fact, as assessed by SESAME project (Site EffectS assessment using AMbient Excitations - <http://sesame-fp5.obs.ujf-grenoble.fr/index.htm>), wind and rain can strongly influence ambient noise characteristics.

Preliminarily to the analysis the signals were detrended and mean was removed, then the rotated receiver functions were calculated. Thus, a time windows selection was performed through the antitrigger algorithm developed by SESAME project, in order to keep the most stationary parts of ambient vibrations, avoiding the transients often associated with specific sources (footsteps, close traffic). To detect transients, a comparison between the short term average "STA" (the average level of signal amplitude over a short period of time), and the long term average "LTA" (the average level of signal amplitude over a much longer period of time) is made by fixing a small value of threshold to the ratio STA/LTA (typically around 1.5 – 2).

The covariance matrix method was applied in the frequency band 1-20 Hz on the selected parts of signals, using a 2s moving windows with 0.1 sec overlap. The circular histograms of the polarization azimuths (AZ) were produced applying the hierarchical criterion described in section 2.2. The rose diagram histogram was fitted through a Gaussian function, finding the mean direction and the standard deviation.

The results from nightly and daily ambient noise were compared, both using RFs and rose diagrams, suggesting that most of the time the polarization is consistent. In some cases during the day cultural activities affect the polarization angle, as observed by Cara *et al.* (2010). This is the reason why only the nightly noise was used in the following steps of the analysis.

With the purpose of defining a value that could express the polarization intensity (POLARIZATION INDEX) as a function of the standard deviation of rose diagrams, a 3rd order function was chosen

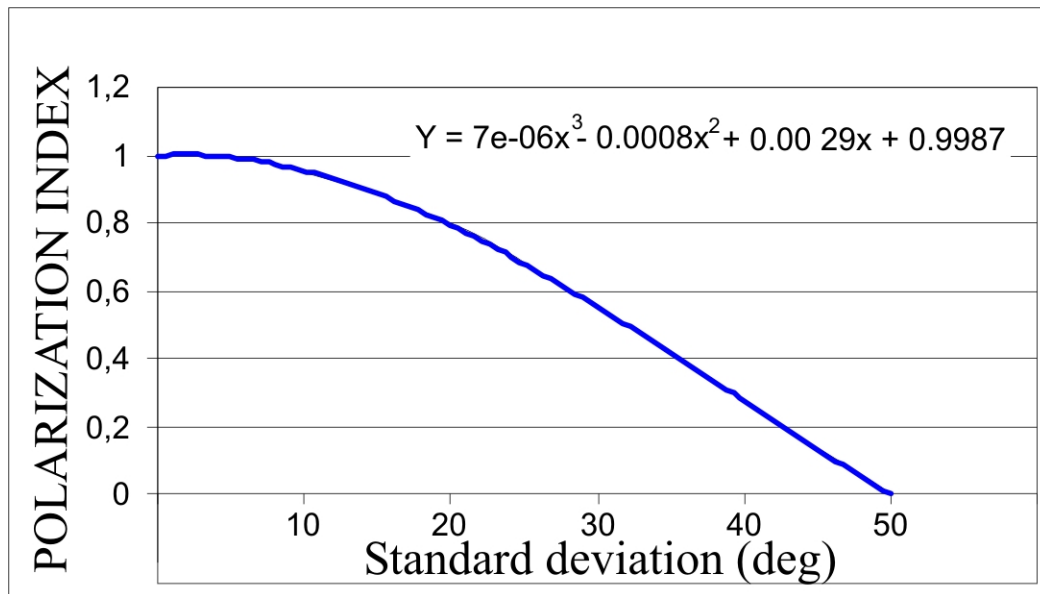


Figure 3.1 – Function used to estimate the POLARIZATION INDEX through the standard deviation of the circular histogram fitting Gaussian.

This function sets very strict conditions, assigning low values to the polarization index when the SSD becomes lower than 30° . Another constraint was applied considering the number of time windows which satisfied the hierarchical criterion, contributing to the rose diagram construction: stations where more than 25% of time windows had values of R and I lower than 0.5, were associated to null polarization index.

Some results are depicted in Figure 3.2, which shows several stations with their histogram of polarization azimuths (applying the hierarchical criterion) and the rose diagrams. At the rose diagram corners there are the values of : the standard deviation (STD) of the Gaussian function interpolating the histogram, the polarization intensity obtained by applying the function shown in Figure 3.1 (indexSTD), the mean direction (MEAN), the percentage of time windows with values of R and I satisfying the hierarchical criterion (indexPESI).

Some representative stations are depicted in Figure 3.2 as examples of different polarization intensities. Station ARVD (a) is a clear example of no evidence of polarization. Here the time window percentage satisfying the criterion is around 50%, a very low value. This is a common aspect of cases with no evidence of polarization. Station SALO (b) seems to be polarized in a defined direction but the peak is broad and standard deviation is quite high being around 40° . The polarization index in fact is quite low, about 0.2.

The polarization of ambient noise distinctly appears on CERT (c) and WTTA (d) stations, with a good consistency between analyzed time windows,

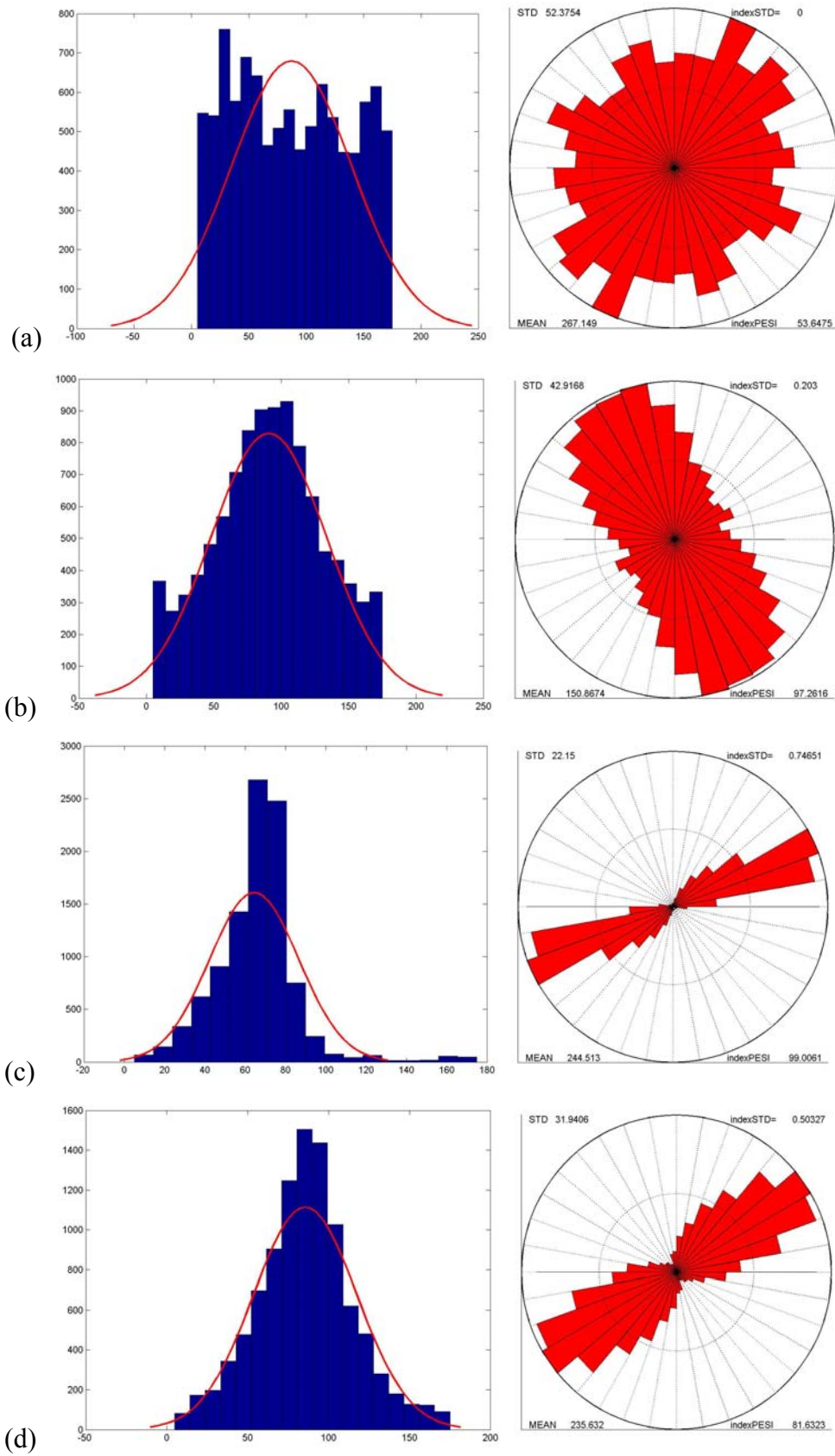


Figure 3.2 – Rose diagrams and Gaussian fitting histograms obtained from stations: (a)ARVD; (b)SALO; (c)CERT; (d)WTTA.

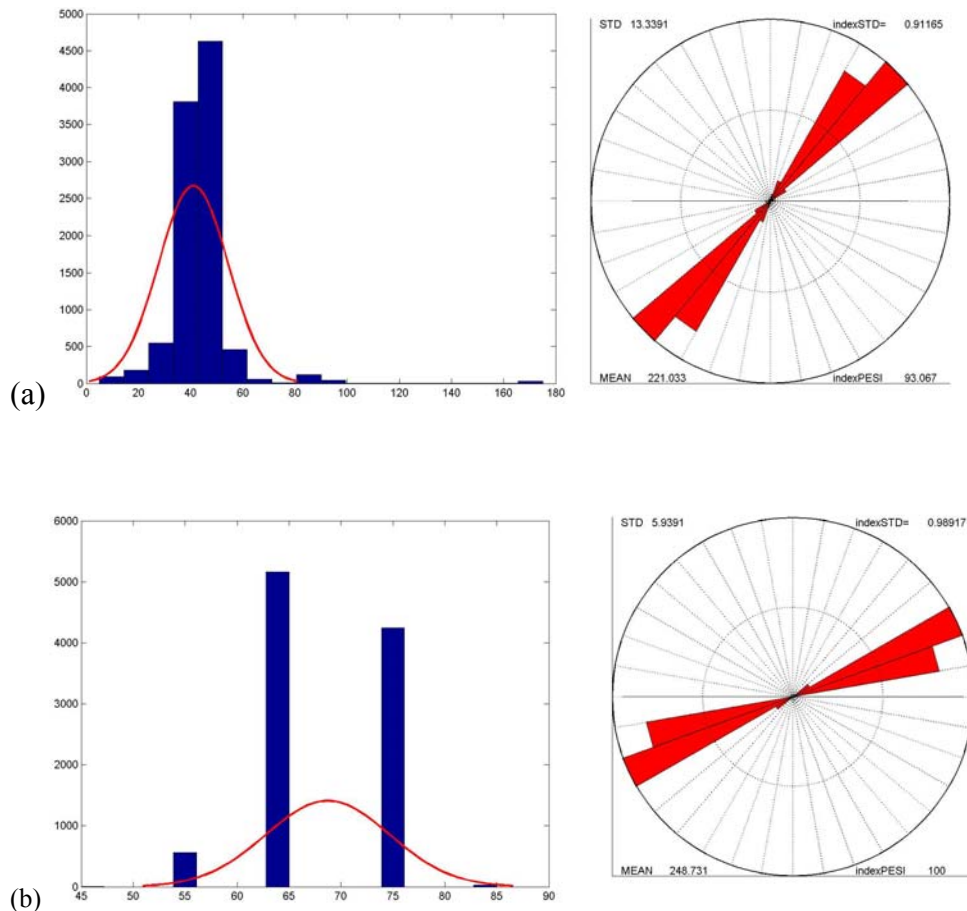


Figure 3.3– Rose diagrams and Gaussian fitting histograms obtained from stations: (a)TRAV; (b)CDRU

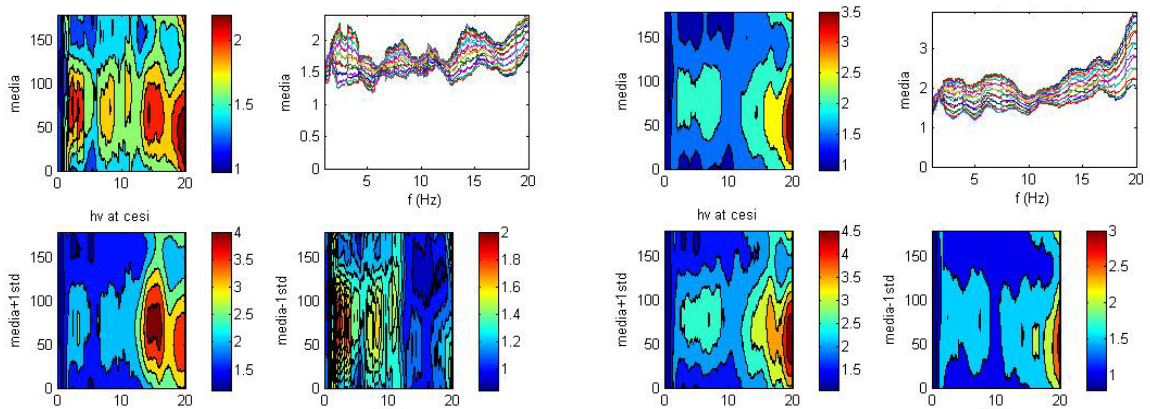


Figure 3.4 – Day & night results (rose diagram and rotated Receiver functions) comparisons for CESI station.

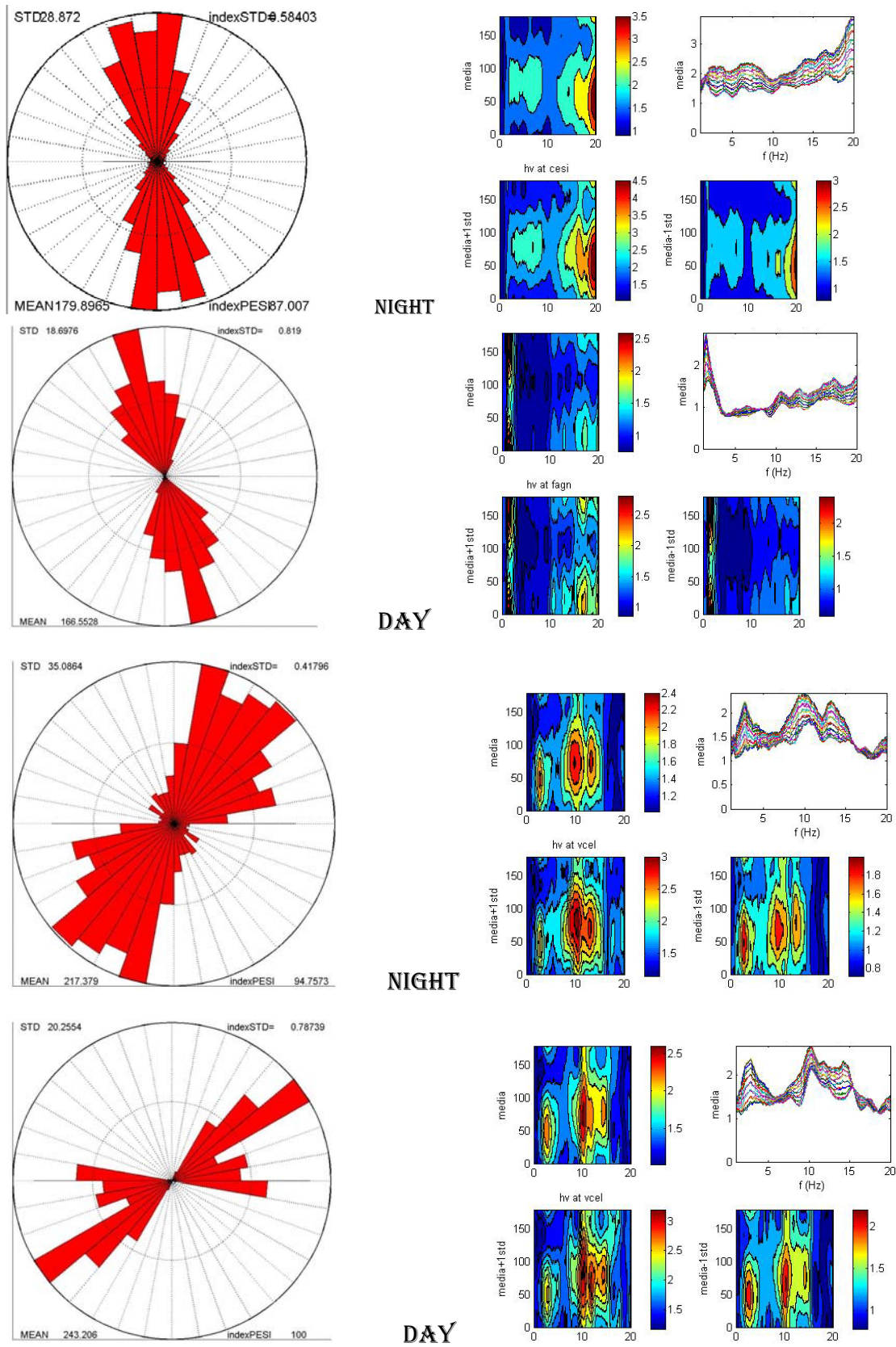


Figure 3.5 – Day & night results (rose diagram and rotated Receiver functions) comparisons for FAGN and VCEL stations.

leading to quite narrow peaks that produce values of polarization index quite high (between 0.5 and 0.7). Very narrow peaks are found in Figure 3.3 at TRAV (a) and CDRU (b) stations, with small standard deviation angles and values of polarization index higher than 0.9. Here the polarization is very recurrent and stable on more than 95% of time windows.

In order to give an example of the comparison between nightly and daily noise, results of three stations are shown in Figures 3.4 and 3.5. Station CESI show a slight polarization effect quite consistent within day and night, as well as FAGN station where the peak is more pronounced. To the contrary station VCEL depicts different frequency peaks between night and day, at is a clear example of how daily sources can affect the analysis.

3.2 Results

The first important result about the occurrence of polarization can be achieved by the statistics of polarization intensity values obtained from the whole data set of stations (Figure 3.6). At least the 50% of stations show null polarization intensity, suggesting that the recurrence of polarization has not overestimated and that the conditions chosen to evaluate the polarization index were enough restraining. On the other hand roughly the 30% of the analyzed stations shows polarization intensity higher than 0.5, which is correlated to standard deviation values smaller than 30° . That means that the polarization is unexpectedly quite diffuse.

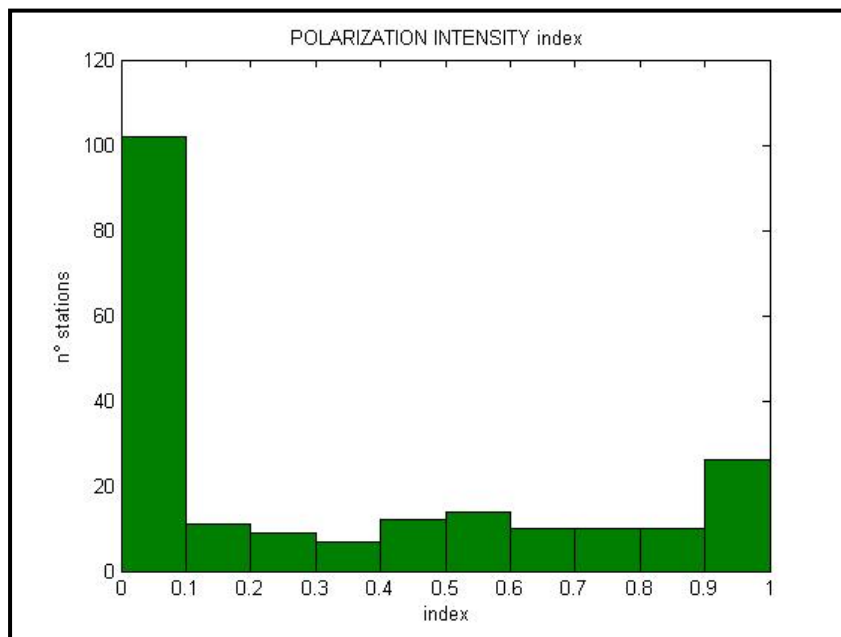


Figure 3.6 – Histogram representing the **POLARIZATION INDEX** obtained by all the analyzed stations.

3.3 The relation with topography

Trying to correlate the polarization to directional resonance due to topographic amplification (for further details see Chapter 4), a selection of stations lying on morphological highs was performed (courtesy by Paola Vannoli) using a 1:10000 digital elevation model (DEM). Around 44 stations were found to be installed across hills with a more pronounced preferential elongation direction. For each station, the angle between the hill major axis and the polarization mean direction was measured. Then these angle values were used to construct the histogram in Figure 3.7, calculated at steps of 10 degrees.

The conclusion is that at least the 60% of stations shows a mean polarization oriented between 60 and 90 degrees from the hill preferential elongation. This transverse relation between polarization and hill axis, could be related to a directional amplification effect of resonance which forces the particle motion in a direction transverse to hill axis, as inferred in Chapter 4.

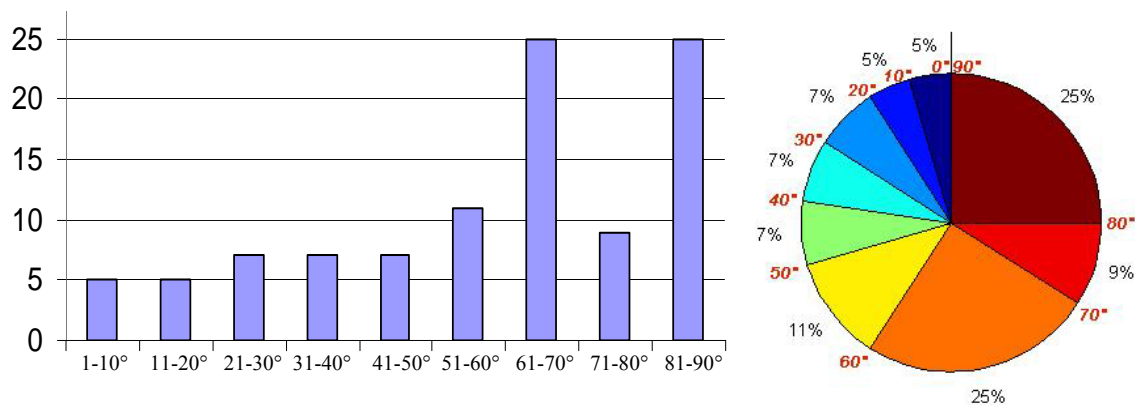


Figure 3.7 – Histogram of percentages and pie chart of angles between the mean horizontal polarization azimuth (from the covariance matrix analysis) and the hill major axis, using 44 stations installed across hills. On the pie chart, black numbers represent the percentage of data lying in the sector and red numbers the sectors border values.

Hence this statistical study performed on a large scale only on half an hour of ambient noise, revealed many interesting new features, as topographies are capable to produce a ground motion polarization in a direction transverse to the hill major axis, which is consistent with the directional amplification effect due to diffraction of seismic waves by topographic irregularities.

3.4 An hypothesis about a correlation with lineament domains

A statistics involving the mean polarization angle at each station is carried out to estimate the distribution of polarization directions all over the Italian region. Because of the study is at the regional scale, the lineament domains distribution by Wise *et al.* (1985) is taken into account as representative of crustal scale structural geological features. These authors performed a lineament domains analysis with the shadowed relief map technique on Italian peninsula, using as definition for lineament “a clear alignment of linear valleys, ridges, passes, coastlines or combination of these features such that their total length is > 10 Km and the aspect ratio > 10”. Lineaments represent fracture zones (areas of more intense, closely spaced fracturing) or other discontinuities (faults, geologic contacts) that undergo differential weathering. In fact, fractured zones are more susceptible to mechanical and chemical weathering than unfractured rocks (Mabee B. S., *et al.*, 1994). Therefore they are assumed to have originally been produced by tectonic stresses in the earth's crust. In their work Wise *et al.* (1985) found 48 lineaments swarms in the Italian region, which were regrouped in 8 super-swarms, here redrawn in Table 3.1 and Figure 3.9. By the correlation with the tectonic domains of Italy (redrawn in Figure 3.10), they found that most of lineaments swarms are associated to tectonic stress zones and were formed perpendicular to the minimum horizontal compressional stress vector σ_3 .

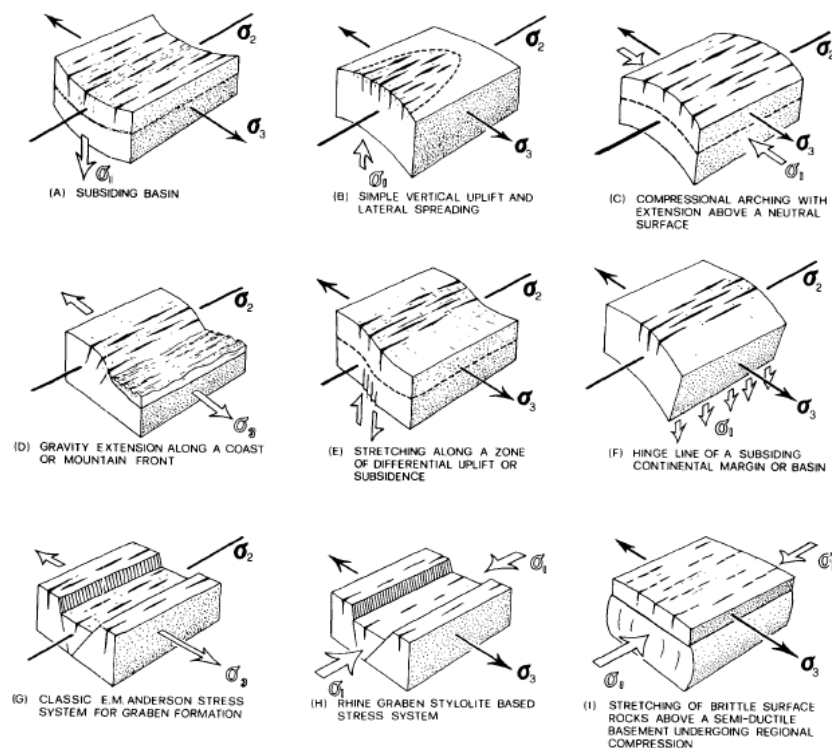


Figure 3.8 – Redrawn from Wise et al. (1985). Possible tectonic settings and stress fields for Italian lineament swarms. Many of the models involve brittle behaviour of a thin surface zone above a deeper layer behaving in slightly ductile fashion. All of the blocks are characterized by the axis of least compression (sigma 3) lying horizontal and being perpendicular to the surface outcrop of the lineaments.

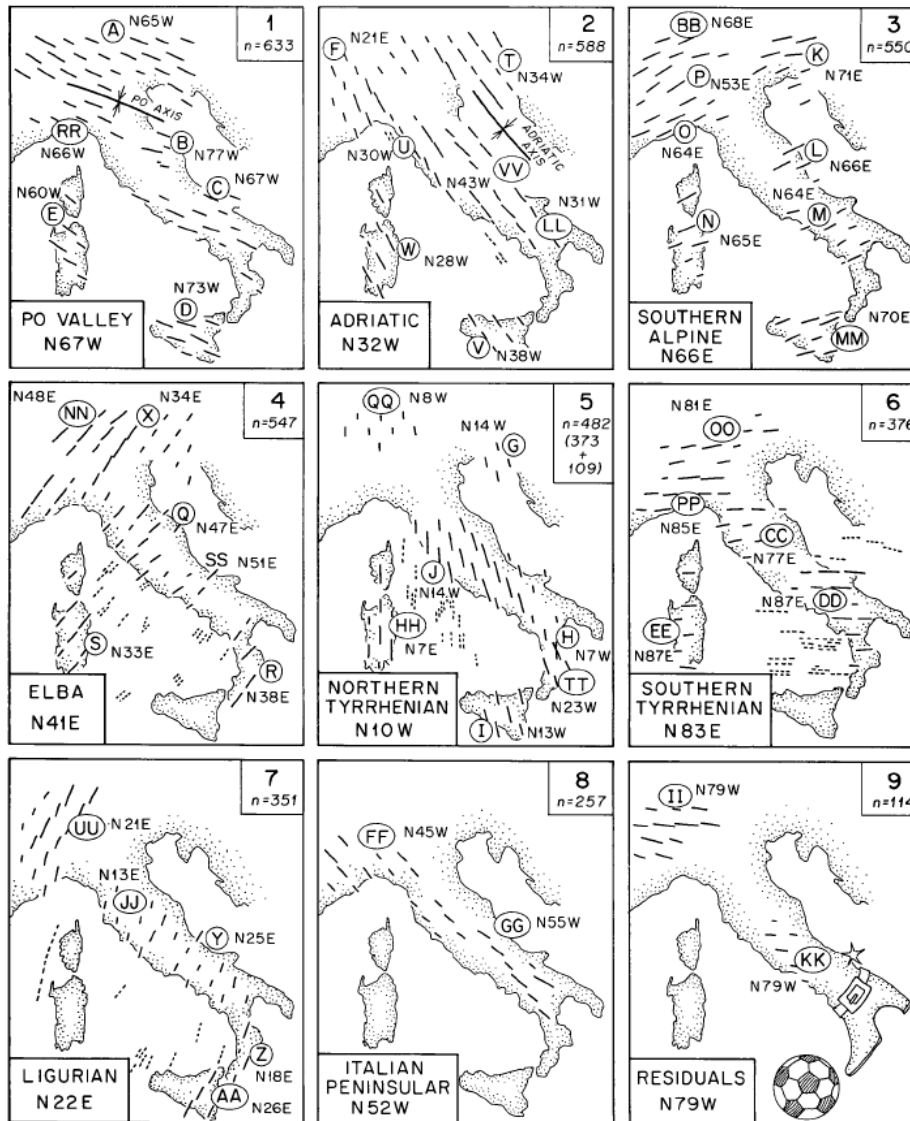


Figure 3.9 – Lineaments super-swarms of Italy, redrawn from Wise *et al.* (1985). Each solid line represents a Gaussian peak.

Name	Domain codes	Average azimuth	Std. dev.	No.	Avg length (km)	Area (km ²)
1. Po Valley	{A, RR, B, C, E, D}	N67°W	8.5	633	37.8	349,142
2. Adriatic	{T, F, U, VV, LL, V, W}	N32°W	9.4	588	36.5	335,389
3. South Alpine	{BB, P, O, K, L, M, N, MM}	N66°E	8.5	550	35.2	285,537
4. Elba	{NN, X, Q, SS, S, R}	N41°E	8.9	547	32.4	287,427
5. Northern Tyrrhenian	{QQ, G, J, HH, TT, H, I}	N10°W	11.0	482	33.0	213,164
6. Southern Tyrrhenian	{OO, PP, CC, DD, EE}	N83°E	7.1	376	31.4	227,088
7. Ligurian	{UU, JJ, Y, Z, AA}	N22°E	7.4	351	30.8	178,095
8. Italian Peninsular	{FF, GG}	N52°W	8.8	257	32.0	145,605

Table 3.1 – Lineaments super-swarms of Italy, redrawn from Wise *et al.* (1985). Gaussian peak.

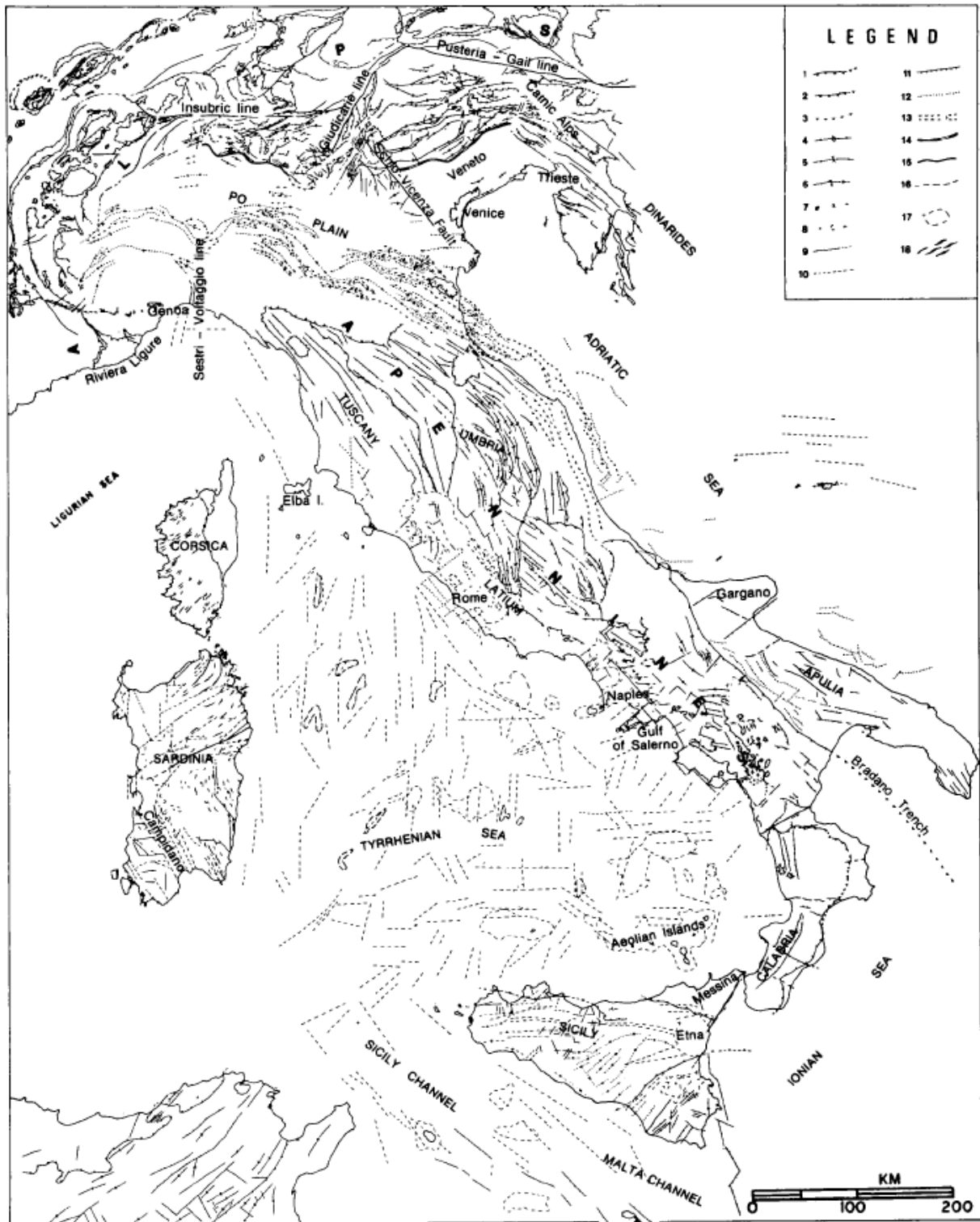


Figure 3.10 – Brittle tectonic features of Italy and adjacent sea floors, redrawn from Wise *et al.* (1985). 1) Frontal thrusts of the main Alpine and Apennine nappe system; 2) fronts of minor Alpine napped, boundaries of minor Apenninic overthrusts and outcrop traces of reverse faults; 3) Buried thrusts and reverse faults; 4) Anticlinal axes; 5) Synclinal axes; 6) Recumbent folds; 7) Buried synclinal axes; 8) Buried anticlinal axes; 9) Faults, mainly subvertical; 10) Faults mainly subvertical, buried of known from geophysics; 11) Normal faults with hachures on down-thrown side; 12) Same as number 11 but buried; 13) Horst and graben structures on the northern and central Tyrrhenian-Apenninic border zone: outcrop and buried; 14) Flexure at the edge of southern Prealps; 15) Main tectonic lines and sutures; 16) Morphological lineaments on Tyrrhenian Sea bottom; 17) Boundaries of volcanic provinces or areas; 18) Dike system in Sardinian-Corsican massifs.

With the aim of performing the statistics of polarization, the 111 stations with **POLARIZATION INDEX > 0.1** were selected and the total circular histogram was calculated. Following the approach of Wise *et al.* (1985) and using the package DAISY 3_480 (Salvini, 2002, [http:// host.uniroma3.it/ progetti/ fralab/](http://host.uniroma3.it/progetti/fralab/)), the best fit method was used to automatically fit the histogram peaks with a multiple Gaussian curve.

The parameters of fitting Gaussian curves were chosen as follow:

- *Fattig factor* = 1.36 . It is proportional to the width of half height of the initial Gaussians and to the attitude to include minor peaks;
- *Tail influence factor* = 0.46 . It is proportional to the interval around each Gaussian mean value to compute the best fit;
- *Max number of Gaussians* = 10 ;
- *Number of the best fit iteration* = 11;
- *Minimum fractional peak height* = 0.10 . This is the height of the shortest Gaussian that can be detected, respecting to the maximum of the histogram.

A Smoothing linear filter of 7% interval with 2 number of cycles was even applied to the data. The statistics was firstly performed using for each station the value of the mean polarization azimuth. Then, to be consistent with the transverse relation between polarization and topography or fracturation field (Chapters 5 and 6), the procedure was repeated using the angles rotated by 90 degrees.

LINEAMENT DOMAINS			POLARIZATION (data rotated by 90°)		POLARIZATION (data not rotated)	
MEAN DIRECTION	STANDARD DEVIATION	LIN. DOMAIN DESCRIPTION	MEAN	ST DEV	MEAN	ST DEV
N67W -67	8,5	Po Valley	-66	6.5	-72.4	7.1°
N32W -32	9,4	Adriatic	-31.3	6.2	-29.1	5°
N66E 66	8,5	South Alpine	60.8	5	58.8	6.2°
N41E 41	8,9	Elba	44.2	3	-45.8	2.7°
N10W -10	11	North Tyrrhenian	-4	5	-3	6.3°
N83E 83	7,1	South Tyrrhenian	87	6.3	85.9	5°
N22E 22	7,4	Ligurian	17.6	7.1	23.9	6.5°
N52W -52	8,8	It. Peninsular	-49.6	2.7	-45.7	3°

Table 3.2 – Comparison between the lineaments superswarms (Wise *et al.* 1985) and polarization statistics peaks.

Figure 3.11 shows the circular histograms of rotated (R) and not rotated (N) polarization angles and the eight fitting Gaussian curves (without filling). The table on the left depicts Gaussian peaks parameters of mean (Azimuth) and standard deviation (sd). To compare polarization and lineament domains, a rose diagram of superswarm is calculated by the original lineament domains data of Wise *et al.* (1985) and plotted with colour filling on the previous one. Moreover the mean direction and standard deviation of lineament domains and of the Gaussian curves fitting the two polarization rose diagrams are displayed in Table 3.2.

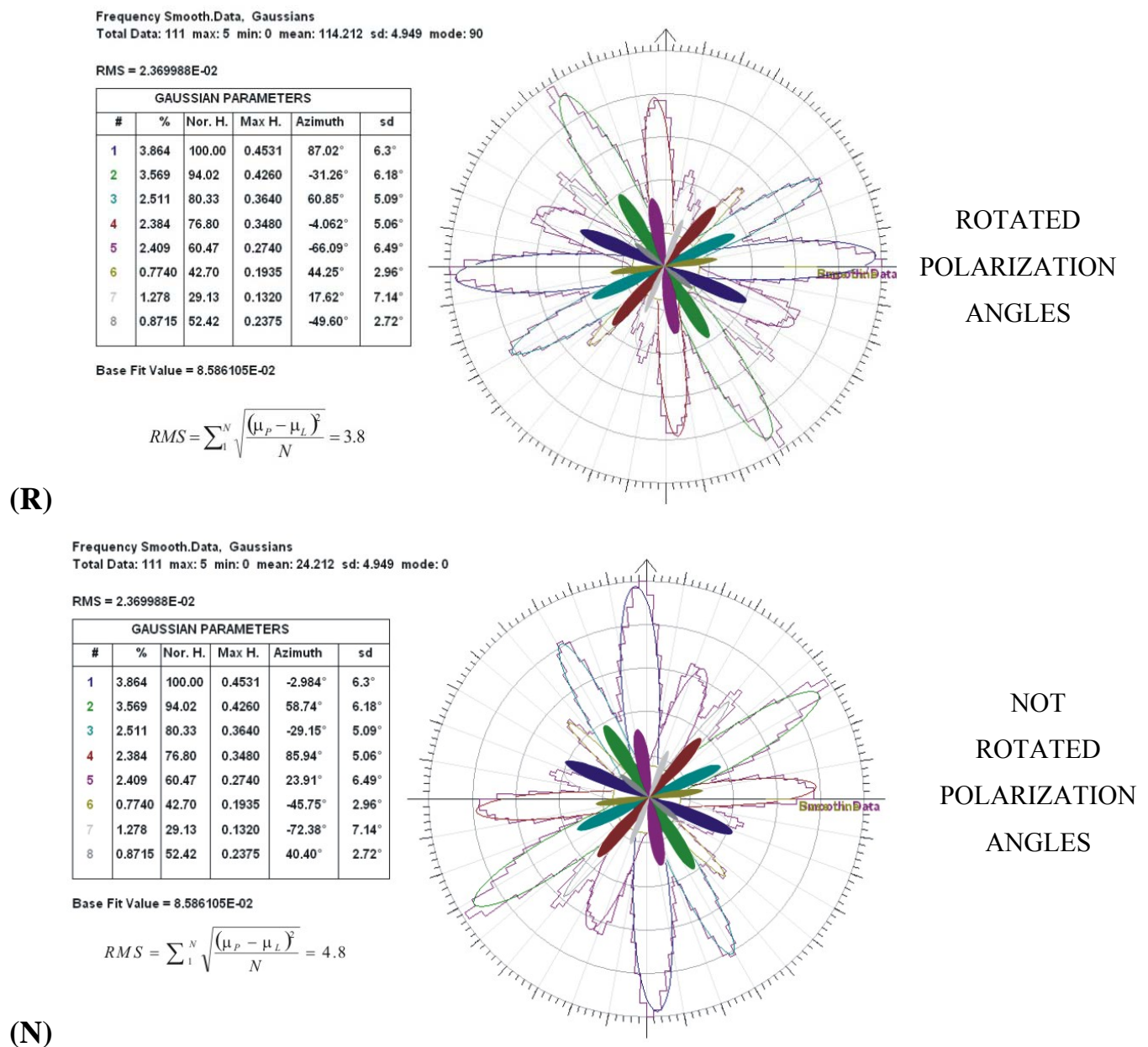


Figure 3.11 – Rose diagrams obtained by the polarization mean directions from the selected stations of Italian seismic network with index > 0.1. The colour filled rose diagram superimposed represents the domains found by Wise *et al.* (1985). (R) Angles rotated by 90°; (N) Normal data (not rotated angles);

To find the best semblance between “R” and “N” polarization peaks and lineaments domains mean directions, an RMS value is introduced, expressed as:

$$3.1 \quad RMS = \sum_1^N \sqrt{\frac{(\mu_P - \mu_L)^2}{N}}$$

where μ_P is the mean direction of the polarization peak, μ_L is the analogous for the domains nearest peak (in Table 3.2) and N is the number of peaks. The resulting RMS values are 3.8 and 4.8 respectively for “R” and “N” polarization angles distribution, revealing that the semblance with lineaments is higher for polarization angles rotated by 90°.

Nevertheless both statistics found a too large number of Gaussians, considering that peaks are distributed in the interval 0°-180° and that the standard deviation is on average 6°. Peaks allotment may be imputed to slight variations of a random distribution of azimuths polarization, and rose diagrams should include the full spectrum of 180° azimuths. Unfortunately, being a polimodal distribution, no statistical test is possible to be applied to check significance, excluding the possibility that polarization angles are randomly distributed all over Italian territory.

A non conventional approach is tried, calculating the RMS values obtained by 100000 synthetic distributions of 8 azimuth randomly generated in the range 0°-180°. At each iteration they are sorted and compared to the 8 polarization peaks mean directions in Figure 3.11, from rotated and not rotated statistics. The RMS value are calculated and plotted in Figures 3.12a and 3.13a, resulting respectively from the comparison with “R” and “N” mean directions. The histograms (Figures 3.12b and 3.13b) and cumulative histograms (Figures 3.12c and 3.13c) are displayed too. For each distribution, a parameter α is calculated as the percentage of the 100000 RMS values (calculated from polarization mean direction and random population) lower than an RMS threshold. This threshold is represented by RMS values previously found by comparing polarization (“R” and “N”) and lineament domains mean directions (3.8 and 4.8, respectively). Furthermore this parameter represents the probability that the distributions would be random, and it is useful to evaluate the reliability and the randomly of polarization distributions without needing statistics tests.

The distribution “R” from rotated polarization angles shows a probability to be random $\alpha=0.001\%$, more than one order of magnitude lower than “N” distribution. As previously explained even the RMS value from the comparison with domains is lower for “R” distribution. This led to the conclusion that “R” distribution from polarization angles rotated by 90° has a

lower probability to be produced by a random distribution and an higher semblance with lineament domains. Thus it is considered to be more representative.

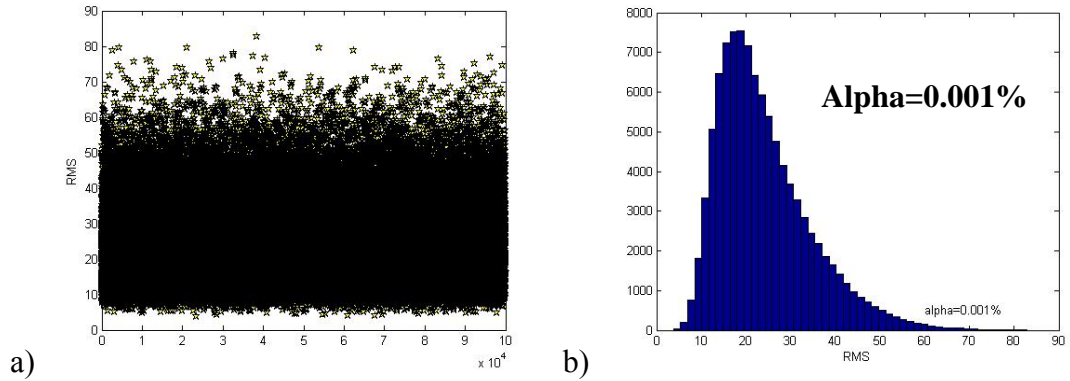


Figure 3.12 – RMS calculation for 100000 synthetic distribution of 8 angles randomly generated in the range 0°-180°. These values are compared with the peaks of the rose diagram by polarization rotated angles “R”, displayed in Figure 3.11R.

a) RMS values (on y-axis); b) histogram of RMS values (on x-axis); c) cumulated histogram of RMS values (on x-axis).

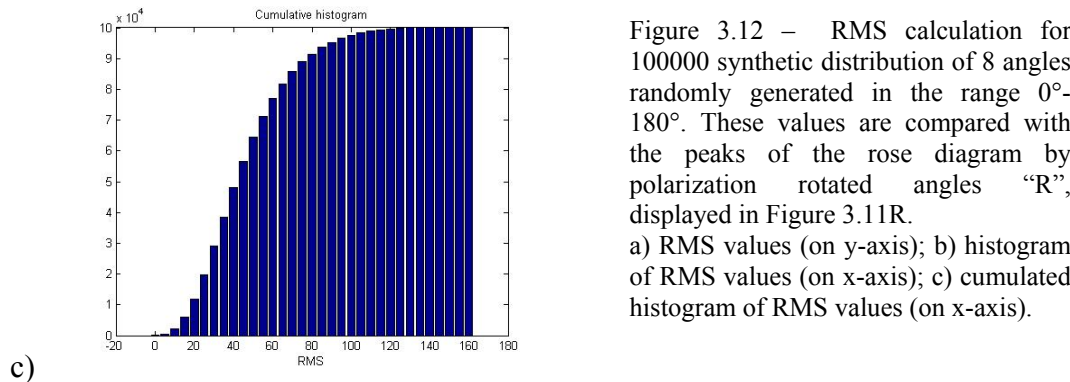
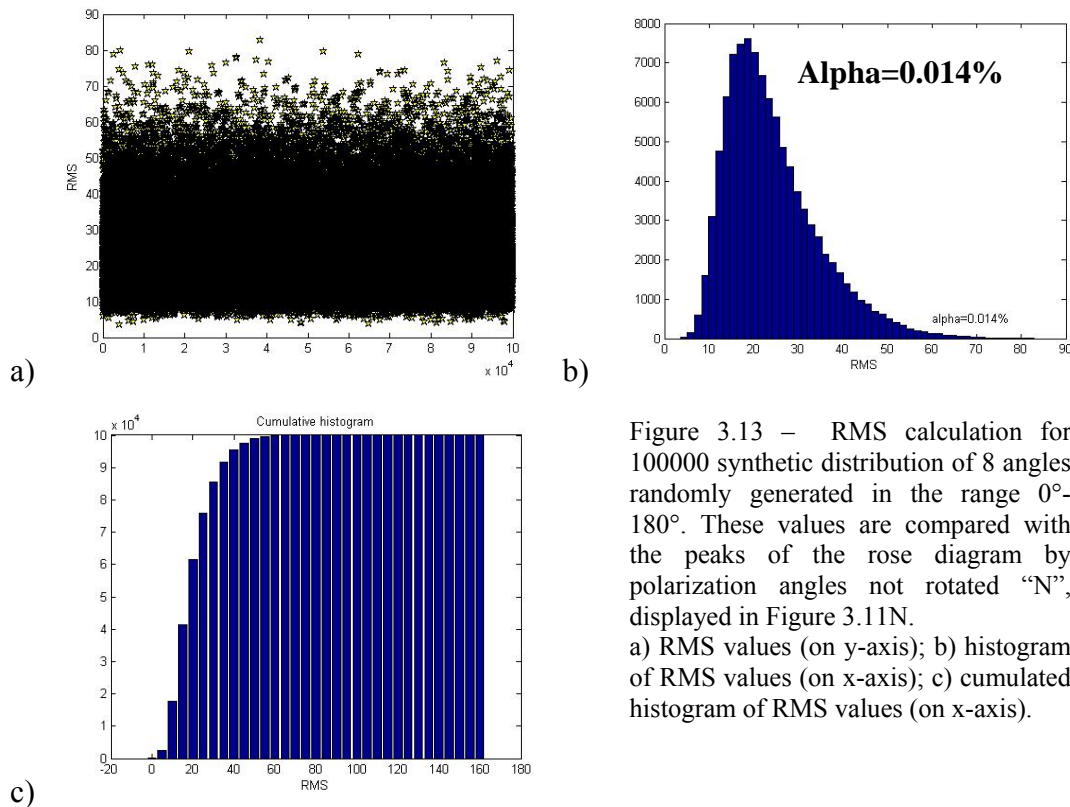


Figure 3.13 – RMS calculation for 100000 synthetic distribution of 8 angles randomly generated in the range 0°-180°. These values are compared with the peaks of the rose diagram by polarization not rotated angles “N”, displayed in Figure 3.11N.

a) RMS values (on y-axis); b) histogram of RMS values (on x-axis); c) cumulated histogram of RMS values (on x-axis).



3.5 Conclusions

The analysis performed on 30 minutes ambient noise on the Italian seismic network, reveals that polarization is quite recurrent noticeably involving at least 30% of total stations.

The correlation with topography (investigated in detail in Chapter 4) is identified on 60% stations, where the angles between ridge alignment and polarization lies in the range 70° - 90° .

An interesting relation is explored using the directions of lineament domains, which reflect stress state and tectonics at the regional scale, where topography and tectonic features are coaxial. A very good correlation is found with polarization mean directions rotated by 90° , identifying a transverse relation between polarization and lineaments swarms azimuths.

Furthermore this is in agreement with observation of topographic amplification effects (Chapter 4) and with polarization across fault fractured zones (Chapter 5).

Chapter 4

Topographic amplification and polarization

effects

4.1 The amplification due to topography

The topographic amplification of seismic waves has received an increasing interest in the last three decades following observations of large amplification on mountain tops, combined with the importance of some of the structures typically built on elevated topographies (e.g., communication and power supply pylons, Kurita et al.2003).

The studies on this effect deal with two types of observations. The former is related to the detection of anomalous arrivals in seismograms recorded on topographic relieves (as observed by Talet, 1954; Gilbert & Knopoff, 1960; Key, 1967; Hudson, 1967; Greenfield, 1971). These phases, consisting mostly of Rayleigh waves, were identified as energy scattered by topographic irregularities (Boore et al. 1981; Bannister et al. 1990; Gupta et al. 1990; Wagner & Langston, 1992; Clouser & Langston, 1995). The latter observation was the recording of very high accelerations during the San Fernando earthquake of 1971 at Pacoima Dam, a site located on a topographic hill (Trifunac & Hudson, 1971; Boore, 1973). The numerical models performed for this hill confirmed that the acceleration level recorded could be ascribed to the topography (Boore, 1972; Bouchon, 1973).

After that, the interest has continued and many works have been performed on mountain ridges and hills. Observation of amplification on mountain tops during earthquakes have been reported by several authors (Davis and West, 1973; Griffiths and Bollinger, 1979; Bard and Tucker, 1985; Çelebi, 1987; Umeda et al., 1987; Pedersen et al., 1994a; Chavez-Garcia et al, 1996; to quote only a few among many) and has been observed during the 1989 Loma Prieta earthquake (Ponti & Wells 1991, Hartzell et al. 1994), and during the 1994 Northridge earthquake (Shakal et al. 1994). Also the damage pattern during the 1987 Whittier Narrows earthquake (Kawase and Aki, 1990) were attributed to a topographic effect. Even another kind of observations were done in

epicentral areas where the shaking can reach high level, as the disruptions of rocks near hill crest (Nanson, 1971, Umeda, 1992, Bouchon 1996) and as shattered earth at the top of prominences.

These studies confirmed that a hill or a ridge can produce an amplification near the hill top or the ridge crest.

The recurrence and consistency of these observations has motivated much work both on the theoretical investigation and on the numerical simulation of the diffraction of seismic waves caused by the hill shapes (Trifunac, 1973; Sabina & Willis, 1975; Wong & Jennings, 1975; Singh & Sabina, 1977; Sills, 1978; Sanchez-Sesma & Rosenblueth, 1979; England et al., 1980; Ilan & Bond, 1981; Bard, 1982; Sanchez-Sesma et al., 1982; Shah et al., 1982; Wong, 1982; Ohtsuki & Harumi, 1983; Bard & Tucker 1985; Bouchon, 1985; Géli et al., 1988; Kawase, 1988; Anoshehpour & Brune, 1989; Gaffet & Bouchon, 1989; Sanchez-Sesma & Campillo, 1991; Pedersen et al., 1994b; Takemiya & Fuijwara, 1994; Le Brun et al., 1999, Paolucci, 2002) .

The simulations and the observations are in qualitative agreement about the amplification of seismic waves near the hill top and for wavelengths comparable to the mountain width. The disagreement concerns the calculated amplification level that always underestimates the amplification observed in the field. Numerical simulations predict that near the hill slopes and close to the hill base, amplification and deamplification alternate as a function of frequency. This makes the choice of a reference station in the field a hard work because it could be biased by the topographic effect.

The discrepancy between observations and numerical simulations may be due to a complex geology beneath the mountain, a complicated incident wave field, or a more complex topography than the ones introduced in the models; e.g., subsurface layering (Bard and Tucker, 1985; Geli et al., 1988), neighboring topography (Geli et al., 1988), or three-dimensional (3D) effects (Sanchez-Sesma, 1983; Pedersen et al., 1994).

4.2 The influence of topography on polarization

Beside the amplification effect, topographic irregularities have been recognized to produce directional effect of resonance; the scattered wave field is polarized in the direction transverse to the hill major axis, as firstly reported by Spudich et al. (1996).

During the 1994 Northridge mainshock, high accelerations (up to 1.78 g) were recorded on the EW component at a site in Tarzana, California, located about 6 km of the epicentre. The sensor was located on the top of a small hill, 15m high, 500m long, 130-m wide and striking about N70°E. After the mainshock, they deployed a denser array recording several aftershocks, and concluded that a directional topographic effect was produced in Tarzana at 3.2 Hz, corresponding to a transverse oscillation of the hill. In fact there was a difference by a factor of 2 between the top/base amplification ratio calculated in the transverse direction (perpendicular to the long axis of the hill) and the same ratio in the parallel direction.

The comparison between observation and the theoretical study by Bouchon et al. (1995) and the numerical simulation by Bouchon & Barker (1995) confirmed the frequencies amplified and the dominance of the transverse motions over the parallel, but underestimated amplitudes. They ascribed this discrepancy to the internal hill structure as well as to some geological features not included into modelling.

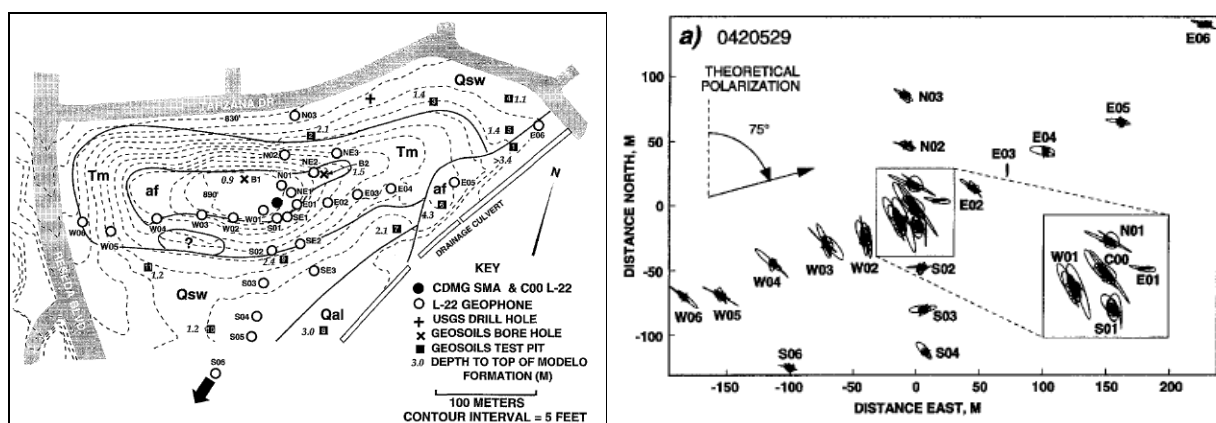


Figure 4.1 – From Spudich et al. (1996). LEFT PANEL: Map of topography (dashed contours), surface geology, and instrument layout, Cedar Hill Nursery. Locations of geologic contacts (solid lines) are approximate. Map unit symbols: af, artificial fill; Qsw, slope wash (Quaternary); Qal, alluvium (Quaternary); Tm, Modelo Formation (Miocene). RIGHT PANEL: Map of particle motions for one selected aftershock. The time series were filtered with a low-pass filter at 4 Hz. Arrow shows expected polarization.

4.3 Nocera Umbra hill case study



Figure IV – Nocera Umbra town view from its northern side (Redrawn from MarcoUzielli thesis).

The town of Nocera Umbra is a typical ancient settlement of central Italy built on a gentle hill and composed mostly of buildings from 18th century. It suffered moderate to heavy damage (MCS intensity VII-VIII) during the two M_w 5.7 and 6.0 Umbria-Marche earthquakes of September 26, 1997. To explain the damage level, two possible causes can be invoked: the town location on the hill top which represents a condition potentially favorable to ground motion amplification, and the high vulnerability of ancient buildings.

To study the effect of topography at a greater detail, ground motion waveforms are here analyzed, and the results are compared with numerical simulation of the hill seismic response.

4.3.1 The damage observed after 1997 earthquakes

On September 26, 1997, at 0:33 GMT a Mw 5.7 earthquake occurred in the Umbria-Marche Apennines, central Italy, with epicenter located between the villages of Cesi and Colfiorito (Amato et al., 1998). This event was followed nine hours later by a Mw 6.0 earthquake, located north of the previous one, between the villages of Colfiorito and Annifo (Figure 4.2). Of these two shocks, the Mw 6.0 earthquake caused the highest damage in Nocera Umbra as the distance from the causative fault was less than 10 kilometers. Significant damage occurred in the historical centre of the town, that, similarly to many historical settlements in the Apennines, was built and developed on the top of a hill. However, no total collapse was observed, except for the ancient (Middle Ages) bell tower situated in the southern part of the hill top (Donati et al., 2001).

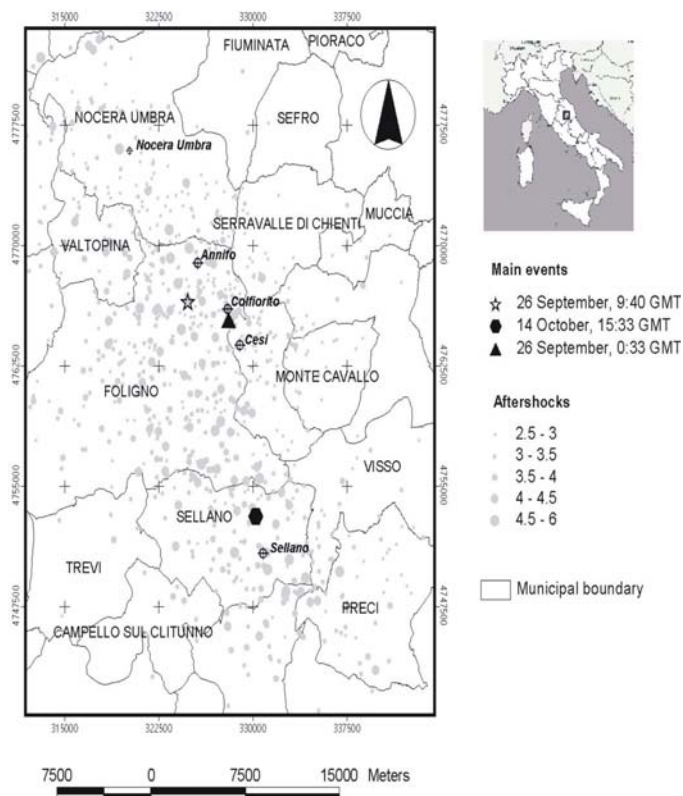


Figure 4.2 – Location of study area, mainshocks and Colfiorito-Sellano seismogenic area aftershocks epicentres.

The building stock in the historical sector consists of regular or irregular masonry, mostly from 18th century, of different degree of quality and without earthquake-resistant design, which have often been modified over the years, without coherence with the original structure. In their work, Donati et al. (2001) assessed that about 90% of the buildings in the historical centre is made of simple stones with poor mortar, as typically found in the ancient settlements of central Italy, and it can be identified with type A of the European Macroseismic Scale (EMS-98, see Grünthal

1998). However, the less vulnerable buildings (EMS-98 type B) on the hill top experienced a damage grade comparable to the undisturbed bedrock, and they are more representative of the level of shaking. This led Donati et al. (2001) to ascribe the occurrence of diffuse damage on the hill top to the predominance of highly vulnerable buildings of type A (see Figure 4.3).

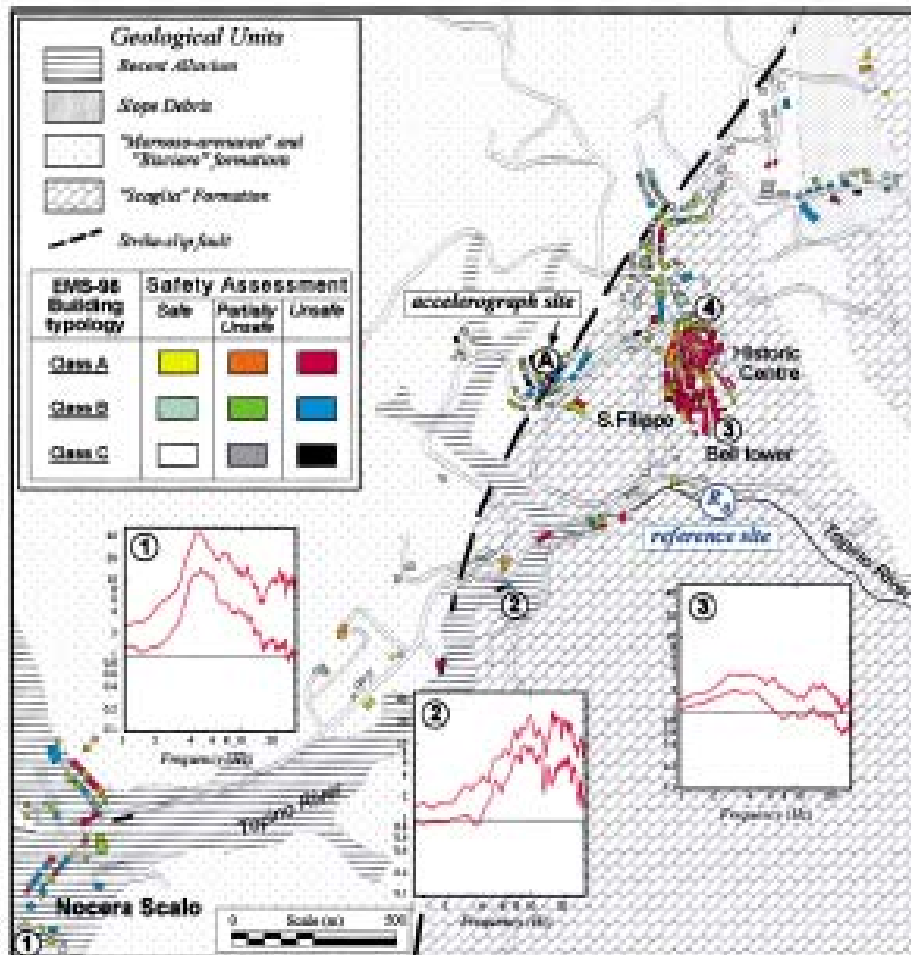


Figure 4.3 – From Donati et al. (2001). Damage distribution in Nocera Umbra area. The different colours represent building typology and damage degree. The three panels show the average amplification of horizontal ground motion of sites 1, 2, and 3 as estimated by Caserta *et al.* (2000) with respect to the undisturbed rock site R_0 . The two curves in each panel represent the ± 1 standard deviation interval around the average spectral ratios.

In principle, topography could have played an important role in increasing the damaging effects. During the long and intermitted seismic activity which lasted several months up to June 1998 (Amato et al., 1998; Deschamps et al., 2000), many experiments were conducted in the town of Nocera Umbra to determine local amplifications and their relations with the different geological features (Marra et al., 2000; Caserta et al., 2000; Rovelli et al., 2002; Cultrera et al., 2003). A possible topographic effect was already observed by Caserta et al. (2000), who applied the standard spectral ratios, the receiver function technique and the Nakamura (1989) method to one station deployed on the hill top, where the amplification attained a factor of 2.5 in the frequency band 2 - 5 Hz.

4.3.2 Geological setting

The study area is located in the Umbria-Marche sector of central Apennines. The outcropping lithotypes belong to the silico-carbonate pelagic sequence known as “Umbria Marche Formation”, a multi-layered alternation of limestones, marly limestones, marls, and flysch sequences. These geological units were first deformed by a compressional structural phase, during the belt construction, but they have been subsequently dissected by the Quaternary extensional regime (Calamita et al., 1994). Many of the structures which were formed during the compressional phase were then reactivated as normal faults. This extensional tectonic regime is also the main cause of the current seismicity of the area, and the 1997-1998 seismic sequence was the most recent manifestation of the activity of these faults. The town of Nocera Umbra was settled on a NNW-SSE trending anticline, where Eocene-Oligocene limestones (Scaglia Formations) overthrust a Miocene flysch sequence (Marnoso-Arenacea Formation) with north-eastward vergence, in agreement with the original NE-SW trend of the Apenninic belt.

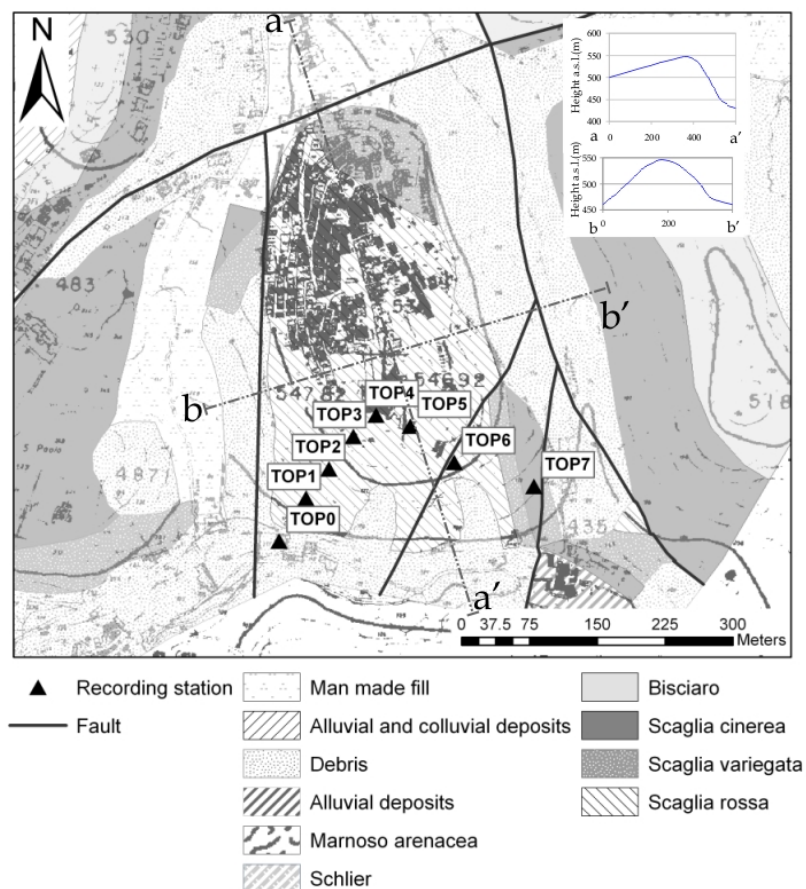


Figure 4.4 – Geological sketch and position of the seismic array on the Nocera Umbra hill. The insets show the topography profiles along the major and minor axis as used in numerical simulations

On the western flank of this anticline, the contact between the carbonatic formations and the Marnoso-Arenacea occurs along a N30°E segment of a regional lineament that extends from the town of Gualdo Tadino down to Capodacqua, with an average N-S trend (Marra et al., 2000, Rovelli et al., 2002). It had formed during Pliocene as right-lateral strike-slip fault, and was reactivated as a normal-to-oblique fault during the Pleistocene extensional phase. This shear zone is responsible for intense degree of fracturation in the outcropping limestones about 500 m from the hill, with decreasing spacing and intensity at increasing distance from the shear zone (Tirelli, 2002).

The hill is elongated in the NNW-SSE direction, with a maximum height of 574 m a.s.l.. The northern side is quite gentle while the southern one is very steep, therefore the longitudinal section is asymmetric with a narrow summit part. In contrast, the transverse section is more regular and symmetric, with a base width of about 400 m (Figure 4.4).

4.3.3 Analysis method & results

To study the effect of topography at a high detail, an experiment was performed during May and June 1998 when a seismic array of 8 stations (Guralp CMG40T seismometers coupled to Reftek 72A07 24-bit digitizers) was deployed on the southern side of the hill. One of the stations (TOP0) was installed at the base of the hill, on a calcareous-marl site, already used as the reference site of previous studies in the Nocera Umbra area (Caserta et al., 2000; Marra et al., 2000; Rovelli et al., 2002; Cultrera et al., 2003).

The array recorded about 134 events, whose hypocenters were taken from the bulletin of the Italian Seismic Network run by the Istituto Nazionale di Geofisica e Vulcanologia (INGV, www.ingv.it). Earthquakes come from two main seismogenic areas: Colfiorito-Sellano area, located 10-35 km SSE from the array, and Gualdo Tadino area, 10-20 km to the north. The hypocentral depths are in the range 5 to 12 km.

At a first step of the analysis, the events with the highest magnitude (M_L between 2.6 and 4.1) simultaneously recorded by at least 5 stations, including the reference one (TOP0) were selected. Then, the signal-to-noise ratio was computed and this check conditioned the selection of the final data set. Only few events recorded by TOP7 were included. A seismometer malfunction is observed at TOP1, as records show a very low signal-to-noise ratio, therefore the station was not included in the analysis. The rest of the stations showed a good signal quality in the frequency

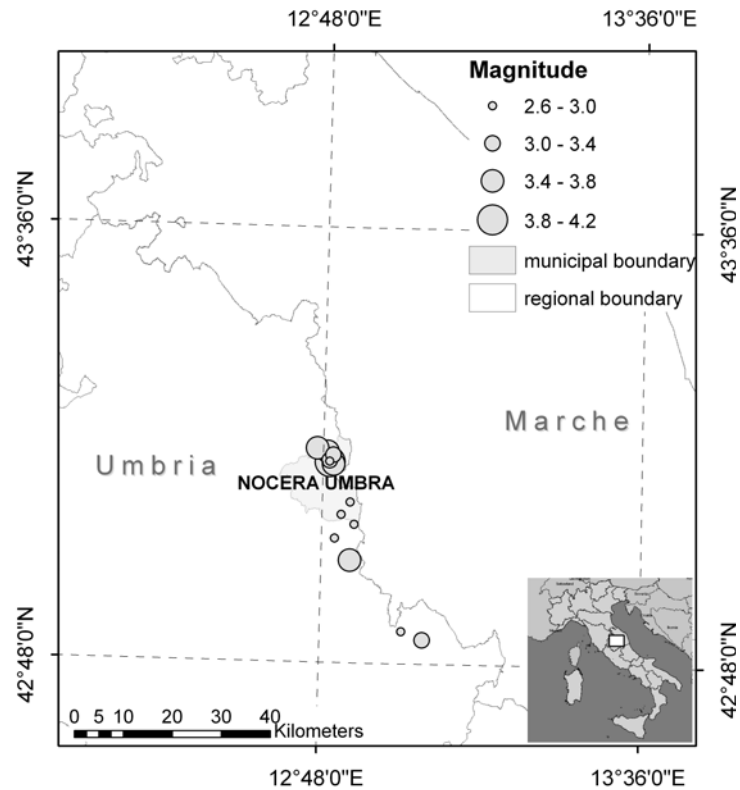


Figure 4.5 – Seismic events recorded by the array and location of the two source areas.

Day/hr/min	Lat.N	Long.E	Depth Km	M_L	Back- azimuth	Top0	Top2	Top3	Top4	Top5	Top6	Top7
21/05/98 09:40	43.1720	12.8159	12	2.4	16	*	*	*	*	*	*	
21/05/98 14:05	43.1699	12.8159	10	1.9	16	*	*	*	*	*	*	
21/05/98 22:07	42.9889	12.8719	8	3.0	146	*	*	*	*	*	*	
23/05/98 18:30	42.845	13.057	10	2.1	135	*	*	*	*	*	*	
25/05/98 06:23	42.86	13.0039	10	1.7	139	*	*	*	*	*		
27/05/98 03:00	43.0730	12.8479	5	1.7	121	*	*	*	*	*	*	
28/05/98 03:01	43.1879	12.8109	10	2.1	14	*	*	*	*	*	*	
28/05/98 06:22	43.096	12.8699	10	1.7	97	*	*	*	*	*	*	
30/05/98 23:11	43.0289	12.833	6	1.6	153	*	*	*	*	*	*	
31/05/98 21:05	43.0550	12.881	10	?	119	*	*	*	*	*	*	*
01/06/98 14:40	43.165	12,826	5	2.8	27	*	*	*	*	*	*	*
01/06/98 17:32	43.1819	12.8249	7	2.1	21	*	*	*	*	*	*	*
02/06/98 23:11	43.1689	12.817	9	4.1	18	*	*	*	*	*	*	*
04/06/98 00:41	43.194	12.7849	10	2.4	354	*	*	*	*	*	*	*

 Table 4.1 – List of earthquakes used in this study. Localization and M_L are taken from the bulletin of the Italian Seismic Network. Asterisks indicate the recording station.

band chosen for the analysis. In order to explore the influence of the direction of the incident waves on the amplification effect, the events were separated in two groups on the base of their source backazimuth. The signals were cut starting 1s before the direct S arrival and including the significant duration of the recording (about 10 s), which was detrended and then windowed by a Hanning taper.

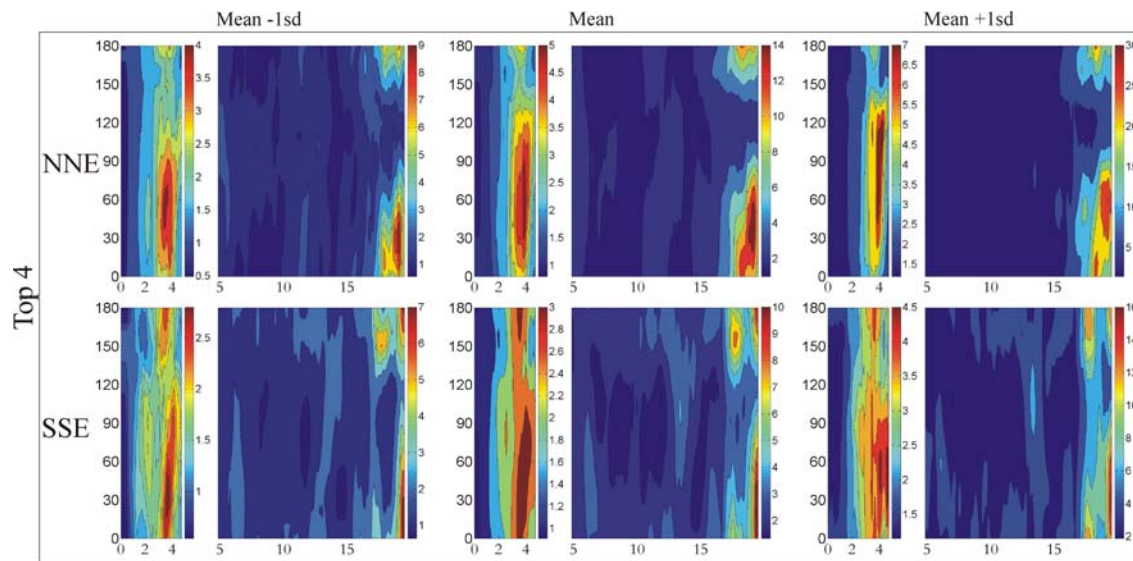
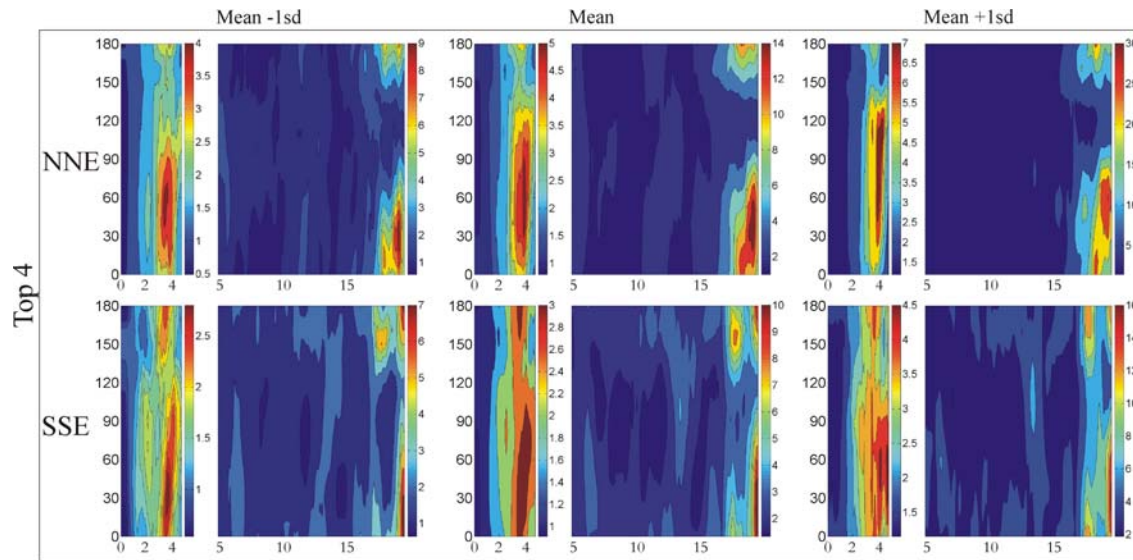
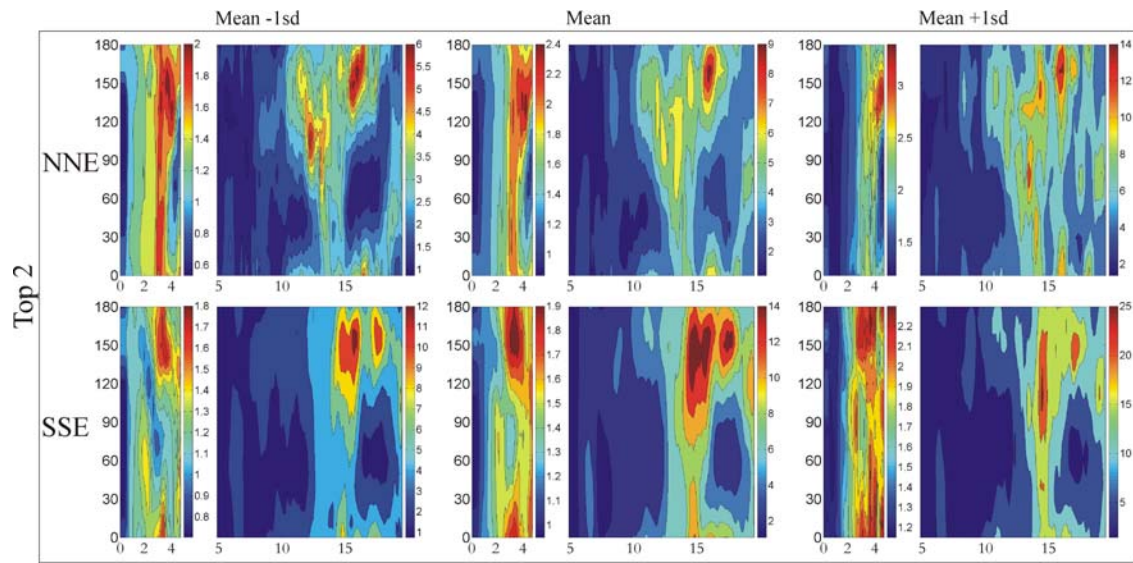
To quantify the level and the frequency band of amplification and investigate possible directional resonance effects, standard spectral ratios (SSRs) using the reference site (TOP0) were calculated after applying a smoothing filter through a 0.4 Hz running frequency window.

The SSRs are exhibited in Figure 4.6. In each panel, two frequency bands ($2 < f < 5$ Hz and $f > 5$ Hz) are shown with a different amplitude scale. The directional resonances are recognized looking at the peaks in the contour map, where frequency and polarization angle are indicated in abscissa and ordinates, respectively.

The frequency band 2 - 4 Hz is in general characterized by a moderate amplification and pronounced horizontal polarization. The largest amplifications, up to a factor of 4, occur at stations located on the hill top (TOP3, TOP4, TOP5) at a frequency of about 3.5. Stations deployed on the hill flanks (TOP2, TOP6, TOP7) reach a maximum amplitude of 2.5, approximately. Even though the level of amplification is not very high, the amplified frequency band can be related to the resonance frequency of a large part of buildings, being the three-storey houses the predominant building typologies.

Exploring the dependence of amplification on source backazimuth, the greatest amplitudes are found for earthquakes incident from NNE. Moreover, while the analysis performed for the NNE earthquakes detects a prevalent N60°E polarization at all stations, earthquakes from SSE produce a systematical N40°E polarization. The unique exception is station TOP7, where the greatest amplitudes are observed for earthquakes from SSE. However, these variations are not significant and an interpretation is difficult without taking into account coupling mechanisms of source and propagation effects in a 3-D geometry.

Large amplifications also occur at frequencies above 10 Hz often exceeding a factor of 20, especially for those stations located on the western flank of the hill, but the polarization pattern is very scattered.



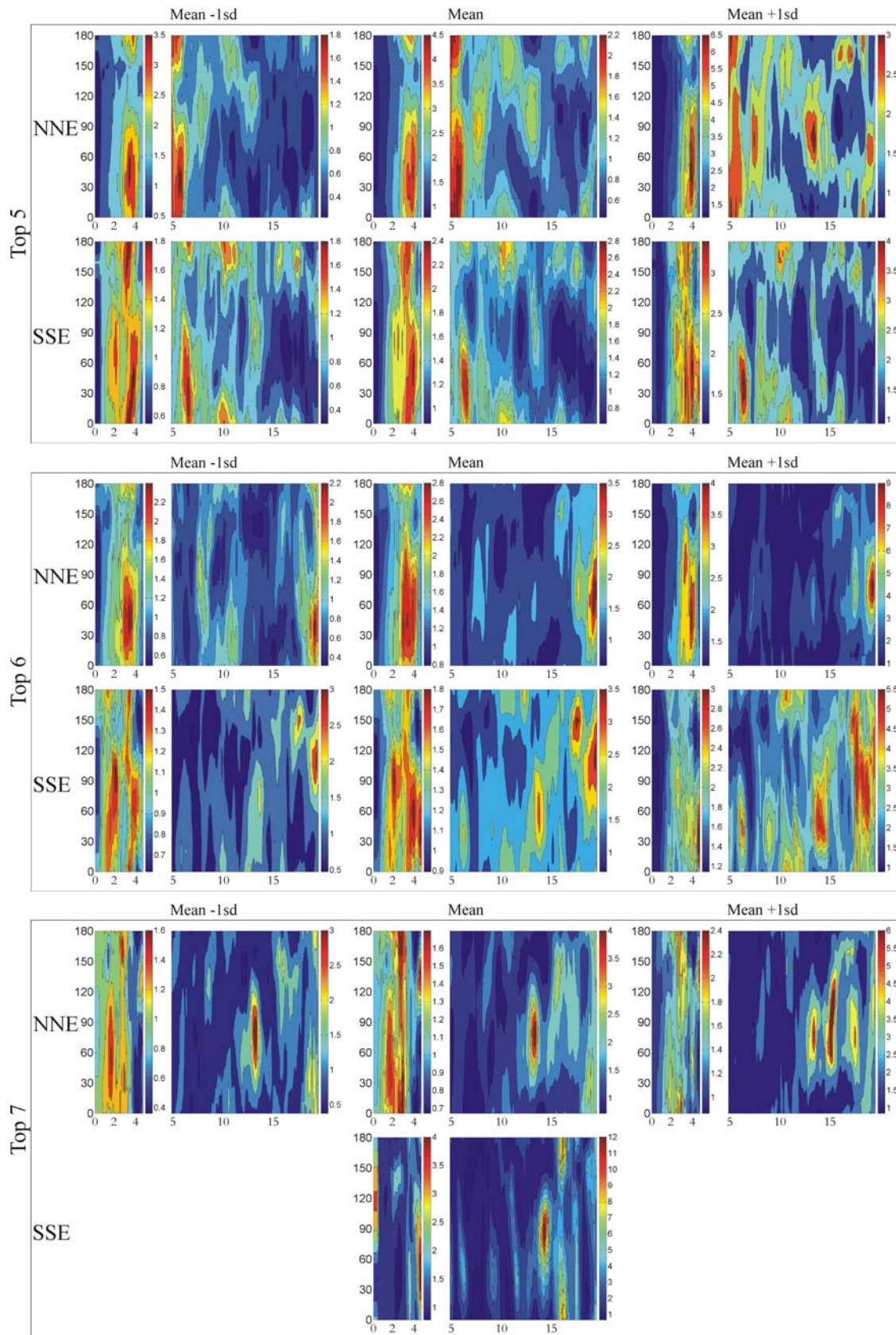


Figure 4.6 – Contour plots of geometric mean \pm 1 standard deviation as a function of frequency in abscissa and azimuth of motion in the ordinate. Events from the two source zones active during the experiment (NNE and SSW) were considered separately. For the station TOP7, only one event was available from SSE source.

In order to achieve a better resolution in the polarization angle, the covariance matrix method is also applied. In the frequency bands 2-5 Hz and 5-10 Hz the polarization is evident in the NE-SW direction, parallel to the minor hill axis. In the high frequency band (10 – 20 Hz) a common trend is not identifiable, since each station shows different polarization features both in terms of direction and frequency. The only station which does not show any polarization above 10 Hz, for events from SSE, is TOP5, whereas TOP2 changes the polarization angle from N50°E in the frequency band 2.5-4 Hz to N120°E-N140°E between 10 and 20 Hz. Station TOP3 is unique in showing a regular behavior with similar polarization at all frequencies.

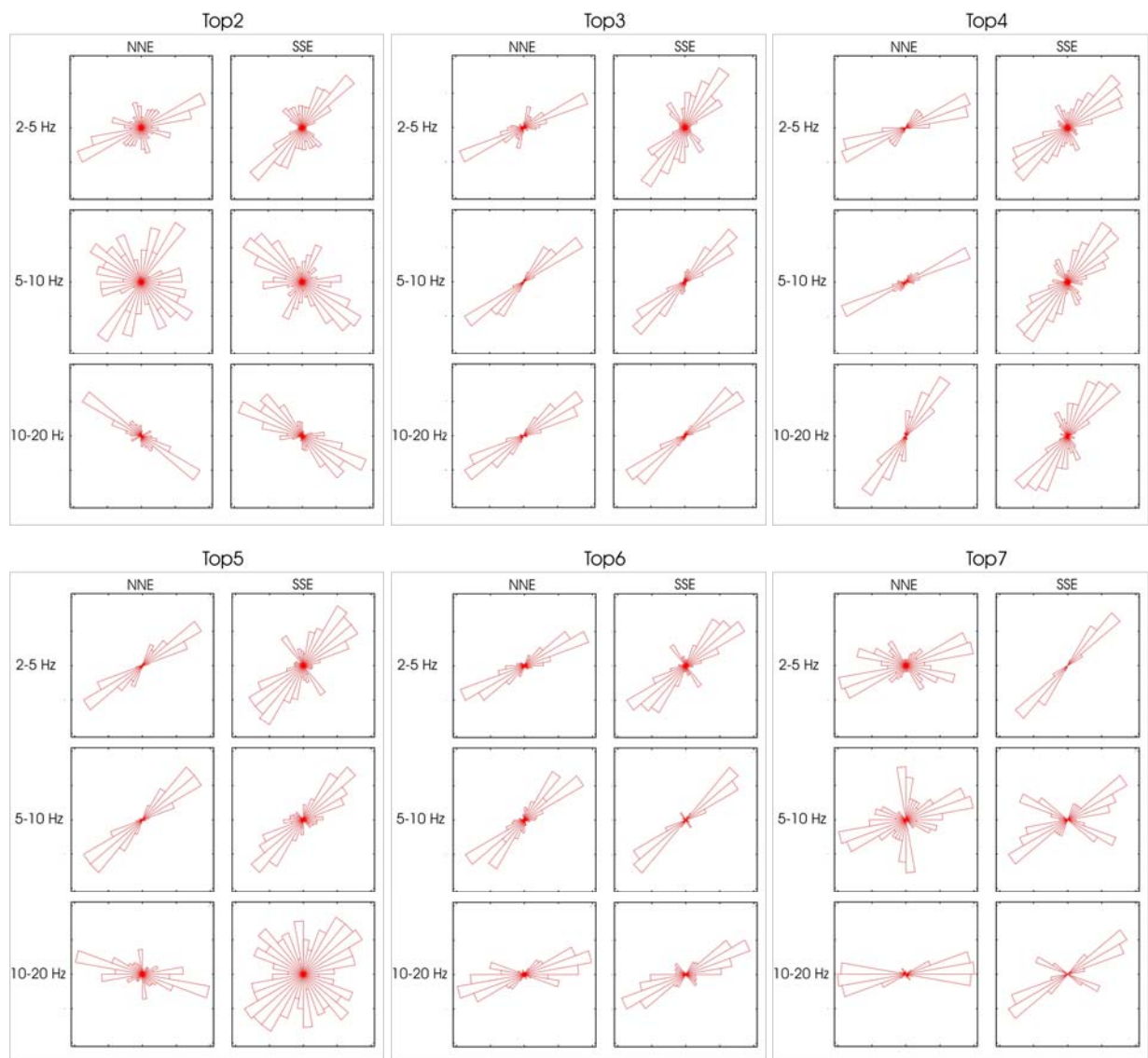


Figure 4.7 – Rose diagrams representing the results of the covariance matrix analysis applied to single station for two groups of azimuth and three frequency bands.

The earthquake data analysis shows that the amplification occurring at about 3.5 Hz is likely consistent with a topographic effect, considering its spatial distribution and that the observed

spectral peak is consistent with the expected order of magnitude of the resonance frequency $F_0=V_s/L$ (Bouchon, 1973; Geli et al., 1988), where L is the topography width (about 400 m) and V_s is shear velocity of outcropping limestones. In situ downhole measurements at a site 500 m away (GNDT, 1999) show values of about 1000 m/s at the hole bottom, in the same geological formation.

4.3.4 2D numerical models

The pattern of the hill is quite complex in its details. In order to better interpret the ground motion observations, numerical simulations of the hill seismic response were performed.

The model

In a first step the 3D shaped hill is approximated with two 2D models, parallel and transverse to the hill major axis (N20°W), respectively. The models reproduce an infinitely elongated topography with cross-sectional shapes which correspond to longitudinal and transversal profiles of the hill. To be consistent with the observed mostly transverse polarization, for the longitudinal section the out-of-plane modeling has been chosen while for the transverse section the in-plane modeling was performed. In order to simulate the topography effects, neglecting smaller scale heterogeneities, no geological or lateral discontinuities were introduced in the half-space, and the effect of neighbouring topographic irregularities (Geli et al., 1988) has been neglected. The materials were assumed to be homogeneous, with shear wave velocity equal to 1200 km/s (the bottom downhole value increased by 20%), a ratio between compressional and shear wave velocity, V_p/V_s , equal to 2 (Michellini et al., 2000), density equal to 2.2 Kg/m³ and quality factor Q_p and Q_s equal to 50.

Input signal

The seismic input is represented by a Dirac-like Gabor impulse $G(\gamma, t_s, f_p, \varphi)$, with vertical plane-wave incidence (Caserta et al., 2000) :

$$G(\gamma, t_s, f_p, \varphi) = e^{-\left[\frac{2\pi f_p(t-t_s)}{\gamma}\right]^2} \cos[2\pi f_p(t-t_s) + \varphi]_0$$

where f_p is the maximum frequency at which the normalized Gabor's spectrum is 30%, φ is the initial phase and $t_s=0.45\gamma/f_p$. The Gabor inputs used in the models are shown respectively in each picture with their specific parameters.

Simulation parameters

The web interface “WISA” (Santoni et al., 2004), available at CASPUR (Consorzio Interuniversitario per le Applicazioni di Supercalcolo Per Università e Ricerca; www.caspur.it) was used to create the two models and run simulations. For the out-of-plane model (SH waves), WISA applies a finite-differences method (Caserta, 1998), whereas for the in-plane model (P-SV waves) it uses a finite-elements approach (Lanucara et al., 2004). All the numerical simulations were carried out through an IBM SP5 cluster.

Results

To visualize ground motion variations due to topography, the delta-like response of the hill is investigated (Figures 4.7 and 4.8, top panels). Then the Fourier amplitude spectra of synthetics are calculated, smoothed with a 1-Hz moving box and divided by the corresponding reference one, obtaining synthetic SSRs.

As a reference spectrum, in the out-of-plane case a receiver is used at the bottom of the model simulating a borehole seismic station; conversely, for the in-plane case, the reference input is computed using a flat topography model with the same elastic and anelastic parameters.

Then the spectral ratios between synthetics and reference (synthetic SSRs) are calculated and plotted along the topographic profile obtaining the results shown in Figures 4.7 and 4.8 (bottom panels).

In both the longitudinal and transverse models, two peaks are observed on the hill top, in the frequency bands 2-4 Hz and 10-14 Hz. Amplitude levels are always smaller than the experimental ones being lower than 1.4 and 1.8 for the SH and P-SV waves, respectively. The in-plane model (Figure 4.7) shows a more regular, symmetric transient-response around the major hill axis. On the hill top a first frequency peak, between 2 and 3 Hz, is clearly visible and a second amplified frequency band is observable between 10 and 12 Hz, consistently with spectral ratios obtained from the recordings. In correspondence with the hill slopes, a significant deamplification can also be noticed. The result of the out-of-plane model (Figure 4.8) is more complex than the in-plane one, because of the asymmetric shape of the cross-section. On the hill top, two frequency bands (2 - 4 Hz and 10 -15 Hz) are amplified whereas along the steepest side (SSE flank), the amplification occurs in a wider frequency band (5 - 14 Hz).

In order to relate the spectral peaks to the hill resonances, two additional simulations are performed for both the in-plane and out-of-plane cases, according to the approach of Bard and

Bouchon (1985) and Moczo et al. (1995). Two nearly-monochromatic Gabor functions peaked at 2.5 and 11 Hz are used to excite the model (for the technique details see Moczo et al., 1995). The resulting synthetics, shown in Figures 4.9 and 4.10, provide useful elements for a physical interpretation of topography resonances. In fact, when both in-plane and out-of-plane models are excited with the 2.5 Hz peaked Gabor, as shown in Figures 7 and 8 mid panels, the motion is in phase across the whole topography and amplitudes attain their maximum on the hill top, regularly decreasing toward to the slopes. This pattern is consistent with the fundamental mode and the peak observed in the in-plane model, between 2 and 3 Hz, can be identified as the fundamental mode (Figure 4.9), with a wavelength corresponding to the hill base width (460 m). In the out-of-plane model, the hill base has the same width as the in-plane one (about 500 m), resulting in a similar fundamental frequency.

Conversely, when the excitation frequency of the Gabor function is 11 Hz, the resulting amplification pattern is more complex. The transient-response of the symmetrical in-plane model is easier to interpret, as in the middle of the hill slopes the motion is equal to zero being in phase with opposite sign. In total three local maxima are generated, one at the hill top and the other two symmetrically on each slope. This behaviour can be related to the second higher mode of the in-plane model. It can also be recognized in the out-of-plane model even though the two zeros are shifted towards NNE because of the hill acclivity on the SSE side.

Both the in-plane and the out-of-plane models show that the Nocera Umbra hill can amplify ground motion between 2 and 4 Hz, consistently with observations. The amplification of the 2D models is smaller than the observed one. This amplitude discrepancy can be explained considering the location of TOP0. The models clearly show that it coincides with a deamplification zone at the hill base. Therefore even the signals recorded by TOP0 could have been deamplified and this deamplification could have caused an overestimation of the empirical spectral ratios.

The observed high frequency amplification is reproduced in the models as well, but the consistency with observations is limited to the spectra of TOP3 for which the frequency band of amplification and polarization of motion are well reproduced, even though there is no agreement in terms of amplitude. In general, the other stations have a very scattered response which might be controlled by small-scale near-site irregularities not included in the models, such as rock fractures and limestone karst, presence of thin soil layers, weathering, and other possible local complications.

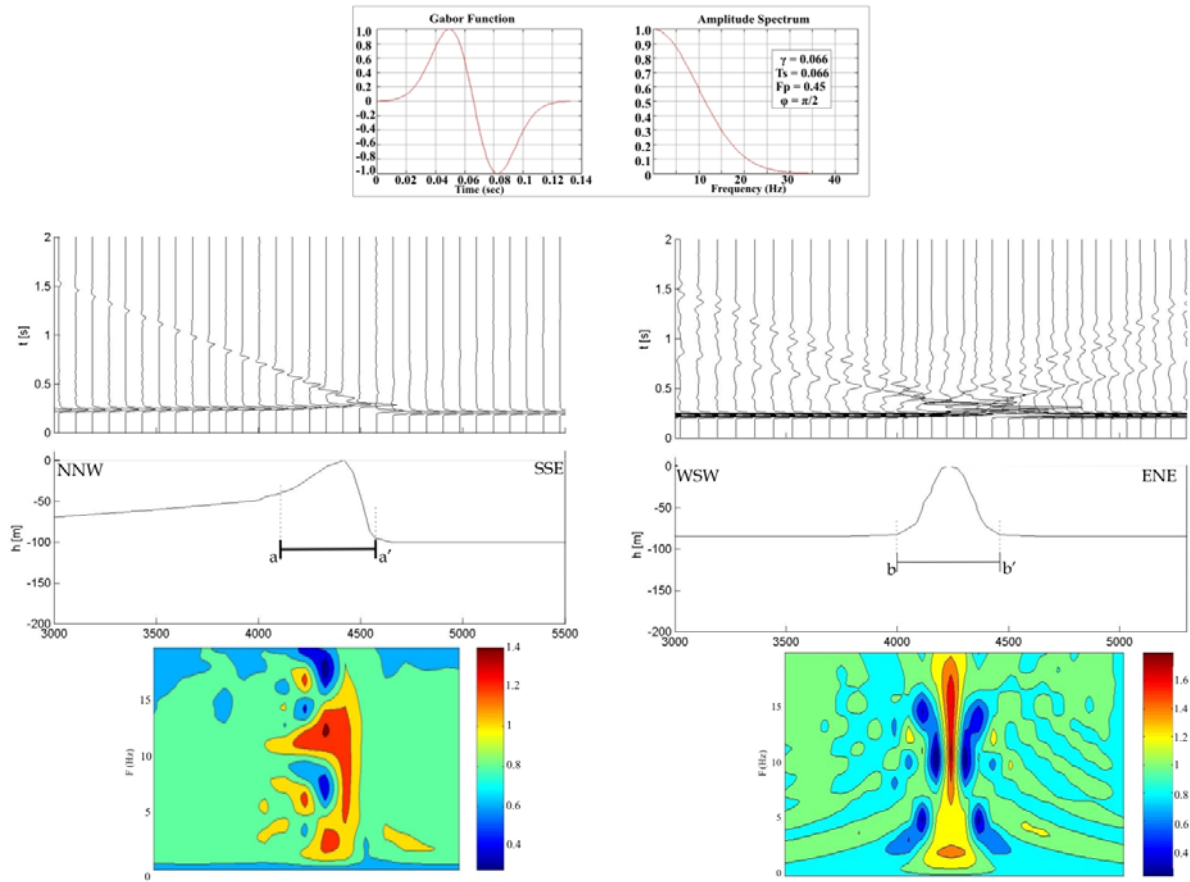


Figure 4.8 – Results of simulation for Nocera hill. TOP PANEL: Gabor input function in the time and frequency domain. LEFT PANEL: In-plane motion model. Synthetic seismograms simulated for the profile orthogonal to the main topography axis (bb' on the inset Figure 4.4) and contouring representing the frequency response of topography to a delta-like SV impulse. RIGHT PANEL: Out-of-plane motion simulation. Synthetic seismograms simulated for the profile parallel to the main topography axis (aa' on the inset of Figure 4.4) and contouring representing the frequency response of the profile to a delta-like SH impulse.

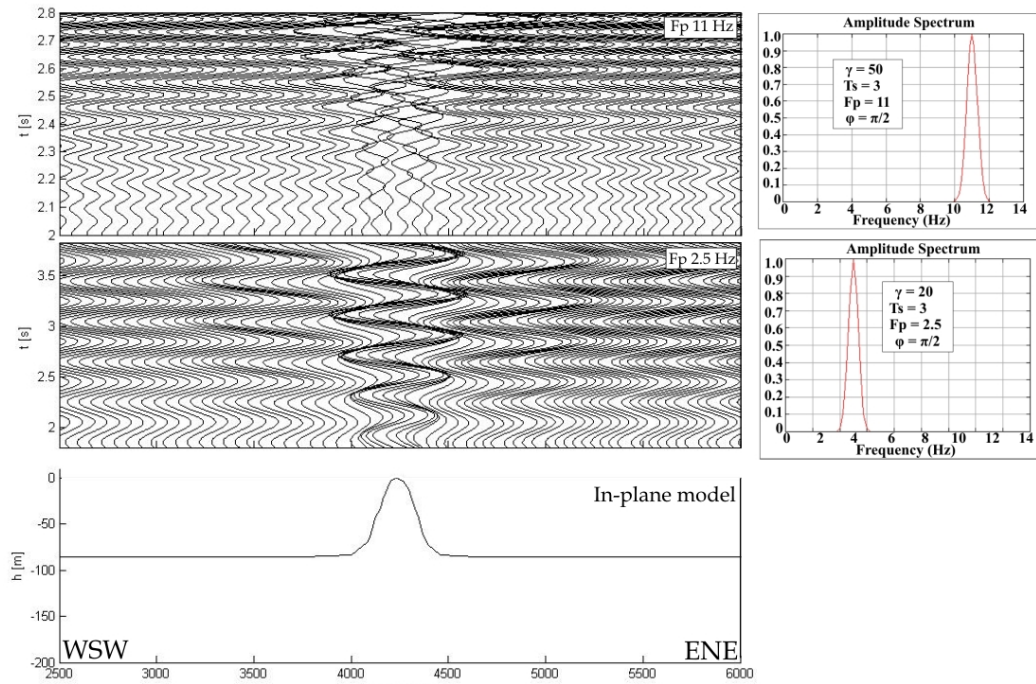


Figure 4.9 – Synthetic seismograms of the in-plane P-SV model, excited with a nearly-monochromatic Gabor function peaked at 11 Hz (top panel) and at 2.5 Hz (mid panel). On the right panels the spectra of the Gabor inputs are shown.

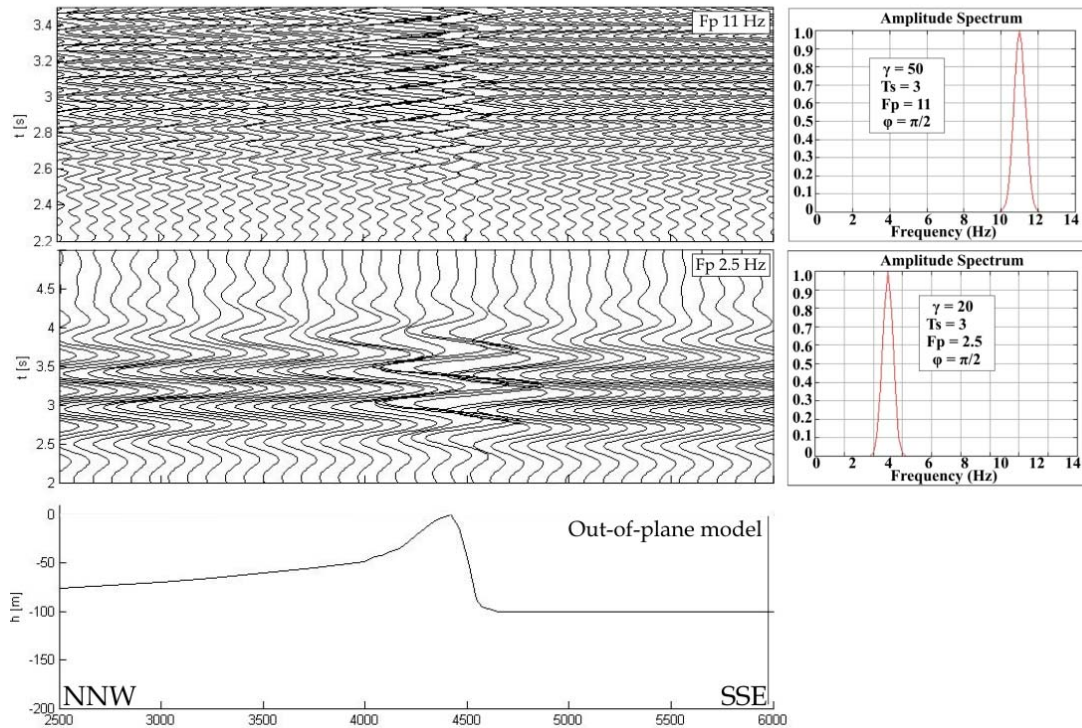


Figure 4.10 – Synthetic seismograms of the out-of-plane SH model, excited with a nearly-monochromatic Gabor function peaked at 11 Hz (top panel) and at 2.5 Hz (mid panel). On the right panels the spectra of the Gabor inputs are shown.

4.3.5 Comparison with 3D Numerical models

To understand whether the discrepancies in terms of amplification levels can be related to the 2D approximation rather than to other geological small scale factors, a comparison with a 3D simulation was done.

3D simulations of the Nocera Umbra hill were performed by Caserta & Oprsal using a DEM (1:5000). 3D simulations used two vertically incident inputs, horizontally polarized in S-N and W-E direction. The results are shown in Figure 4.11 as response spectra in five frequency bands. In the band 0.1-3 Hz is still possible to recognize the fundamental vibration mode, with an amplitude peak of a factor of 2.5 near the hill top. This evidence is clear on the two models performed with S-N and W-E polarized input, and the pattern is in agreement with 2D models.

Around 10 Hz two nodes are visible along the major and minor hill axis performed with S-N and W-E polarized inputs. Also this pattern is in agreement with 2D numerical models suggesting that this second peak is related to the second higher mode of resonance.

Two deamplification peaks are produced near the hill bases, and this is more evident on the model performed with W-E polarized Richer input pulse.

After verifying the agreement between 2D and 3D models in terms of frequencies of resonance and the resonance pattern on the hill morphology, a comparison in terms of amplitudes has been carried out. In the 3D model, synthetic signals at locations comparable to the experimental instruments position on Nocera hill have been selected, calculating the synthetic SSRs (Figure 4.12). The analytical input has been used as reference, being representative of the incident signal before the interaction with the near-surface heterogeneities. They show an amplification effect of a factor of 1.5 at station TOP4 and TOP5 at frequencies between 2 and 4 Hz, and another spectral peak at frequencies higher than 10 Hz. These results are consistent with the 2D model results suggesting that the agreement between 2D and 3D models is verified in terms of frequencies and amplitudes produced.

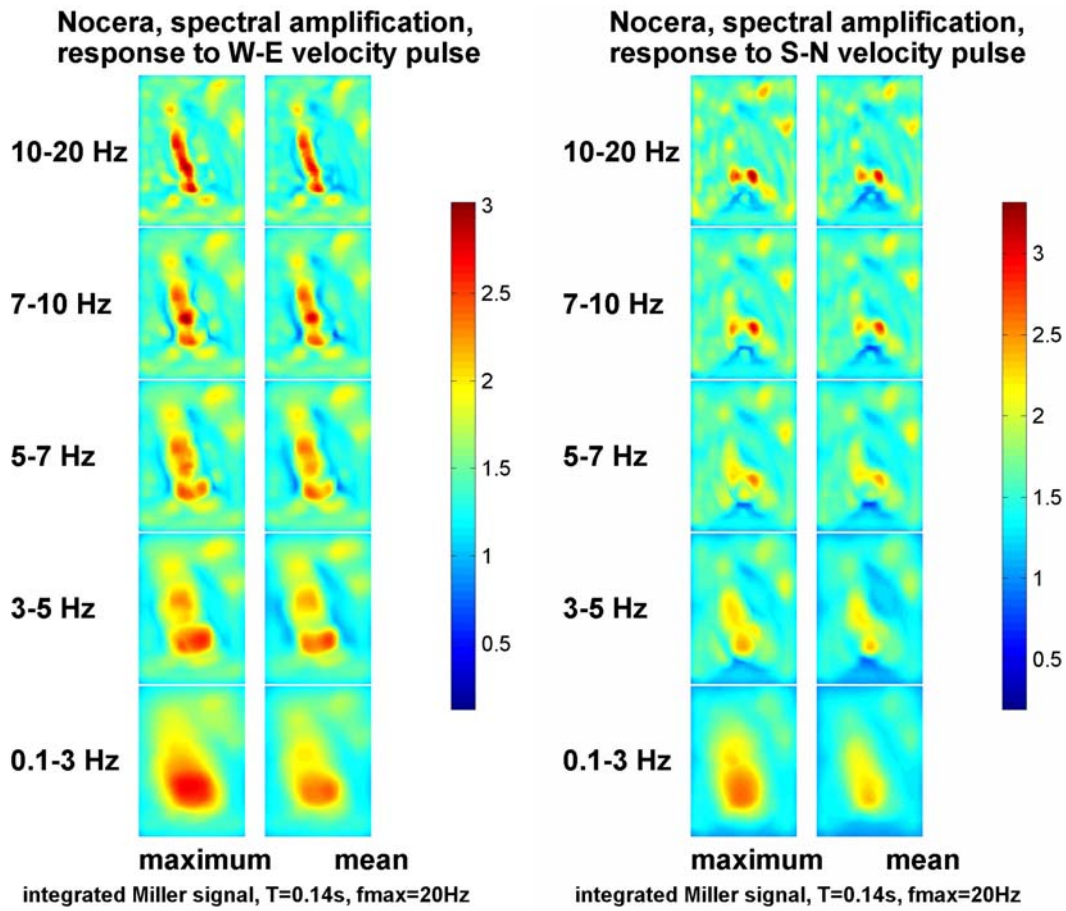


Figure 4.11 – Response spectra of 3D model.

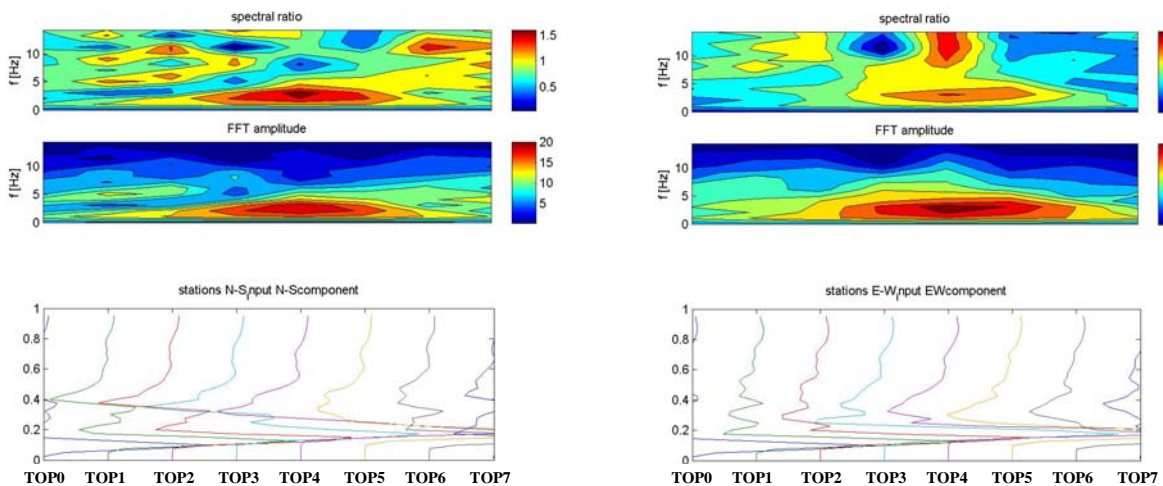


Figure 4.12 – Spectral ratios to the analytical reference of the synthetic signals recorded at stations TOP 1-7 in the 3D simulation. The left panel is related to the model with S-N polarized input, the right one to W-E polarized input.

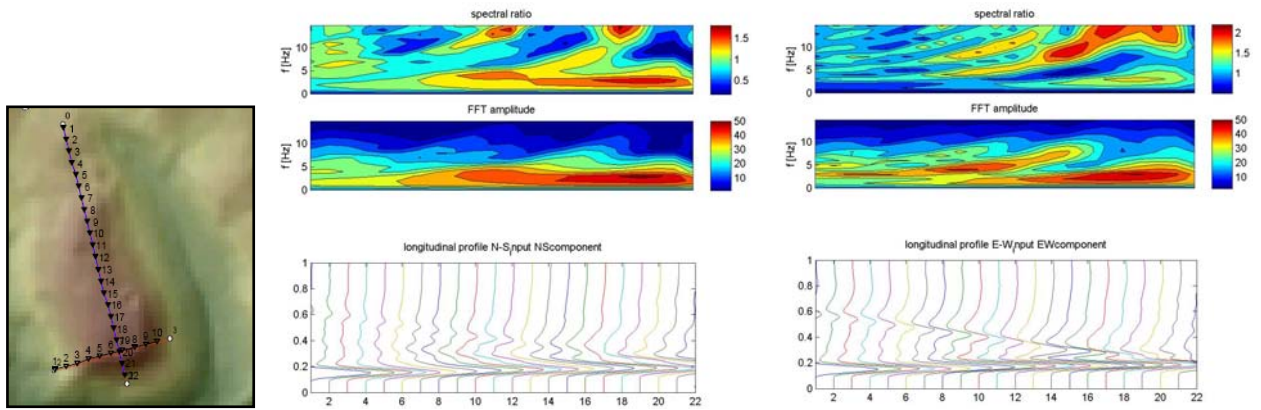


Figure 4.13 – Spectral ratios to the analytical reference of the synthetic signals recorded along the hill major axis in 3D simulation (blue profile in left panel map). The middle panel is related to the model with S-N polarized input, the right one to W-E polarized input.

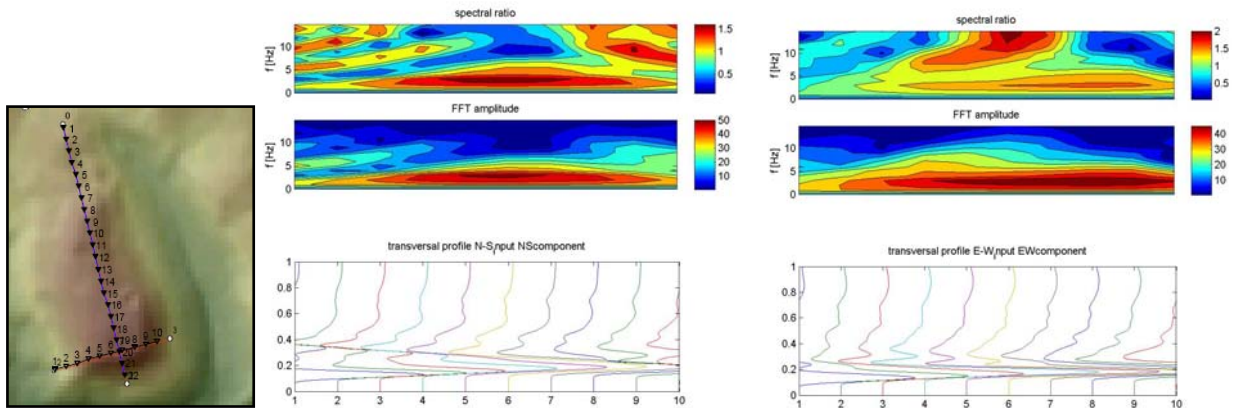


Figure 4.14 – Spectral ratios to the analytical reference of the synthetic signals recorded along the hill minor axis in 3D simulation (red profile in left panel map). The middle panel is related to the model with S-N polarized input, the right one to W-E polarized input.

Therefore the underestimation of amplitudes observed on 2D synthetic spectral ratios (up to a factor of 1.6) compared to amplitudes of empirical SSR (up to 4), cannot be accounted to 2D approximation, being 2D and 3D synthetic spectral ratios of the same rank. An alternative way to explain this discrepancy between models and data results, is to consider the choice of TOP0 reference site as too close by the hill base where a deamplification peak has been observed both on 2D and 3D models. To explore this hypothesis transfer function for a 3D model synthetic recorded at TOP0 site is shown in Figure 4.15, pointing out that amplitudes often are lower than 1. Also the spectral ratios using TOP0 station as reference are calculated to appreciate the differences in amplification level. As shown in Figure 4.16 the amplification reaches a factor of 2.

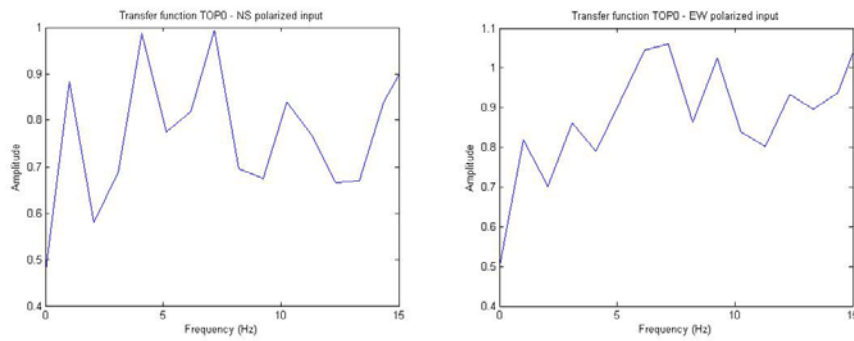


Figure 4.15 – Transfer functions of TOP0 station 3D synthetic .The left panel is related to the model with S-N polarized input, the right one to W-E polarized input.

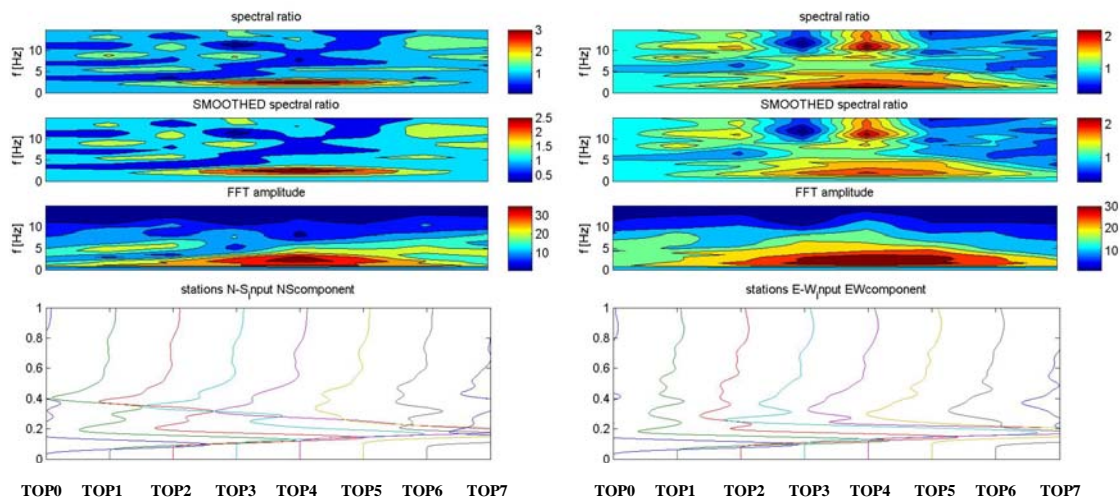


Figure 4.16 – Spectral ratios to TOP0 of the synthetic signals recorded at stations TOP 1-7 in the 3D simulation. The left panel is related to the model with S-N polarized input, the right one to W-E polarized input.

4.3.6 Nocera Umbra hill case conclusions

Nocera Umbra hill has been recognized to be responsible of an amplification effect due to scattering of seismic energy.

The amplification observed using earthquake records is generally moderate, although occurring in a frequency band relevant to building excitation, with a maximum amplification of 4 at stations deployed on or near the hill top (TOP3, TOP4, TOP5). It occurs at all stations in the frequency band 2-4 Hz showing a predominant polarization at 60-70°N, transversal to the major axis of the hill. The results of 2D and 3D models, the hill dimensions and local shear wave velocity of a downhole identify this frequency band as the fundamental resonance frequency of the hill. This result is also in agreement with findings by Caserta et al. (2000), who recognized a broad amplification peak between 2 and 5 Hz, with amplitudes up to a factor of 2.5, at one station deployed on the hill top.

Larger amplifications are observed at frequencies above 10 Hz, with significant amplitudes (up a factor of 25) but without coherence among the different stations both in terms of amplified frequency bands and directions of polarization. These variations make an interpretation of the high-frequency amplification difficult. Only station TOP3 shows a second peak in the frequency band 10-11 Hz with a predominant polarization direction (N70°) similar to the one observed for the fundamental mode. A second amplification peak between 10 and 12 Hz, with amplitudes slightly larger than the fundamental one, is also indicated by theoretical 2D and 3D models and has been interpreted as the second higher resonance mode.

The earthquake backazimuth seems to be relevant in the amplification and polarization pattern only at the lower frequency band, as earthquakes from NNE cause higher amplitudes and a polarization pattern consistent with the hill orientation. Above 10 Hz there are few negligible differences between NNE and SSE events.

2D and 3D models agree in finding two amplified frequency bands near the hill top, 2-4 Hz (fundamental mode) and 10-12 Hz (second higher mode), and a deamplification peak at the hill bases. The amplification levels are never higher than 2, depending on which reference is chosen. An important remark here is that approximating a 3D shaped hill with two 2D profiles is not too unsuitable and imprecise being the amplification effect similarly reproduced.

Unfortunately models agree with empirical results only in terms of the fundamental resonant frequency of the hill, but not in amplification as models underestimate the record amplitudes. These findings agree with results from previous literature studies that indicate frequent underestimation of observations in theoretical models (Bouchon and Barker, 1996). This is justified if we consider the complexity of the reality compared to the simplified models, which do not take into account relevant features such as subsurface layering (Bard and Tucker, 1985; Geli et al., 1988), neighbouring topography (Geli et al., 1988) and small-scale geological features.

In the frequency band corresponding to the building fundamental frequencies (2-5 Hz) the observed amplification effect is moderate, never exceeding a factor of 4, and also limited to a small portion of the profile, reaching a factor of 2 close to the slopes. These estimates of amplification might be exaggerated by a small deamplification occurring close to the reference station, as 2D and 3D simulations demonstrate. The amplification of models is a factor of 2 smaller. The small values lead to the conclusion that the vulnerability of the ancient buildings in the historical centre prevailed over topography effects, in strict agreement with previous damage analyses by Donati et al. (2001).

4.4 Cerreto Laziale hill case study



While performing the polarization study on the Italian National Seismic Network stations data, Cerreto Laziale station (CERT), located on a hill top was recognized as an interesting site to be thoroughly studied.

CERT station is located near the top of a prominent and narrow ridge elongated in N160 direction, with a maximum height of 985m and around 2 km wide. The noise analysis performed (as reported in Chapter 3) showed a clear, marked polarization oriented perpendicularly to the hill major axis.

In order to better understand the nature of the recorded noise wavefield, an array of six stations was deployed near the hill top recording ambient noise and four aftershocks of the L'Aquila seismic sequence. The analysis of covariance is performed and the Frankel *et al.* (1991) method is applied to estimate the backazimuth of the incoming wavefields.

4.4.1 Geological setting

The hill of Cerreto Laziale is located in the central Apennines, an east to northeast vergent fold and thrust belt that developed as a result of convergence between the European and African (i.e., Nubia), within the framework of Alpine-Himalayan orogenesis (Billi & Tiberti, 2009). The parallel migration of the trench and orogenic wedge toward east occurred concurrently with westward and northwestward subduction of oceanic lithosphere beneath the European plate, and with the progressive involvement of the Adriatic (African affinity) continental margin with contractional deformation (Malinverno and Ryan, 1986; Royden *et al.*, 1987; Dewey *et al.*, 1989; Faccenna *et al.*, 2004; Rosenbaum and Lister, 2004). As a result, the Apennines are characterized by major NW-striking thrust sheets generally dipping toward to southwest with gentle angles and a vergence toward to northeast. Thrust imbrication occurred mostly in a forelandward piggyback sequence with some out-of-sequence or backward thrusting episodes (e.g., Ghisetti and Vezzani, 1997; Cavinato and DeCelles, 1999; Patacca *et al.*, 2008).

Miocene to Early Pleistocene thrust accretion across the Adriatic continental margin was accompanied by Tyrrhenian back-arc extension (Mazzoli and Helman, 1994, and references therein), driven by gravity-induced sinking of the Adriatic and Ionian Sea lithosphere, and by related subduction roll-back (e.g. Malinverno and Ryan, 1986; Mazzoli and Helman, 1994, and references therein). The thrust front migrated eastward over time with a following extension, so that folds and thrusts along the east margin of the Italian peninsula are the products of the final stages of contractional deformation in the Apennines (end of Early Pleistocene).

In these extensional phases much of the Apennine chain has been dissected by normal and strike-slip faults, that locally post-date thrust structures. In fact, normal faults and associated extensional basins of Miocene–Pleistocene age are widespread in the Tyrrhenian side of the Apennines and also in the axial sector of the fold-and-thrust belt (Malinverno and Ryan, 1986; Barchi *et al.*, 1998; Jolivet *et al.*, 1998; Cavinato *et al.*, 2002).

The lithotypes which outcrop in Cerreto Laziale area belong to the “Sabina succession”, that is made of carbonate slope deposits. It is similar to the Umbria–Marche basin succession, being richer in detrital limestones (Corda and Mariotti, 1986). Here, the Detritic Scaglia Group is overlain by the marly limestones of the Guadagnolo Fm. (Aquitanian–Langhian), which in turn passes upwards into the Calcari a briozoi e litotamni Fm. and then into hemipelagic and turbiditic deposits of Upper Miocene age.

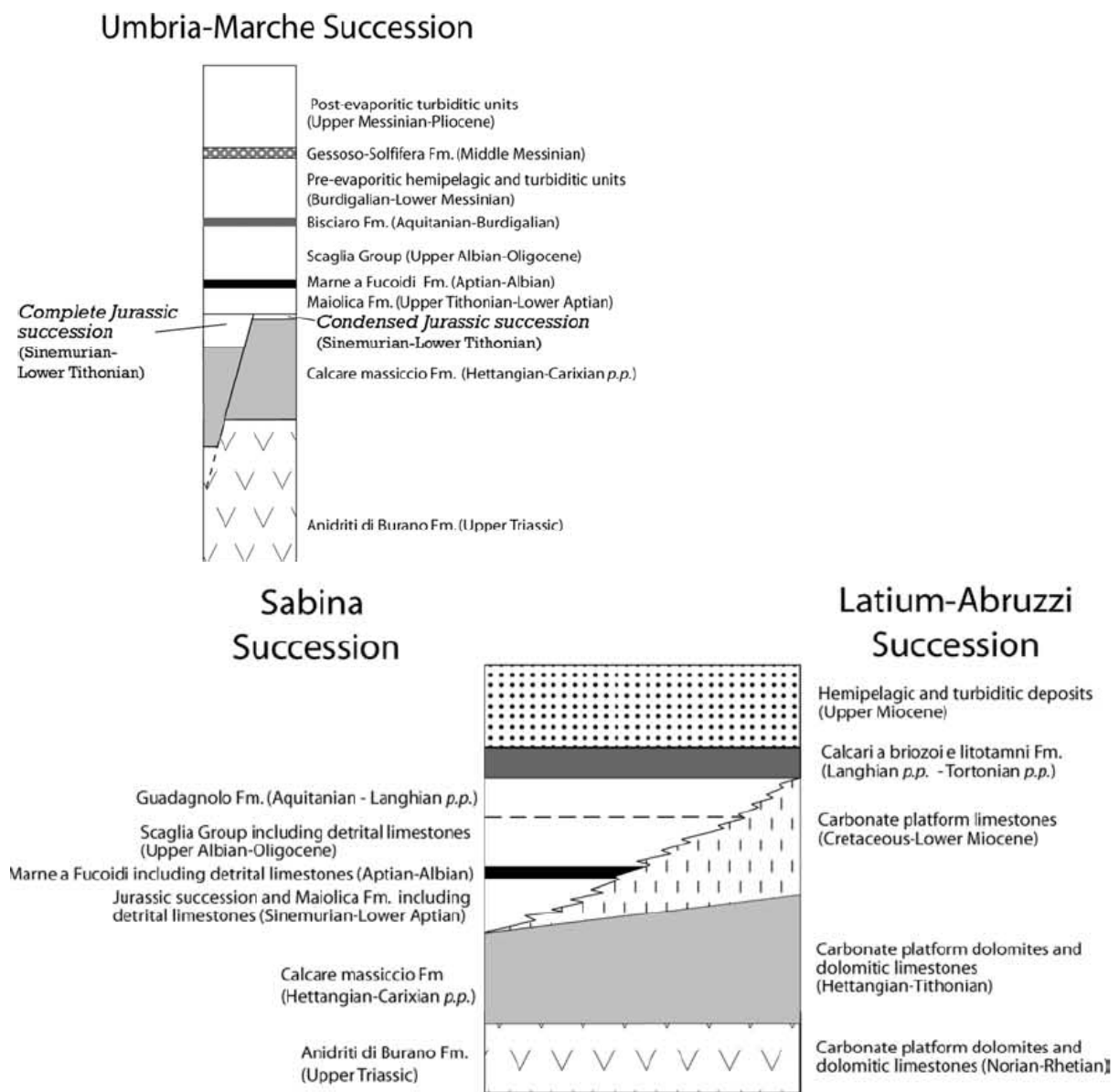


Fig. 4.17. Schematic stratigraphic column (top) for the Umbria–Marche basin succession, and (bottom) stratigraphic relationships between Latium–Abruzzi carbonate platform and Sabina transitional successions. Redrawn by Mazzoli et al .2005.

The Sabina overthrust nappe is bounded to the east by the Olevano-Antrodoco out-of-sequence major thrust fault, that is arc shaped in its northern part and has a N-S strike to the south. It can be referred to the late Messinian (post-evaporite) time, with locally continuing activity and/or reactivation during the Pliocene. The southernmost portion of the thrust consists of two minor segments displaying a right-stepping en-échelon geometry, Ascrea and Canterano Thrusts. The latter one runs few kilometers from Cerreto Laziale hill.

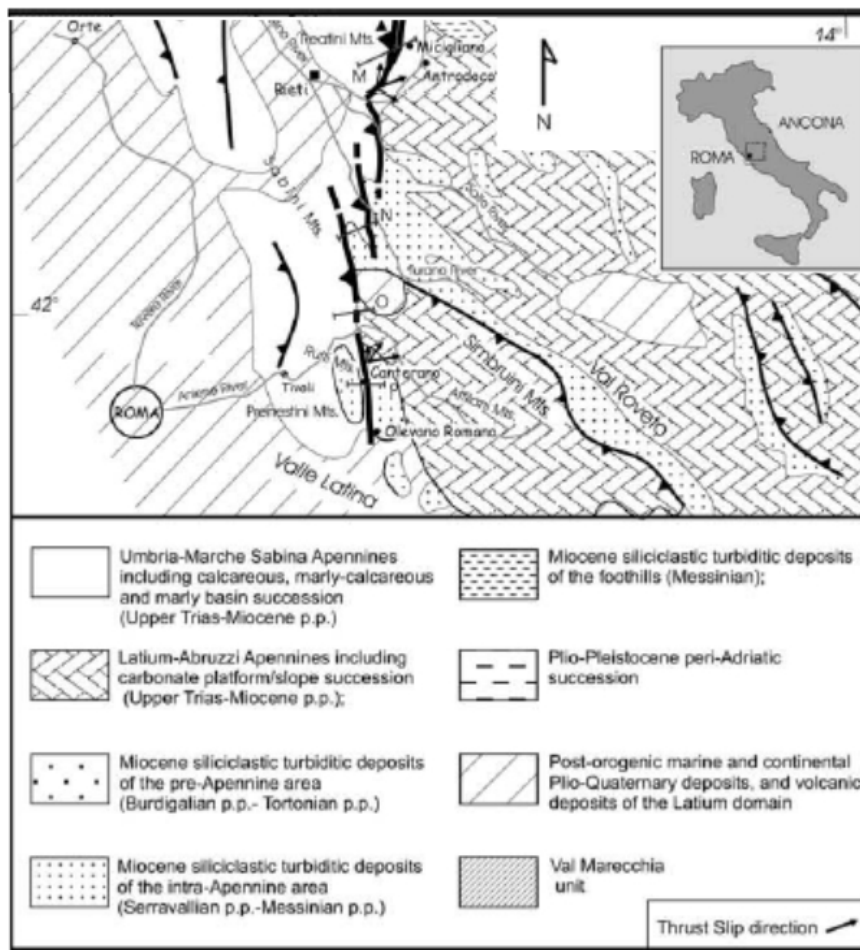


Fig. 4.18. Geological sketch map of the study area, showing the OAMT (bold thrust fault) with mean orientation of thrust slip direction. Redrawn from Mazzoli *et al.* 2005

The hanging-wall unit mainly consists of an asymmetric, east-verging anticline showing a western gently dipping limb and an eastern vertical to overturned limb. The thrust surface is locally folded into antiforms and synforms of different size, as on Cerreto Laziale hill where the outcropping Calcari a briozoi e litotamni Fm. form an drag fold anticline that becomes a plunging fold toward to South.

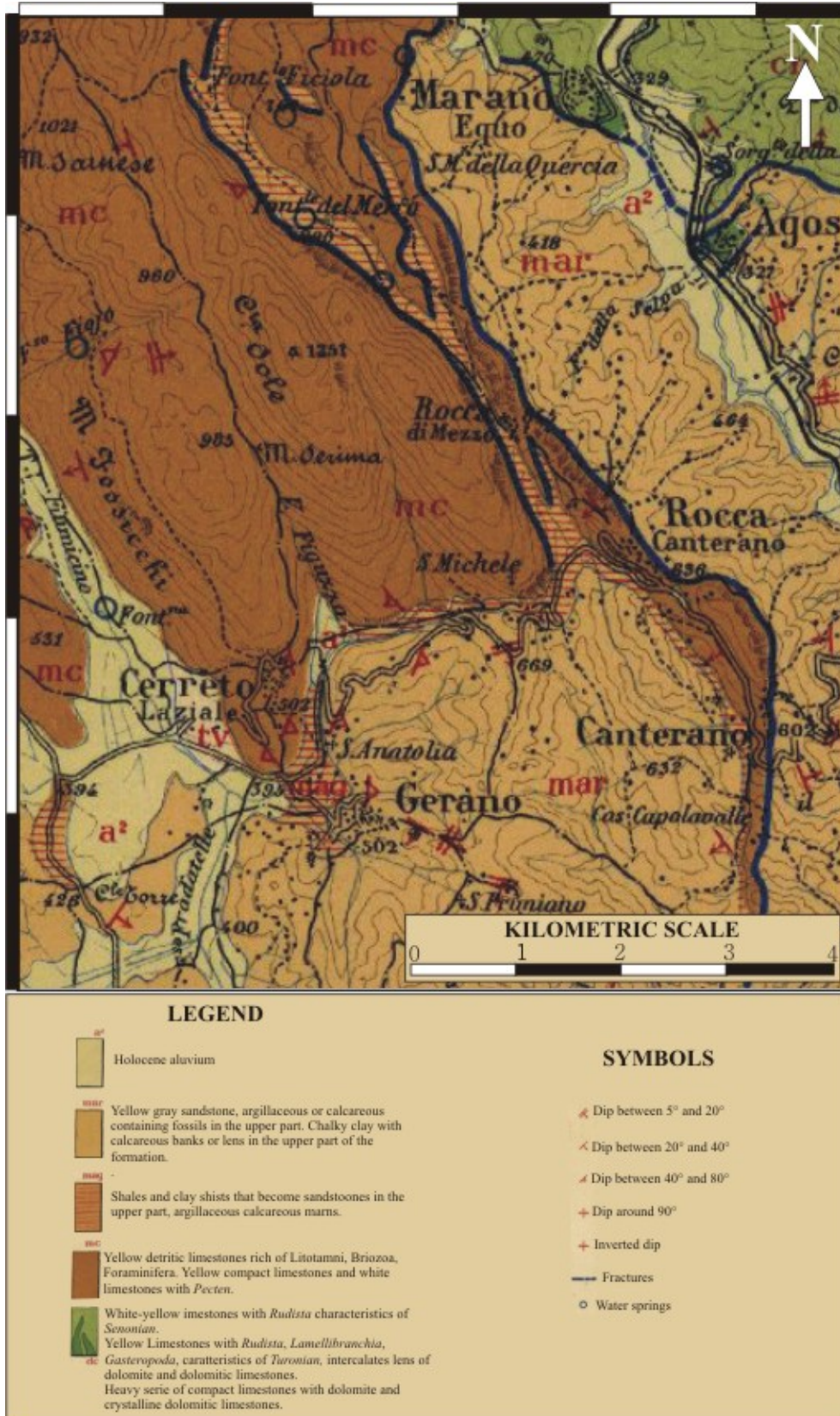


Figure 4.19 – Geological map at 1:100000 scale, edited by “Servizio Geologico d’Italia”, 1939, sheet n° 151 ALATRI.

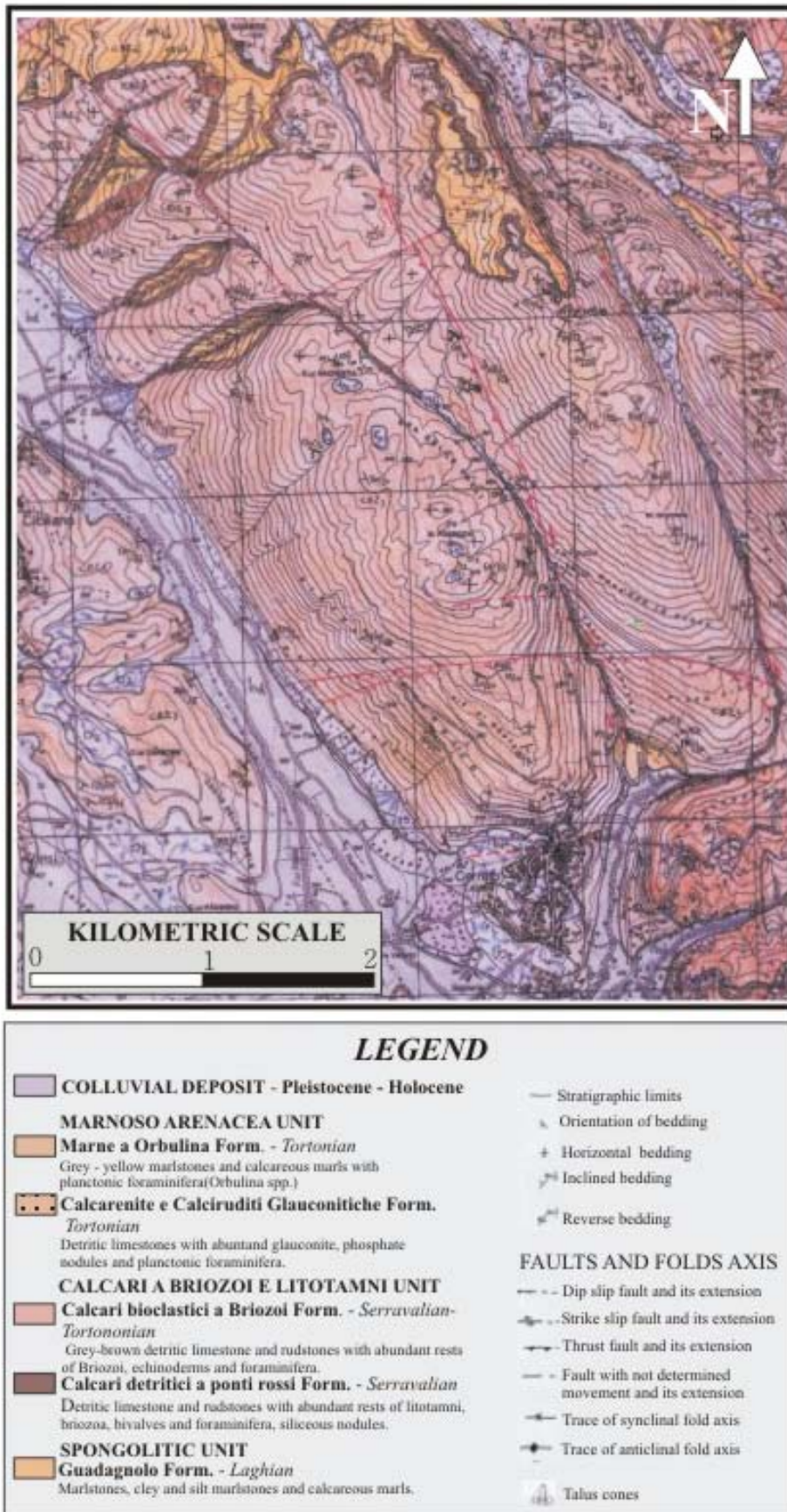


Figure 4.20 – Geological map at 1:150000 scale , preliminary version by “Servizio Geologico d’Italia”.

4.4.2 Polarization at CERT station

Station CERT lies near the top of an elongated ridge with steep and regular slopes, a morphology typical of calcareous rocks. It is part of the Italian Seismological Network run by INGV, whose data were used to perform the statistics of noise polarization analysis shown in Chapter 3.



Figure 4.21 – Cerreto Laziale station and its location on the investigated ridge.

The rotated receiver functions and the polarization calculated through the covariance matrix analysis revealed a marked directional resonance effect in $N80^{\circ}E$ direction. It is related to frequencies between 1 and 2 Hz with an amplification up to a factor of 4 (mean), that is a quite high level. It is also important to notice that day and night hours did not show any significant differences, confirming that the noise is most likely not influenced by human activities and can be considered to be mostly conditioned by local geological and morphological features (Figure 4.22).

Moreover station CERT recorded L'Aquila earthquake occurred on 6 April 2009; the RFs were calculated and the polarization analysis was carried out in the frequency band 1-9 Hz. The results are shown in Figure 4.23. The covariance analysis resulting azimuths are graphed through the green rose diagram, revealing again a polarization direction around $N80^{\circ}E$. The polarization azimuths are also plotted versus time with a colour intensity scale that is related to the *hierarchical criterion* weight factor **WH** (see Section 2.2). The converted S waves, the late S phases and the coda (surface waves) show the highest values of **WH**, that indicate more horizontal ground motion ellipsoids. Also these azimuths show polarization angles in $N80^{\circ}$ direction. This orientation is also shown by the rotated receiver functions with two peaks between 1 and 3 Hz. Other peaks at higher frequencies can also be noted with higher amplitudes,

detecting a direction roughly N-S. Anyway, as demonstrated by the circular histogram, their influence is minimal.

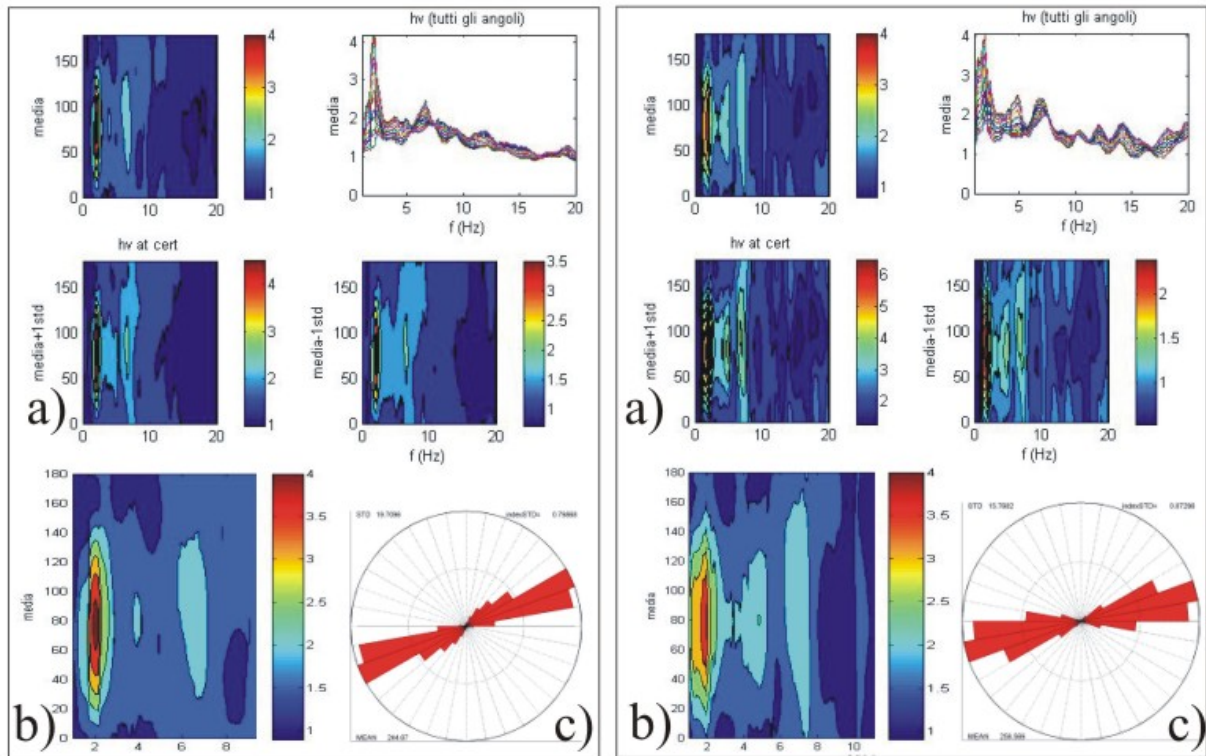


Figure 4.22 – Statistical analysis of ambient noise on the Italian seismic network (see Chapter 3): results by CERT station. LEFT PANEL depicts results from nightly ambient noise, RIGHT PANEL shows results from daily ambient noise. a) Rotated receiver functions represented through the media, the media \pm the standard deviation and through the spectrum from every rotation angle; b) Detail of the media of rotated receiver function; c) Rose diagram by covariance matrix analysis in the frequency band 1-20 Hz.

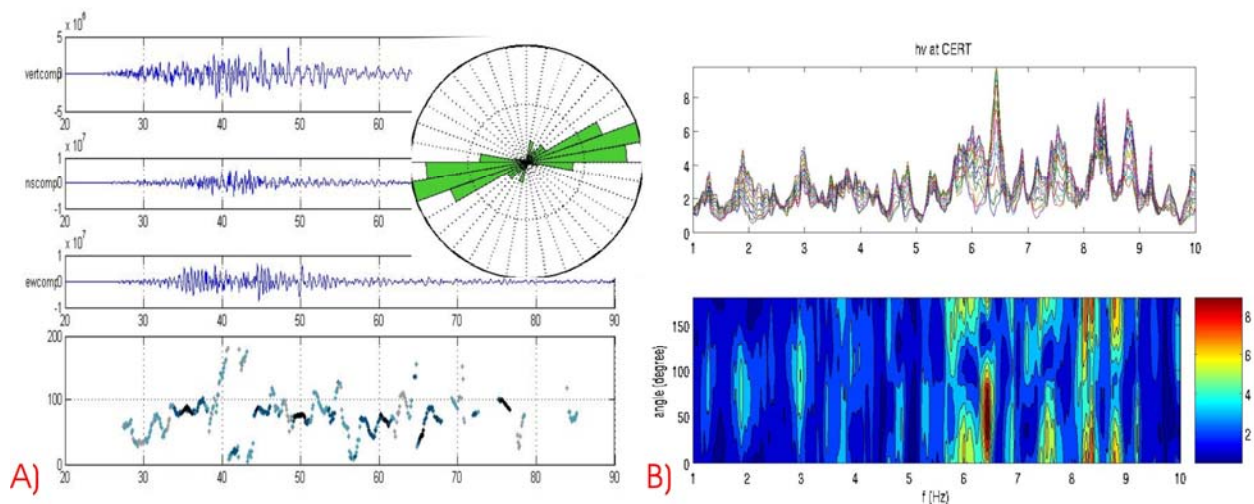


Figure 4.23 – L'Aquila 6 April 2009 earthquake polarization on station CERT. A) Covariance matrix analysis results in the frequency band 1-9 Hz. B) Rotated receiver function and spectra.

4.4.3 Array polarization analysis

On 17 April 2009 a temporary array of six stations was deployed around station CERT, to continuously record ambient noise near Cerreto Laziale hill top. Each station was equipped with Kinementrics Q330 digitizers coupled to Lennartz 5s seismometers and synchronized by the GPS timing system. The geometry was chosen in order to detect wavelengths between 100 m to 1000 m, as displayed in figure 4.24.

Considering that L'Aquila earthquake occurred only 11 days before, in the five working hours the array recorded three aftershocks coming from NE.

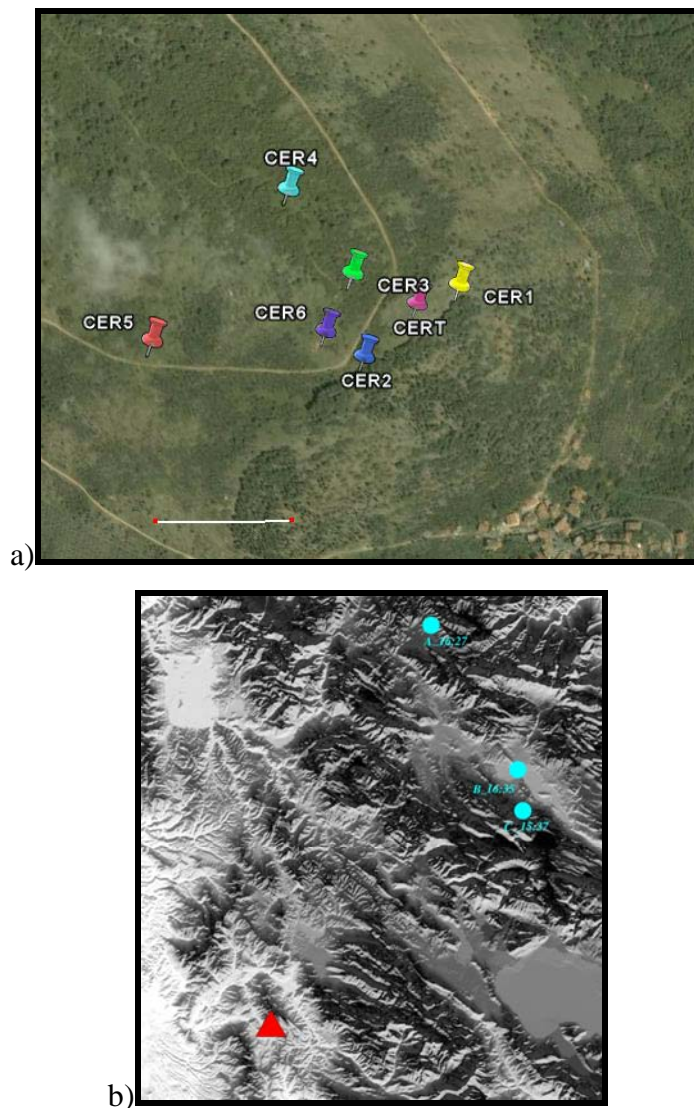


Figure 4.24 – a) Array deployment on Cerreto Laziale hill. White bar at the bottom represents 200m; b) recorded earthquakes epicenters (cyan circles) and array position (red triangle)

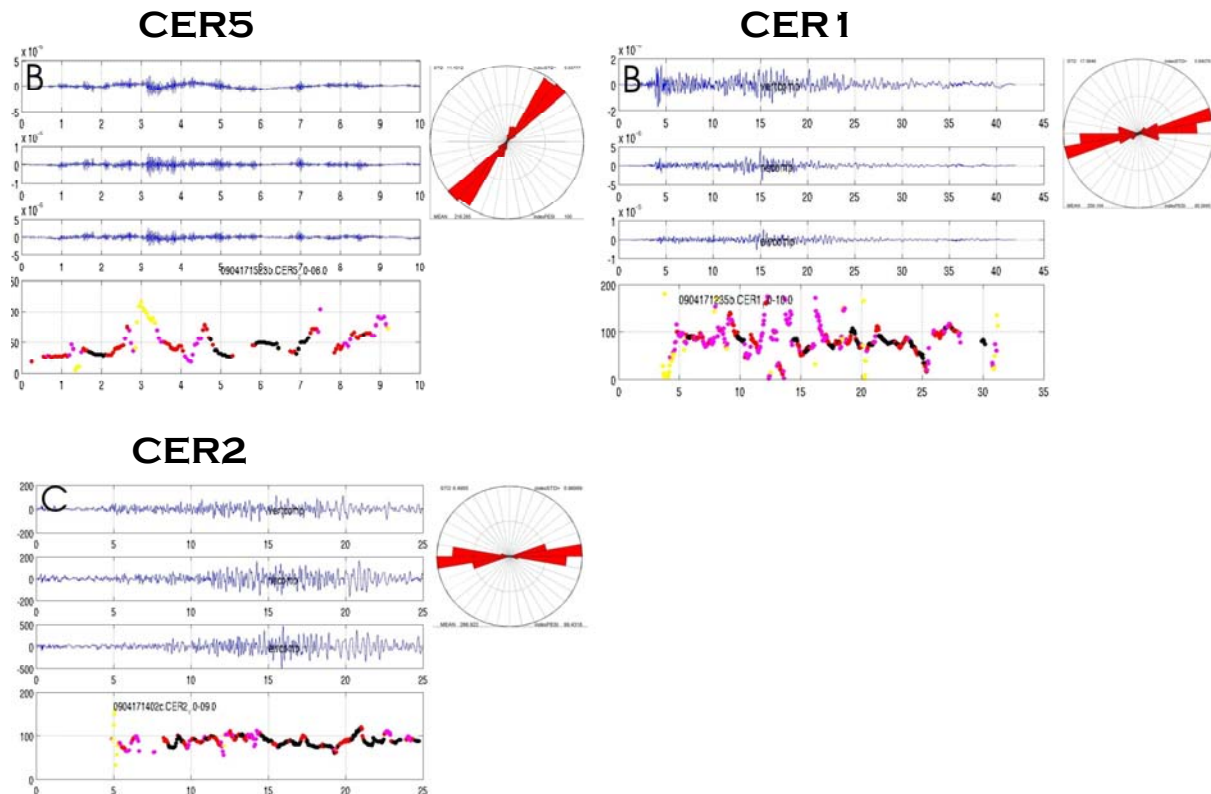
4.4.3.1 Seismic events polarization analysis results

The array recorded three aftershocks of L'Aquila earthquake with magnitudes between 2.2 and 2.4. Unfortunately they were not recorded by all stations, due to the low signal to noise ratio and to the recording period only partially in overlap.

	Day/hr/min	Lat.N	Long.E	Depth Km	M _L	CER1	CER2	CER3	CER4	CER5	CER6
A	17/04/09 16:27	42.54	13.29	11	2.3			*			*
B	17/04/09 16:35	42.33	13.46	25	2.4	*		*	*	*	*
C	17/04/09 15:37	42.27	13.47	10	2.2		*		*		

Table 4.2 – Events recorded by the temporary array deployed on 17 April 2009 on the top of Cerreto Laziale hill.

The polarization analysis was carried out in the frequency band 1-15 Hz, and the results are depicted in Figures 4.25. Looking at the distribution of polarization angle along time, there are no clear relations with seismic phases and with the weight factor (**WH**). They are also quite dispersed around the mean value, excepting station CER2. Nevertheless the mean polarization angle is predominantly oriented in N80°E-N90°E direction but CER5 which shows a polarization in N40°E direction.



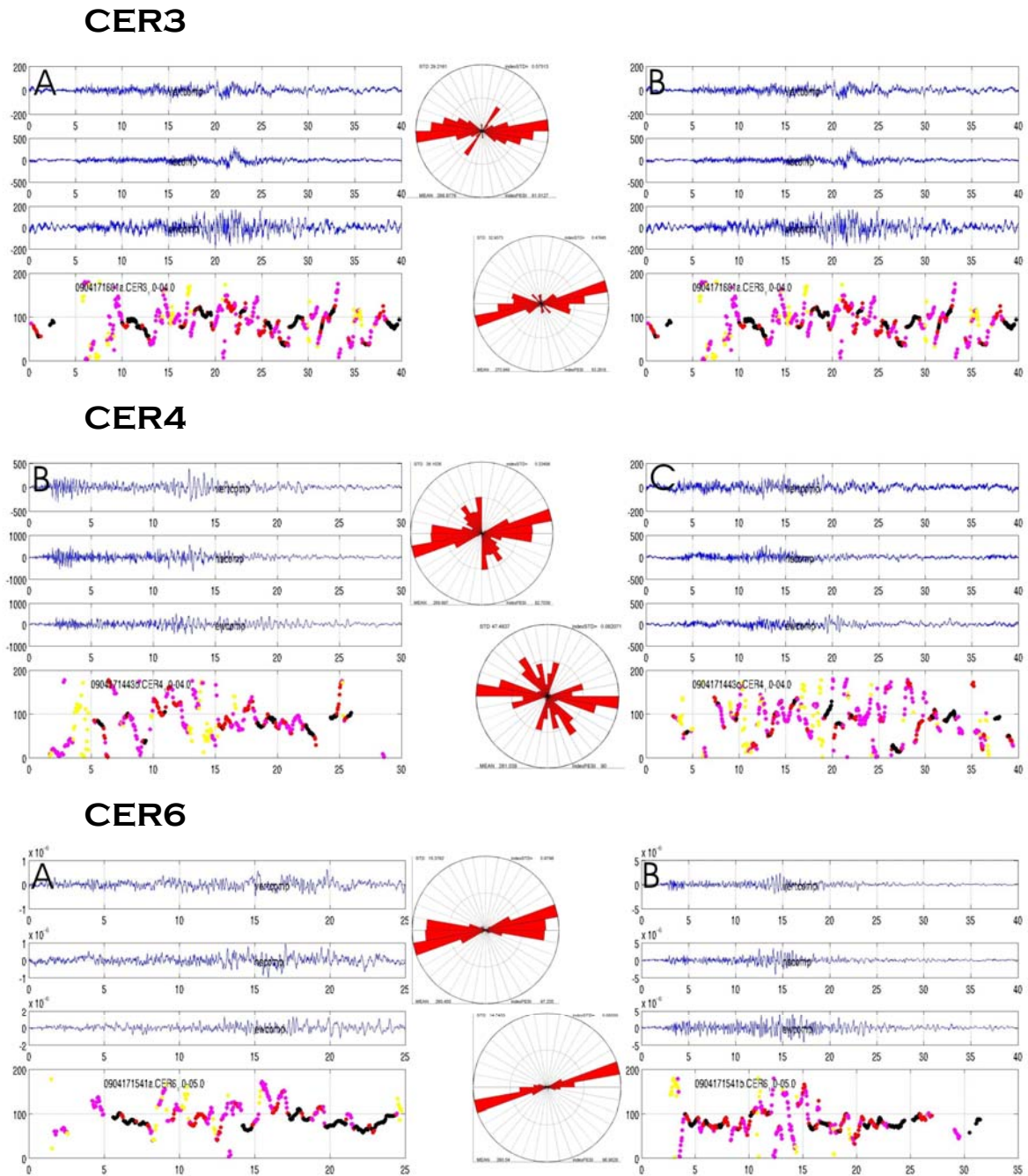


Figure 4.25 – Results by covariance matrix analysis on the aftershocks described in Table 4.2.

4.4.3.2 Ambient noise polarization analysis results

The array was installed and removed not simultaneously, then each station recorded different hours in the day, and the common recording period overlaps only 40 minutes. In order to apply method by Frankel *et al.* (1991), these 40 minutes were firstly windowed on each station.

The RFs were calculated, bringing out that the polarization peaks are related to frequencies between 1 and 5 Hz, and to rotation angles around N80°E-N90°E, consistently with the analysis

of CERT ambient noise performed previously (see Section 4.4.2). Thus the polarization analysis of ambient noise at stations installed on the hill was carried out in the frequency band 1-5 Hz through a 0.5 s wide moving window with 0.1s overlap. It reveals a stable polarization oriented N80-90 on all stations but CER5 which shows again N40°E direction.

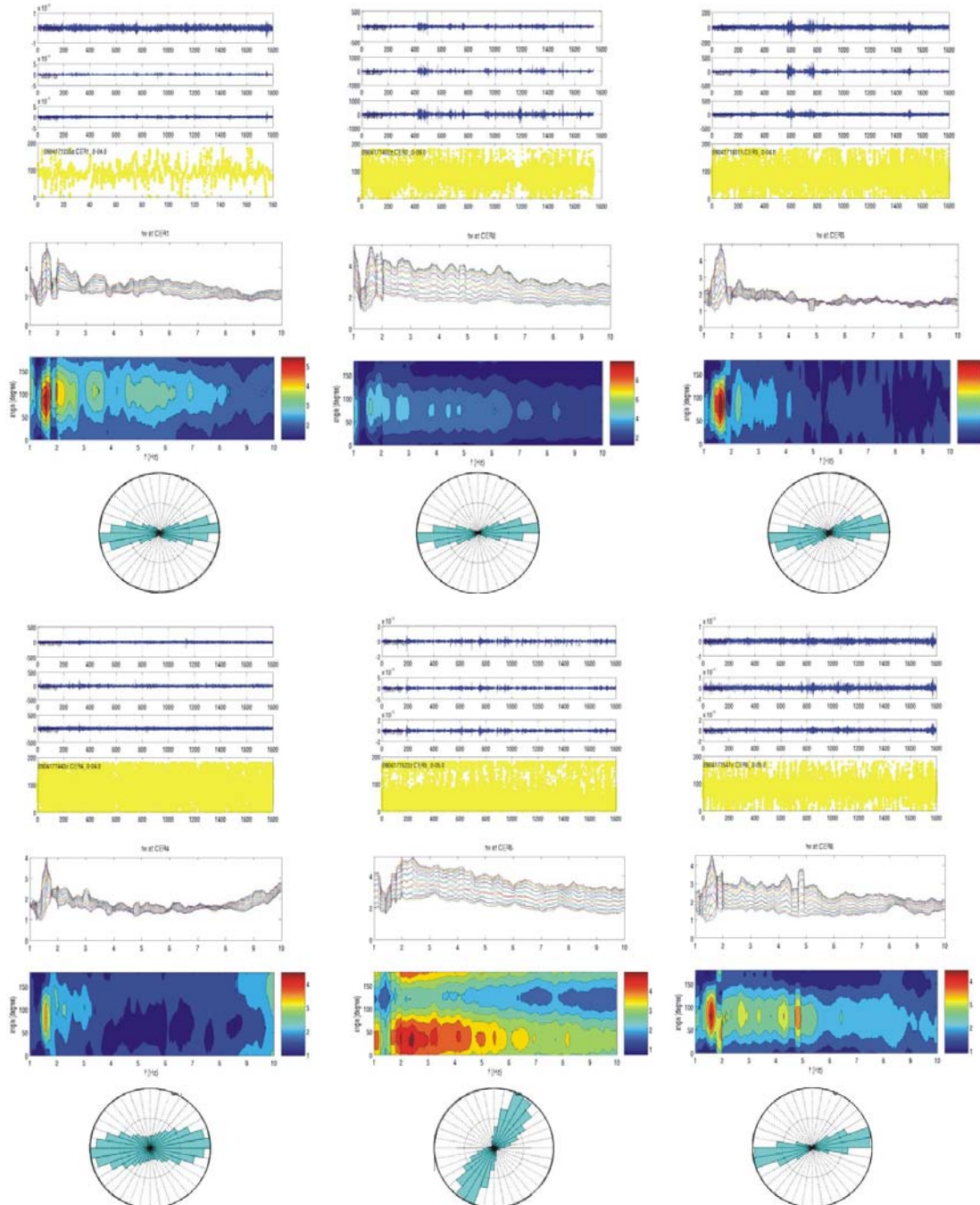


Figure 4.26 – Polarization analysis results performed on ambient noise recorded on 17/04/09 by the array; stations CER1, CER2, CER3, CER4, CER5, CER6. For each station are displayed: the signals (top panel), the polarization angles (Covariance matrix analysis) versus time (upper-mid panel), spectra and contour plots of the rotated receiver functions (lower-mid panels) and the rose diagram of polarization azimuths (bottom panel).

4.4.4 Backazimuth and apparent velocity

The running-window zero-lag cross-correlation technique proposed by Frankel *et al.* (1991) was used to estimate the instantaneous direction of propagation and apparent velocity (V_{app}) of coherent wave trains travelling across the array.

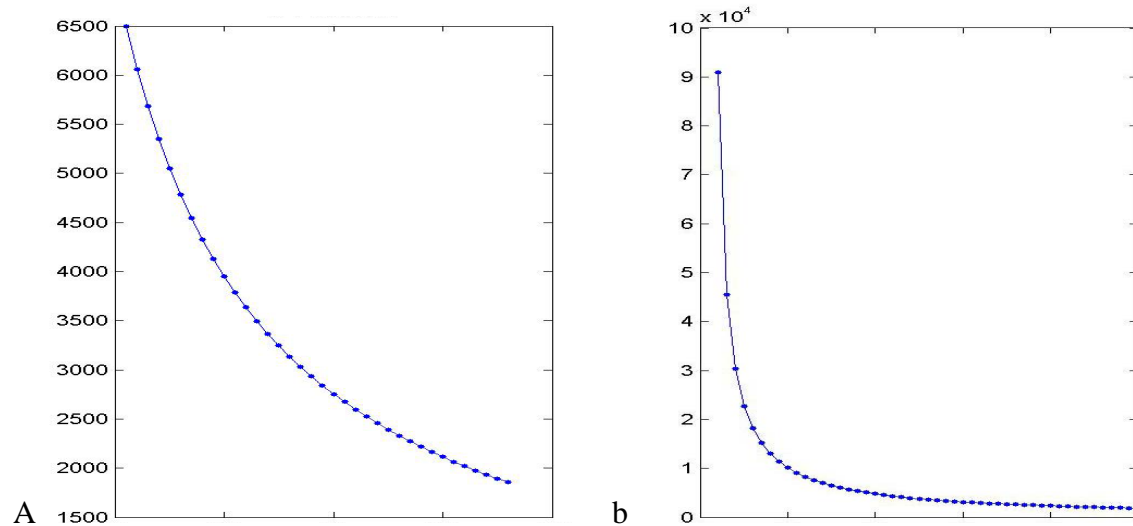


Figure 4.27 – Values of velocities (in y-axis) associated to positive slowness V_{app} values of the range chosen for this study ($0 < V_{app} < 5.5 \times 10^{-5}$)

The technique is based on a grid search over a range of time shifts Δt between the different array stations. The length of the running time window used in the Frankel's code is taken equal to 1 sec, consistently with the observed predominant frequency, with a partial overlapping of 0.5 sec. In each window, the algorithm estimates the average zero-lag cross-correlation C between waveforms of the array as a function of E–W and N–S components of the slowness vector \mathbf{P} (\mathbf{P}_x and \mathbf{P}_y respectively).

The slowness components have been investigated in an equispaced 100-step grid in the interval -0.00055 to 0.00055 sec/m, considering the more reliable velocity values of outcropping lithotypes. This range corresponds to absolute values of velocities between 1800m/s and 90000m/s, as shown in figure 4.27.

For each slowness vector of that interval, the time delay Δt for each site was found from:

$$\Delta t = P_x D_x + P_y D_y$$

where \mathbf{D}_x and \mathbf{D}_y are the distance between stations along two Cartesian directions and the reference station, arbitrarily chosen to be CER1. Then the windowed signal for each site was shifted in time by the value of $-\Delta t$ calculated for that site. The cross-correlation \mathbf{CCOR} was

calculated between each pair of shifted seismograms. Being $u(t)$ and $v(t)$ signals of two stations, the zero-lag cross correlation is :

$$CCOR = \frac{\sum [u(t)v(t)]}{\sqrt{\sum [u(t)u(t)] \sum [v(t)v(t)]}}$$

where the sums are taken over the number of time points in the windowed seismograms. Finally the average of the cross-correlations between all pairs of stations is found. This provides a measure of the coherence of the windowed seismograms for that particular slowness components.

For each window, the values of P_x and P_y that maximize the array-averaged cross-correlation coefficient **CCOR** provide the instantaneous apparent velocity :

$$v_{app} = \frac{1}{\sqrt{P_x^2 + P_y^2}}$$

and backazimuth (measured clockwise from north):

$$\phi = a \tan \frac{P_x}{P_y}$$

4.4.4.1 Frankel method ambient noise results

In order to estimate apparent velocity and backazimuth, figuring out more about the nature of incoming noise wavefield, the method introduced by Frankel *et al.* (1991) was applied to the ambient noise simultaneously recorded by the six array stations, separately to each component of motion. Based on the frequency band where the polarization effect was previously detected, the signals were bandpass filtered in the frequency band 1-5 Hz.

The results are presented in Figure 4.28. For each component (on rows) the values of apparent velocity (transformed from slowness, left column) and the values of backazimuth of incident wavefield (central column) are displayed versus time. On the right hand side backazimuths are plotted with rose diagrams fitted through a Gaussian curve using the software DAISY (Salvini, 2002). The CCORR value found in every time window (velocity or backazimuth), is expressed through a colour scale (CCORR<0.3; cyan, 0.3 < CCORR < 0.5; blue, 0.5 < CCORR < 0.7; black , CCORR > 0.7). Even though the CCORR values vary along time, no differences in results were found selecting the time windows with CCORR > 0.8 (Figure 4.29), which were the 40% of total.

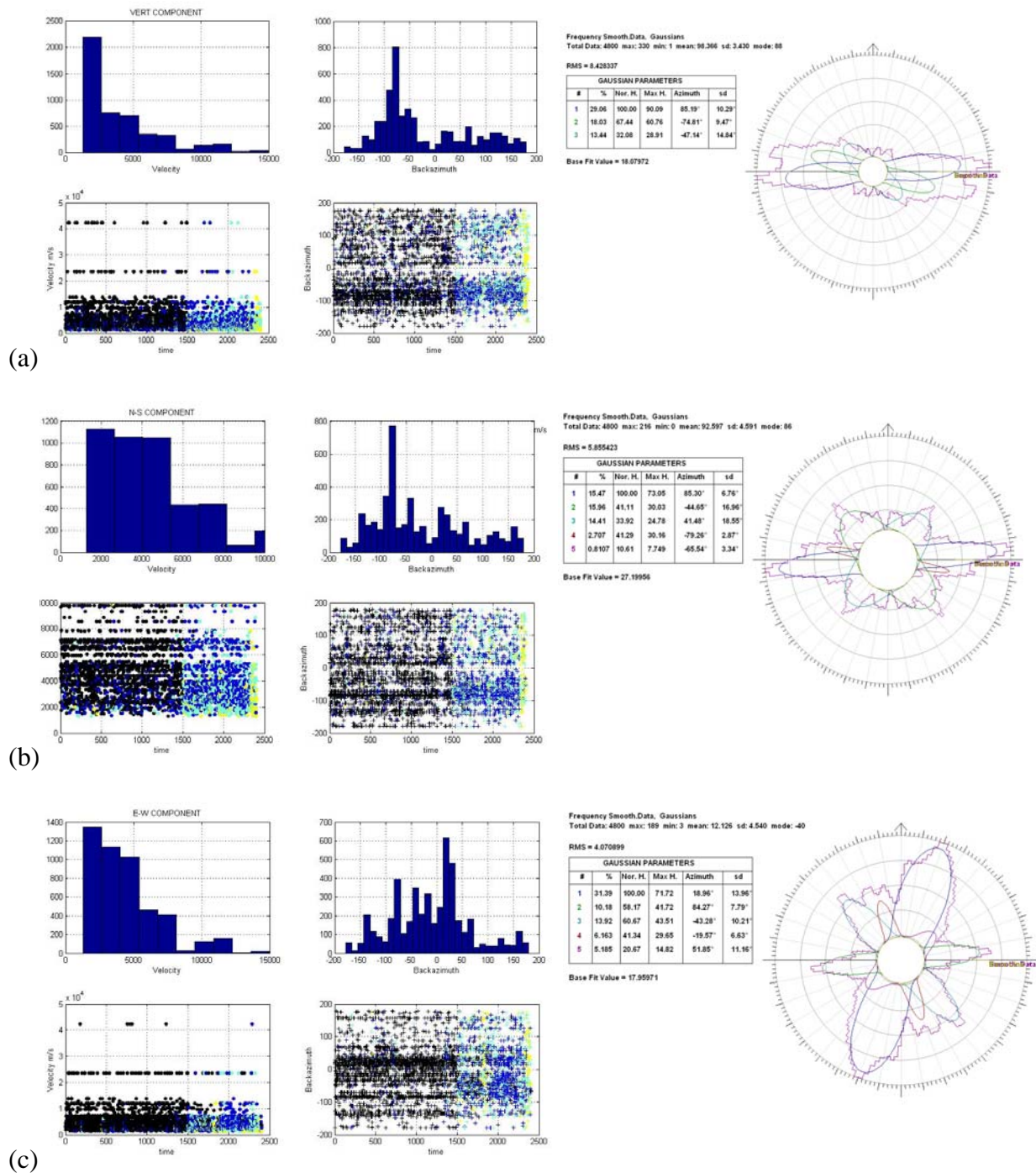


Figure 4.28 – Frankel method results.(a) Vertical component; (b) N-S component; (c) E-W component. The two columns on the left show the apparent velocity and backazimuth values detected by time windows and histograms fitted trough Gaussian curves, with associated mean and standard deviation values. The points colour indicates the value of the correlation coefficient : Yellow, $CCORR < 0.3$; cyan, $0.3 < CCORR < 0.5$; blue, $0.5 < CCORR < 0.7$; black, $CCORR > 0.7$. Right column depicts rose diagrams of backazimuth values using the software DAISY (Salvini, 2002) .

Statistically, the three components yield comparable values of apparent velocity, mostly in the range 2000-4000 m/s, while there is an inconsistency regarding backazimuth: vertical and N-S components produce a defined and similar peak in $N90^{\circ}E$ - $N100^{\circ}E$ direction, conversely on the

E-W component this direction is detected only by a secondary and less important peak. An explanation of this inconsistency is hard to be found.

However, in order to check the consistency among the three components, we selected those time windows where the resulting values of backazimuth differ less than 30° among them. The results are depicted in Figure 4.30. In this way the three components yield very similar values of both velocity (again between 2000 and 4000 m/s) and backazimuth (around -80° - 90°), but a small amount of time windows contributed to calculations, being this percentage around 14%.

4.4.4.2 Frankel method seismic events results

The same method of analysis was applied to the two events recorded by at least 5 array stations. Results from event “B” are shown in Figure 4.31, with quite high values of the correlation coefficient. Here an interesting feature is found on all the components of motion. The first 15-20 seconds of recording give very stable backazimuth values, that are consistent with the backazimuth evaluated by the epicentre localization. After that, the late S phases and the coda result in a broad dispersion without a preferential and well defined direction. A similar pattern can be observed on E-W component velocity results, with a mean velocity of about 3000 m/s. Two peaks are observed on vertical component histogram, one consistent with EW component one, the other detecting a mean velocity between 6000 and 7000 m/s. To the contrary N-S component shows a large dispersion in the interval 2000-10000 m/s which makes difficult the evaluation of the significant value of mean velocity.

More stable results are obtained from event “C” (Figure 4.32), where the mean velocities lie in the interval 2000-3000 m/s and the backazimuth values are consistent with the earthquake backazimuth. This is observed along the whole signal duration and similarly on the three components of motion. Anyway the very low values of the correlation coefficient, make the results less reliable and will not be taken into account.

4.4.4.3 Discussion of results

The analysis performed on ambient noise reveals that wavetrains cross the array from N90W ($\pm 10^\circ$), and with apparent velocities between 2000 and 4000 m/s. Minor but equally consistent values of velocities are obtained using seismic events, but the backazimuth values are predominantly related to the source backazimuth.

Considering that the array was installed near the top of a hill elongated roughly in N170°E direction, it is reasonable to hypothesize that ambient noise is diffracted by the hill sides, thus it crosses the array in a direction quite perpendicular to the hill axis. Using waveforms of seismic events, there is a strongest role played by the source backazimuth which predominates in the histograms. Nevertheless, a backazimuth dispersion is observed during late S arrivals and coda phases, where some individual values appear to be consistent with scattering from topography.

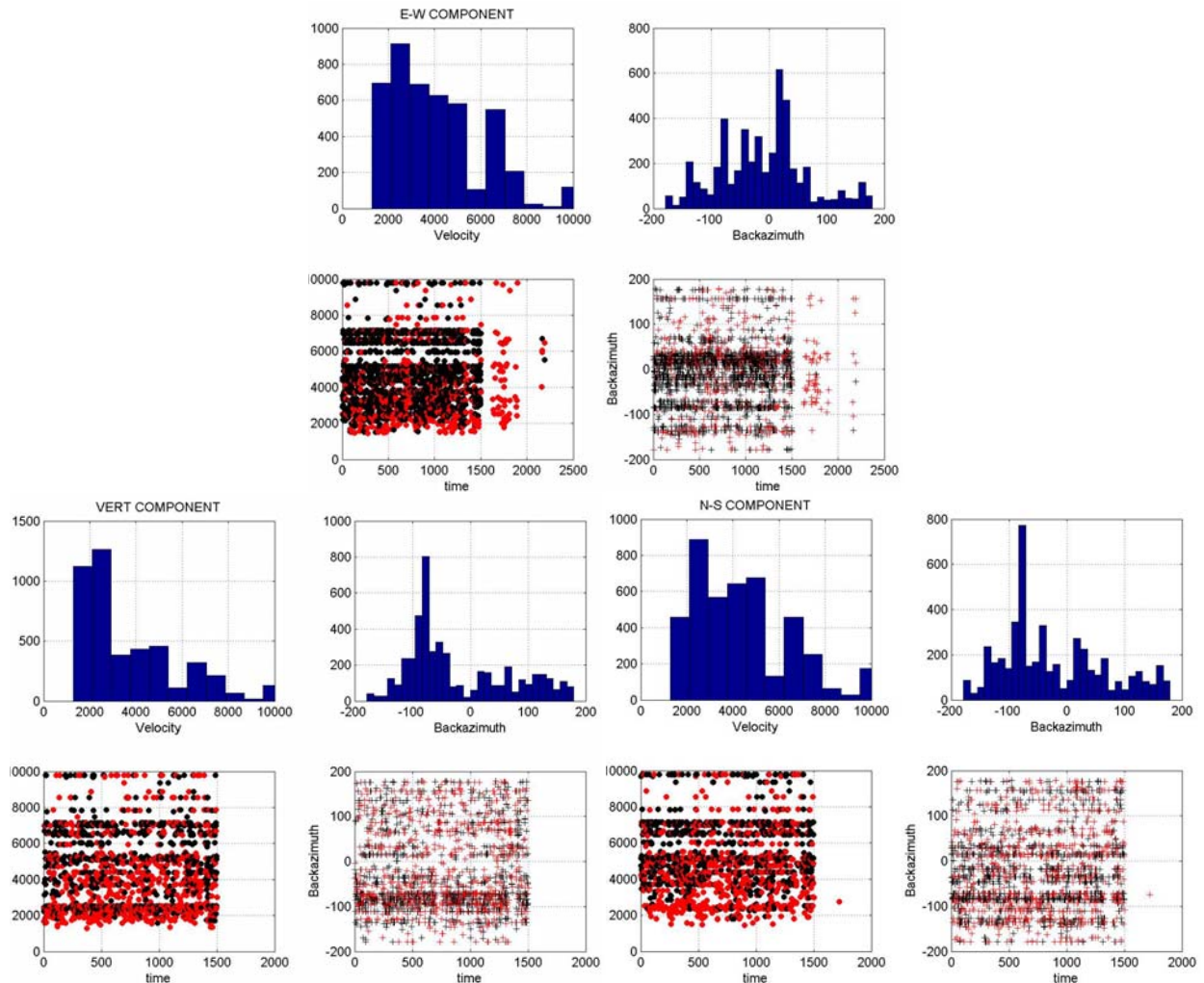


Figure 4.29 – Frankel method results selecting time windows with $0.8 < \text{CCORR} < 0.9$ (red) and $\text{CCORR} > 0.9$ (black), for both velocity and backazimuth calculations. They were the 40% of total.

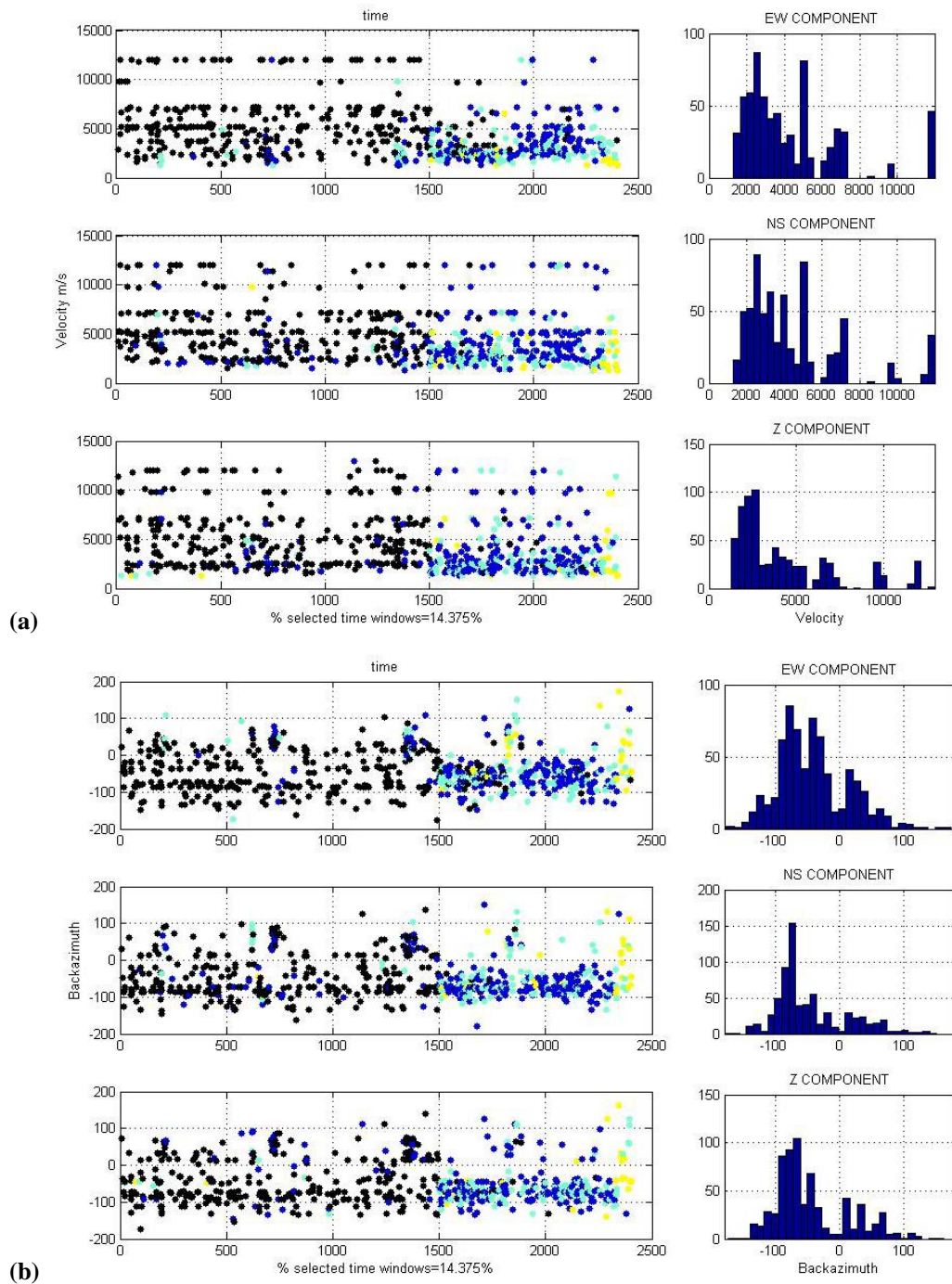


Figure 4.30 –Frankel method results selecting time windows with backazimuth values differing less than 30° between the three components. For each component of motion the resulting velocities (a) and azimuths (b) versus time are illustrated. The points colour indicates the value of the correlation coefficient : Yellow, $CCORR < 0.3$; cyan, $0.3 < CCORR < 0.5$; blue, $0.5 < CCORR < 0.7$; black , $CCORR > 0.7$.

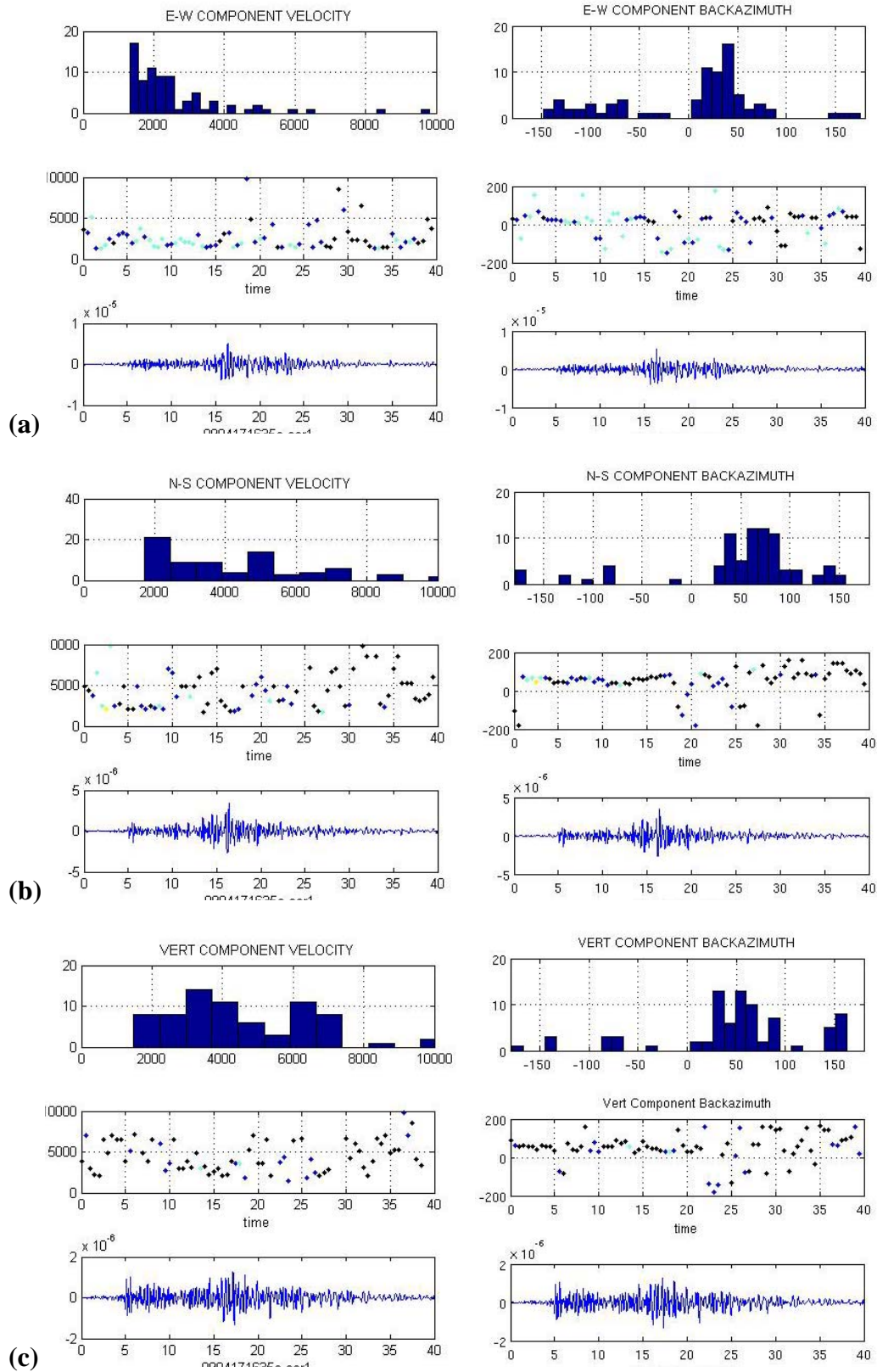


Figure 4.31 –Frankel method applied to “B” event (17/04/09,16:35) to E-W (a), N-S (b) and vertical (c) components, respectively. For each one the values of velocity (left panels) and backazimuth (right panels) are plotted along the seismogram of CER1 station, in addition to histograms. The points colour indicates the value of the correlation coefficient : Yellow, $CCORR < 0.3$; cyan, $0.3 < CCORR < 0.5$; blue, $0.5 < CCORR < 0.7$; black , $CCORR > 0.7$.

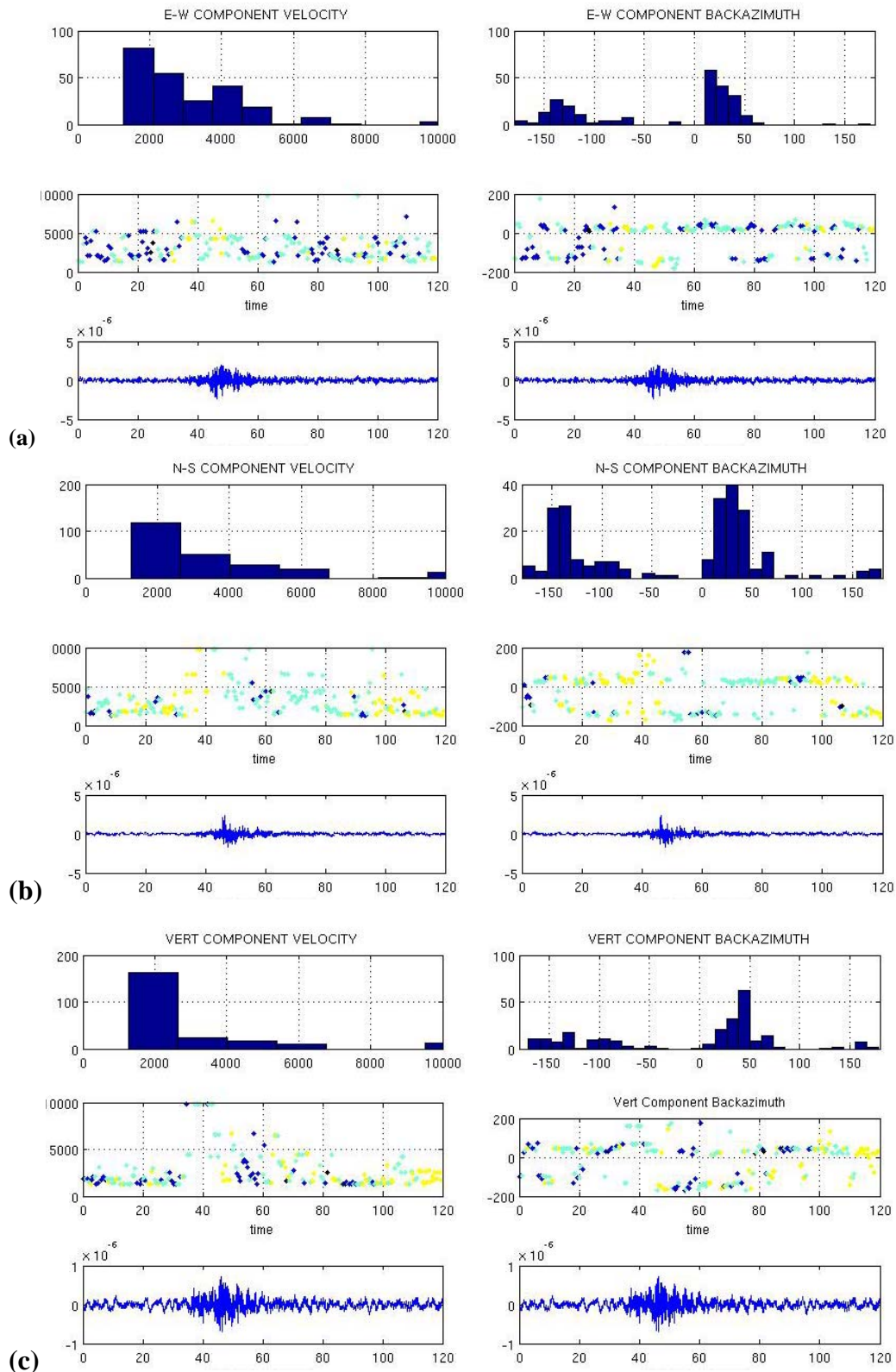


Figure 4.32 –Frankel method applied to “C” event (17/04/09 15:37) to E-W (a), N-S (b) and vertical (c) components, respectively. For each one the values of velocity (left panels) and backazimuth (right panels) are plotted along the seismogram of CER1 station, in addition to histograms. The points colour indicates the value of the correlation coefficient : Yellow, $CCORR < 0.3$; cyan, $0.3 < CCORR < 0.5$; blue, $0.5 < CCORR < 0.7$; black, $CCORR > 0.7$.

4.4.5 Conclusions

Cerreto Laziale hill with its steep morphology elongated in N170°E direction, has been recognized to produce a horizontal polarization of ground motion in N80°E -N90°E direction, perpendicularly to its major axis trend. This has been observed consistently and repeatedly both on ambient noise and on earthquakes, at frequencies on average between 1 and 5 Hz.

Nothing can be inferred about the level of topographic amplification, due to the absence of a reference station and to the lack of locally measured seismic waves velocities.

The Frankel method was used to assess the direction from where the wavetrains travel across the array. In ambient noise, the diffraction from the hill ridge controls the observed backazimuth distribution. Using the earthquake waveforms, the predominant backazimuth corresponds to the source direction. However, for both ambient noise and earthquakes a strong polarization is found around N80°E.

Chapter 5

Polarization across faults

5.1 Introduction

So far, polarization of ground motion across fault zones is observed rarely and mostly associated to trapped-wave generation process.

Zones of intensely damaged rocks are found near faults, especially for faults that accommodated significant slip levels, showing a seismic velocity lower than the surrounding materials (Ben-Zion & Sammis 2003, and references therein). This low velocity layer behaves as a waveguide where constructive interference of critically reflected phases occurs, trapping incident seismic energy and causing a local amplification in the fault zone. Trapped waves (e.g. Ben-Zion & Aki, 1990; Li *et al.*, 1990; Ben-Zion, 1998) are dispersed waves that follow the direct S waves, and their amplitude and frequency content is related to the geometrical and seismic properties of the fault zone at depth. In the last two decades trapped waves have been observed to be produced along many active (e.g., Cormier and Spudich, 1984; Li *et al.*, 1990, 1994, 2000; Hough *et al.*, 1994; Ben Zion *et al.*, 2003) and inactive faults (Rovelli *et al.*, 2002; Cultrera *et al.*, 2003) by earthquakes with hypocentre located both inside and outside the fault zone. To explore the trapping efficiency for different fault geometries, theoretical studies (Ben-Zion and Aki, 1990; Li and Vidale, 1996; Igel *et al.*, 2002; Jahnke *et al.*, 2002) and numerical modelling (e.g., Leary *et al.*, 1991; Huang *et al.*, 1995; Li & Vidale, 1996; Igel *et al.*, 1997 Michael & Ben-Zion, 1998; Ben-Zion *et al.*, 2003) were carried out.

In the few studies where the polarization was investigated, several authors found a predominantly fault-parallel particle motion of trapped waves in the fault zone (Lewis *et al.*, 2005; Rovelli *et al.*, 2002; Cultrera *et al.*, 2003; Boore *et al.*, 2004).

Rigano *et al.* 2008 introduced a new issue about polarization in fault zones, finding that in some cases its orientation is different from fault-parallel direction. They found that the damaged lava at two stations in the Tremestieri fault zone (Mount Etna) amplified ground motion independently of source azimuth and incidence angle. Particle motion was strongly polarized on the horizontal plane in NE-SW direction both on earthquakes and ambient noise recordings.

They repeated noise polarization analysis on other faults on Mount Etna (Pernicana, Moscarello, Acicatena faults),

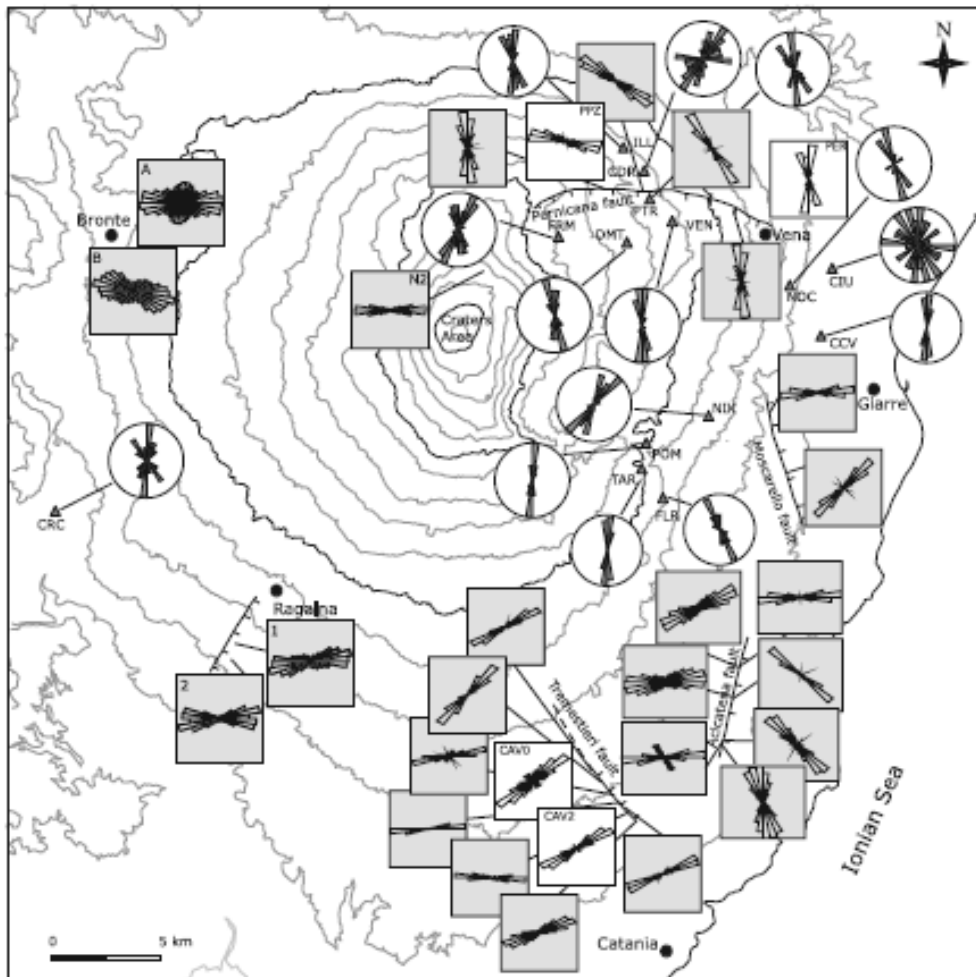


Figure 5.1 – Rose diagrams of ambient noise polarization (gray squares) and of earthquakes (white squares) in Mount Etna faults. White circles show the results of velocity anisotropy found by Bianco *et al.* (1996) and Bianco and Zaccarelli (2007). Redrawn from Rigano *et al.* (2008)

developing for tens of kilometres, without defined boundaries and small width, that are related to recent tectonic activity. They observed again a polarization not fault parallel, persisting too far away from the fault trace (Figure 5.1). This led them to exclude an effect limited to a narrow low-velocity zone hosted between harder wall rocks. Rigano *et al.* (2008) investigated a possible relation with topography, making measurements at sites with sharply varying topographical conditions, but the resulting polarization did remain quite stable. They inferred another possible interpretation, observing that polarization is normal to the fault strike. Normal polarization could be consistent with an in-plane resonance of seismic waves in an wider area not restricted to the narrow fault adjacent zone. Rigano *et al.* (2008) also hypothesized that polarization could be related to anisotropy in the uppermost crust.

The role of crustal velocity anisotropy on earthquake has been already investigated by Bianco *et al.* (1996, 2006) and Bianco & Castellano (1997). Bianco *et al.* (2006) performed an anisotropy study using shear wave splitting method and found evidences of an anisotropic volume with high density cracks in the eastern slope of Mount Etna with an estimated depth of 5 km. Rigano *et al.*(2008) compared S waves splitting fast directions with polarization orientation, without finding any clear relations, probably due to the fact that the two methods investigate different rock volumes.

Among the fault zones of Mt. Etna, the Pernicana fault was thoroughly investigated by Di Giulio *et al.* (2009), who performed denser microtremor measurements in the NE rift segment and in intensely deformed zones of the Pernicana fault at Piano Pernicana. They found a strong directional resonances of horizontal components around 1 Hz in the most damaged part of the fault zone, both on local earthquakes and volcanic tremor recordings (Figure 5.2). They ascribed the horizontal polarization effect to local fault properties, and its resonant frequency to lateral variations of the fault zone. They tried an interpretation involving the role of stress-induced anisotropy and microfracture orientation in the near-surface lavas of the Pernicana fault, hypothesizing that is consistent with the sharp rotation of the polarization angle within the damaged fault zone. The basic idea is that, as pointed out by Cochran *et al.* (2003, 2006) and Boness & Zoback (2004), at a smaller scale the anisotropy along faults is strictly dependent on the local stress conditions field of the shallow crust. Stress-induced anisotropy on Mount Etna could cause aligned cracks in specific direction implying likely local changes of seismic velocities, with the faster direction along the crack orientation. Faster velocity directions would imply lower attenuation directions resulting in polarized motions. Di Giulio *et al.* (2009) used the results by Bianco & Zaccarelli (2009) assessing that shear wave splitting of local earthquakes are consistent with the predominant north-south polarization observed on tremor data on the eastern flank of Mount Etna (Figure 5.2). They explained the observed variation up to 40° of the polarization direction of the volcanic tremor in terms of stress rotation Faulkner *et al.* (2006). Thus they advanced the idea that polarization could be an indicator of the stress field in the upper crust of Mount Etna, and consequently of the anisotropic features of the medium.

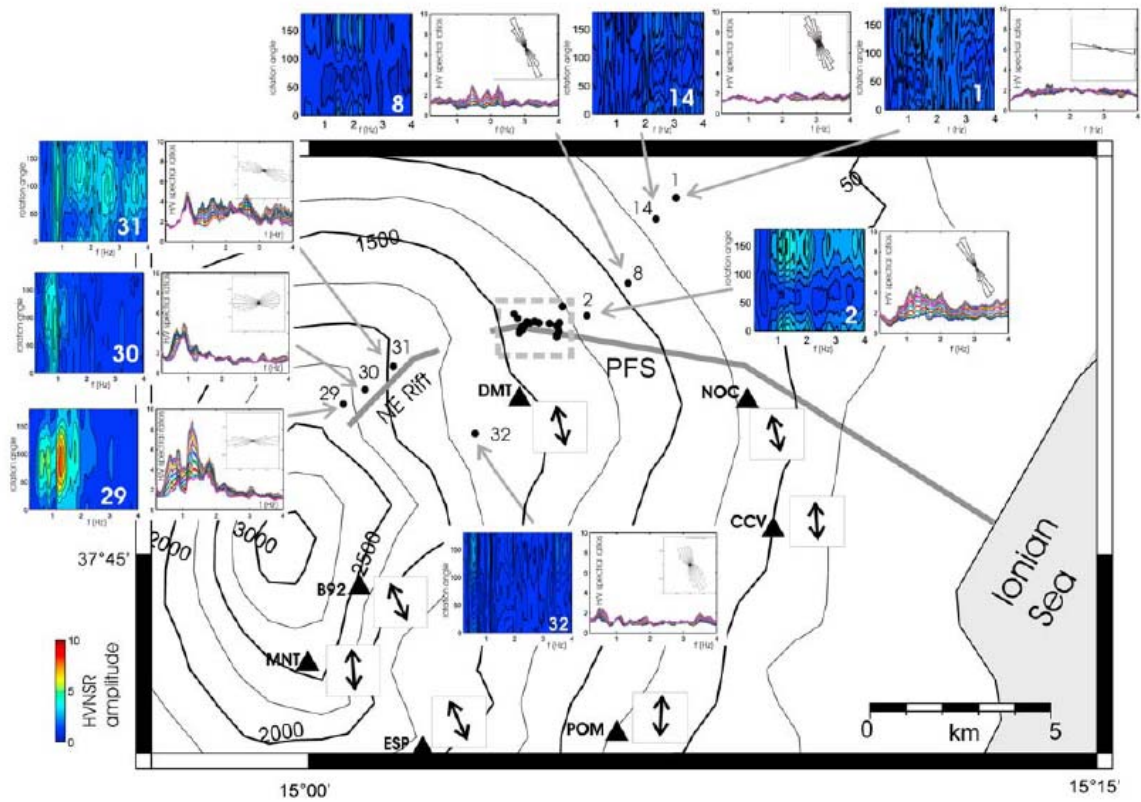


Figure 5.2. HVSR and polarization results across the Pernicana fault. The thick gray lines indicate the NE rift and the Pernicana fault system. The direction of fast velocity found by Bianco and Zaccarelli (2009) using shear wave splitting analysis is also shown (thick black arrows). Redrawn from Di Giulio *et al.* (2009).

5.2 The Hayward fault experiment



Figure Va – Digital elevation model of the eastern side of San Francisco bay area. Red line represents the Hayward fault trace at the surface (<http://www.sfbayquakes.org>).

The Hayward Fault is located on the eastern side of San Francisco Bay, extending from San Pablo Bay (North) to Fremont (South), for roughly 85 km. It passes across densely populated areas, and is considered the most probable source of a future major earthquake in the area. Thus it is one of the most hazardous faults in the United States.

In Niles Canyon, Fremont, an array of seismic station was installed across the fault that recorded seismic events and ambient noise. The analysis of covariance was carried out to study the effect of the fault zone on ground motion polarization.

5.2.1 Geological setting

The Hayward Fault belongs to the San Andreas fault system (Figure 5.3) that represents the boundary between the Pacific plate and the Sierra Nevada microplate, accommodating 75–80% (38–40 mm/year) of present Pacific–North American plate motion (e.g., Argus & Gordon, 2001, Wakabayashi *et al.*, 2004).



Figure 5.3 - The northern San Andreas fault system, showing major dextral strike– slip faults and other features. Redrawn from Wakabayashi (2004).

The regional component of fault-normal convergence is relatively lower than transpression, because the northern part of the San Andreas fault system strikes slightly oblique to the direction of relative motion between the Pacific Plate and Sierra Nevada microplate (Wakabayashi *et al.* 2004). Thus the most relevant transpressional features are represented by restraining bends or stepovers along strike slip faults (e.g., Aydin & Page, 1984; Burgmann *et al.*, 1994, Unruh & Sawyer, 1995). San Andreas fault system is composed by several major dextral strike-slip faults, whose activity irregularly moved during the transform fault system history (Wakabayashi, 1999). All of them show pullapart basins and local transpressional structures related to step-overs and bends. Local transpressional and transtensional geologic features along strike–slip faults occur across a range of scales, from tens of km for large basins and push-up regions, to meters for sag ponds and small pressure ridges (Wakabayashi *et al.*, 2004 and references therein).

The structure is quite complex, but the general strike is N160°E. Following its features from North to South, San Pablo Bay is located in an extensional basin formed in a right step over from the Hayward fault to the Rodgers Creek fault (Parsons *et al.*, 2003, Schmidt *et al.* 2005) with which it joins at depth. Moving to the South, the high resolution seismic relocations performed

by Waldhauser & Ellsworth (2002) delineated a subvertical fault plane, with a seismicity highly organized in space. Near Berkeley the seismicity formed horizontal slip-parallel streaks of hypocenters of only a few tens of meters width, bounded by areas almost absent of seismic activity that were assimilated to several off-fault, subparallel structures. Near San Leandro the seismicity remained diffuse, with strong variation in focal mechanisms between adjacent events indicating a highly fractured zone of deformation resembling an inverted flower structure (Schmidt *et al.*, 2005). South of San Leandro the seismicity started to diverge from the mapped surface trace of the Hayward Fault, following a more easterly trend down to Fremont. The southern surface trace of the Hayward Fault is aseismic and exhibits the highest surface creep rate (10 mm/yr) observed anywhere along the fault (Lienkaemper *et al.*, 1991). Thus San Leandro represents a transition zone where the more westerly striking trend of the Mission seismicity intersects the surface trace of the aseismic southern Hayward Fault.

No evidence of faulting at the surface was found to follow the seismicity trend from the Hayward to the Calaveras Faults (Wong and Hemphill-Haley, 1992; Andrews *et al.*, 1993; Graymer *et al.*, 1995). Waldhauser & Ellsworth (2002) called this sector the “*Mission trend*”, which has been hypothesized to accommodate the compressive strain in the left step over configuration between the Calaveras and the Hayward Faults (Oppenheimer *et al.*, 1993; Andrews *et al.*, 1993). Due to the lack of a definite evidence of surface rupture, Wong & Hemphill-Haley (1992) suggested that the Mission Trend represents a seismically active buried trace of the Hayward Fault located east of its mapped trace. Other authors (Manaker *et al.*, 2005; Simpson *et al.*, 2004; Ponce *et al.*, 2003), alternatively, suggested that the mapped southern Hayward fault dips to the east to connect with the deeper seismicity trends in the 3 to 6 km depth range.

A more recent study by Williams *et al.* (2005) provided a direct evidence that the southern Hayward fault dips about 70° east in the 100 to 650 m depth range. It projects upward to the mapped creeping surface trace, and downward to connect with the “off-fault” east-dipping Mission trend in the 3 to 10 km depth range (Figure 5.4). This interpretation implies that the southern Hayward fault at depth is not a vertical fault lacking microseismicity, but that the Mission trend, rather than being an independent structure, actually represents the main Hayward fault trace at depth.

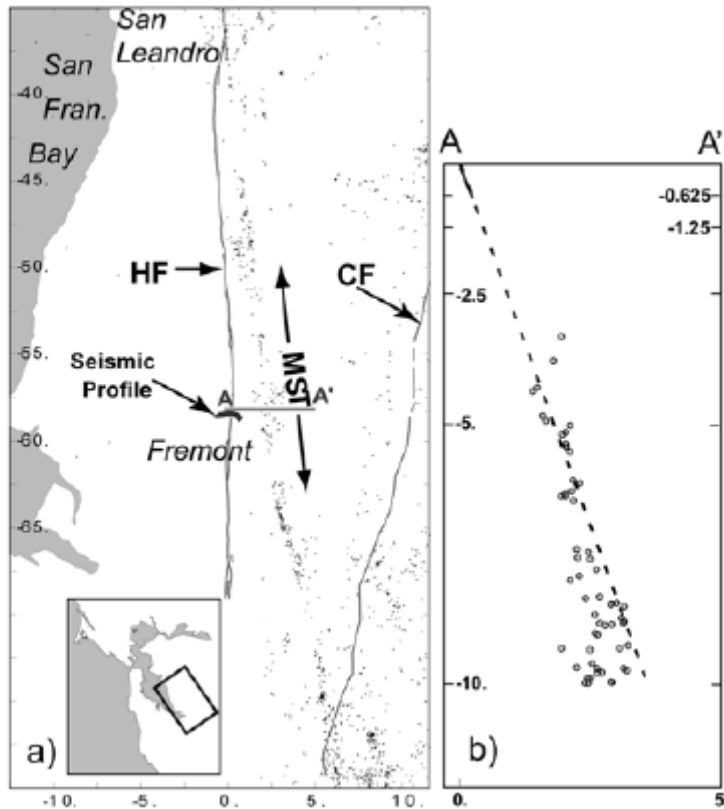


Figure 5.4 –a) Map view showing the surface trace of the creeping Hayward Fault (HF), the Calaveras Fault (CF), and the Mission Seismicity Trend (MST) connecting the two faults at depth at the south end of the MST. Small dots show the epicenters of double-difference (d-d) relocated earthquakes (Waldhauser & Ellsworth, 2002). The numbers along the left and bottom sides follow Lienkaemper (1992) and are the distances in kilometers along the Hayward Fault trend measured from Point Pinole where the fault goes offshore. Gray dashed line A–Ao is the location of the seismicity cross section where Williams et al (2005) acquired the 1.6 km seismic reflection profile. b) Cross section view of seismicity along A–Ao. Circles show the hypocenters of d-d relocated earthquakes. The numbers along the left and bottom indicate depth and distance in kilometers. Hayward fault dip at 70° interpreted from seismic reflection profile shown as heavy line in the near surface. Projection of 70° dip down to seismicity shown by dashed line. Redrawn from Williams et al (2005).

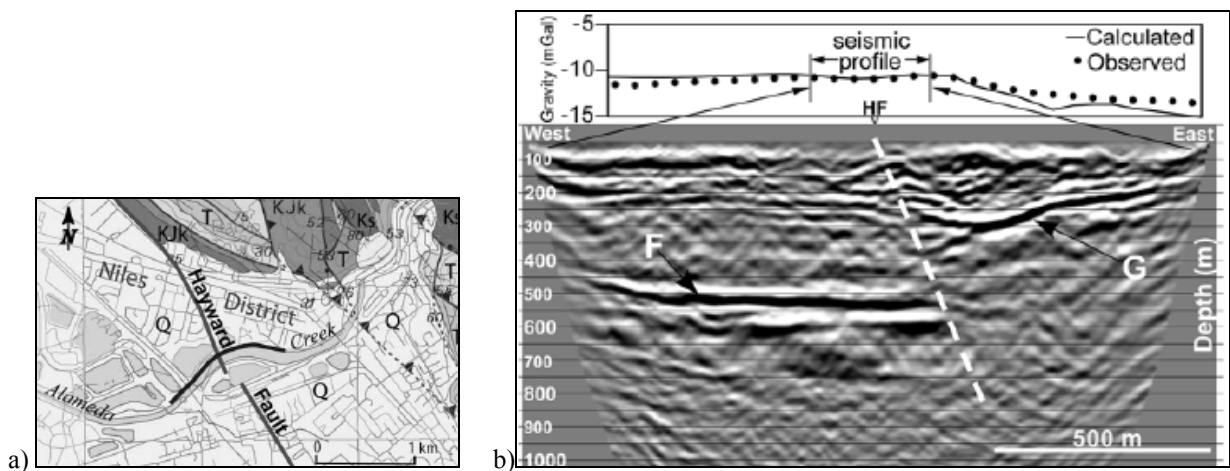


Figure 5.5 –a) Geologic map in the vicinity of the seismic profile showing the Hayward fault trace through Niles and across Alameda Creek. Lightest gray areas are Quaternary alluvium (Q), darker gray areas to the north and east of the seismic profile are Mesozoic (KJk and Ks) rocks of the Great Valley Sequence and Tertiary rocks (T). b) Observed and calculated gravity along the seismic profile and across the Hayward fault. Bottom - Migrated depth section from seismic reflection profile showing location of the east-dipping Hayward fault (dashed line) and its projection to the mapped surface trace (HF). Reflections labeled F (top of Franciscan Complex) and G (top of Great Valley Sequence). Redrawn from Williams *et al.* (2005).

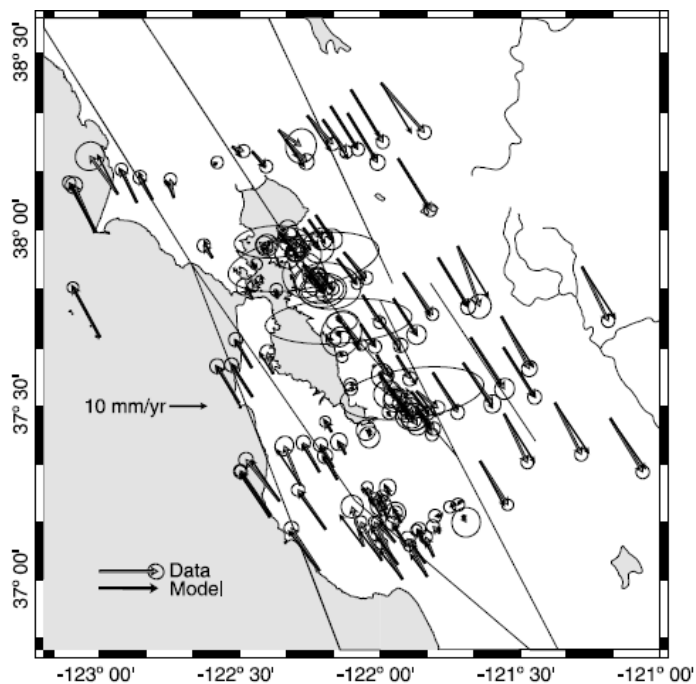


Figure 5.6. GPS displacement rates (gray arrows) observed from 1994 to 2003 with 2-sigma error ellipses. Redrawn from Schmidt *et al.* 2005

The Hayward fault zone, is predominantly a strike-slip right-lateral fault with about 100 km of offset during the past 12 Ma and at least a few hundred meters of east-up displacement over the past 2 Ma (Kelson and Simpson, 1995; Graymer *et al.*, 2002).

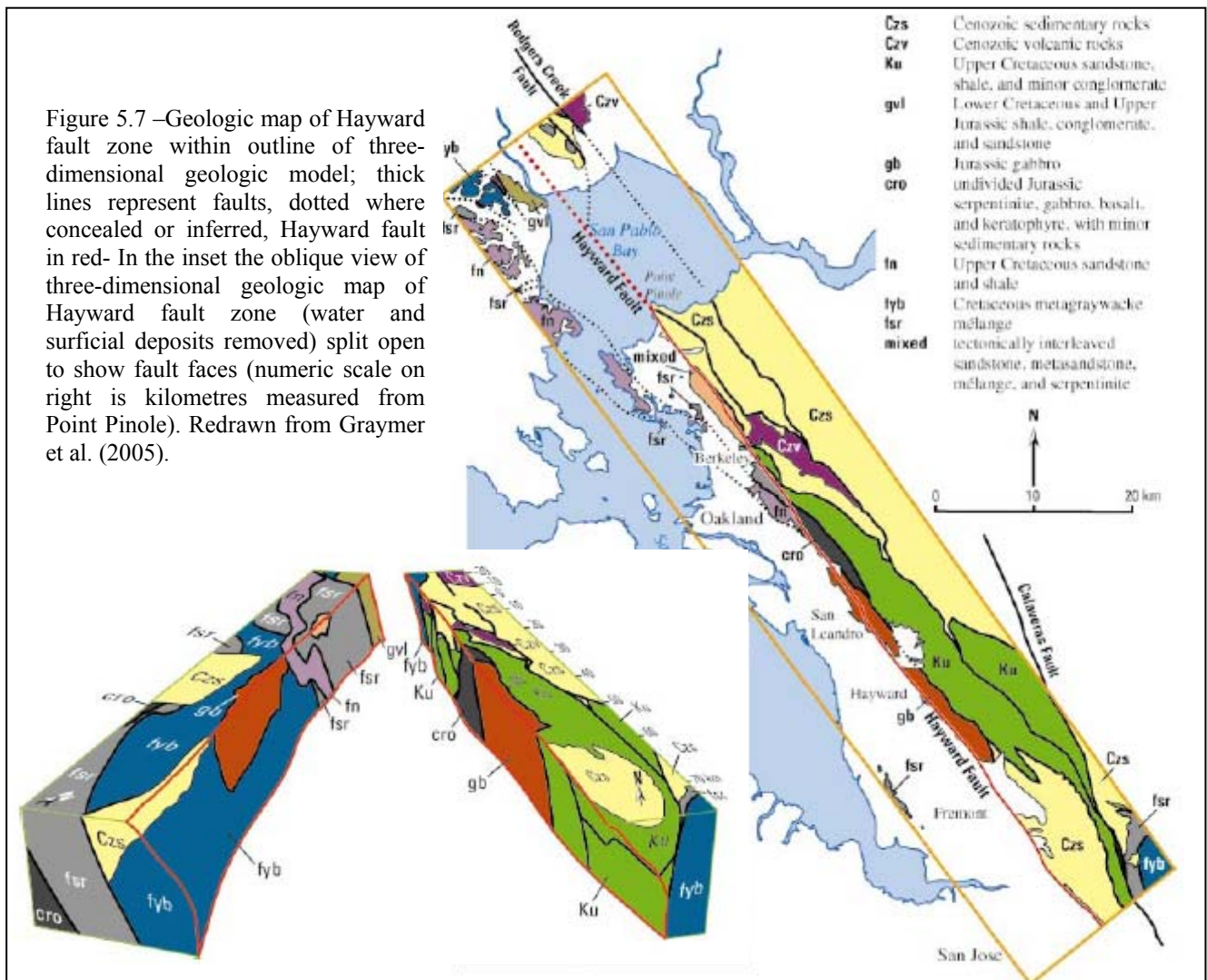
The active surface trace of the Hayward fault is well documented from both geomorphic evidence and from the offset of man-made structures (Lienkaemper *et al.*, 1991), that is undergoing significant creep (Savage and Lisowski, 1993; Lienkaemper, 1992) with some patches accommodating 50% or more of the long-term fault displacement.

In spite of this, the fault has also experienced moderate to large earthquakes as the M6.8 earthquake that occurred in 1868, which rupture in surface was at least 30 km long or more (Lawson, 1908; Lienkaemper *et al.*, 1991; Yu and Segall, 1996; Bakun, 1999). A Paleoseismic study performed in a trench on the southern Hayward Fault (Fremont) by Williams (1992), concluded that at least six ruptures on the Hayward Fault occurred during the past 2100 years.

By comparing the patterns of microseismicity observed on the fault with models of fault zone creep, Gans *et al.* (2003) investigated the long-term displacement/deformation history of the fault in terms of: the relative roles of aseismic creep; the amount of fault slip accommodated through microseismicity; the strain accumulation (slip deficit). They used the relocation of Hayward fault seismicity for the period 1967-1998, by Waldhauser & Ellsworth (2002), who found that seismicity occurred along the fault in clusters spaced of 10 km on average separated by

quiet regions characterized by very low seismicity (Figure 5.8). The absence of microearthquakes over large contiguous areas of the northern Hayward Fault plane in depth interval 5 to 10 km, and the concentrations of seismicity at these depths led Waldhauser & Ellsworth (2002) to conclude that the aseismic regions are either locked or retarded and are storing strain energy for release in future large-magnitude earthquakes. This was also the conclusion of Gans *et al.* (2003) who calculated the area of asperities on the creeping fault, observing that microseismicity on the Hayward fault produces a negligible percentage of the seismic moment dissipated on the fault. This is finally confirmed by the factor of 2 difference between the long-term slip rate and the observed surface creep rate by InSAR data (Schmidt *et al.*, 2005).

The three-dimensional geologic map by Graymer *et al.* (2005) constructed from hypocenters, potential field data and surface map data, is shown in Figure 5.7. They concluded that fault behaviour (seismic or aseismic) as well as fault shape are better correlated with the extent of rock units and with their strengths and contacts location (when they abut the fault), rather than with variations in rock-body juxtapositions across the fault.



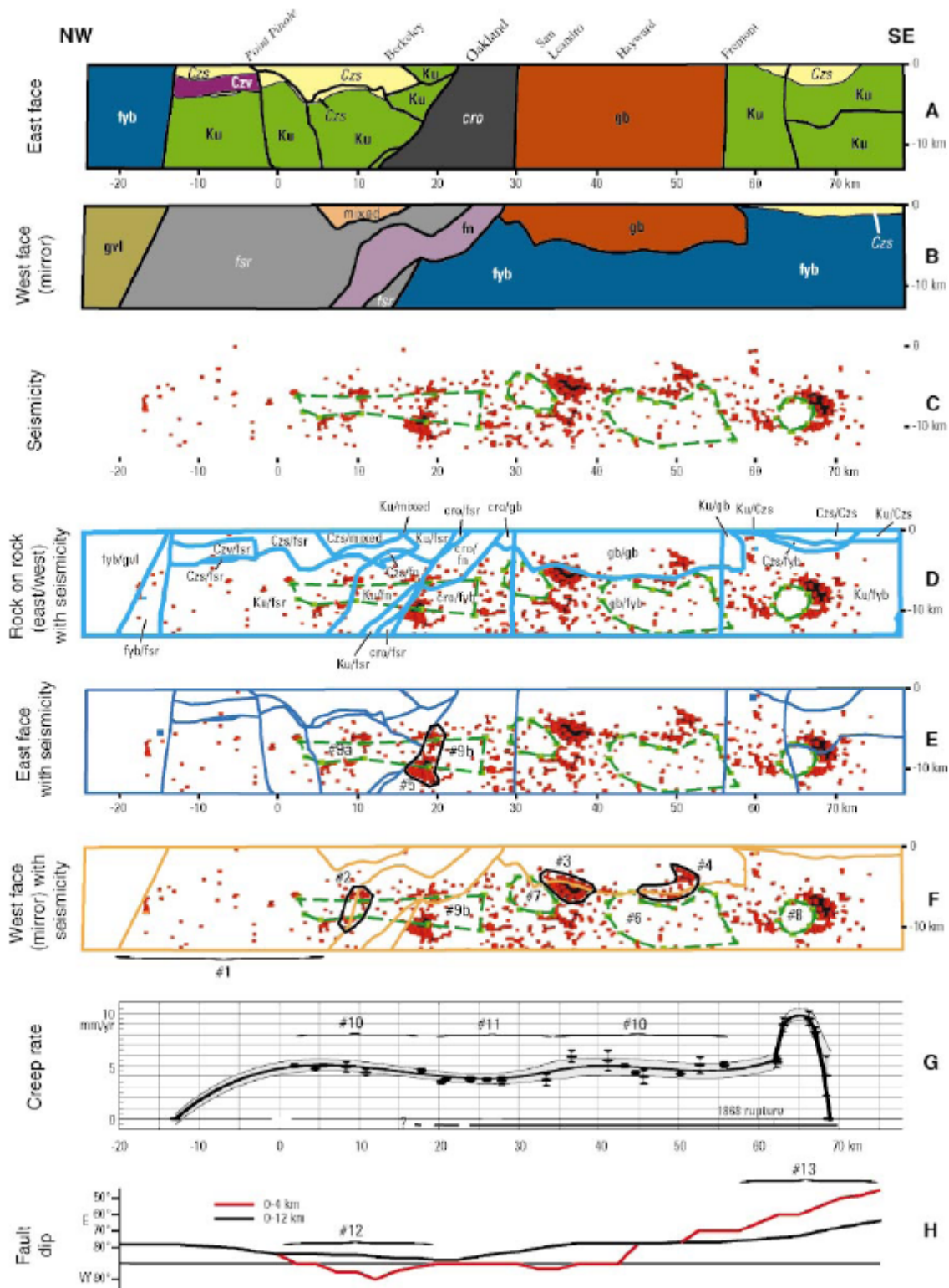


Figure 5.8 – Fault-surface maps. A) and B) - East and west faces of Hayward fault (horizontal scale is in kilometers measured from Point Pinole); relatively strong units are labeled in bold, weak units in italics). C) Seismicity (from Waldhauser & Ellsworth (2002)); squares are double-difference hypocenters within 3 km of fault surface; green lines outline aseismic [possibly locked] patches). D) - Rock-on-rock map with seismicity, showing rock types that are adjacent and presumably sliding past one another (first unit 5 east face; second unit 5 west face). E) – East face geology with seismicity. F) - West face geology with seismicity. G) - Distribution of creep rate (Lienkaemper *et al.*, 2001). H) - Variation in fault dip (black line is average fault dip; red line is average fault dip in upper 4 km). Redrawn from Graymer *et al.* (2005).

5.2.2 Site and station deployment

To study the polarization across the Hayward fault, an area close to Niles Canyon (Fremont) shown in Figure 5.11 was chosen. Here, since July 2008 researchers of the US Geological survey has installed an array of 6 accelerometers just across the fault. The array (stations ND1 to ND7 in the inset of Figure 5.11) was composed of seven accelerometric stations equipped with Episensor and K2 Kinematics digitizer.



Figure 5.11 – Location the two seismic arrays used in the polarization analysis (red point and star): coloured labels = accelerometric array, back labels = velocimetric one. The epicentres of the selected earthquakes are identified by a blue point and the label indicates date & estimated magnitude. Cyan lines represent projection of San Andreas Fault System. The inset shows stations deployment. The Hayward fault trace at the surface digitized by (Lienkaemper et al., 2001) is represented through a red line

On June 2009, a six-station array was installed in order to record ambient noise at sites closer to the fault trace. The array was composed of six velocimetric stations equipped with Mark L4 1Hz seismometer and reftek 72A/05 seismic recorder. Stations were deployed in houses backyards, the sensor posed on the concrete and synchronized through a GPS receiver (Figure 5.12). The array continuously recorded ambient noise for 12 days (6th to 17th of June), with a sampling rate of 100 sps. Stations ND8 to ND11 were installed in new sites closer to the fault, and other two velocimetric stations reoccupied the previous ND2 and ND3 location (Figure 5.11). The goal was to investigate whether the changing sensor influenced polarization.



Figure 5.12 – Deployment of seismic stations. Location ND3 with accelerometric (A) and velocimetric (B) stations. Velocimetric stations at locations ND9 (C) and ND8 (D),(E).

5.2.3 Seismic events analysis & results

In the period July 2008 – March 2009, the accelerometric array recorded around 30 events, whose hypocenters were taken from the Northern California Earthquake Data Center (<http://quake.geo.berkeley.edu/>). The seismogenic areas were located along the San Andreas fault system, with hypocentral depths in the range 5-16 km. Between those recorded, 12 events were selected, with a high signal to noise ratio and with different backazimuth, to distinguish the occurrence (if any) of different site effects for different provenances directions.

The signals were cut and detrended then the rotated receiver functions were calculated at each station separately for each event. Amplitude spectra of the two horizontal components were also smoothed with a 0.5 Hz running frequency window. Based on the RFs spectra, the frequency band 1-7 Hz was chosen to bandpass filter the signals before performing the covariance analysis. The covariance analysis was performed on to the entire length of seismograms, using a moving window of 1 sec with 0.5 s overlap. The hierarchical criterion illustrated in section 2.2 was applied to the resulting polarization azimuths.

Because of the large amount of information coming from the analysis, the results from the whole data set were plotted together both in the time domain and averaged in the circular histograms. They are depicted in Figure 5.13. For each station a rose diagram is calculated showing the percentage of time windows satisfying the *hierarchical criterion* (bottom-right-corner). Moreover the polarization azimuth are plotted versus time, with a color scale related to the weigh **WH**. Stations are divided as “in-fault” (i.e. tens of meters distant from the fault trace at the surface) and “off-fault” (i.e. hundreds of meters from the fault trace at the surface).

Covariance Matrix analysis results

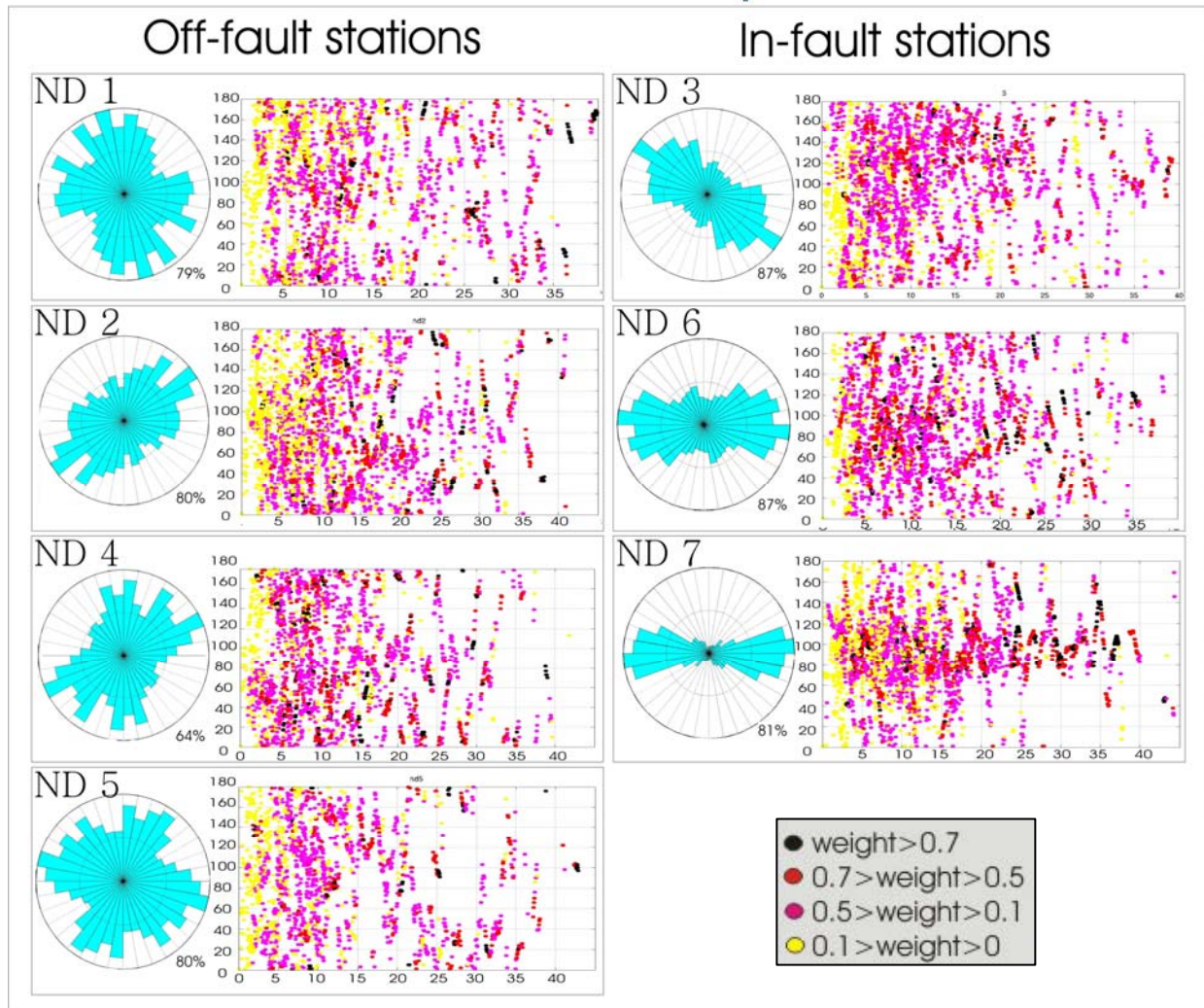


Figure 5.13 – Covariance matrix analysis results at each accelerometric station by averaging the results of the 12 events selected. For each station the rose diagram is shown with the percentage of time windows satisfying the *hierarchical criterion* (at its bottom). Right to each rose diagram, the polarization azimuth are plotted versus time, with a color scale related to the weigh **WH**.

The four off-fault stations **ND1**, **ND2**, **ND4**, **ND5** (left panel), show dispersion of polarization angles as a results of differences related to the seismic path. In contrast, the three in-fault ones **ND3**, **ND6**, **ND7** (right panel) show a defined polarization direction which seems to be persistent independently from the earthquake mechanism and provenance. Stations ND6 and ND7 depict a polarization oriented in E-W direction, being a very stable and persistent feature. On the contrary ND3 seems to be affected by something different being the polarization azimuth oriented N120°-130°.

Rotated Receiver Functions

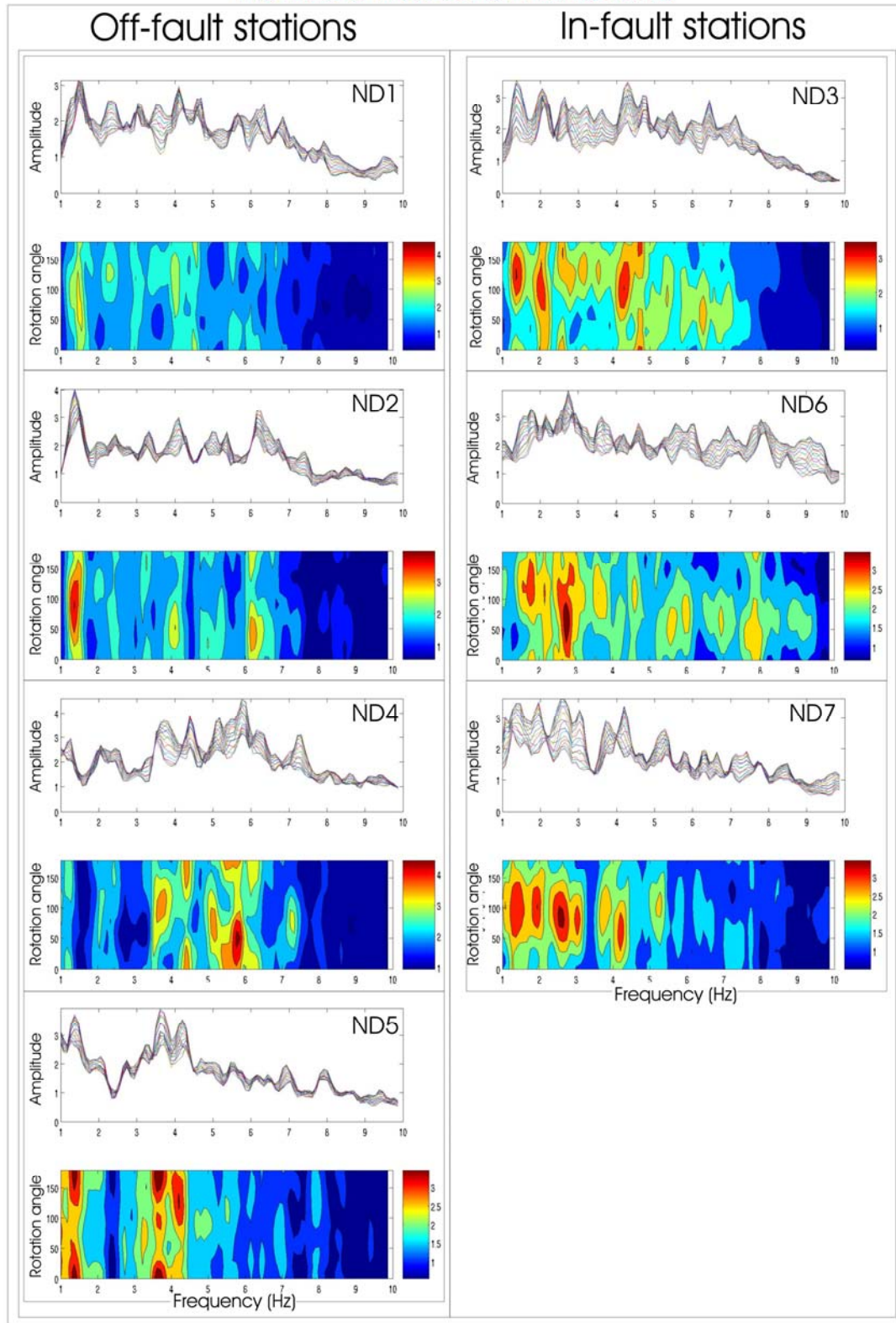


Figure 5.14 – Rotated receiver functions at each accelerometric station by averaging the results of the 12 events selected. For each station the contour plot of amplitudes with rotation angle versus frequencies is shown at the bottom, while at the top the amplitude spectra of rotated components are plotted.

Date & Time	Lat.N	Long.E	Depth Km	M	ISOSYN	ND1	ND2	ND3	ND4	ND5	ND6	ND7
2008/09/06 04:00	37.8620	-122.0075	16.61	4.10 Mw	I	*	*	*	*	*	*	*
2008/09/21 16:20	37.7245	-121.9783	10.41	2.26 Md				*	*			
2008/10/10 23:19	37.8365	-122.2153	12.65	3.05 ML		*	*	*	*		*	*
2008/11/10 19:56	37.4335	-121.7750	10.02	3.20 Mw	I	*	*	*	*	*	*	*
2008/12/09 16:25	37.4835	-121.8095	6.13	3.49 ML		*	*	*	*	*	*	*
2008/12/21 17:35	36.6748	-121.3002	7.24	4.00 Mw		*	*	*	*	*	*	*
2009/02/15 22:05	36.8615	-121.5978	6.66	3.29 ML				*			*	
2009/02/21 19:01	37.6262	-121.9500	11.79	3.20 ML	I	*	*	*	*	*	*	*
2009/02/26 16:08	36.8627	-121.5997	6.70	3.24 ML			*	*				*
2009/03/08 14:47	37.4743	-121.8045	9.58	3.50 Mw	I	*	*	*	*	*	*	*
2009/03/18 02:26	37.4575	-121.7698	7.87	3.11 ML				*			*	
2009/03/30 17:40	37.2848	-121.6157	7.65	4.30 Mw	I	*	*	*	*	*	*	*

Table 5.1 – Seismic events selected for the analysis. Label “I” identifies events selected for the calculation of source synthetic polarization.

Exploring the distribution of weights **WH**, lower values (yellow) are given by the first parts of signals related to P waves, while higher values can be found near S waves and surface waves. Anyway this feature is more evident observing separately single events. (as in Figure 5.15).

The rotated receives functions calculated at each station by averaging the results of the 12 events selected, are displayed in Figure 5.14. For each station the contour plot of amplitudes with rotation angle versus frequencies is shown under the amplitude spectra of rotated components.

No significant amplitude variations between off-fault and in-fault stations are observed in contour amplitude plots. Looking at the spectra from rotated components, off-faults stations do not show relevant differences between different rotation angles; on the contrary, in-fault stations (right column) generally depict variations up to factor of 2 for different rotation angles in the band 1-7 Hz. This is a clear indicator of polarization in the horizontal plane. Stations ND6 and ND3 (in-fault) interestingly show a double behavior at changing frequencies, that is very pronounced on the most part of analyzed events: while in the range 4- 8 Hz the polarization is roughly between N60°E-N80°E degrees, at lower frequencies it is directed along higher angles, closer to the fault strike. Anyway a better detail is impossible to be reached using the rotated receiver functions, and this double polarization behavior has to be observed separately on each event results.

In order to verify that the observed polarization cannot be imputed to source effects the software ISOSYN (Spudich & Xu, 2003) was used to model the source polarization. For each of the five chosen events (depicted in Table 5.1 with label “I”), the source expected polarization was calculated on the basis of focal mechanism, of stations distance and orientation from the source area. The observed polarization was never correlated to source effects, leading to the conclusion that it is related to path or site effects.

The results for one event occurred on 19/02/2008 are presented as typical in Figure 5.15. On the left, covariance matrix analysis results performed in the frequency range 1-7 Hz are shown with two rose diagrams for each station: the cyan one is made through all the time windows along the signal, the yellow rose diagram is constructed applying the “*hierarchical criterion*” described in Section 2.2. Moreover the weighted azimuths are plotted versus time and along signals, clearly showing that P waves are associated to polarization azimuth with a low **WH** while S waves and surface waves are related to higher **WH** values. The construction of the yellow weighted circular histogram thus reflects more S and surface waves polarization than P waves one. The yellow rose does not significantly differ from the cyan one, just excluding less horizontal azimuths related to P waves few elongated polarization ellipsoids (as explained in Section 2.2).

Figure 5.15 also displays the polarization modeled for P and S waves, due to source effect. While the former can be recognized on recorded P-waves, the latter is quite never observed.

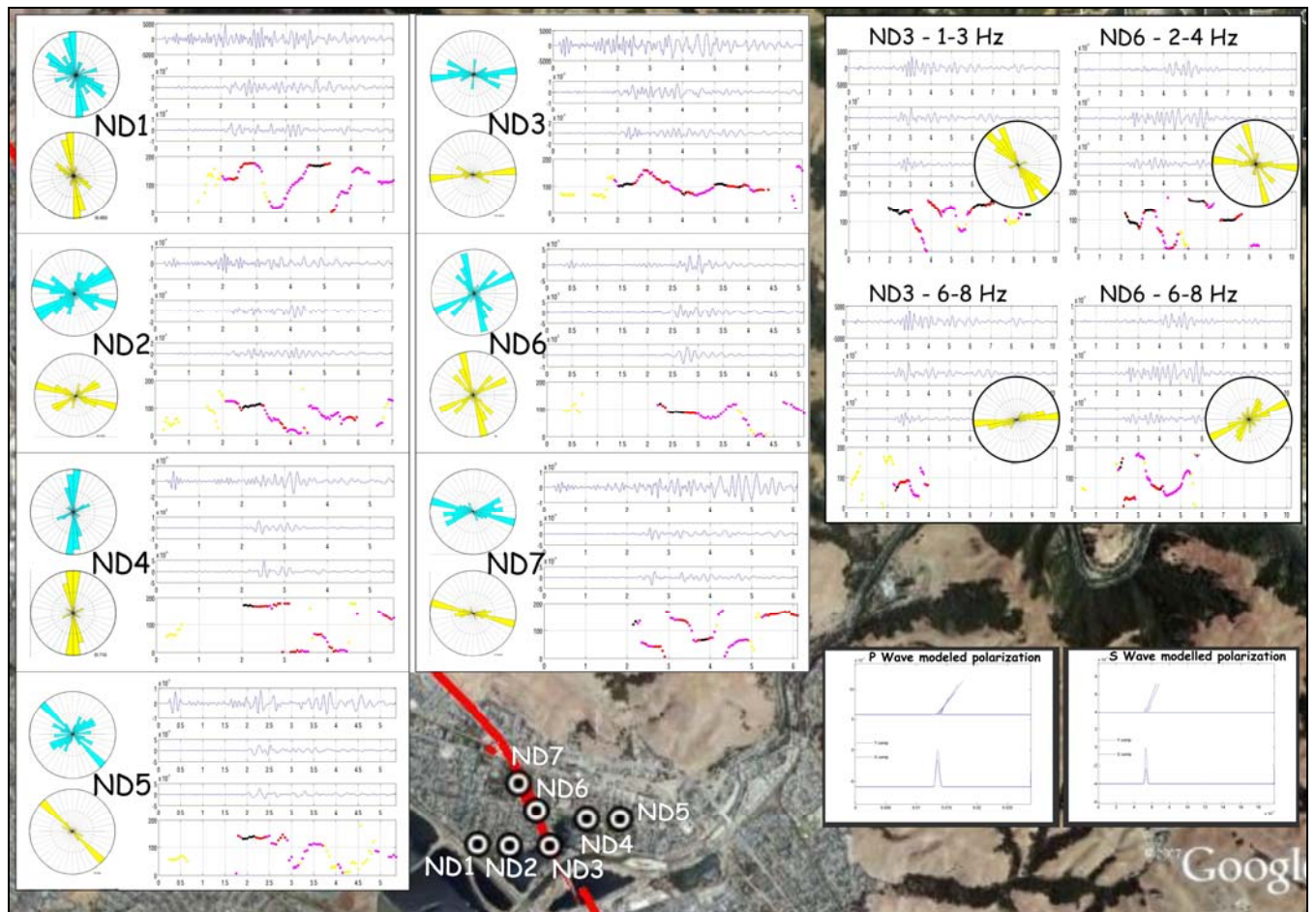


Fig.5.15– Covariance matrix analysis results performed for one exemplificative event occurred on 19/02/2008. For each station two rose diagrams are displayed : the cyan one is made through all the time windows along the signal, the yellow rose diagram is constructed applying the “*hierarchical criterion*” described in Section 2.2. The weighted azimuths are even plotted versus time, using the same colour scale of Figure 5.13 that represents **WH** values associated to each azimuth. Plots of recorded signals are even shown representing from the top to the bottom: vertical, N-S and E-W components. On the right panel the results of the covariance matrix analysis performed for station ND3 and ND6 and differing two frequency bands, are shown. At the right-bottom panel there is the source modelled polarization for P and S waves.

Exploring the differences of polarization at ND3 and ND6 for varying frequencies, the results of the covariance matrix analysis performed in two frequency bands are additionally shown in Figure 5.15 on the right panel. Two polarizations can be identified: one parallel to fault strike, mostly at TOP3 in the band 1-3 Hz but even at TOP6 in the band 2-4 Hz; the other one in N70°E-N90°E direction at both stations. This is a very interesting feature because the former polarization could be related to trapped waves in fault zone, that can also be recognized looking at the rotated receiver function, calculated for this event (Figure 5.16).

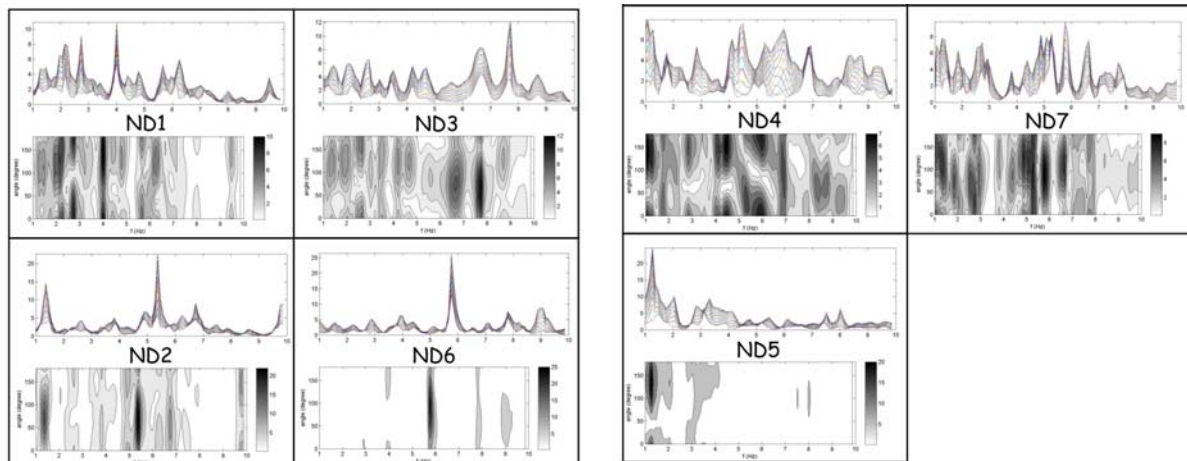


Figure 5.16 – Amplitude Contour map of rotated receiver functions calculated at each station for one exemplificative event occurred on 19/02/2008. The rotation angles are plotted versus frequency.

5.2.4 Ambient noise recordings data : analysis & results

Trying to follow the N80-90 polarization in the fault zone and to better understand the differences between ND3 and ND6-ND7 stations, a denser array of 6 velocimetric stations was installed inside the previous one, that recorded ambient noise from 6 to 17 June 2009 in continuous modality.

Before proceeding to the analysis, all signals were detrended and the mean was removed. The rotated receiver functions were calculated for one day of recording, revealing a frequency content mostly between 1 and 6 Hz.

Considering the high influence of the cultural activity on ambient noise in this area, a test was made by applying an antitrigger algorithm to select the most stationary parts of ambient vibrations, as explained in section 3.1. By comparing the polarization angles obtained by applying and not applying the antitrigger algorithm, results did not change probably due to the large amount of data compared to the smaller number of spikes.

The covariance matrix analysis was led out on the entire 12 days data set in the selected frequency band, cutting signals in 30-minute windows each hour of the day.

Observing the distribution of polarization along each day and its change between day and night, the control of the cultural activity on ambient noise appears to be significant. During the day the polarization orientation is substantially scattered, whereas remains quite stable in the night, particularly out of railways running times (1-4am). In Figure 5.17 the variation of polarization during one day for stations ND8, ND10 and ND11 is shown. While ND8 holds the polarization

direction quite stable, ND10 and ND11 very different orientations during day times. This could be ascribed to a different cultural noise level, even due to inhabitants activities.

For this reason, the rose diagrams were calculated only using nightly hours (1 to 4 am) of the 12 recording days. They are shown in Figure 5.18. A clear interpretation is hard to be found, being the most part of rose diagrams very dispersed, excepting for ND8 that shows a persistent and fairly peaked polarization oriented around N60°E. The same orientation is shown by ND10 and ND2, the latter being also in agreement with the polarization previously seen on earthquakes. Only ND11 shows a polarization oriented N90, while ND3 is polarized around N20.

Analyzing the polarization along time and days, station ND9 reported many differences being strongly influenced by some artificial sources during the most part of recording periods. Its results are therefore considered to be not reliable.

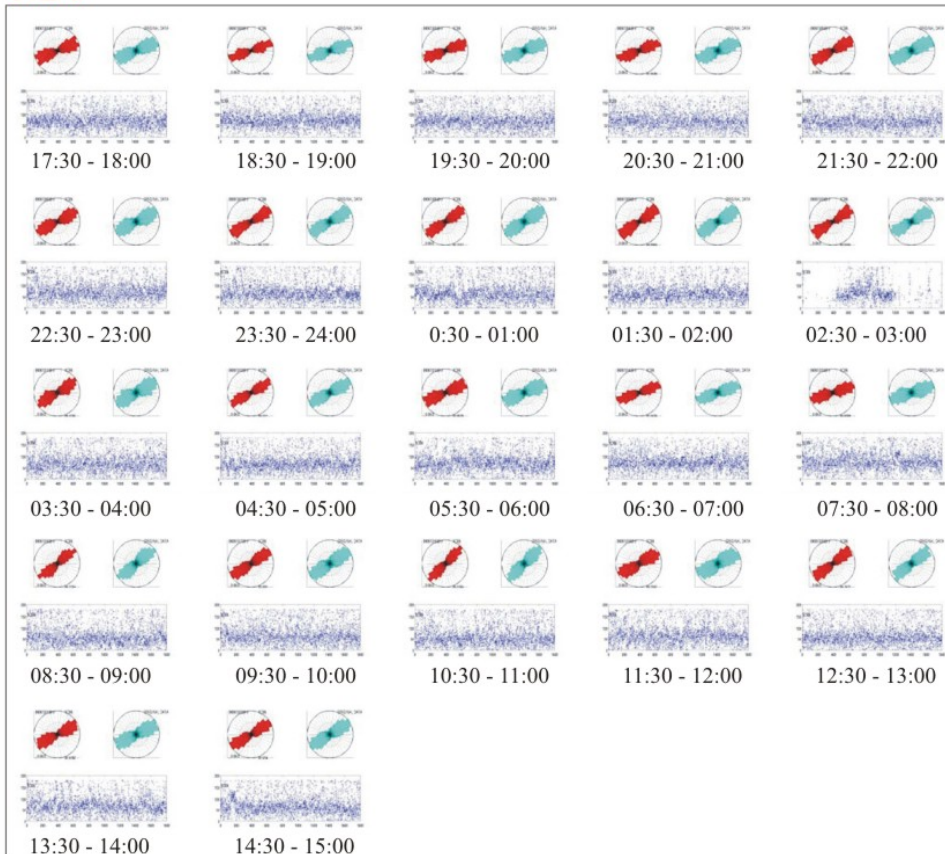
From this experiment on ambient noise the main conclusion is that the polarization angle becomes N90°E going closer to the fault trace.

The array also recorded two small earthquakes, and the analysis of polarization was carried out as well, partially confirming the features previously described, in particular for stations ND2, ND8 and ND10 (Figure 5.19).

ND11



ND8



ND10

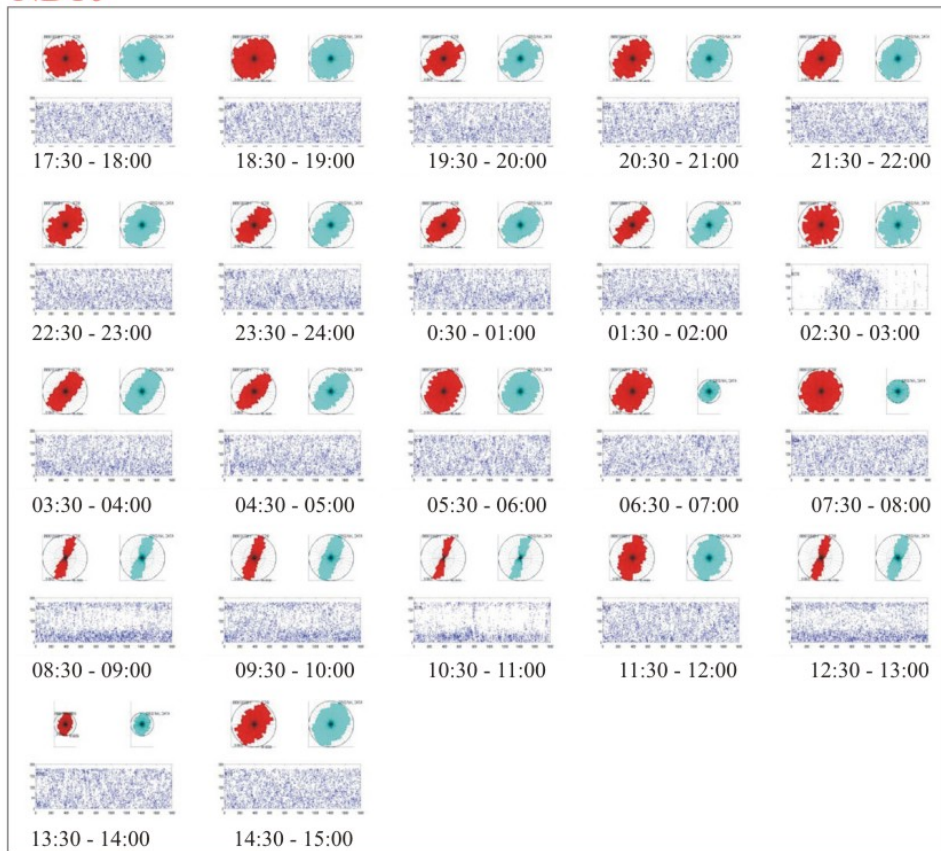


Figure 5.17 – Nightly ambient noise polarization for 12 recordings days from covariance analysis in the frequency range 1-4 Hz and 16-20 Hz (only ND11).



Figure 5.18 – Nightly ambient noise polarization for 12 recordings days from covariance analysis in the frequency range 1-6 Hz and 16-20 Hz (only ND11).

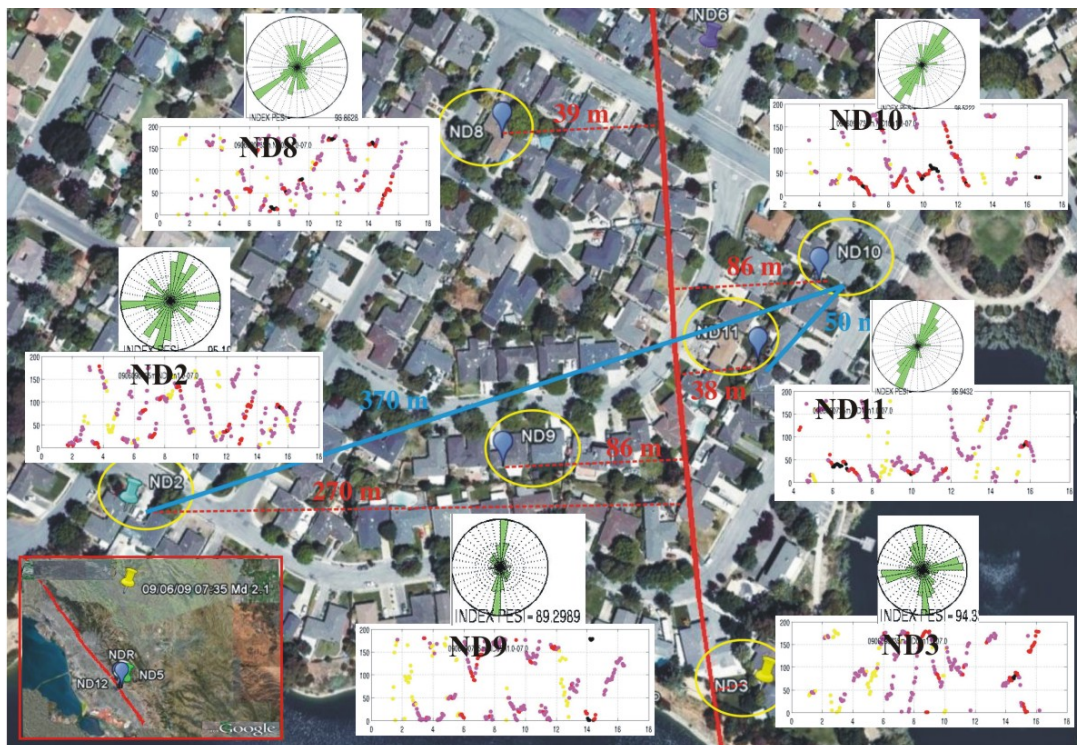
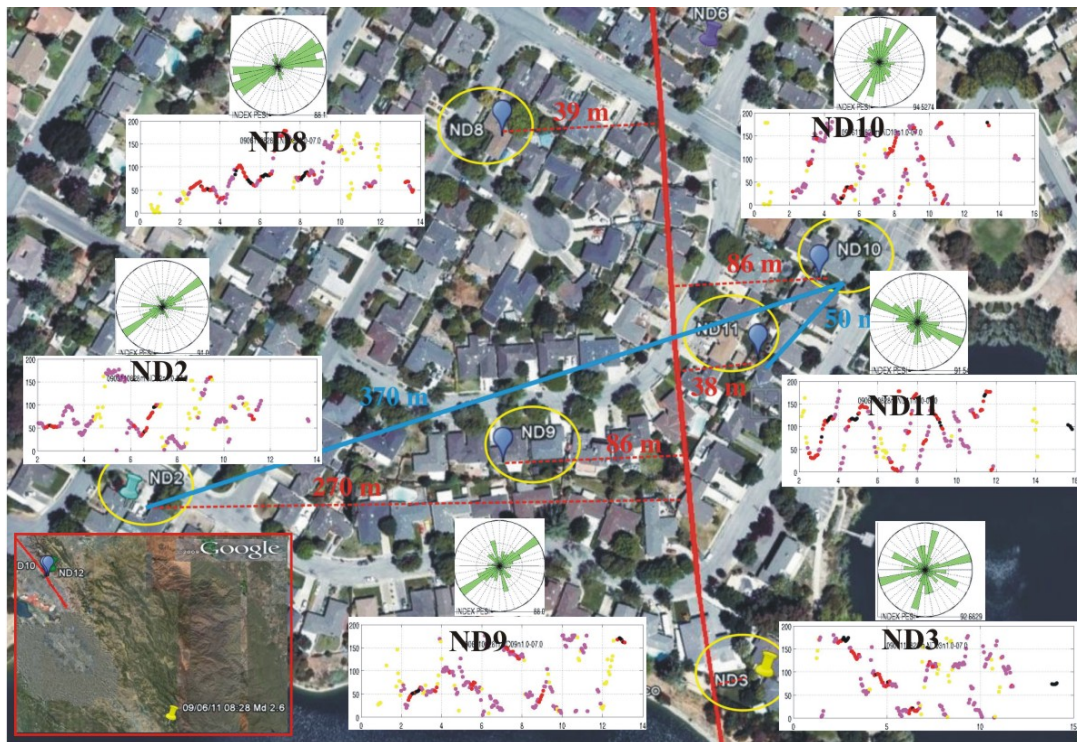


Figure 5.19 – Analysis of polarization performed in the frequency range 1-7 Hz on two events recorded by the velocimetric array. The insets show the epicentre position in respect to the array location.

5.2.5 Brittle deformation models

Fault zones are composed of a fault core where most of the displacement is accommodated, and an associated fault deformation zone also called “damage zone” (Caine *et al.*, 1996). The elastic stress accumulation in the fault zone and the friction during the movement of the fault in the damage zone produces a confined stress field that is named “kinematic stress component” (Figure 5.20 a). It commonly overrides the regional stress and may produce three types of fractures systems (i.e. Riedel fractures): joints (extensional fractures), synthetic and antithetic cleavages, and pressure solution surfaces (Figure 5.20 b).

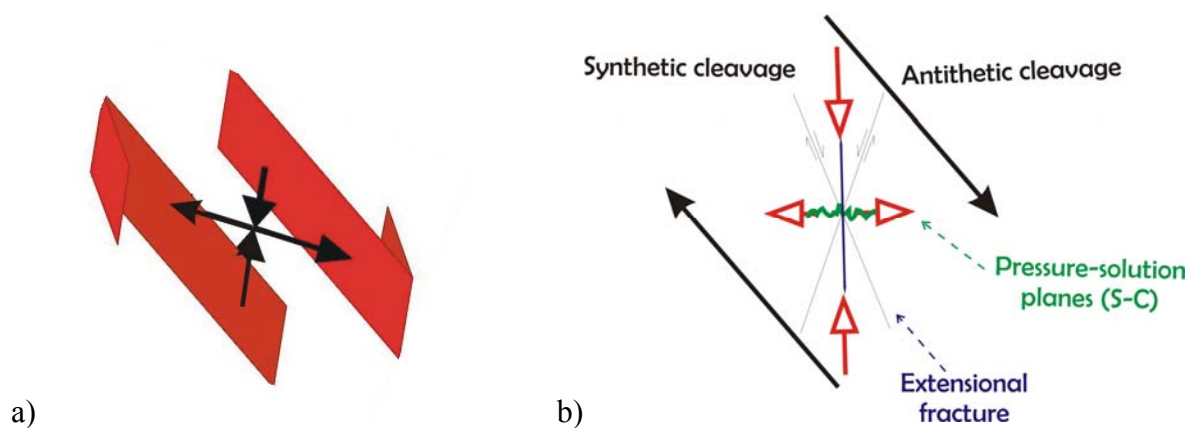


Figure 5.20 – a) The kinematics component of stress; b) Brittle deformation types related to the kinematics stress field in the damage zone (plane view).

The brittle deformation pattern associated to the Hayward fault was analytically computed using the package FRAP (Salvini, 2002) to explain the spatial distribution of the observed polarization. The fault was modelled as a 20x8 km surface reaching 11.5 km depth, dipping 70° to East, and with an average strike of N20°W, according to Williams *et al.* (2005). No minor irregularities were added on the fault surface since the fault movement occurred over a large time scale.

Even though, as shown by Graymer *et al.* (2005), the Hayward fault separates very heterogeneous regions with different lithotypes, in this model the rock rheological parameters were chosen to be the same on the two sides of the fault. They were fixed as: density 2400 kg/m³, cohesion 5MPa, Poisson ratio of 0.25, Friction angle of 30°, stress drop coefficient 50%, shale content 10%, since lateral heterogeneities would have introduced differences in features orientations of the order of few degrees, that were considered to be irrelevant at the purposes of this study. The movement was fixed to be right-lateral strike-slip with the total displacement fixed to 200 m.

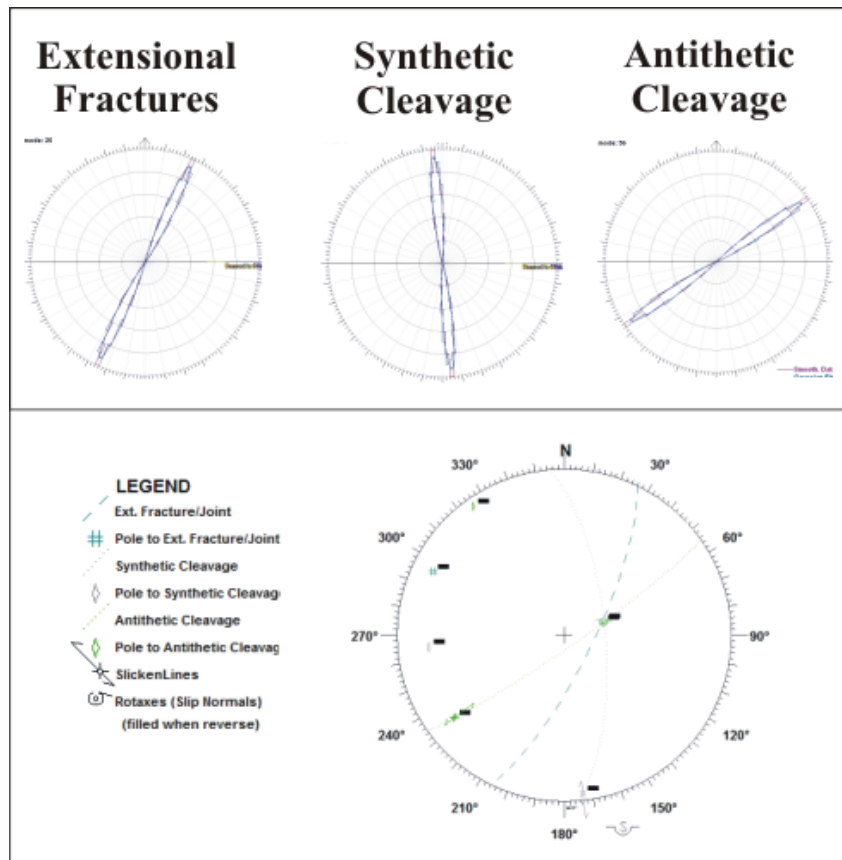


Figure 5.21 – top - Rose diagrams of modelled extensional fractures and cleavages produced using the package FRAP 3 (Salvini, 2002) related to the stress kinematics component; -bottom- Schmidt Lower Hemisphere projections of extensional fractures and cleavages. All the plots are made through the software DAISY (Salvini, 2002).

According to the several works performed in the area to define the orientation of tectonic stress principal axis (e.g. Provost & Houston, 2003), the axis of maximum compression σ_1 was set to be oriented N-S and the axis of minimum compression σ_3 oriented E-W, both lying on the horizontal plane, with vertical σ_2 . Their modulus were arbitrary chosen to be 110, 10 and 0 MPa, respectively for σ_1 , σ_3 and σ_2 . Stress conditions related to fault movement and to the kinematics component of stress were applied. The brittle deformation pattern produced (extensional fractures and cleavages) is plotted as Schmidt Lower hemisphere projection and as rose diagrams in Figure 5.21.

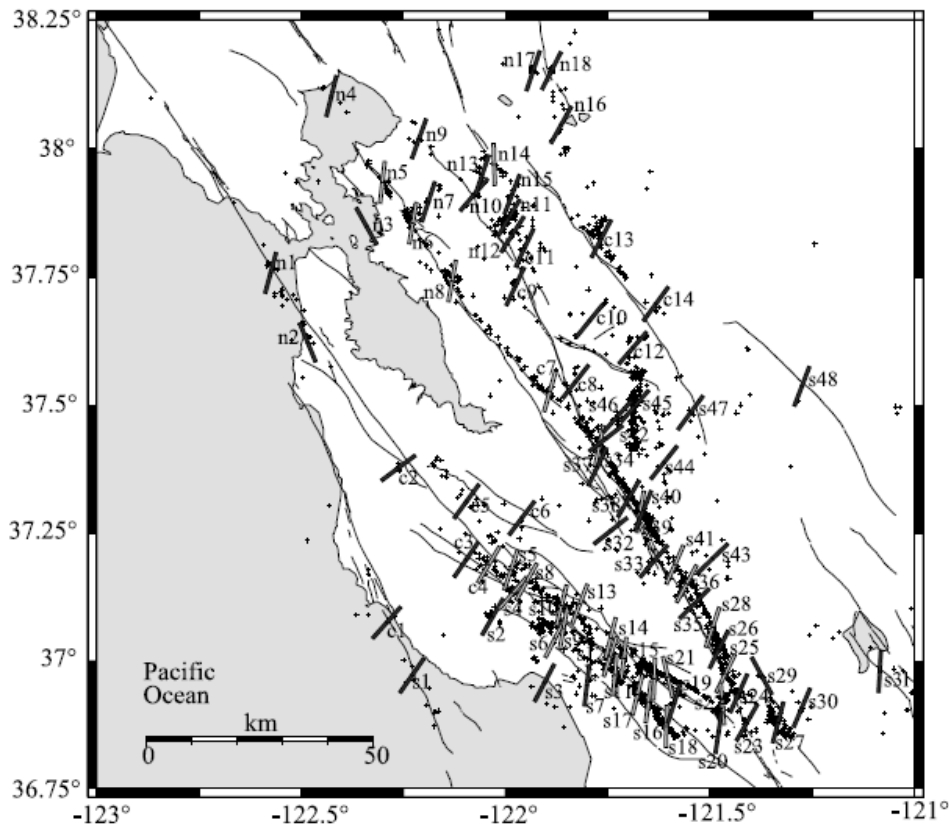


Figure 5.22 –Orientation of the maximum horizontal compression in San Francisco Bay Area by the inversion of ≈ 3200 seismic events with $M \geq 1.5$, occurred between January 1969 and October 2000. Light gray bars represent stress orientation for events occurring on-fault; dark gray ones represent the stress for events occurring off-fault. The bars are plotted at the centroid latitude and longitude of the events contained in each bin. Redrawn from Provost & Houston (2003).

5.2.6 Discussion

The Hayward fault experiment showed many interesting features although difficult to interpret. The analysis of polarization performed on earthquakes shows that it cannot be ascribed to the seismic source and has to be related to path effects or to some local geological structural features. By averaging results of selected earthquakes coming from different azimuths, a scattered distribution of polarization is observed on stations “off-fault”, hundreds of meters from the fault trace at the surface as mapped by Lienkamper (2001). This means that polarization effects observed on each individual earthquake could be related to the path. On the contrary, ND6 and ND7 deployed tens of meters from the fault trace show a common and persistent polarization effect oriented in N90°E direction, independently of earthquake backazimuth. For stations ND3, located close to the fault as well, a selection has to be done differing two frequency bands: in the range 1-4 Hz a polarization oriented as the fault strike is observed while in the range 5-8 Hz a polarization N90°E, according to ND6 and ND7. This is an important observation, demonstrating that these polarization effects can coexist with the already known, fault-parallel polarization of trapped waves, but at different frequencies. Ambient noise analysis does not show significant and recurrent features, probably because it is affected too much by

cultural activities, even in the night. Then it does not add useful information in the understanding of this process.

As pointed out by Di Giulio *et al.* (2009), polarization could be related to the fracturation fields associated to the fault, and to local stress field, but in the brittle deformation model (Figure 5.21) no directions close to N90°E are found.

The antithetic cleavage is oriented N60°E, and this orientation is close to the polarization observed on ambient noise at ND8, ND2, and ND10 (Figure 5.18), and on seismic events on ND2, that show a polarization between N50° and N70°.

The main expected cleavage is the synthetic one, oriented N175°E (Figure 5.21). Its orientation is quite perpendicular to the polarization direction observed at stations located very close to the fault trace (ND6, ND7, ND11 and ND3), that show a marked polarization oriented N90°E (Figure 5.13). This led to the conclusion that polarization is perpendicular to fractures favourably oriented to the active stress field. Considering that σ_3 orientation is roughly E-W, polarization is related to fractures oriented roughly N-S.

This behaviour is opposite to what we would expect from the maximum velocity direction inferred from S-waves splitting, that is parallel to the maximum compressional stress component σ_1 (see section 5.3.3).

5.3 Agri Valley case study



Figure Vb – The Agri valley viewed from the southern side of Mount Volturino (from P.M.Petrone, upload.wikimedia.org)

In order to investigate the relations between polarization, cracks orientations and active stress field, the comparison with S waves anisotropy was carried out. To this purpose, Agri valley was chosen as an interesting test site with a geological context well known. It hosts the largest European on-shore oil field and it has been deeply explored by geophysical, seismic and wells. Moreover Pastori *et al.* (2009) performed a study of S waves splitting. Using their data set, on the same stations the analysis of polarization was carried out, and the comparison with S waves splitting fast directions.

5.3.1 Geological setting

Agri valley is a quaternary extensional basin located in the central southern Apennines, approximately 30 km long and 5 km wide (Pastori *et al.*, 2009). It is bounded to the East by SW-dipping transtensional faults (Figure 5.23), and to South-West by a NE-dipping fault (Monti della Maddalena fault system). Its tectonic evolution was explained through two interpretations as while many authors (Benedetti *et al.* 1998; Mazzoli *et al.* 2000; Michetti *et al.* 2000; Cello *et al.* 2000, 2003; Barchi *et al.* 2007) consider the Eastern Fault system to be the most important structure of the area, other authors (Maschio *et al.*, 2005 and Pastori *et al.*, 2009) consider the Monti della Maddalena fault system to have mostly controlled the basin evolution. Here, the former interpretation was considered to be the most reliable.

The basin is filled by continental deposits up to 500 m thick, and lies on a complex thrust-and-fold system deriving from a poli-phase thin-skinned tectonic history (Catalano *et al.* 2004, Pastori *et al.*, 2009): the Lagonegro basin cherty-limestones and cherts are overthrust by the Western Carbonate Platform Mesozoic carbonates, that in turn overlay tectonically deeply deformed Mio-Pliocene foredeep deposits (Figure 5.25). These thrust-sheets lie above shelf limestones of the Apulia Platform, up to 7 km thick (Shiner *et al.* 2004, Menardi Noguera & Rea 2000).

In the basin north-eastern part, the largest onshore oil field in Europe was discovered in the late 1980. Thus the area was deeply explored by commercial reflection profiles and wells (Menardi Noguera & Rea 2000; Dell'Aversana 2003; Shiner *et al.* 2004), to improve the understanding of fracture distribution and the relation with the stress field (Trice 1999; Pastori *et al.*, 2009).

Agri Valley basin is located in an area with high seismological potential as the historical seismicity catalogues (e.g. Boschi *et al.* 2000; Valensise & Pantosti 2001) report two destructive events: the 1857 Me 7.0 earthquake (Burrato & Valensise 2008; and reference therein), with epicentre localized in central Agri Valley, and the 1561 Me 6.5 event localized in the Pergola–Melandro basin (Pastori *et al.* 2009). The seismicity is related to a NE–SW extensional stress regime confirmed by all stress indicators: T-axes inferred from moment tensors and focal mechanisms of moderate-large earthquakes (Gasparini *et al.* 1982; Pondrelli *et al.* 2006), borehole breakouts analysis (Amato & Montone 1997) and GPS measurements (Hunstad *et al.* 2003; Serpelloni *et al.* 2005). As observed by Cucci *et al.* (2004), local stress field is quite homogeneous and consistent with the regional SW–NE extension (Figure 5.24).

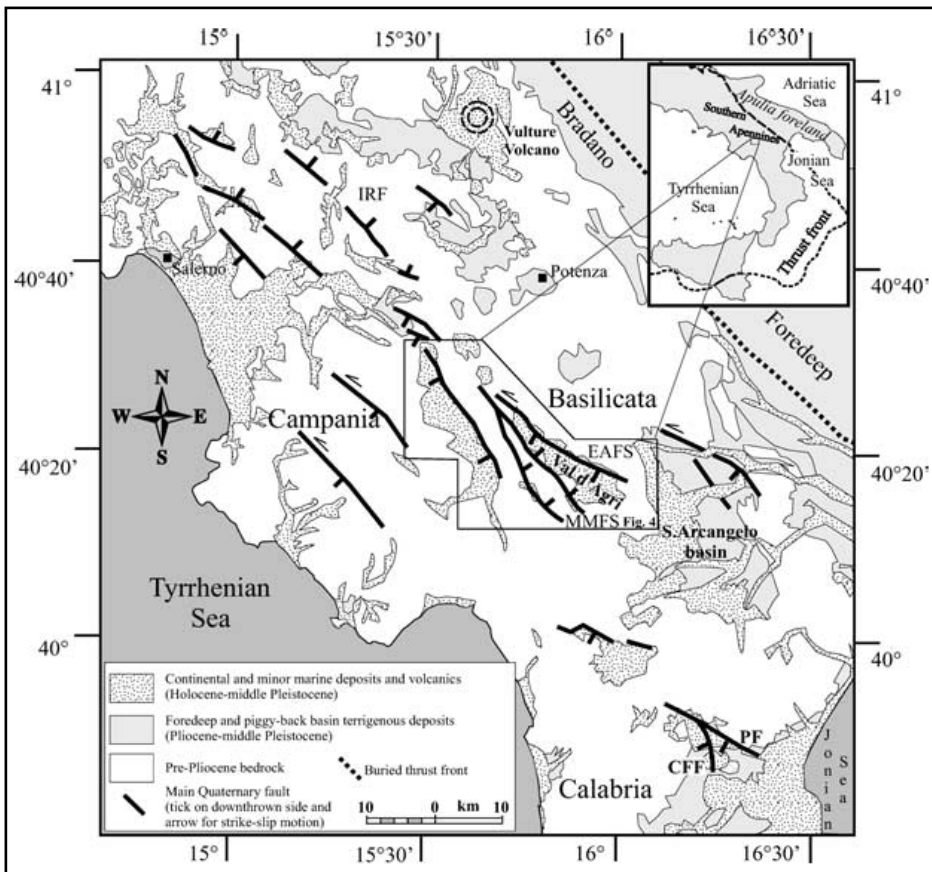


Figure 5.23 –Map of the Campania–Basilicata Apennines showing the distribution of Quaternary intermontane basins and major Middle Pleistocene-Holocene normal and strike-slip faults. Faults with present activity, ascertained by coseismic surface motion or palaeoseismological investigations, are labelled as follow: Irpinia fault (IRF); Castrovillari-Frascineto fault (CFF); Pollino fault (PF). The study area with mapped fault arrays (Eastern Agri fault system, EAFS; Monti della Maddalena fault system, MMFS) is framed in the central part of the region. Inset shows a schematic map of the Southern Apennines and location of the study and surrounding areas. Redrawn from Maschio et al. (2005).

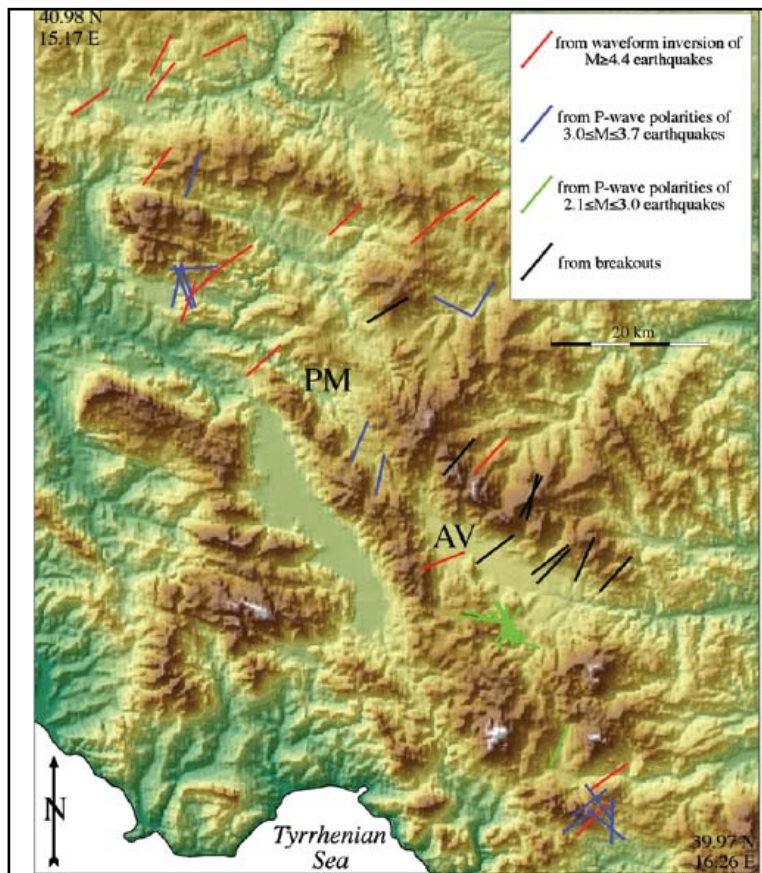


Figure 5.24 – Orientation of the minimum horizontal stress from focal mechanism inversion and from breakout analyses. Redrawn from Cucci et al. (2004).

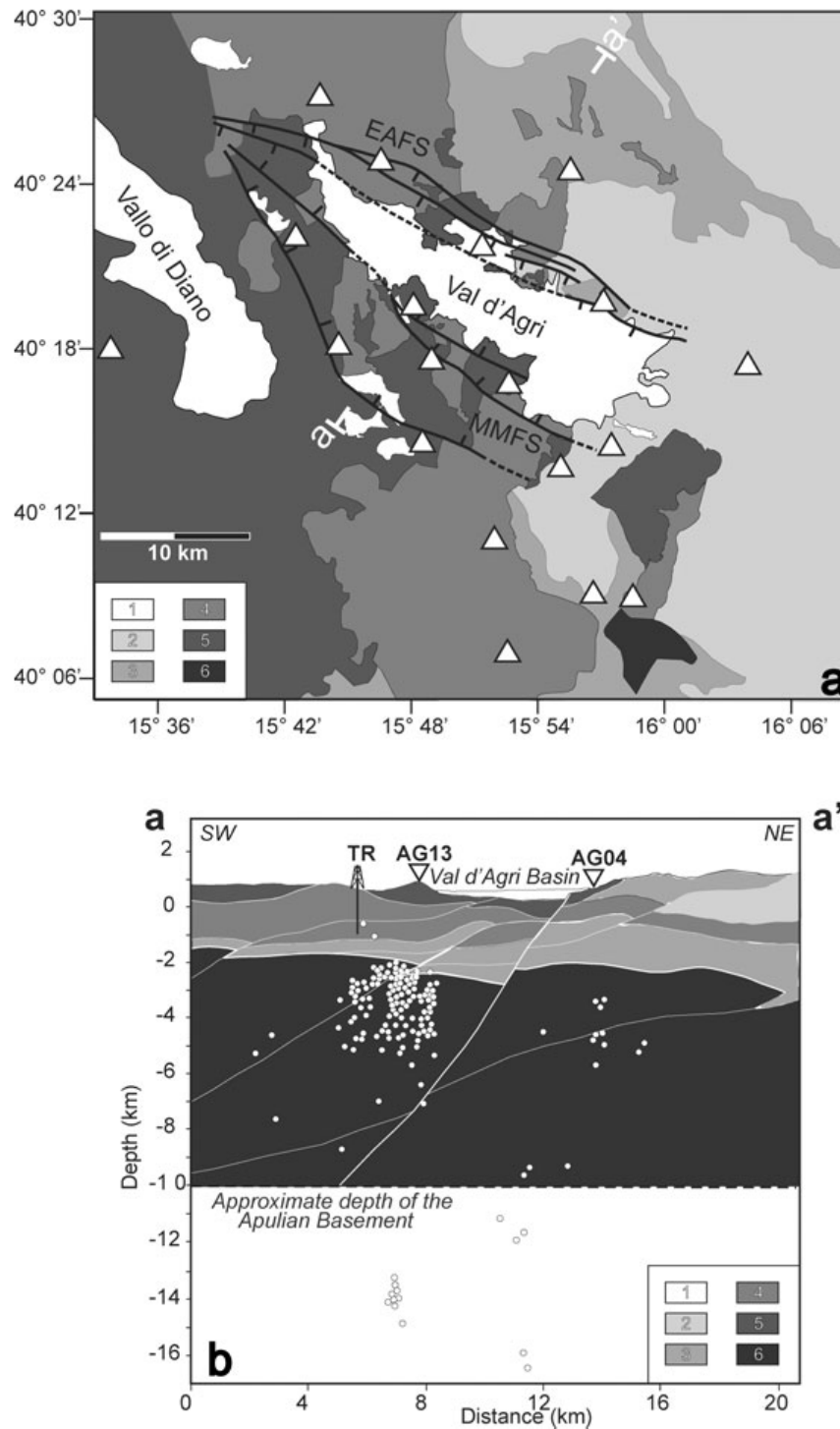
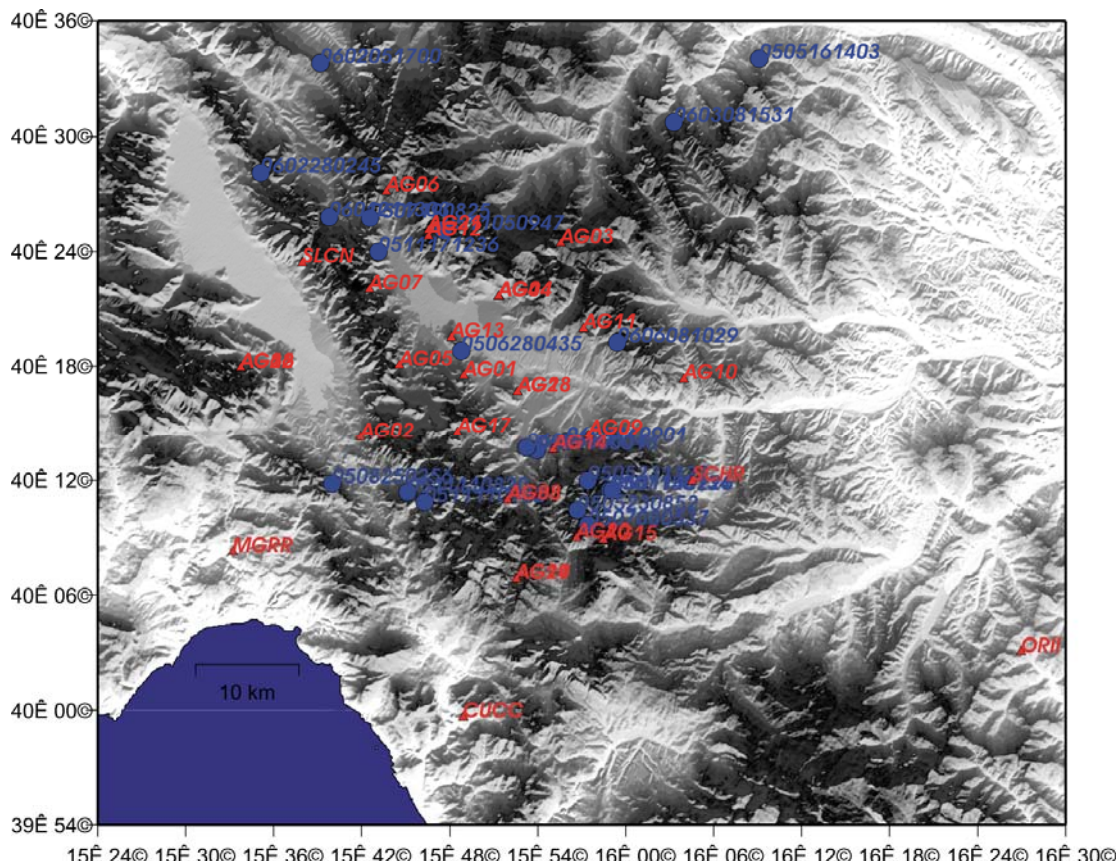


Figure 5.25 –Schematic geological map of the Agri Valley region. (1) Quaternary continental deposits, (2) foredeep and flysch deposits (Middle Miocene–Pliocene), (3) basinal deposits of the Sicilide and Liguride nappes (mainly clays and slope carbonates; Cretaceous–Lower Miocene), (4) Lagonegro basin Mesozoic rocks (cherty limestones, cherts, claystones), (5) limestones of the Western Platform (Mesozoic), (6) limestones of the Apulia Platform exposed in the Mt.Alpi tectonic window (Mesozoic–Miocene). EAFS: Eastern Agri Fault System, MMFS: Monti della Maddalena Fault System. Solid triangles depict seismic stations. The approximate trace of the cross-section a-a' is also reported. (b) Schematic vertical cross-section a-a' across the Agri Valley basin (modified after Menardi Noguera & Rea (2000) and Dell'Aversana (2003). AG13 and AG04 stations (triangles), earthquakes analyzed by Pastori *et al.* 2009 (white dots). Redrawn from Pastori *et al.* (2009).

5.3.2 Data analysis & results

To study the distribution of horizontal polarization across the Agri valley basin, an earthquakes data set collected in the period May 2005 – June 2006 (Valoroso *et al.* 2009) was used. Among them, 22 events with different backazimuth and magnitudes between 0.5 and 2.7 were selected considering the signal to noise ratio. They are listed in Table 5.2. Around 21 stations were deployed during the experiment performed by Valoroso *et al.* (2009), mapped in Figure 5.26 with epicentres of selected earthquakes. Before proceeding with the analysis, signals were detrended and the mean was removed, then tapered through a Hanning window.

The rotated receiver functions were calculated at each station as the geometric mean between events, each station showing its characteristics resonance effect at a different frequency. They are displayed in Figure 5.28. To have a more direct visualization of polarization, the covariance matrix analysis was performed in the frequency band 1-15 Hz, through a 2.0 s window with 0.1s overlap. Rose diagrams were calculated applying the “*hierarchical criterion*” (see Section 3.2). They are shown in Figure 5.27, depicting at the top corners the values of standard deviation and associated index, and at the bottom corners the mean direction and the percentage of time windows satisfying the “*hierarchical criterion*” (=INDEXPESI).



Date & Time	lon	lat	dept h km	M	1	2	3	4	5	6	7	8	9	10	11	12	13	14	15	16	17	18	19	20	21	
2005/05/11 04:32	15.8995	40.2597	6	0.5	*																					
2005/05/13 15:51	15.9267	40.2258	0.9	1.1	*																					
2005/05/14 02:16	15.8965	40.2605	1.5	0.7	*	*	*	*	*	*	*	*	*	*	*									*		
2005/05/16 14:03	16.1355	40.5577	18.5	2.0	*			*		*														*		
2005/05/23 11:24	15.9542	40.2002	0.5	1.6																				*		
2005/05/31 13:37	15.7413	40.3310	0.4	1.1							*															
2005/06/02 07:17	15.7523	40.3350	?	1.1							*															
2005/06/28 04:35	15.8148	40.3137	11	2.3		*	*	*	*	*	*	*	*	*	*	*	*	*	*	*	*	*	*	*	*	
2005/07/15 00:16	15.8985	40.2287	2.9	2.1				*		*						*				*	*		*			
2005/07/15 01:34	15.9802	40.1918	0.2	1.3																*			*			
2005/07/19 08:26	15.7098	40.4280	5.5	2.0				*		*						*				*	*		*			
2005/08/25 02:57	15.6692	40.1998	3.8	1.9												*				*	*	*				
2005/11/11 08:21	15.7527	40.1920	6.1	2.7	*		*	*	*	*		*	*	*	*	*	*	*	*							
2005/11/17 12:37	15.7188	40.4002	3.9	1.3												*										
2006/01/05 06:35	15.8867	40.2305	3.3	2.0		*	*	*	*	*				*	*		*								*	
2006/03/11 09:01	15.9318	40.2352	3.8	2.1	*	*	*			*		*	*	*	*		*	*	*						*	
2006/03/14 13:33	15.2777	40.8563	0.3	2.4	*		*		*	*		*	*	*											*	
2006/04/15 23:36	15.9235	40.2373	3.8	2.2	*	*			*	*			*	*	*		*	*	*						*	
2006/04/19 04:15	15.9242	40.2377	3.8	2.0	*	*			*	*			*	*	*		*	*							*	
2006/04/22 08:15	15.9228	40.2390	4.2	2.7	*	*	*		*	*		*	*	*	*		*	*	*	*	*				*	
2006/04/22 08:19	15.9218	40.2415	3.8	2.4	*	*	*		*	*		*	*	*	*		*	*	*						*	
2006/04/22 18:06	15.9067	40.2280	4	2.1	*	*	*		*	*		*	*	*	*		*	*	*						*	

Table 5.2 – Seismic events selected for the polarization study in the frequency band 1-15 Hz.

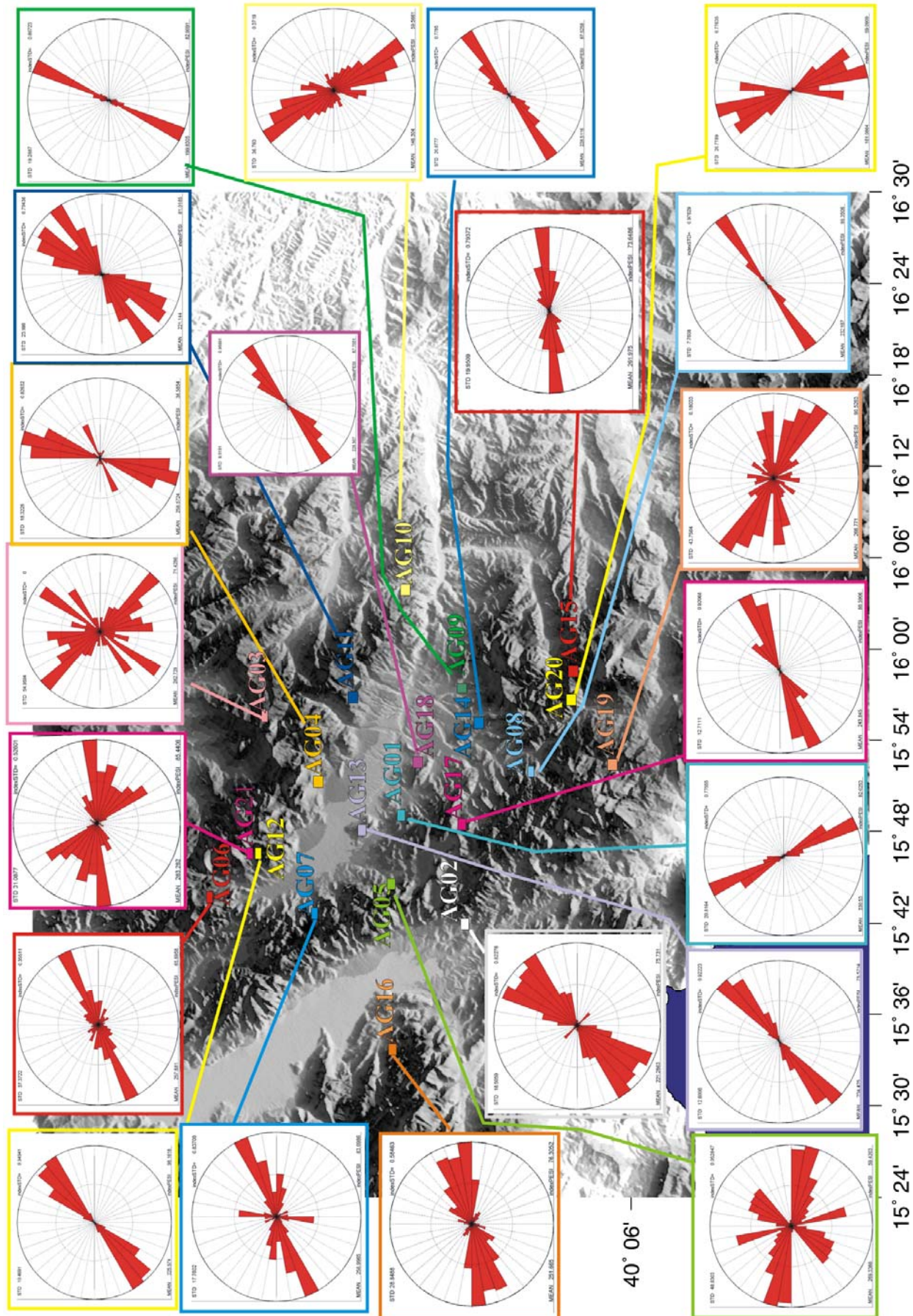
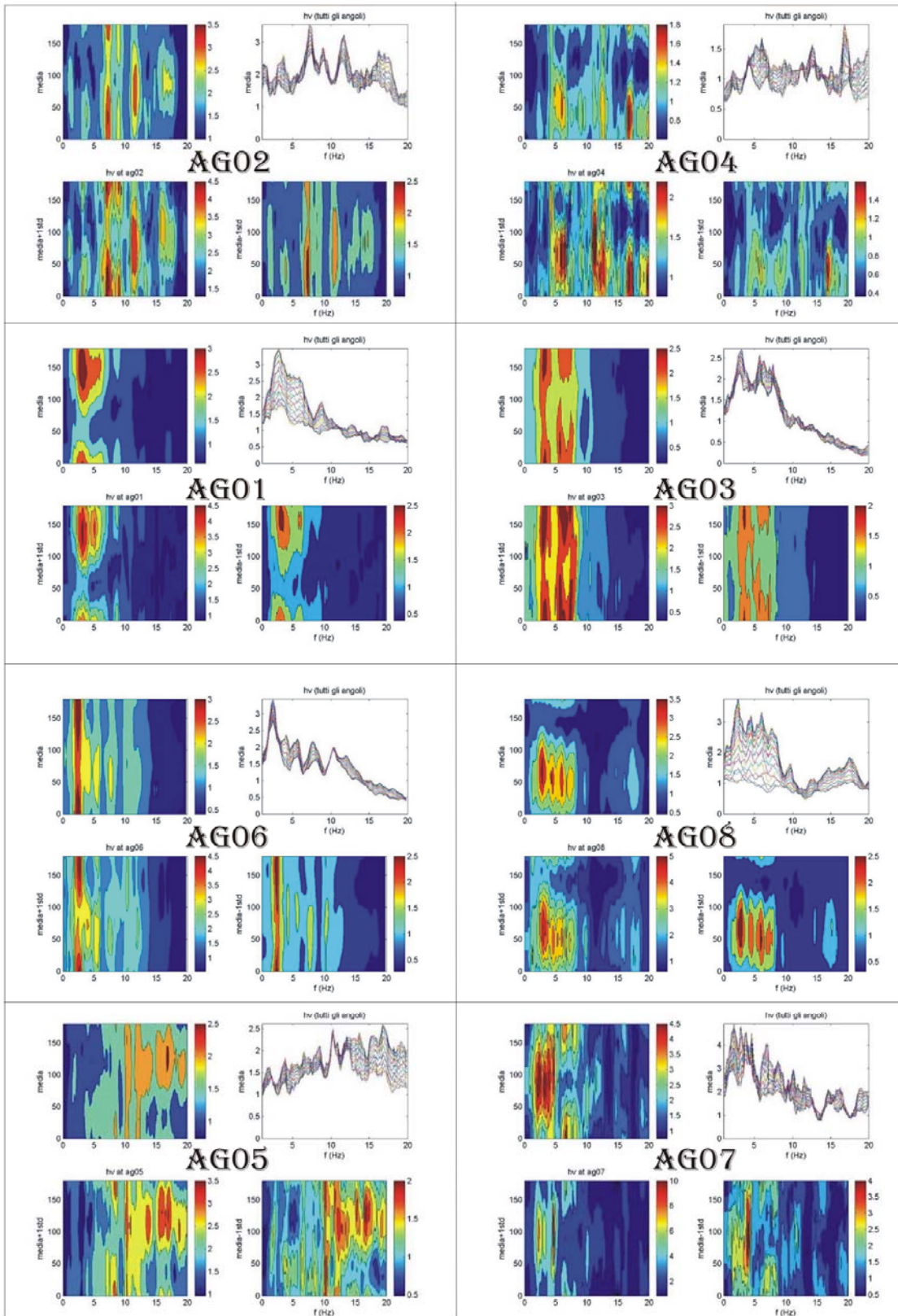
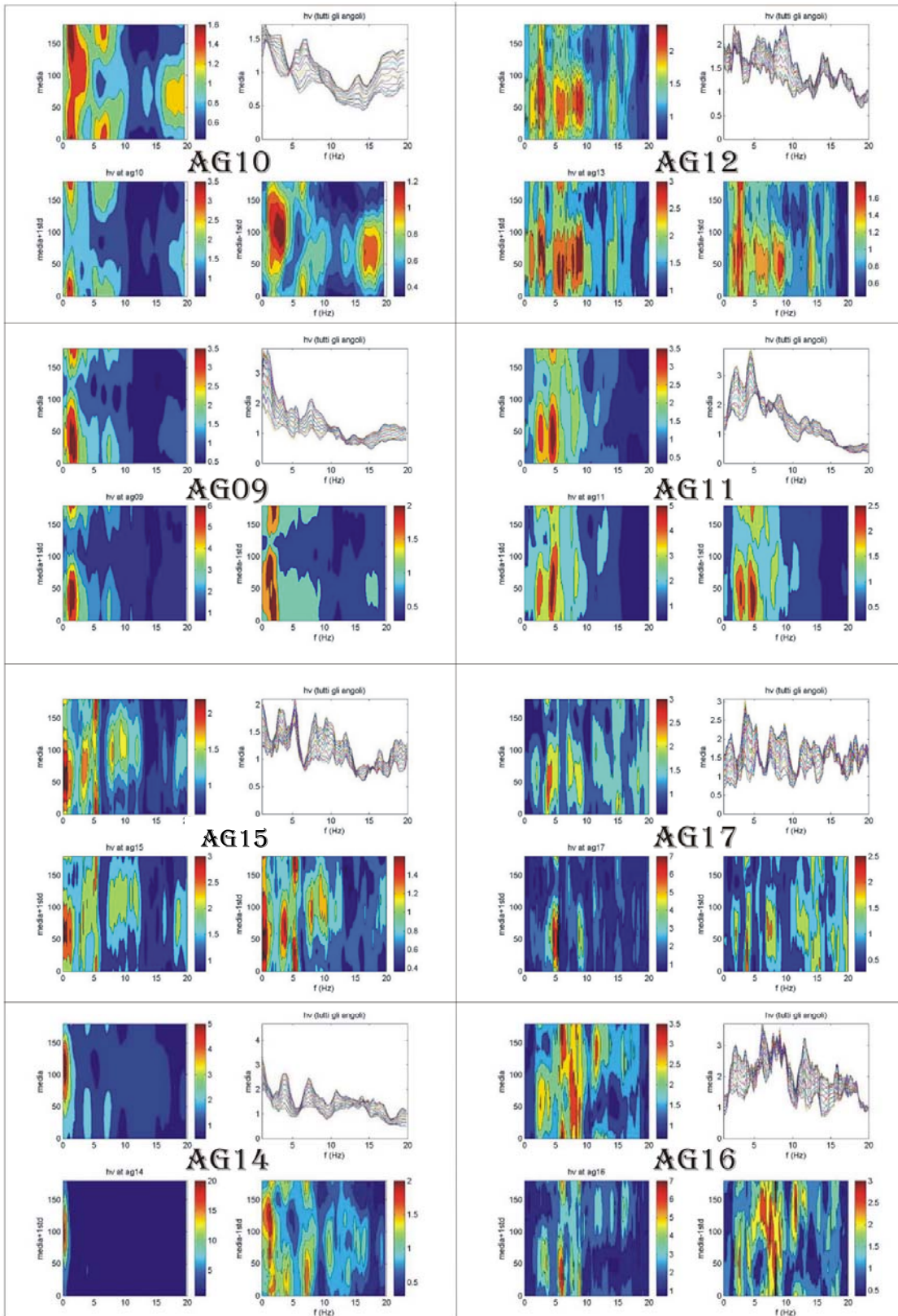


Figure 5.27 – Rose diagrams calculated in the frequency band 1-15 Hz. At top corners the values of standard deviation and associated index are depicted, and at the bottom corners the mean direction and the percentage of time windows satisfying the “*hierarchical criterion*” (=INDEXPESI).





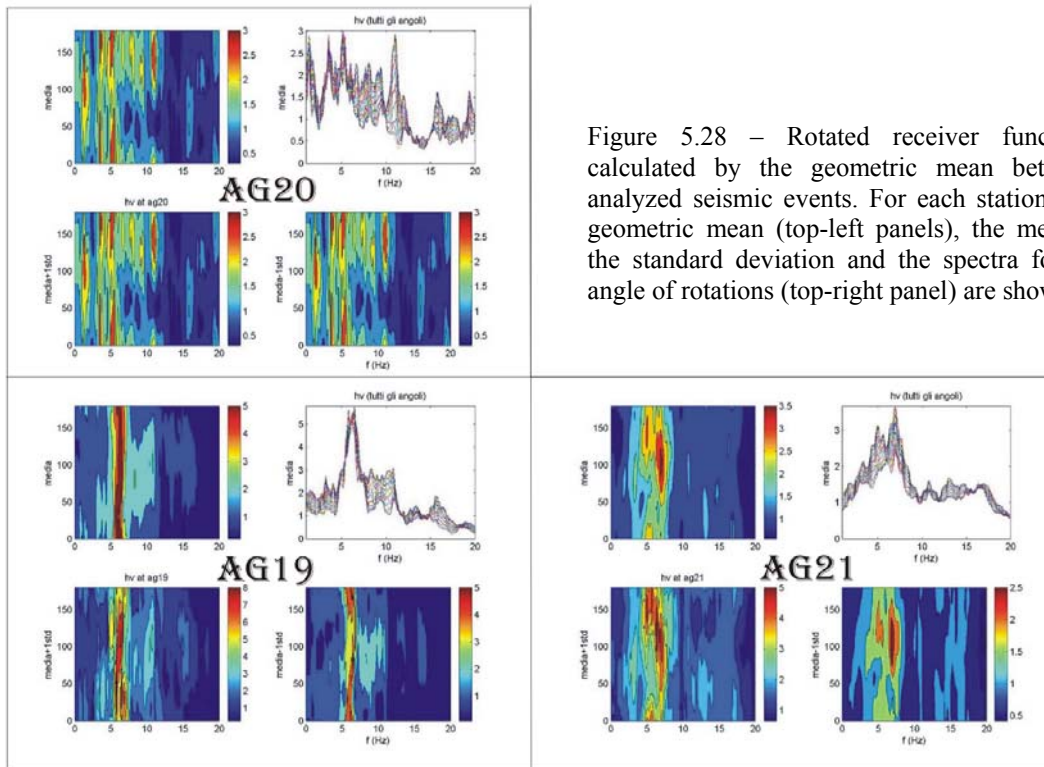


Figure 5.28 – Rotated receiver functions calculated by the geometric mean between analyzed seismic events. For each stations the geometric mean (top-left panels), the mean \pm the standard deviation and the spectra for all angle of rotations (top-right panel) are shown.

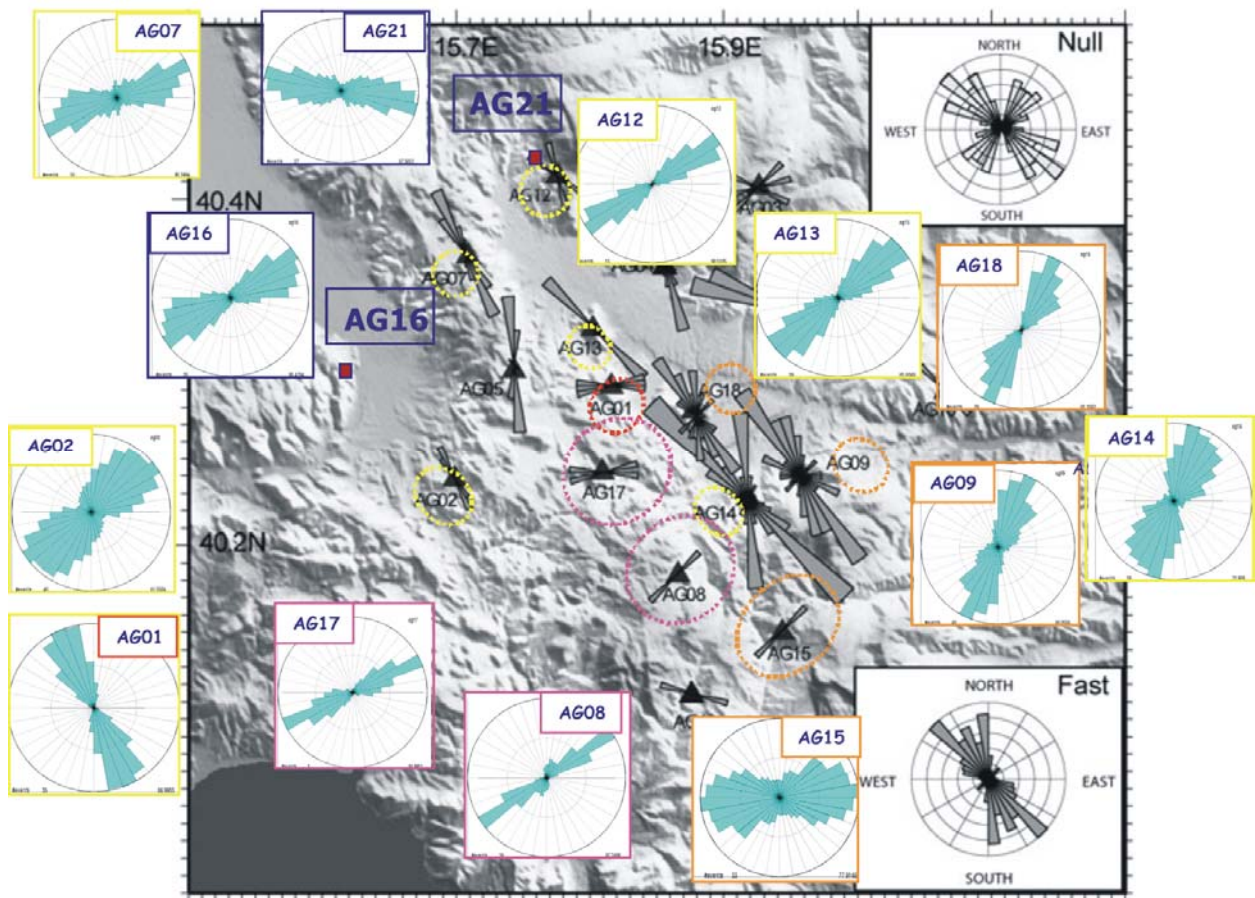


Figure 5.29 – Orientation of horizontal polarization (cyan rose diagrams) at stations showing a marked polarization effect; comparison with the direction of fast S-waves component found by Pastori *et al.*(2009). The colour around each station is related to the angle estimated between polarization and the fast velocity of S waves: yellow= $75^\circ < \text{angle} < 90^\circ$, orange= $60^\circ < \text{angle} < 70^\circ$; rose= $50^\circ < \text{angle} < 25^\circ$; blue=anisotropy data not available. between polarization and fast S wave between

The rotated receiver functions and rose diagrams reveal that stations with low standard deviation index and/or low percentage of time windows satisfying the “*hierarchical criterion*” show low evidences of polarization, as stations: AG3, AG4, AG5, AG6, AG10, AG19. To the contrary stations AG1, AG2, AG7, AG8, AG9, AG12, AG13, AG14, AG15, AG16, AG17, AG18 and , AG21 show significant and marked polarization, mostly in N60-80 directions.

5.3.3 Comparison with s-waves splitting fast velocity

To evince a relation with S waves anisotropy, the study of Pastori *et al.* (2009) was used. These authors performed the S waves splitting analysis on the same stations that were investigated through the analysis of polarization, but using a wider data set, finding the orientations of fast directions shown in Figure 5.29 (gray circular histograms). They related the S waves splitting occurrence to the presence of seismic anisotropy in upper 15 km of the crust in Agri Valley, due to cracks aligned in NW-SE direction, perpendicular to the regional and local minimum horizontal stress (Amato & Montone, 1997; Cucci et al, 2004; Maschio *et al.*, 2005; Valoroso *et al.* 2009).

The covariance matrix analysis was performed again but in the frequency band 1-9 Hz, selecting a higher number of events (Table 5.3) with magnitude >1.0 and at least recorded by 12 stations, with a significant signal to noise ratio. The resulting rose diagrams are shown in Figure 5.29 (cyan coloured) near histograms related to fast directions (gray coloured) found by Pastori *et al.* (2009). Moreover at each station the average angle between the means of polarization and fast direction was measured, revealing a predominant angular relation in the range 70°-90°. Results are equally consistent considering station without a preferential direction of polarization (Figure 5.30) that are related to stations where the S waves splitting method generally found low degree of anisotropy.

The polarization is even compared to the orientation of the minimum axis of local stress field inferred by Cucci *et al.* (2004) in Figure 5.31. Polarization is quite always parallel to the minimum axis of local stress field, revealing again a contrary behaviour compared to S waves splitting fast directions orientations.

Date & Time	lon	lat	depth (km)	M	1	2	3	4	5	6	7	8	9	10	11	12	13	14	15	16	17	18	19	20	21	
2005/05/16 14:03	16.1355	40.5577	18.5	2.0	*	*	*	*	*	*	*	*	*	*	*									*		
2005/05/23 08:53	15.9542	40.2002	0.5	1.3	*	*		*	*	*	*	*	*	*	*	*		*							*	
2005/05/23 11:24	15.9542	40.2002	0.5	1.6	*	*		*	*	*	*	*	*	*	*	*		*							*	
2005/05/31 13:37	15.7413	40.3310	0.4	1.1	*	*		*	*	*	*	*	*	*	*	*		*							*	
2005/06/02 07:17	15.7523	40.3350	1.1	1.1	*	*		*	*	*	*	*	*	*	*	*		*							*	
2005/06/28 04:35	15.8148	40.3137	11	2.3		*	*	*	*	*	*	*	*	*	*	*	*	*	*	*	*	*	*	*	*	
2005/07/08 05:37	15.9012	40.2640	4.8	2.0		*	*	*	*	*	*	*	*	*	*	*	*	*	*	*	*	*	*	*		
2005/07/15 01:34	15.9802	40.1918	0.2	1.3		*	*	*	*	*	*	*	*	*	*	*	*	*	*	*	*	*	*	*		
2005/07/19 08:26	15.7098	40.4280	5.5	2.0		*	*	*	*	*	*	*	*	*	*	*	*	*	*	*	*	*	*	*		
2005/08/25 02:57	15.6692	40.1998	3.8	1.9		*	*	*	*	*	*	*	*	*	*	*	*	*	*	*	*	*	*	*		
2005/11/05 09:47	15.9930	40.1967	9.5	1.1	*	*	*	*	*	*	*	*	*	*	*	*	*	*	*	*	*	*	*	*		
2005/11/11 08:21	15.7527	40.1920	6.1	2.7	*	*	*	*	*	*		*	*	*	*	*	*	*	*	*	*	*	*			
2005/11/11 09:32	15.8103	40.2982	5.3	1.3	*	*	*	*	*	*		*	*	*	*	*	*	*	*	*	*	*	*			
2005/11/17 12:37	15.7188	40.4002	3.9	1.3	*		*	*	*		*	*	*	*	*	*	*	*	*	*	*		*	*		
2006/01/05 06:35	15.8867	40.2305	3.3	2.0		*	*	*	*	*				*	*		*						*	*		*
2006/01/14 02:26	15.9050	40.2472	4.2	1.1	*	*	*	*	*	*		*	*	*	*		*	*	*	*	*		*	*		*
2006/01/21 13:03	15.9295	40.2392	3.6	1.4	*	*	*	*	*	*		*	*	*	*		*	*	*	*	*		*	*		*
2006/02/05 17:00	15.9173	40.2162	5.3	-	*	*	*	*	*	*		*	*	*	*		*	*	*	*	*		*	*		*
2006/02/28 02:45	15.9043	40.2462	3.3	1.7	*	*	*	*	*	*		*	*	*	*		*	*	*	*	*		*	*		*
2006/03/08 15:31	15.8920	40.2722	4.2	2.0	*	*	*	*		*		*	*	*	*		*	*	*	*	*		*	*		*
2006/03/11 09:01	15.9318	40.2352	3.8	2.1	*	*	*	*		*		*	*	*	*		*	*	*	*	*		*	*		*
2006/03/14 13:33	15.2777	40.8563	0.3	2.4	*	*	*	*	*	*		*	*	*	*		*	*	*	*	*		*	*		*
2006/03/17 01:27	15.9005	40.2393	3.4	-	*	*	*	*	*	*		*	*	*	*		*	*	*	*	*		*	*		*
2006/04/15 23:26	15.9235	40.2373	3.8	2.2	*	*		*	*	*			*	*	*		*	*	*	*	*		*			*
2006/04/19 04:15	15.9242	40.2377	3.8	2.0	*	*		*	*	*			*	*	*		*	*		*	*		*			*
2006/04/22 08:15	15.9228	40.2390	4.2	2.7	*	*	*	*	*	*		*	*	*	*		*	*	*	*	*		*	*		*
2006/04/22 08:19	15.9218	40.2415	3.8	2.4	*	*	*		*	*		*	*	*	*		*	*	*	*	*		*	*		*
2006/04/22 18:06	15.9067	40.2280	4	2.1	*	*	*	*	*	*		*	*	*	*		*	*	*	*	*		*	*		*
2006/06/03	15.9253	40.2402	4.3	1.1	*	*	*		*	*			*	*	*		*	*	*	*	*		*			*

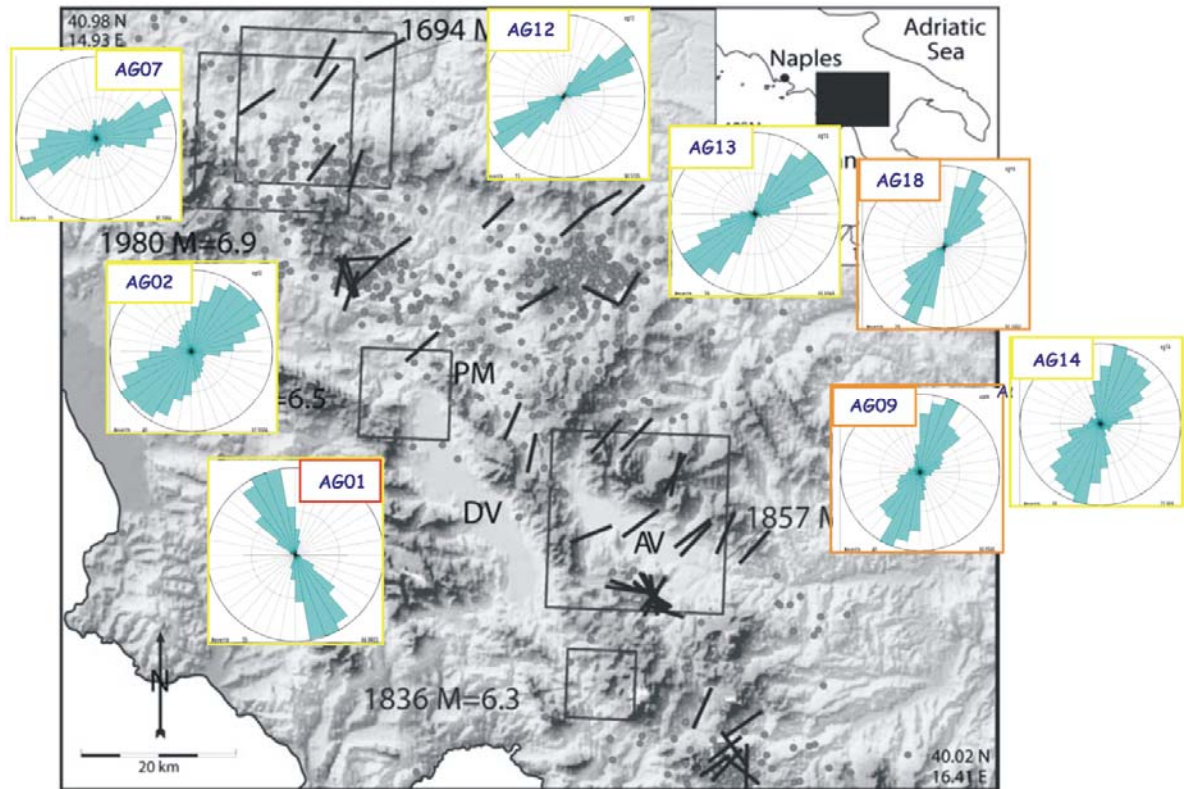


Figure 5.31 – Comparison between the horizontal polarization and the orientation of the minimum axis of local stress field by Cucci *et al.* (2004).

5.3.4 Brittle deformation models

To model the brittle deformation associated to Agri Valley Eastern Fault system, the package FRAP (Salvini, 2002) was used, analogously to Section 5.2.5. The stress kinematics component and the associated brittle deformation pattern are displayed in Figure 5.32.

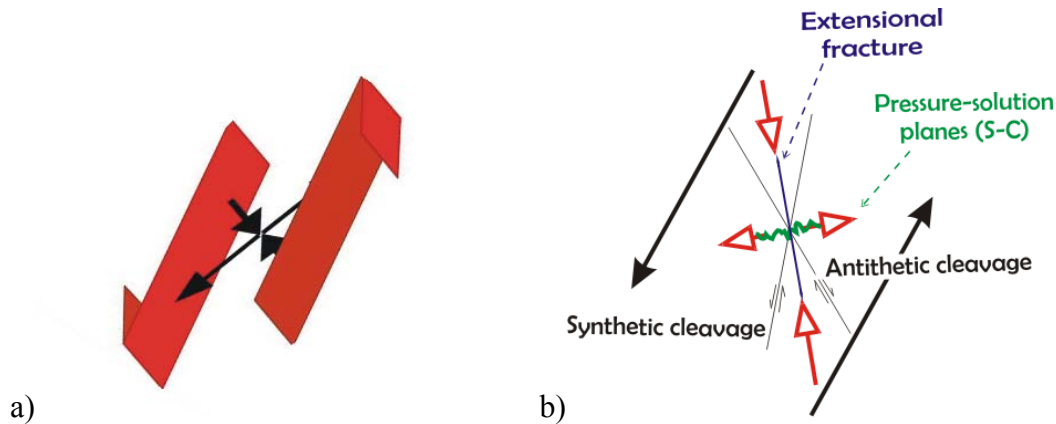


Figure 5.32 – a) The kinematics component of stress; b) Brittle deformation types related to the kinematics stress field in the damage zone (section view).

The rocks rheological parameters were chosen to be the same on the two sides of the fault and set as: density 2600 kg/m³, cohesion 5MPa, Poisson ratio of 0.25, friction angle of 30°, stress drop coefficient 50%, Vshale content 10%. The fault was modelled as a 10x8x10 km surface without irregularities, and the movement was fixed to be dip-slip with a displacement of 200 m. According to Cucci *et al.* (2004), the axis of minimum compression σ_3 and the intermediate one σ_2 were set to be oriented respectively N45°E and N135°E, both lying on the horizontal plane, with maximum compression σ_1 being vertically lying. Their modulus were arbitrary chosen to be 80, 30 and 0 MPa, respectively for σ_1 , σ_2 and σ_3 .

Different stress conditions were applied to the model as to be related only to lithostatic load (“static”) or depending on fault movement (“kinematics”), plus a combination of them (“statics & kinematics”). Synthetic extensional fractures, pressure solutions and cleavages produced by these different stress conditions are plotted as rose diagrams (Figure 5.32) and as Schmidt Lower hemisphere projection (Figure 5.33). Because of kinematics and regional stress fields are orientated in a similar way, no significant differences are observed by applying different stress conditions.

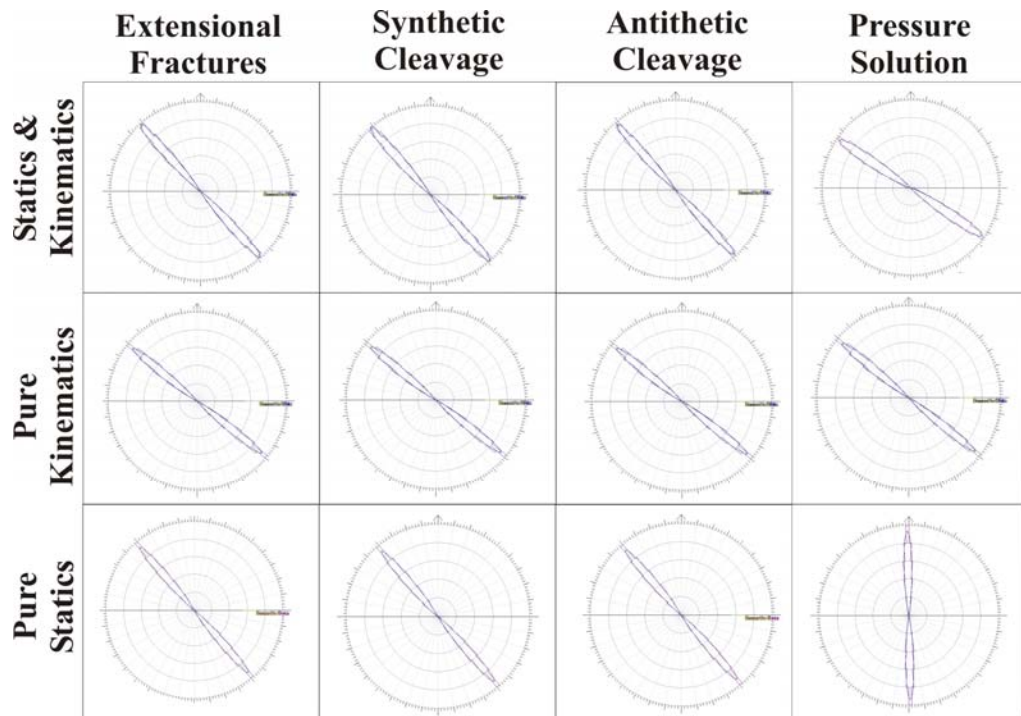


Figure 5.32 – Rose diagrams of modelled extensional fractures, cleavages and pressure solutions produced by different stress conditions (as explained in the text), using the package FRAP 3 (Salvini, 2002).

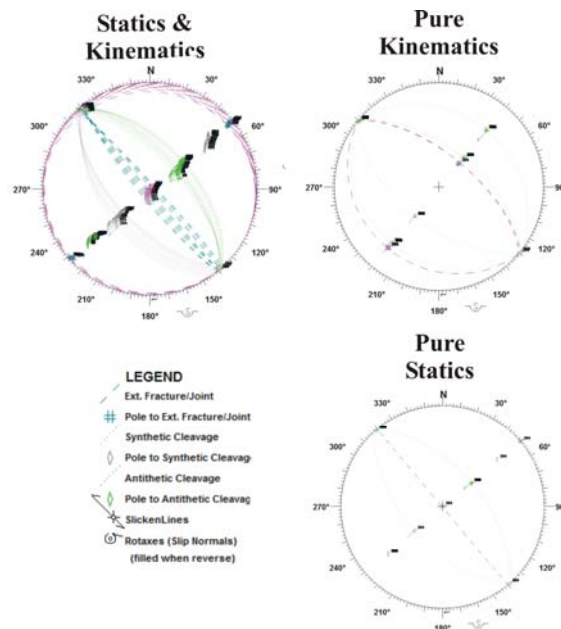


Figure 5.33 – Schmidt Lower Hemisphere projections of extensional fractures, pressure solutions and cleavages produced by different stress conditions (as explained in the text), modelled using the package FRAP 3 (Salvini, 2002).

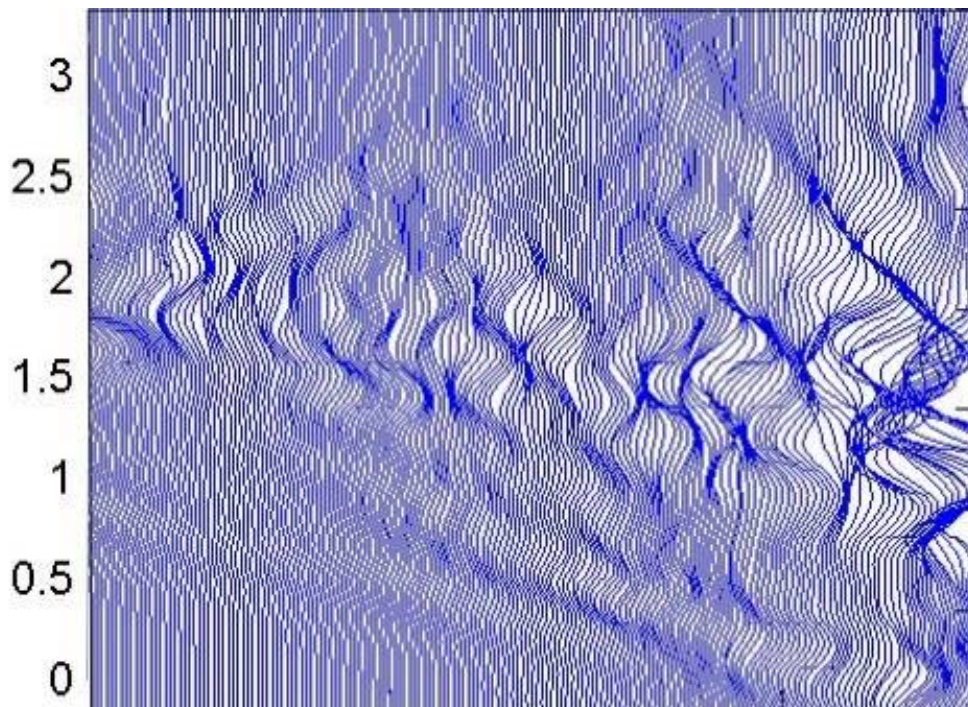
5.3.5 Discussion

Agri valley represents a simpler case to study the relations between polarization and either regional stress field and brittle deformation related to the kinematics component. In fact, being the brittle deformation pattern related to a dip-slip fault, the orientation of the kinematics deformation is consistent to regional stress field. Pastori *et al.*(2009) found an S waves fast velocity oriented parallel to the horizontal maximum compressional axis. It was ascribed to the orientation of fluid-filled cracks.

The polarization was studied on the same stations, resulting very stable within earthquakes, independently of their focal mechanism, and backazimuth. The relation between polarization and S waves fast velocity was recognized to be mostly perpendicular. The same relation is recognized when comparing polarization to σ_3 orientation by Cucci *et al.* (2004) and to the azimuth of modelled brittle deformation pattern. The conclusion is that even though S waves propagate faster in a direction parallel to fluid filled microcracks (that are oriented parallel to the horizontal maximum compressional axis), the particle motion is polarized in a perpendicular direction. This perpendicular direction is consistent to what observed across the Hayward fault (Section 5.2).

Chapter 6

Numerical simulations involving fractured media



So far, all observations done at different scales agreed in finding a polarization roughly perpendicular to the direction of fractures that are held open by tectonic stress field. Trying to reproduce this relation between polarization and fractures, 2D numerical models involving fractured media were performed in partnership with Prof. A. John Haines, (Cambridge University, UK).

A method to create fracture distributions was developed and numerical models were performed using the triangular finite element method developed by John Haines (presented in Elena Klien's, PhD thesis).

6.1 Method

At first the main effort was devoted to develop a fracture distribution method and code to reproduce the randomly but also systematic distribution of fractures in earth. Then the TDEM method by Haines & Klein was used to model the propagation of a Ricker pulse through the fractured medium, using both SH (out-of-plane motion) and PSV (in-plane motion). Comparing in-plane (ground motion both perpendicular and parallel to fracture planes) and out-of-plane (ground motion parallel to fracture planes) synthetic seismograms, possible indications as to the geometrical relationships that result in the differential attenuation were investigated.

6.1.1 Fracture distributions

Fracture distributions were created in way to properly reproduce the systematic variability and chaos of nature. Probability distribution parameters for orientation, length, distance and position of every crack within the half space were initially randomly generated in the interval 0-1; then each distribution was forced to spread around a desired “expected” value with a chosen degree of uniformity.

A generic example will be presented as follow, considering a set of points in the 3D Cartesian reference system, assuming a normal distribution of x around a mean value μ with a standard deviation σ :

$$6.1 \quad p(x) = \frac{1}{\sigma\sqrt{2\pi}} \exp\left(-\frac{1}{2\sigma^2}(x-\mu)^2\right)$$

In the 3D case, x, y, z are the principal directions, and \hat{z} is the z component of the unit vector in the direction of a general-length vector (x,y,z) , the other two components of the unit vector are given by:

$$6.2 \quad \hat{x} = \sqrt{1-\hat{z}^2} \cos \phi$$

and

$$6.3 \quad \hat{y} = \sqrt{1-\hat{z}^2} \sin \phi .$$

Assuming $\mu_x = \mu_y = \mu_z = 0$ equation 6.1 becomes;

$$6.4 \quad p(x, y, z) = \frac{1}{\sigma_x \sigma_y \sigma_z \sqrt[3]{2\pi}} \exp\left(-\frac{1}{2}\left(\frac{x^2}{\sigma_x^2} + \frac{y^2}{\sigma_y^2} + \frac{z^2}{\sigma_z^2}\right)\right)$$

Because of fractures are planar features we can consider $\sigma_x = \sigma_y < \sigma_z$, and defining

$$6.5 \quad \alpha = \sqrt{1 - \frac{\sigma_x^2}{\sigma_z^2}}$$

the expected value of the square of the z component of the unit vector becomes

$$6.6 \quad E(\hat{z}^2) = \frac{1}{\alpha^2} \left[1 - \frac{1}{\alpha} \sin^{-1} \alpha \sqrt{1 - \alpha^2} \right]$$

and the expected values of the squares of the x and y components are

$$6.7 \quad E(\hat{x}^2) = E(\hat{y}^2) = \frac{1}{2} [1 - E(\hat{z}^2)]$$

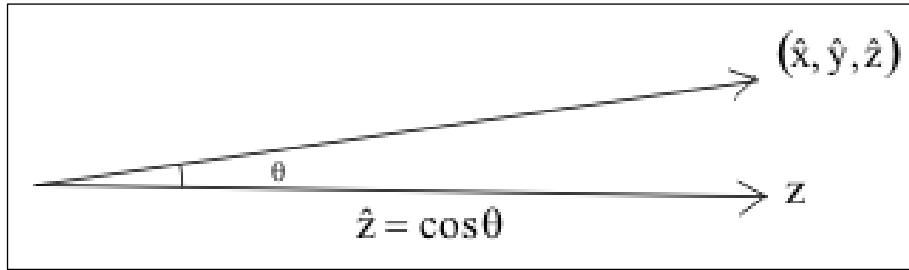


Figure 6.1 – Expected value \hat{z} of the component along the z axis.

Then for each crack the joint probability of the component \hat{z} in the z direction of the unit normal vector and the ϕ angle for the x and y components is:

$$6.8 \quad p(\phi, \hat{z}) = \frac{1}{\sigma_x \sigma_y \sigma_z (4\pi)} \times \left(\frac{\hat{x}^2}{\sigma_x^2} + \frac{\hat{y}^2}{\sigma_y^2} + \frac{\hat{z}^2}{\sigma_z^2} \right)^{-\frac{3}{2}}$$

Considering $\sigma_x = \sigma_y < \sigma_z$, and replacing the parameter α of equation 6.5, equation 6.8 becomes :

$$6.9 \quad p(\phi, \hat{z}) = \frac{\sigma_x}{\sigma_z (4\pi)} \times \left(\hat{x}^2 + \hat{y}^2 + \frac{\sigma_x^2}{\sigma_z^2} \hat{z}^2 \right)^{-\frac{3}{2}} = \frac{\sqrt{1 - \alpha^2}}{4\pi [1 - \alpha^2 \hat{z}^2]^{\frac{3}{2}}} = \frac{1}{2\pi} \cdot \frac{\sqrt{1 - \alpha^2}}{2 [1 - \alpha^2 \hat{z}^2]^{\frac{3}{2}}}$$

from which it is clear that $p(\phi, \hat{z}) = p(\phi)p(\hat{z})$, meaning that the two probabilities are independent:

$$6.10 \quad p(\phi) = \frac{1}{2\pi}$$

$$6.11 \quad p(\hat{z}) = \frac{\sqrt{1-\alpha^2}}{2[1-\alpha^2\hat{z}^2]^{\frac{3}{2}}}$$

Transforming these equations as functions of integrated probability P between 0 and 1, the z component \hat{z} of the unit normal vector of each crack is given by:

$$6.12 \quad \hat{z} = \frac{(2P-1)}{\sqrt{(1-4\alpha^2P(1-P))}},$$

while the angle ϕ is given by:

$$6.13 \quad \phi = 2\pi P$$

To see how the parameter α can affect the uniformity of a distribution, two sets of random numbers were generated in the range 0-1 and assigned to the integrated probability values P in equations 6.12 and 6.13. Then the x and y components \hat{x} and \hat{y} of the unit normal vectors were found by applying equations 6.2 and 6.3.

In Figure 6.2, the resulting points produced by choosing different α values are plotted. Only very high values of α (over 0.99), are able to generate very lowly dispersed distributions of points.

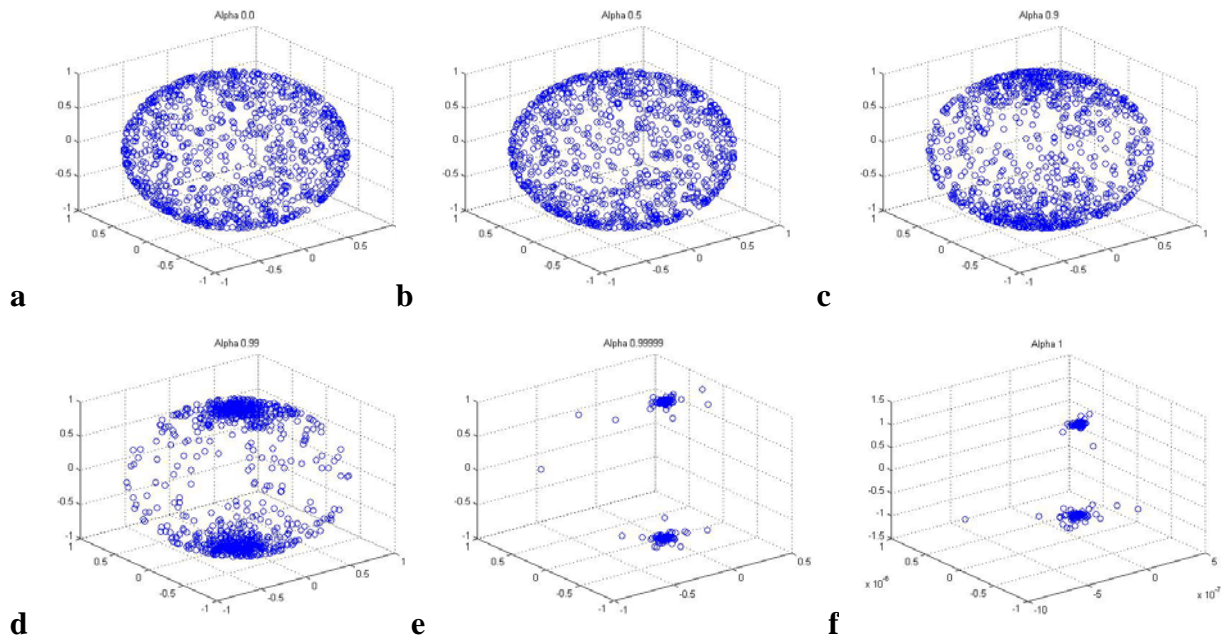


Figure 6.2 – Different distributions assigning to the parameter α the following values:(a) $\alpha = 0$; (b) $\alpha = 0.5$; (c) $\alpha = 0.9$; (d) $\alpha = 0.99$; (e) $\alpha = 0.99999$;(f) $\alpha = 1$ (to machine precision – for α exactly equal to 1 $\hat{z} = \text{sign}(2P-1)$ and both \hat{x} and \hat{y} are zero).

This approach for 3D fractures was applied in much the same way to create 2D fracture distributions, analogously producing the fracture populations by forcing random distributions through arbitrarily chosen values similar to α

The “Main Region” is the top part of the half space with cracks, which was where the surface seismic response was modeled. At its edges and in particular at its base space was added, to prevent unwanted reflections being present on the surface traces during the time of interest.

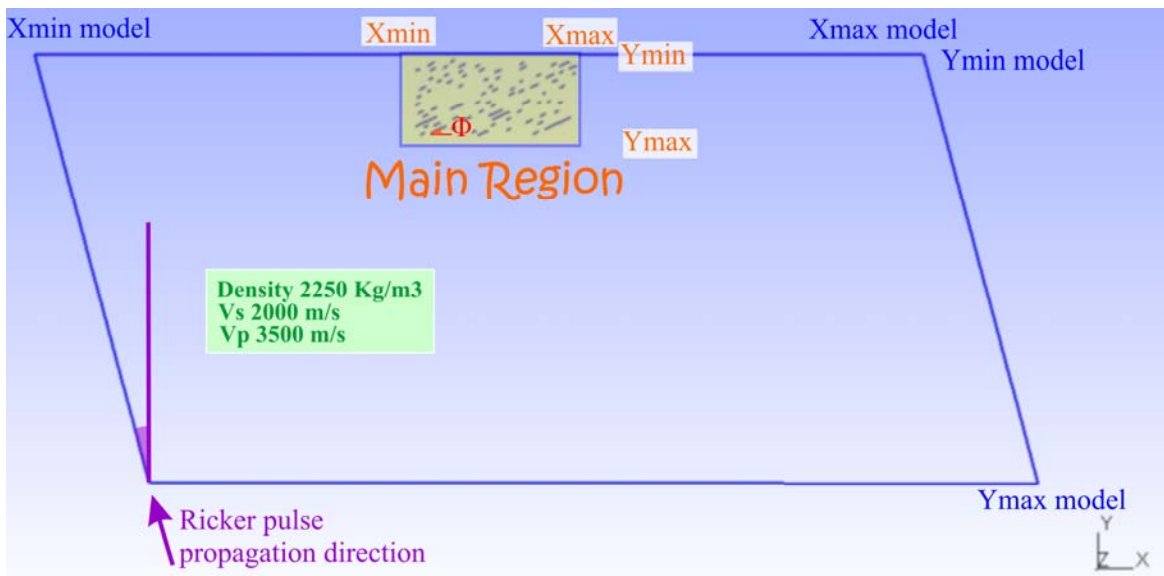


Figure 6.3 –The modeled half space

6.1.1.1 Models with one set of fractures homogeneously distributed across the half space

Firstly some models with one set of fractures homogeneously distributed across the half-space were produced. The probability of each point in the Main region to be the mid point of a crack is given by:

$$6.14 \quad P(x) = \frac{x - x_{\min}}{x_{\max} - x_{\min}},$$

$$6.15 \quad P(y) = \frac{y - y_{\min}}{y_{\max} - y_{\min}}.$$

These values are randomly defined in the interval 0 and 1, using a random number generator.

The position (x, y) of the crack mid point inside the half-space is found through:

$$6.16 \quad x = x_{\min} + P(x)[x_{\max} - x_{\min}]$$

$$6.17 \quad y = y_{\min} + P(y)[y_{\max} - y_{\min}]$$

Then, the orientation ϕ of each crack is calculated to simulate a distribution around a mean preferential orientation ϕ' , which was arbitrarily chosen.

The probability of each orientation $P(\phi)$ for ϕ between $\phi' - \frac{\pi}{2}$ and $\phi' + \frac{\pi}{2}$ is given by:

$$6.18 \quad P(\phi) = \frac{1}{2\pi} \int_{\phi' - \frac{\pi}{2}}^{\phi} \frac{d\phi}{\left[\eta \sin^2(\phi - \phi') + \frac{1}{\eta} \cos^2(\phi - \phi') \right]}$$

where η is

$$6.19 \quad \eta = \frac{\sigma_x}{\sigma_y}$$

and expresses the ratio of variability in the x and y directions and so the uniformity of the distribution, and is arbitrarily chosen.

$$6.20 \quad p(\phi) = \frac{1}{2\pi\sigma_x\sigma_y \left[\left(\frac{\hat{x}'}{\sigma_x} \right)^2 + \left(\frac{\hat{y}'}{\sigma_y} \right)^2 \right]}$$

Similarly to $P(x)$ and $P(y)$, the value of $P(\phi)$ is randomly generated in the range 0 and 1. The orientation ϕ of each crack is then calculated through:

$$6.21 \quad \phi = \phi' - \tan^{-1} \frac{1}{\eta \tan(2\pi P(\phi))}$$

Then, the crack lengths are defined with a similar integrated probability distribution $P(L)$ between the chosen variability range L_{\max} and L_{\min} ,

$$6.22 \quad P(L) = \frac{L_{\min}^{-1} - L^{-1}}{L_{\min}^{-1} - L_{\max}^{-1}}$$

The length L of each crack is given by:

$$6.23 \quad L = \frac{1}{L_{\min}^{-1} - P(L)[L_{\min}^{-1} - L_{\max}^{-1}]}$$

and the coordinates of the two points defining each crack are finally calculated through:

$$6.24 \quad P_1 = \left(x + \frac{L}{2} \cos \phi; \quad y + \frac{L}{2} \sin \phi \right),$$

$$6.25 \quad P_2 = \left(x - \frac{L}{2} \cos \phi; \quad y - \frac{L}{2} \sin \phi \right).$$

Finally, two conditions are added in order to exclude crossing cracks and cracks extending outside the main region. The condition to exclude cracks extending outside the main region is implemented by introducing a minimum distance d_{min} that each crack is allowed to be from the region's boundaries. This distance is chosen to match the element size in the wave propagation modelling, with the effect that all cracks are at least one element from the boundaries. The same distance d_{min} is used also as part of the condition to exclude crossing cracks: all cracks in the wave propagation modelling are required to be at least one element, or equivalently d_{min} , apart. The randomly generated cracks are tested sequentially, and cracks are rejected that either cross or are too close to previous cracks in the sequence.

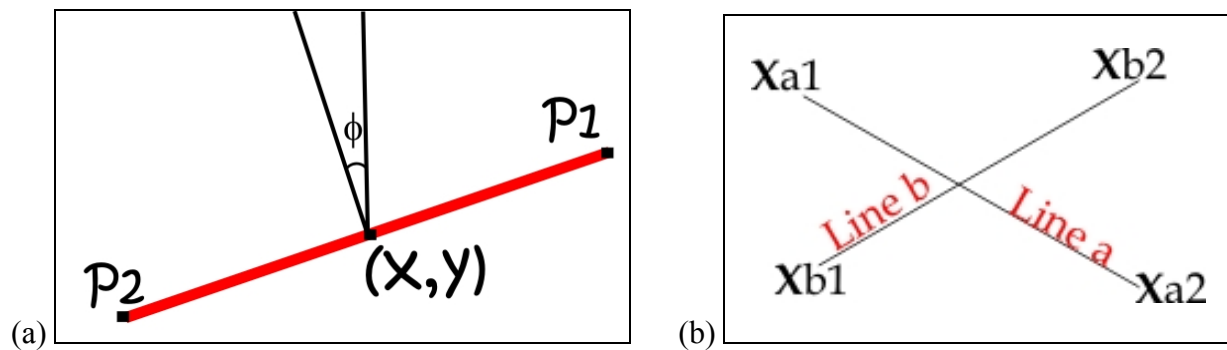


Figure 6.4 –(a) Crack (red) with its orientation Φ and its mid point in (x,y) ; (b) Crossing cracks.

6.1.1.2 Models with faults

Other models were produced inserting one (or more) fractures longer than the others in the middle of the half space, in order to simulate the presence of faults. The fracture density and lengths are forced to be higher close to the fault, as is the uniformity of orientations, through being dependent on fracture length.

The crack lengths are ordered in decreasing size starting with the main fault whose length is $L_1 = L_{max}$:

$$L_1 > L_2 > L_3 > \dots > L_{i-1} > L_i > \dots > L_{n_{max}}.$$

In our examples the minimum length L_{min} is set equal to d_{min} , corresponding to element size in the wave propagation modelling. There are two related parameters n_i and q_i , associated with each of the crack lengths L_i :

$$6.26 \quad n_i = \frac{L_i - L_{min}}{L_{i-1} - L_{min}} n_{i-1} = \frac{L_i}{L_{min}} - 1,$$

$$6.27 \quad q = \sqrt{1 + n_i} = \sqrt{\frac{L_i}{L_{\min}}}$$

The values of n_i are chosen in a random sequence, starting from $n_i = \frac{L_{\max}}{L_{\min}} - 1$:

$$6.28 \quad P(n_i) = \left(\frac{n_i}{n_{i-1}} \right)^k \text{ for a random sequence of numbers } P_{i-1} = P(n_{i-1}) \text{ between 0 and 1, with } k$$

having a prescribed value. That is:

$$6.29 \quad n_i = n_{i-1} (P_{i-1})^{-\frac{1}{k}}$$

For a large number of k the value of n_i will be slightly smaller than the value of n_{i-1} . The limiting value $n_i = 0$ corresponds to $L_i = L_{\min}$, and in general the value of L_i is obtained using the relationship:

$$6.30 \quad L = L_{\min} + n_i L_{\min}$$

The other parameter q_i in 6.27, which has limiting value $q_i = 1$ corresponding to $L_i = L_{\min}$, is used to construct probability functions for the other properties ϕ_i , x_i and y_i for each crack.

The parameter η_{i-1} that controls how close ϕ_i is to the expected value ϕ_i' is given by the value:

$$6.31 \quad \eta_{i-1} = \eta_{\min} \left(\frac{\eta_{\max}}{\eta_{\min}} \right)^{\frac{q_i}{q_1}}$$

$$\text{where } \frac{q_i}{q_1} = \sqrt{\frac{L_i}{L_{\max}}}$$

When $L_i = L_{\max}$, $\eta_{i-1} = \eta_{\max}$, and when $L_i = 0$, $\eta_{i-1} = \eta_{\min}$. That means that when $\eta_{\max} \gg \eta_{\min}$, the larger the value of L_i , the larger the value of η_{i-1} and the more ϕ_i is required to be close to ϕ_i' . No crack is allowed to have length $L_i = 0$, but a reasonable value of η_{i-1} corresponding to that case is $\eta_{\min} = 1$ which means that ϕ_i is equally likely to be any angle.

The probability density functions for x_i and y_i for the limiting case $q_i = 1$ corresponding to $L_i = L_{\min}$ are based in part on stress fields. Suppose that a fault is locked above a depth d_{\max} and continuously slipping below that. Then as functions of horizontal position x the associated stress magnitude will be roughly proportional to

$$\frac{1}{(d_{\max}^2 + x^2)}$$

Hence, assuming the likelihood of a small crack forming in the stress field around a major fault (at $x=0$) is proportional to stress magnitude for the limiting case $q_i = 1$,

$$6.32 \quad p(x_i) = \frac{1}{2} \left(\frac{d \max}{\tan^{-1}\left(\frac{x \max}{d \max}\right)(d \max^2 + x^2)} \right).$$

Similarly the pressure in the Earth resisting the formation of cracks is proportional to the depth y , and assuming the likelihood of a small crack forming is inversely proportional to the resisting pressure, again for the limiting case $q_i = 1$,

$$6.33 \quad p(y_i) = \frac{1}{[\ln|y \min| - \ln|y \max|]} \frac{1}{|y_i|}.$$

Note that here x_{\max} , $y_{\min} (< 0)$ and $y_{\max} (< 0)$ are the extreme values possible, taking into account the element sizes and the values of L_i and q_i , and symmetry of the model is assumed so that $x_{\min} = -x_{\max}$.

Working on the presumption that the larger the crack is the more likely it is to be close to the main fault (where the associated stresses are higher) and to the ground surface (where the pressures are smaller), for general values of q_i these expressions are taken to be:

$$6.34 \quad p(x_i) = \frac{q_i}{2} \left(\frac{\tan^{-1}\left(\frac{|x_i|}{d \max}\right)}{\tan^{-1}\left(\frac{x \max}{d \max}\right)} \right)^{q_i} \frac{d \max}{\tan^{-1}\left(\frac{x \max}{d \max}\right)(d \max^2 + x_i^2)},$$

$$6.35 \quad p(y_i) = \frac{(q_i - 1) \left| \frac{y \max}{y_i} \right|^{q_i - 1} \frac{1}{|y_i|}}{\left(1 - \left| \frac{y \max}{y \min} \right|^{q_i - 1} \right)}.$$

The resulting integrated probabilities are:

$$6.36 \quad P(x_i) = \frac{1}{2} \left\{ 1 + \text{sign}(x_i) \left[1 - \left(\frac{\tan^{-1}\left(\frac{|x_i|}{d \max}\right)}{\tan^{-1}\left(\frac{x \max}{d \max}\right)} \right)^{q_i} \right] \right\},$$

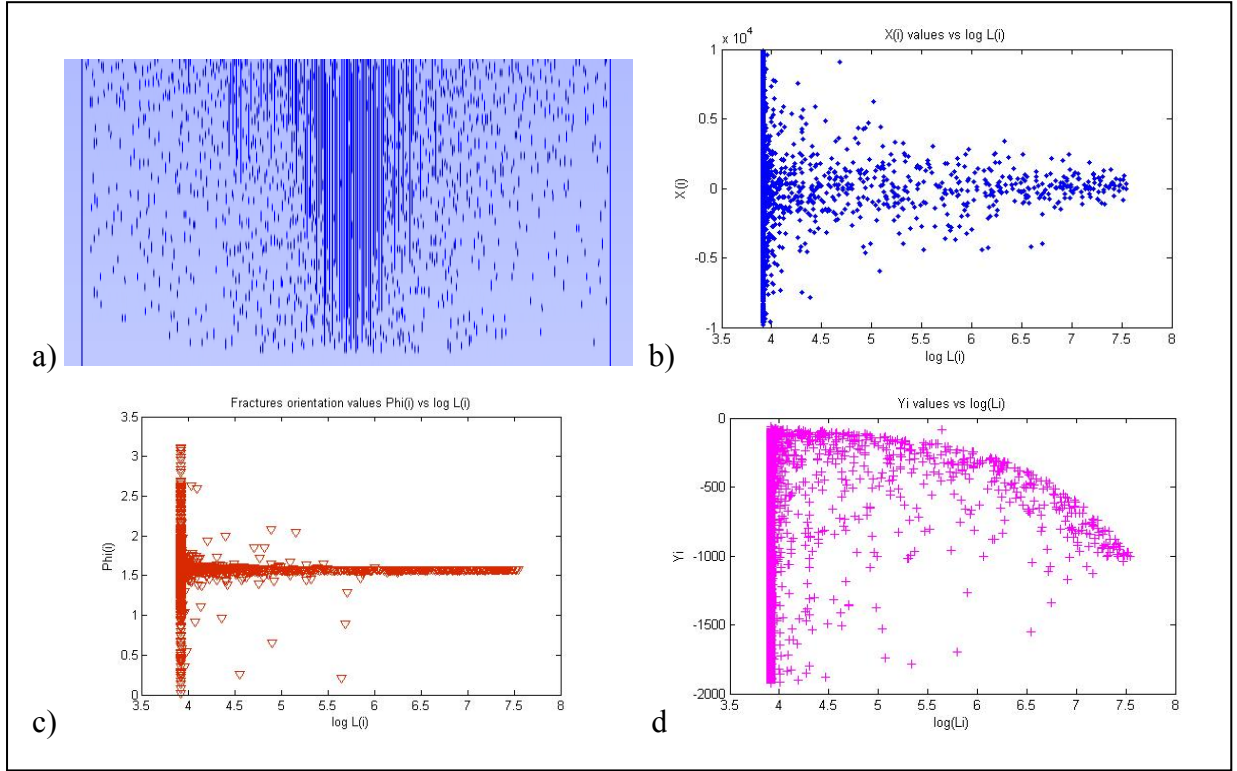


Figure 6.4 – Plots of values x_i (b), ϕ_i (c) and y_i (d) versus $\log(L_i)$, related to fracture distribution in (a).

$$6.37 \quad P(y_i) = \frac{\left(1 - \left|\frac{y_{\max}}{y_i}\right|^{q_i-1}\right)}{\left(1 - \left|\frac{y_{\max}}{y_{\min}}\right|^{q_i-1}\right)}.$$

With separate random probabilities $P_{i-1} = P(x_i)$ and $P_{i-1} = P(y_i)$ between 0 and 1, the values of x_i and y_i are given by:

$$6.38 \quad x_i = d_{\max} \cdot \tan \left\{ \tan^{-1} \left(\frac{x_{\max}}{d_{\max}} \right) \cdot \text{sign}(2P_{i-1} - 1) \left[1 - (1 - |2P_{i-1} - 1|)^{\frac{1}{q_i}} \right] \right\},$$

$$6.39 \quad y = \frac{y_{\max}}{\left[1 - P_{i-1} + P_{i-1} \left| \frac{y_{\max}}{y_{\min}} \right|^{q_i-1} \right]^{\frac{1}{q_i-1}}}.$$

Figure 6.4 shows the dependence of ϕ_i , x_i and y_i values with $\log(L_i)$, for an example of a fracture distribution. This process of generating values L_i , ϕ_i , x_i and y_i for a trial set of cracks is followed by testing whether cracks cross. Cracks that are either too close to preceding cracks in

the sequence or cross those cracks are removed. This considerably reduces the number of cracks in the final set.

6.1.1.3 Models with a fractal distribution of fractures

Trying to better reproduce the real pattern and shape of a fractured zone, models with fracture distributions were created imposing a fractal relation between spacing (d_{min}) and length (L). In the last paragraph the distance used in determining whether cracks are too close is based solely on the element size for the wave propagation modelling. Here a prescribed fraction $frac$ of the length L_i of each crack is used as well, so that the minimum allowed separation of that crack from preceding cracks in the sequence is set equal to the larger of the original value d_{min} (related to element size) and the fractional length $frac * L_i$. This results in a very high rejection rate of large cracks, particularly those close to the main fault. It is important to note that because the cracks are ordered with decreasing lengths, each crack is tested for its separation from longer cracks retained in the sequence. More often than not almost all the very large cracks will be rejected because they are too close to the main fault. A typical value of $frac$ is 0.25. For very small cracks with lengths close to d_{min} the fractional length $frac * L_i$ is irrelevant because it is smaller than d_{min} . In fact the rejection rate for small cracks is lower than without the extra condition involving $frac * L_i$, since small cracks can occupy gaps that would have been filled by large cracks in the absence of this condition.

6.1.2 TFEM method

The seismic response of the fracture fields was simulated using the triangular finite element method (TFEM) whose theory and codes were developed by John Haines at the Department of Earth Sciences of Cambridge University (Elena Klien, PhD thesis). This method was presented by Klien & Haines (2007) as a new technique to simulate the propagation of pressure (P) and in-plane shear waves (SV) within a 2D half space.

The spatial discretization is made through triangular elements with 7 nodes (2 on each face, plus 1 at the midpoint of each triangle) where the equations solutions are found. This discretization is accurate for integrals of quadratic functions inside each element, and for integrals of cubic functions on each face (Figure 6.4).

On each element the equations are solved and the following values are determined at each node.

- The velocity vector is :

$$6.26 \quad v_i = \frac{\partial u_i}{\partial t},$$

where u_i is the i -th component of displacement.

- The strain tensor is :

$$6.27 \quad e_{ij} = \frac{1}{2} \left(\frac{\partial u_i}{\partial x_j} + \frac{\partial u_j}{\partial x_i} \right).$$

- The stress tensor is given by:

$$6.28 \quad \sigma_{ij} = \lambda \delta_{ij} e_{kk} + 2\mu e_{ij},$$

where λ and μ are Lamé parameters and e_{kk} is the isotropic deformation.

Then on each element face the following related values are calculated.

- The tangential strain tensor is :

$$6.29 \quad \tilde{\varepsilon}_{ij} = (\delta_{iq} - n_i n_q) e_{qp} (\delta_{pj} - n_p n_j),$$

where δ is the Kronecker delta and n_i is the i -th component of the normal vector for the face.

- The traction is:

$$6.30 \quad t_i = \sigma_{ij} n_j.$$

Afterwards continuity over the whole domain is verified, assembling combined values on interfaces where adjacent triangles meet. Consider two adjacent triangles with defined density (ρ), volume (V) and Lamé constants (μ and λ), the i -th component of the velocity field at a common point “is established in terms of the values evaluated inside the elements through a weighting of the latter in proportion to the weights associated with the elements”:

$$6.31 \quad v_i = \frac{(\rho_1 V_1) v_i^1 + (\rho_2 V_2) v_i^2}{(\rho_1 V_1) + (\rho_2 V_2)};$$

In a similar way the normal (t_n) and tangential (\tilde{t}_i) components of traction (t_i), the diagonal component of tangential strain $\tilde{\varepsilon}_{ii}$ and the remainder of the tangential strain tensor $\tilde{\varepsilon}_{ij}$ are calculated, respectively through:

$$6.32 \quad t_n = \frac{\left(\frac{V_1}{\lambda_1 + 2\mu_1} \right) t_n^1 + \left(\frac{V_2}{\lambda_2 + 2\mu_2} \right) t_n^2}{\left(\frac{V_1}{\lambda_1 + 2\mu_1} \right) + \left(\frac{V_2}{\lambda_2 + 2\mu_2} \right)};$$

$$6.33 \quad \tilde{t}_i = \frac{\left(\frac{V_1}{\mu_1}\right)\tilde{t}_i^1 + \left(\frac{V_2}{\mu_2}\right)\tilde{t}_i^2}{\left(\frac{V_1}{\mu_1}\right) + \left(\frac{V_2}{\mu_2}\right)};$$

$$6.34 \quad \tilde{\varepsilon}_{ii} = \frac{(E_1 V_1)\tilde{\varepsilon}_{ii}^1 + (E_2 V_2)\tilde{\varepsilon}_{ii}^2}{(E_1 V_1) + (E_2 V_2)}, \text{ where } E = \frac{\mu(3\lambda + 2\mu)}{(\lambda + 2\mu)} \text{ is the Young Modulus;}$$

$$6.35 \quad \tilde{\varepsilon}_{ij} = \frac{(\mu_1 V_1)\tilde{\varepsilon}_{ij}^1 + (\mu_2 V_2)\tilde{\varepsilon}_{ij}^2}{(\mu_1 V_1) + (\mu_2 V_2)}.$$

Different boundary conditions are applied when triangles border surfaces of different nature :

- RIGID BOUNDARY – with the outer part of model, as the case of having only element 1 (because $\rho_2 = \infty$, $\lambda_2 = \infty$, $\mu_2 = \infty$), where $v_i = 0$, $\tilde{\varepsilon}_{ii} = 0$, $\tilde{\varepsilon}_{ij} = 0$, but $\tilde{t}_i \neq 0$ and $t_n \neq 0$;
- STRESS FREE BOUNDARY – like a rigid boundary except the reverse, where there is only element 1 (because $\rho_2 = 0$, $\lambda_2 = 0$, $\mu_2 = 0$), but tractions are zero $\tilde{t}_i = 0$, $t_n = 0$ and $v_i \neq 0$, $\tilde{\varepsilon}_{ii} \neq 0$, $\tilde{\varepsilon}_{ij} \neq 0$;
- FRACTURE (fluid filled crack) - where the normal components of traction and velocity are continuous while the tangential traction $\tilde{t}_i = 0$, with the tangential components of velocity being independent because the triangles can slide against each other, and similarly $\tilde{\varepsilon}_{ii}$ and $\tilde{\varepsilon}_{ij}$ is not continuous.

6.1.3 Simulation parameters

The fracture populations were created using a Matlab code developed in this PhD thesis, as described in section 6.1.1. This code generates an input file for the 2D and 3D finite element grid generator GMSH, that is used to interpolate the fractured medium through a triangular mesh with dimension Δx (for which the condition $\Delta x \leq d_{min}$ has to be valid).

Then the simulation code by John Haines was used to model the propagation of a Ricker input throughout the medium. The pulse peak frequency can be chosen depending on the case, but in this thesis it was fixed to 2Hz in almost all the simulations performed. As shown in Figure 6.3, the rheological parameters for the medium are: density 2250 Kg/m³, Vs 2000 m/s, Vp 3500 m/s (only in PSV). In all the simulations the free surface boundary conditions are used at the top of the model.

In order to avoid during the time period of interest having artificial reflection from the sides and bottom of the modelling arriving at the main region, big distances were added both to the sides and to the bottom, as displayed in Figure 6.5 (a). Taking T to be the length of time of interest, these distances need to be more than $0.5 \cdot V_s \cdot T$.

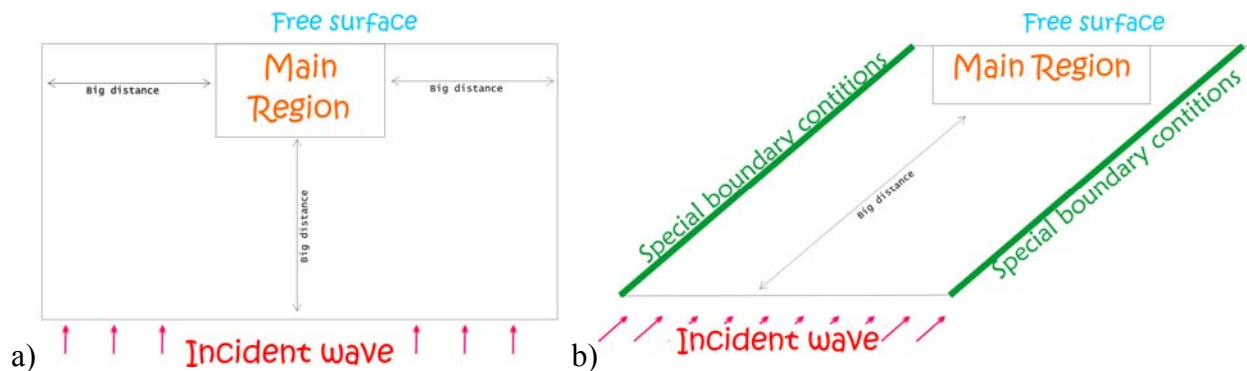


Figure 6.5 – Distances added to the main region in the modelling domain in order to avoid bottom/side reflections.

Unfortunately, when using an oblique incident wave one of the sides produced a reflected wave arriving in the main region during T , and was included in the synthetics. To prevent this problem the sides of the modelling domain were sloped so that they were parallel to the direction of propagation of the incident wave, as displayed in Figure 6.5 (b). Moreover to reduce reflections, special boundary conditions were applied along the sides by forcing the derivatives of the wavefield to be zero perpendicular to the boundaries. Also, in this way the size of the modelling domain was reduced, resulting in each simulation requiring lower computational time.

The following parameters need to be chosen and tailored on the medium dimension and element size, which in turn is dictated by the minimum length of fractures and their minimum separation :

- dt – internal sampling rate, that needs to be smaller than a maximum value imposed by the program on the basis of element size to ensure numerical stability of the wavefield calculations,
- dt for output, which has to be a multiple of the internal sample rate and is set equal to 0.01 s,
- total number of time steps that have to be evaluated, considering both the travel time from the bottom boundary where the incident wavefield is input and the significant duration to be produced in the synthetics.

6.2 Results

To evaluate the effect of fractures on seismic propagation the synthetic seismograms are processed and graphed in several manners. Firstly they are plotted along the half space, to assess variations in amplitude. Then the spectral ratios relative to a reference are calculated and graphed with contour lines. They are moreover displayed with contour plots of Fast Fourier Transforms of the synthetics, to recognize whether the peaks in spectral ratios are produced by a low values of amplitude in the reference signal. The reference synthetic comes from a simulation performed using an half space with the same rheological parameters but without fractures.

The main aim of this modelling is to observe in which direction the maximum amplification occurs compared with the main fracture orientation. So, the ratios between SH and PSV synthetics are calculated and graphed in a log scale when the PSV simulation was performed.

6.2.1 Models with one set of fractures

As described in section 6.1.1.1, several models were performed each with one set of fractures homogeneously distributed across the half space, in order to observe the seismic response of models where the conditions previously described near fractures were imposed. The fractures density, orientation and direction homogeneity were varied with the length ranging from 20 m to 10 km. A Ricker pulse peaked at 2Hz (and 3Hz) was used as input, both with vertical and oblique angles of incidence and with out-of-plane (SH simulations) and in-plane motion.

6.2.1.1 SH simulations

At first many simulations were performed involving fracture distributions with very different geometries and shapes, in order to understand the effects induced by a fractured medium on the Ricker pulse polarized in the out-of-plane direction. The results of some representative models are displayed in Figure 6.5, showing that fractures cause an attenuation effect that can be recognized both as an amplitude decrease and as a time delay. This effect is higher with increasing:

- The density of fractures;
- The homogeneity in fractures orientations;
- The horizontality of fractures (i.e. decreasing the angle ϕ).

To define which of these factors plays the most relevant role, several models were performed decreasing the minimum length to 20 m, increasing fractures density and varying the degree of

homogeneity around the preferential orientation. Some representative model are illustrated in Figure 6.6, with preferential orientations of 5° , 15° , 25° and 35° going from “e” to “h”. As previously discussed, the attenuation effect decreases increasing the angle ϕ , from model “e” to “h”. Considering model “e” with cracks roughly parallel and comparing these results to model “a” in Figure 6.5, the time delay and the level of the attenuation effect in frequency domain are of the same order of magnitude, suggesting that the fracture minimum length value has a minor influence when the total length is comparable. As well the density of fractures seems to affect much more the attenuation than the homogeneity of fractures orientations

Exploring the influence of the peak frequency of the Ricker input, several models excited with Ricker pulses peaked at 2Hz and 3Hz were compared. Figure 6.8 shows the results of two typical models, with the same fracture distribution. The attenuation effect is of the same order of magnitude, and the only difference is that the frequencies where it occurs are slightly shifted to higher values using the pulse peaked at 3Hz. This happens because the wavelengths are in both cases higher than the fractures distances and much more closer to the fractured zone width, thus the response does not change considerably.

To investigate the effect of the input pulse angle of incidence, several simulations were performed on some homogeneous fracture distributions changing only the incoming pulse incidence angle from 0 (vertical incidence) to 60° , in steps of 15° . The results from this set of simulations indicate that the angle between the main fracture orientation and the direction of propagation of the pulse plays the most important role. In fact, as this angle gets closer to 90° the greater is the attenuation effect in both the frequency and time domains. On the other hand, when the propagation direction of the pulse is parallel to the main dip of the fracture field, the attenuation effect is less pronounced.

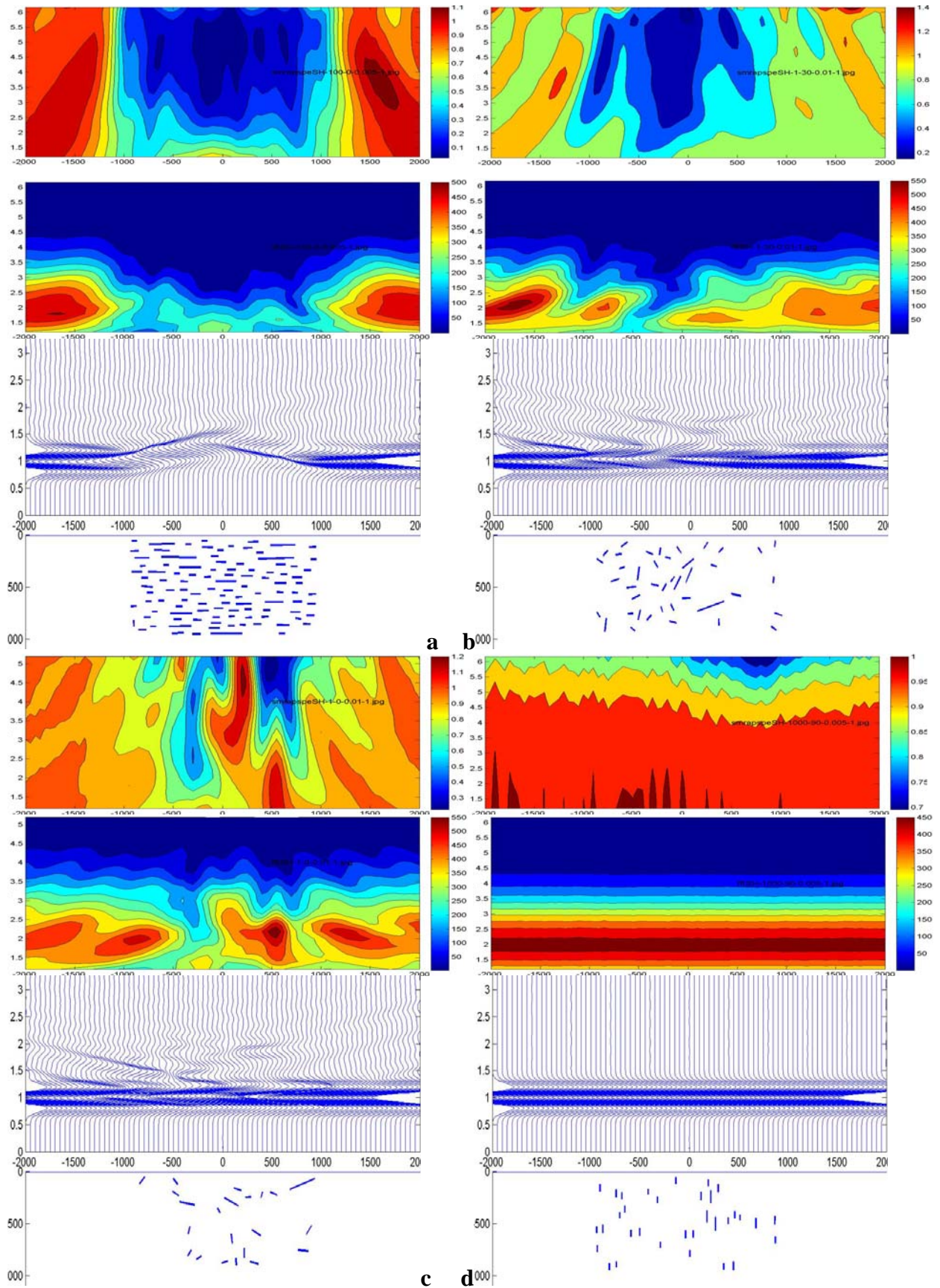


Figure 6.5 – Models **a-b-c-d**, with one set of fractures with different orientation direction and uniformity. For each one, the panels from the bottom to the top depict: vertical profile of fracture distribution; synthetic seismograms; contour plot of FFT; contour plot of spectral ratio

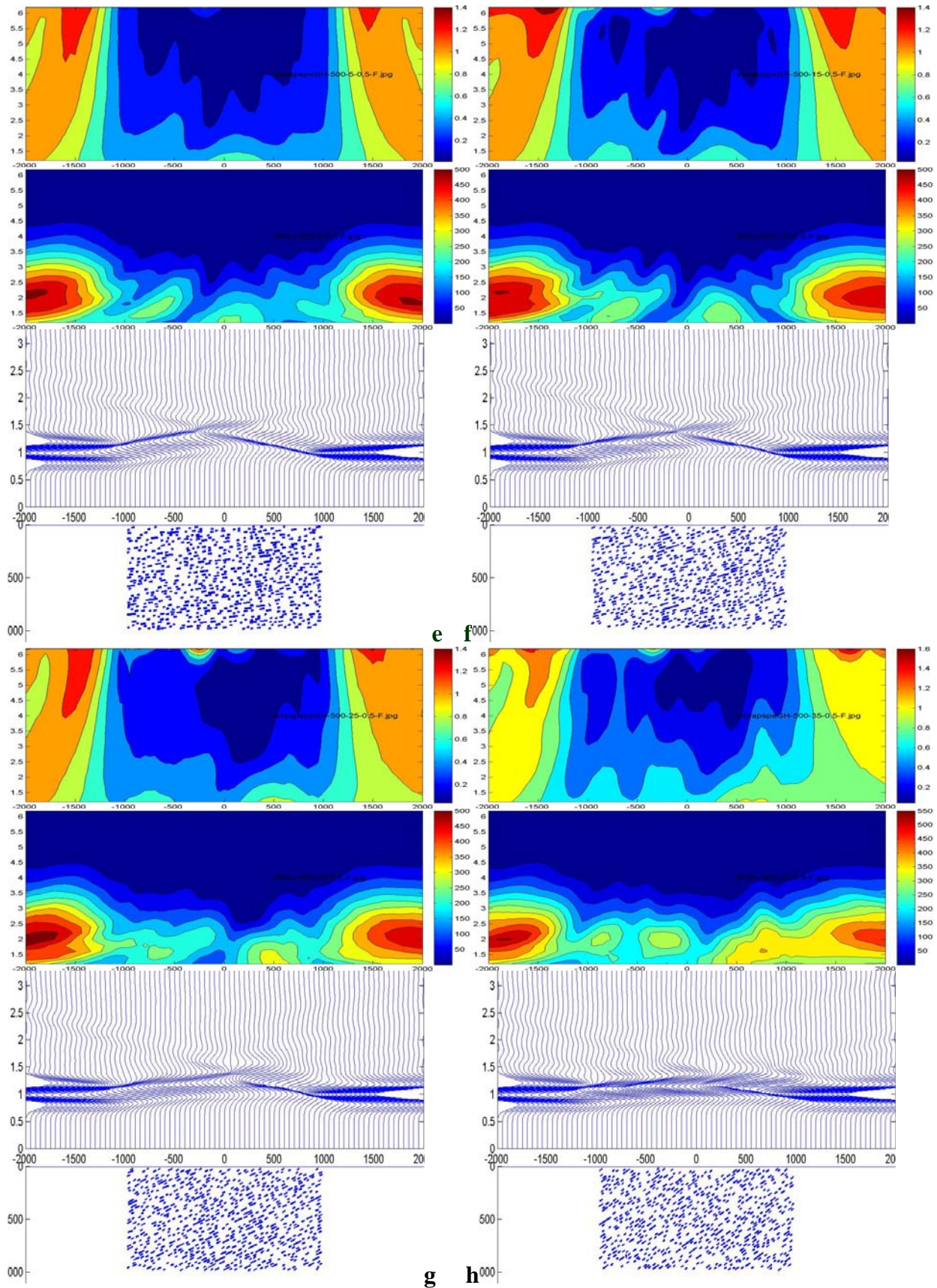


Figure 6.6 – Models **e-f-g-h**, with a higher fractures density. For each one, the panels from the bottom to the top display: vertical profile of fracture distribution; synthetic seismograms; contour plot of FFT; contour plot of spectral ratio.

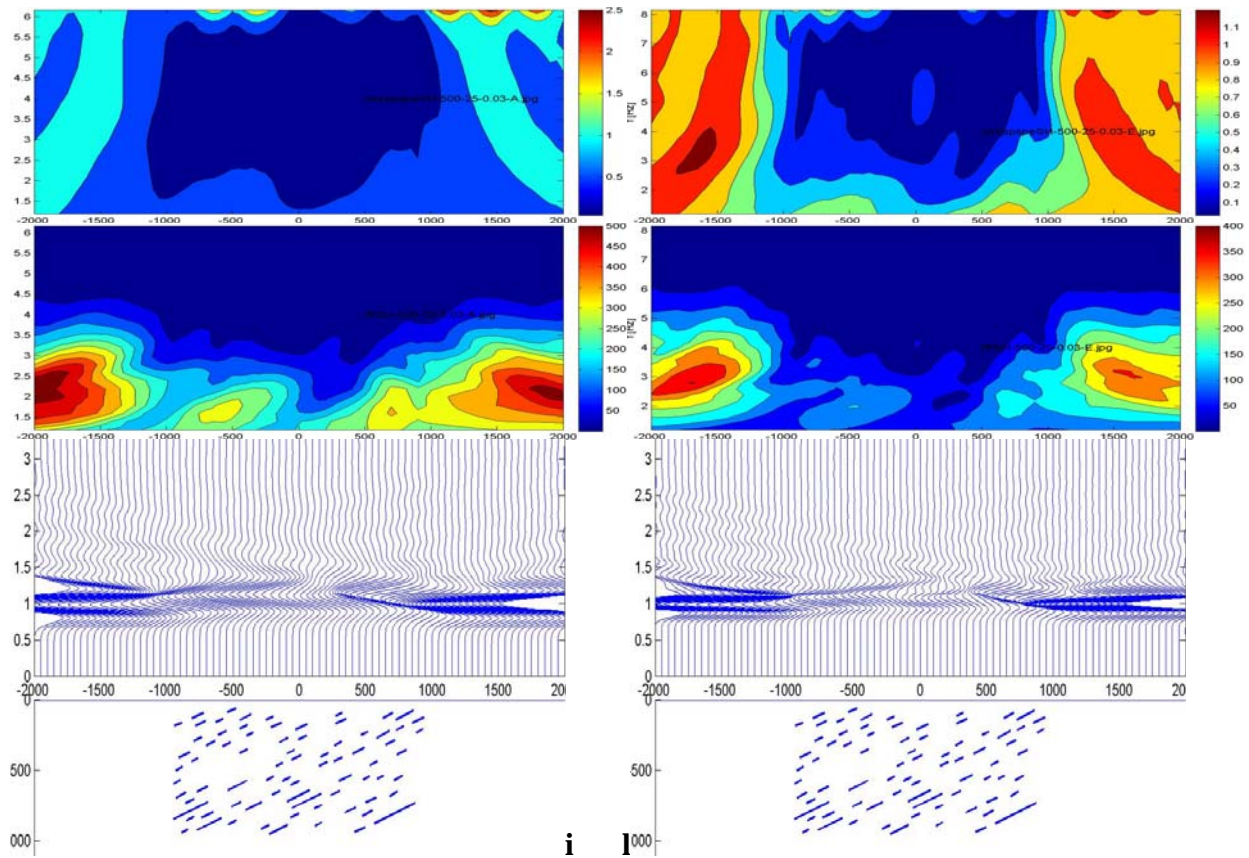


Figure 6.8 – Models with the same fracture distribution excited with two Ricker pulses respectively peaked at 2Hz (**i**) and 3Hz (**l**). For each one, the panels from the bottom to the top depict: vertical profile of fracture distribution; synthetic seismograms; contour plot of FFT; contour plot of spectral ratio.

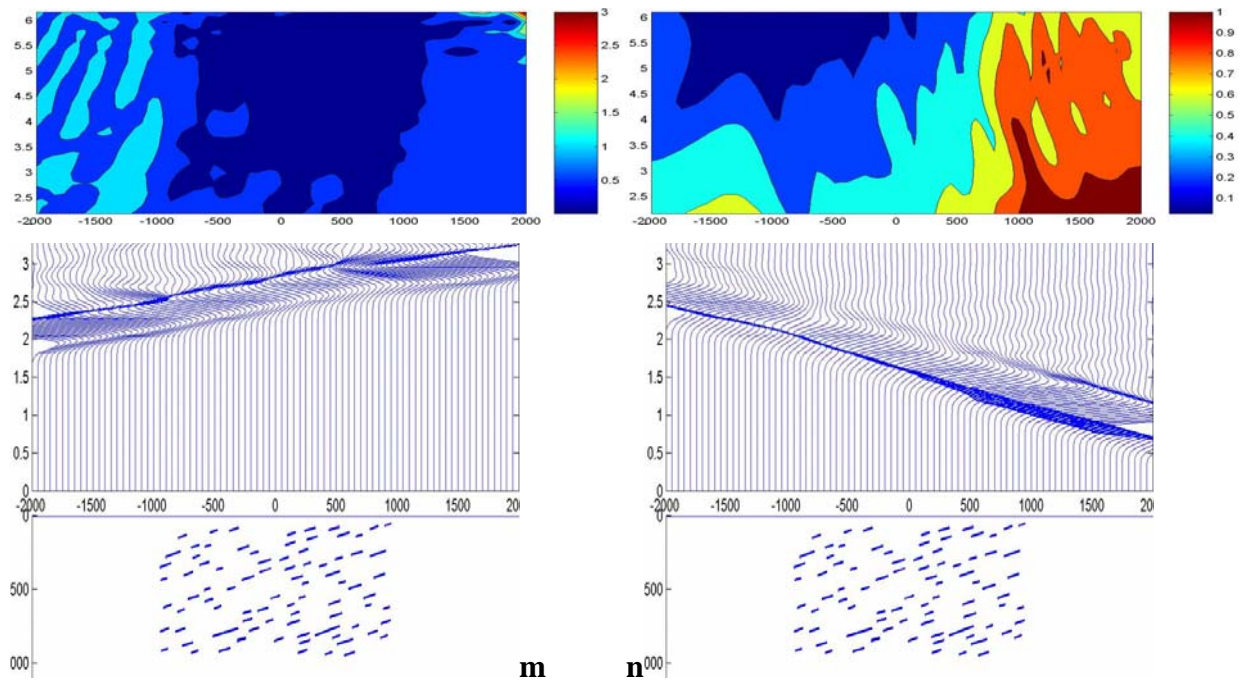


Figure 6.9 – Models with the same fracture distributions excited with two Ricker pulses respectively with angle of incidence of 30° (**m**) and -60° (**n**). For each one, the panels from the bottom to the top display: vertical profile of fracture distribution; synthetic seismograms; contour plot of FFT; contour plot of spectral ratio.

6.2.1.2 SH and PSV simulations

The simulations performed with out-of-plane motion input revealed a marked attenuation effect in both the frequency and time domains, that is higher with greater fracture density and homogeneity. The attenuation also increases when the angle between fracture dip and the input pulse propagation direction becomes closer to 90° . The response of the same medium to a Ricker pulse with in-plane motion is quite different and more complex considering the conversion of P to S waves and vice-versa. Moreover in these simulations two components of motion are produced as synthetic seismograms, representing vertical and horizontal motion. Referring to the fracture model pictures, these components correspond respectively to oscillation along the y-axis (upward vertical) and the x-axis (horizontal). The results from a typical and insightful simulation are presented in Figure 6.10 (model “o”), showing synthetics from SH and PSV models and contour plots of the FFTs. Here the fracture distribution has a higher density in the middle of the model, to reproduce partially the pattern near a shear zone, as explained in section 6.1.1.2. The SH model does not show a significant attenuation effect because the fractures are near vertical, while the horizontal component of PSV simulation shows a relevant deamplification effect that is both strong and increases with fracture density.

In order to better visualize the differences between motion in-plane and out-of-plane, the spectral ratios are calculated and graphed as logarithms through a contour map along the half-space (Figure 6.10, right column, middle-bottom panel). Log spectral ratios are always higher than 1 reaching a factor of 3 in the middle part where the fracture density is higher; thus they show that a distribution of subvertical 50 m long fractures generates an attenuation effect that is more pronounced in transversal in-plane direction than in parallel out-of-plane one.

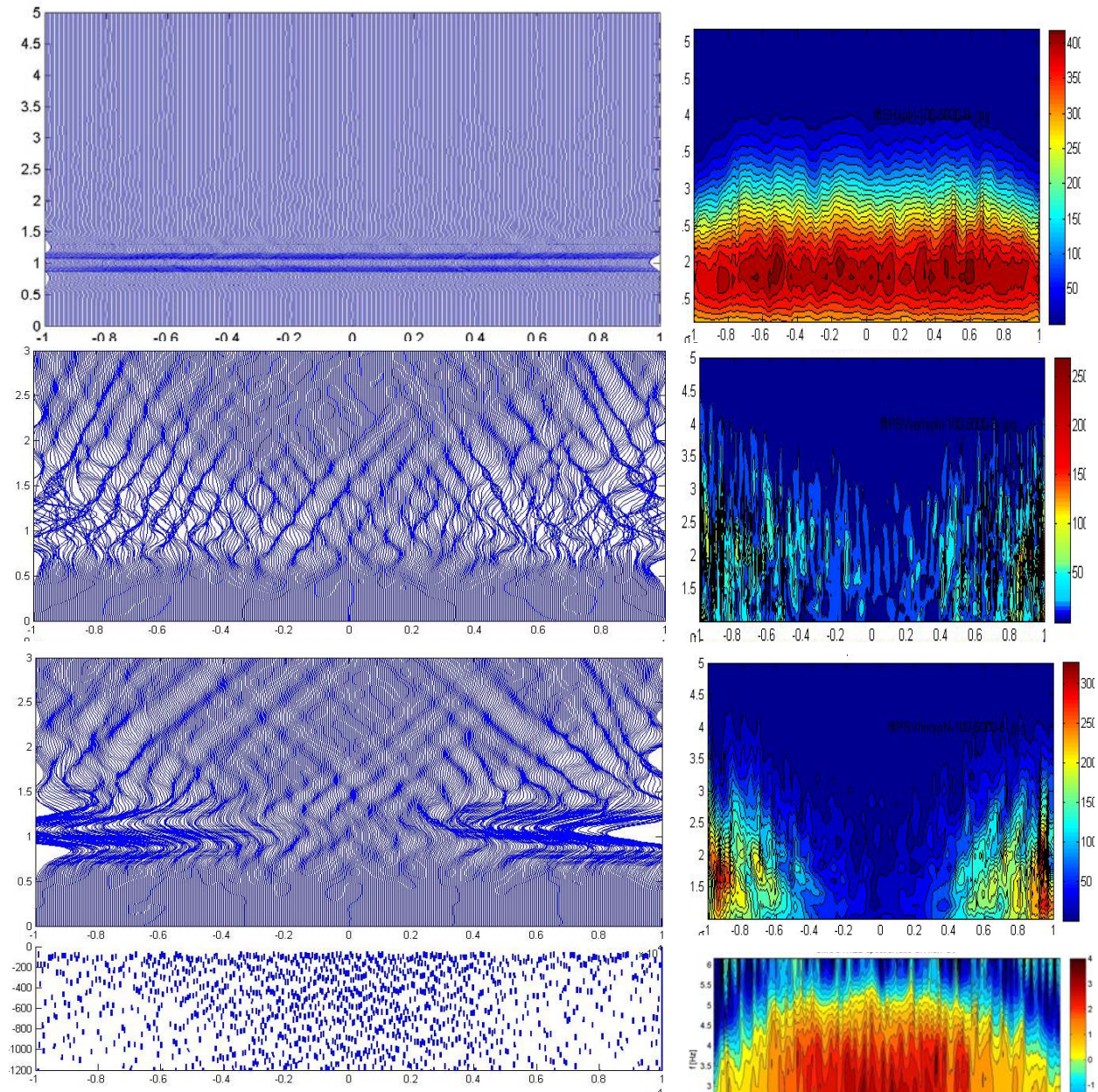


Figure 6.10 – Results of “o” distribution simulation, excited with a 2Hz peaked Ricker pulse vertically incident. Left column shows the synthetics: SH simulation (top), PSV simulation vertical (mid-top) and horizontal (mid-bottom) components. Right column displays the contour plots of the synthetics FFT in the same order and at the bottom the contour of logarithm of spectral ratio of SH out-of-plane synthetic seismograms relative to PSV in-plane horizontal component synthetic seismograms. At the bottom of both columns the fracture distribution is displayed in the x and z (depth) references system. x values along the model have to be multiplied * 10^4 .

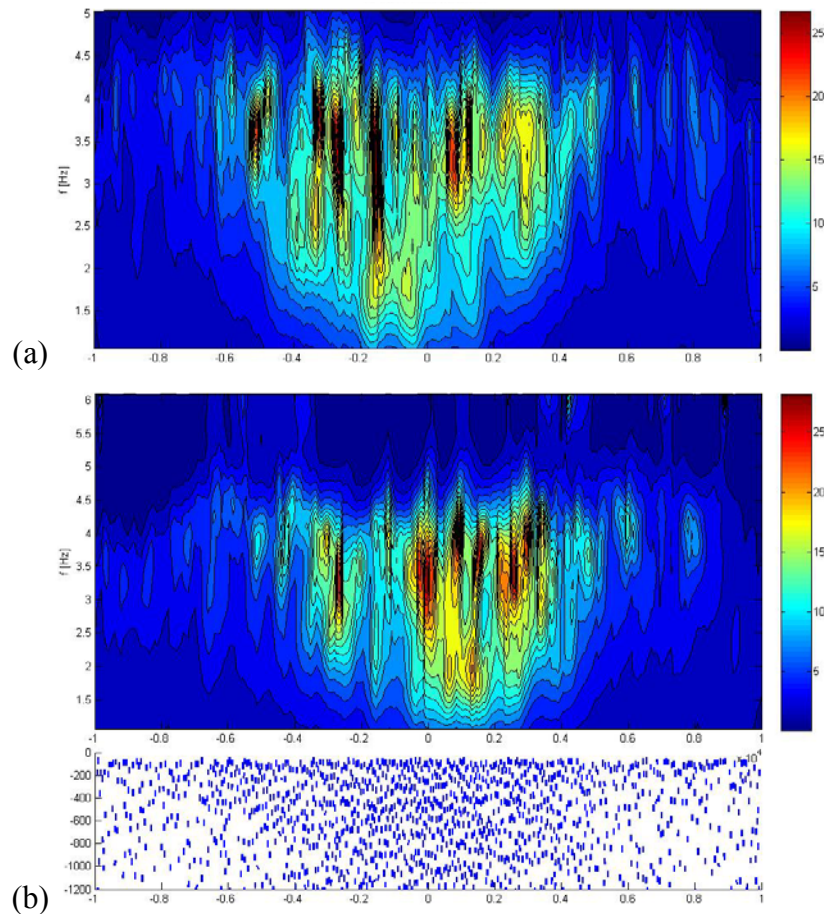


Figure 6.11 - Spectral ratios of SH out-of-plane simulation synthetics relative to PSV in-plane, horizontal component. (a) Ricker pulse with incidence angle of -15° ; (b) Ricker pulse with incidence angle of $+15^\circ$. x values along the model have to be multiplied $\cdot 10^4$.

6.2.2 Models with several sets of fractures and faults: SH and PSV simulations

Trying to create fractures populations more similar to the natural shape and pattern, two sets of fractures were introduced, differing in length and dip parameters (section 6.1.1.3). Moreover one or more fractures longer than the others were added to reproduce a fluid-filled fault, as described in section 6.1.1.2. Figure 6.12 displays the results of model “p”, where three longer subvertical fractures are added. The incidence is vertical as the main crack field dip. The PSV horizontal component reveals an attenuation effect that is absent on the SH model, leading to a logarithm of the spectral ratio SH/PSV-horizontal component that is always higher than 1.

The same trend is again shown by model “q” in Figure 6.13, with a subvertical fractures field with denser fractures, suggesting that neither density and length values nor the presence of faults

can significantly influence the fact that SH out-of-plane synthetics are less attenuated than PSV horizontal in-plane ones.

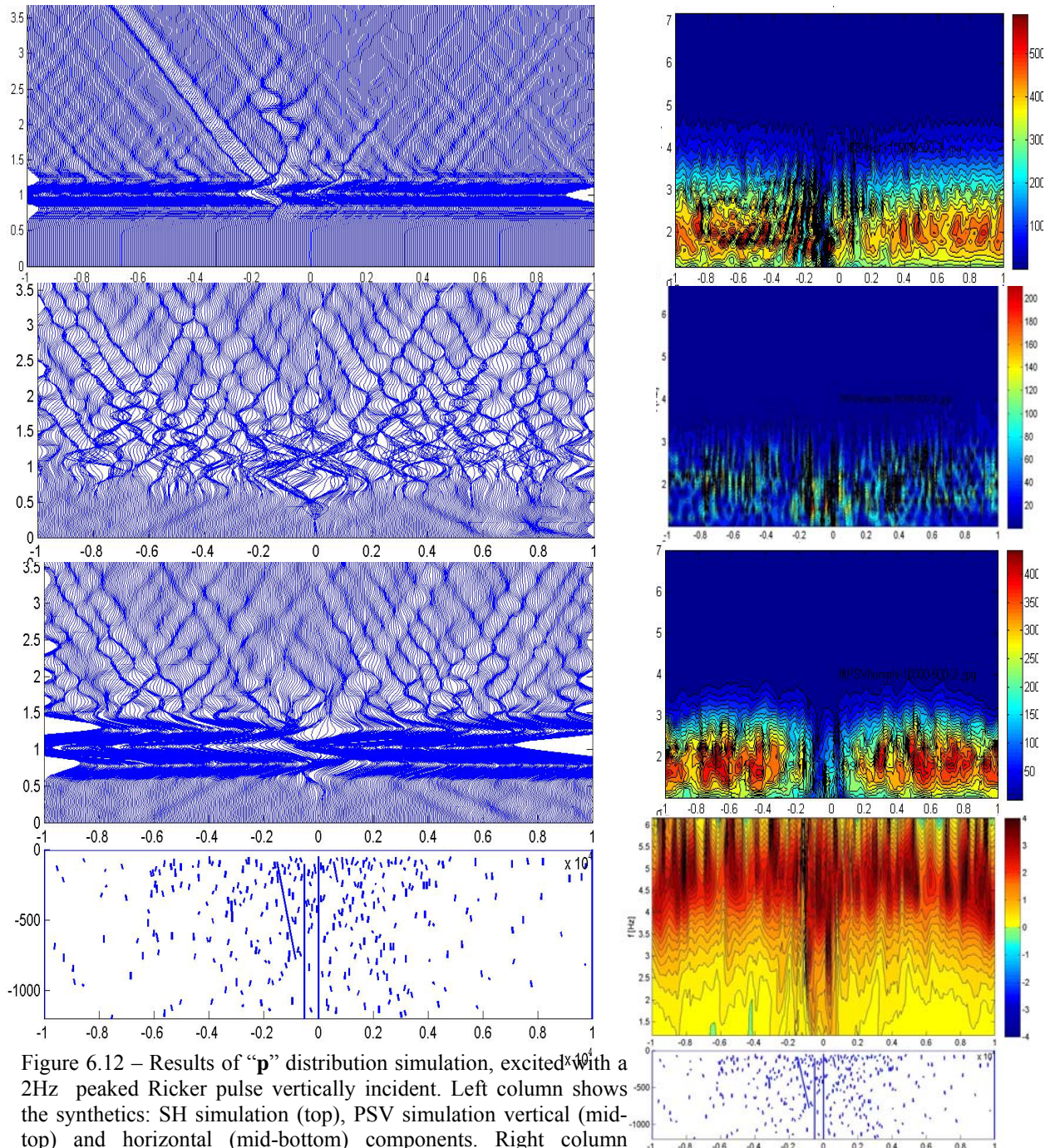


Figure 6.12 – Results of “p” distribution simulation, excited with a 2Hz peaked Ricker pulse vertically incident. Left column shows the synthetics: SH simulation (top), PSV simulation vertical (mid-top) and horizontal (mid-bottom) components. Right column displays the contour plots of the synthetics FFT in the same order and at the bottom the contour of logarithm of spectral ratio of SH out-of-plane synthetic seismograms relative to PSV in-plane horizontal component synthetic seismograms. At the bottom of both columns the fracture distribution is displayed in the x and z (depth) references system. x values along the model have to be multiplied * 10.

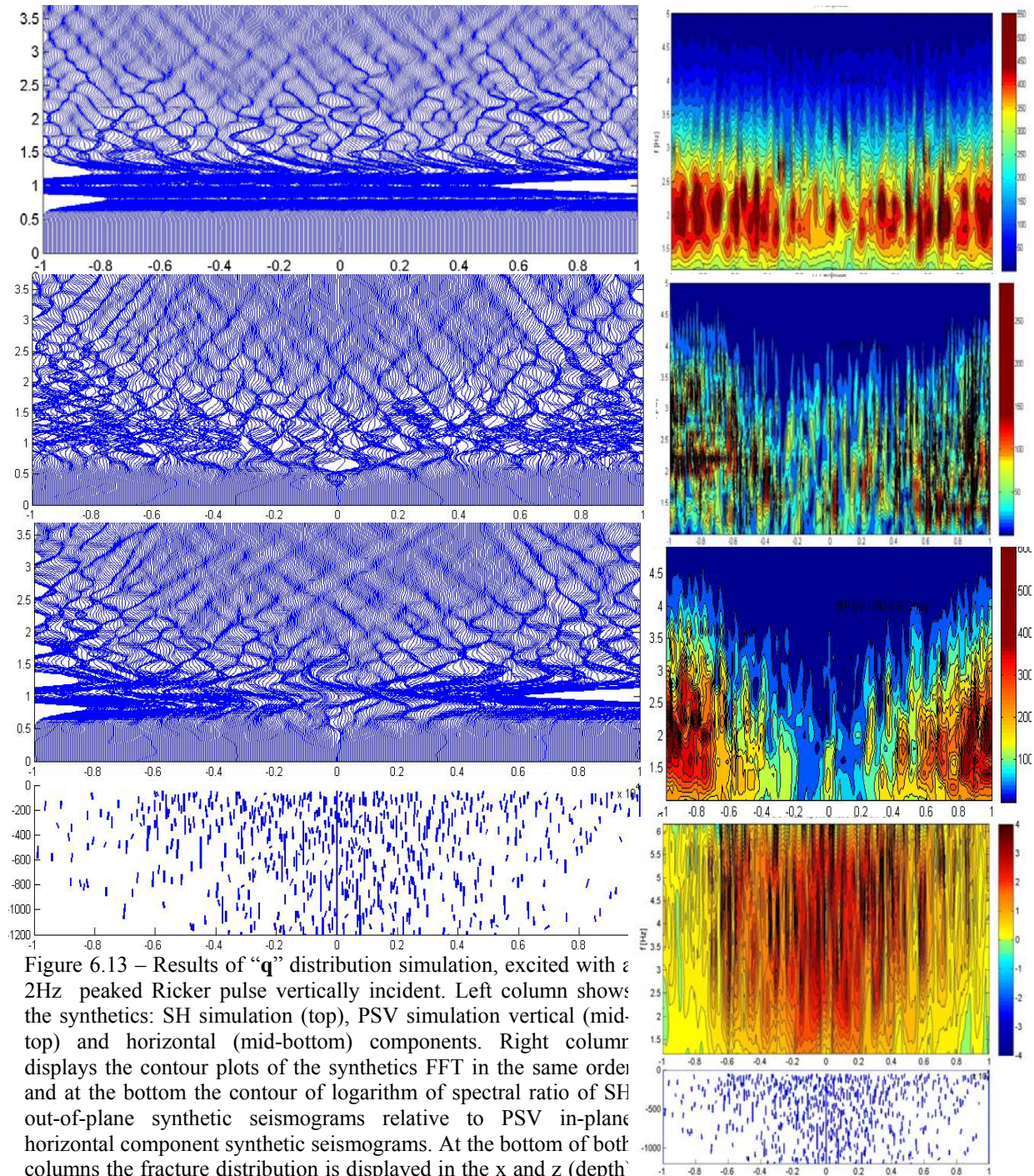


Figure 6.13 – Results of “ q ” distribution simulation, excited with ε 2Hz peaked Ricker pulse vertically incident. Left column shows the synthetics: SH simulation (top), PSV simulation vertical (mid-top) and horizontal (mid-bottom) components. Right column displays the contour plots of the synthetics FFT in the same order and at the bottom the contour of logarithm of spectral ratio of SH out-of-plane synthetic seismograms relative to PSV in-plane horizontal component synthetic seismograms. At the bottom of both columns the fracture distribution is displayed in the x and z (depth) references system. x values along the model have to be multiplied $\times 10^4$.

To investigate the influence of two sets of fractures with different length and dip joined to the presence of a fault, models “r” and “s” were created and excited with pulses with incidence angles of $+15^\circ$ and -15° .

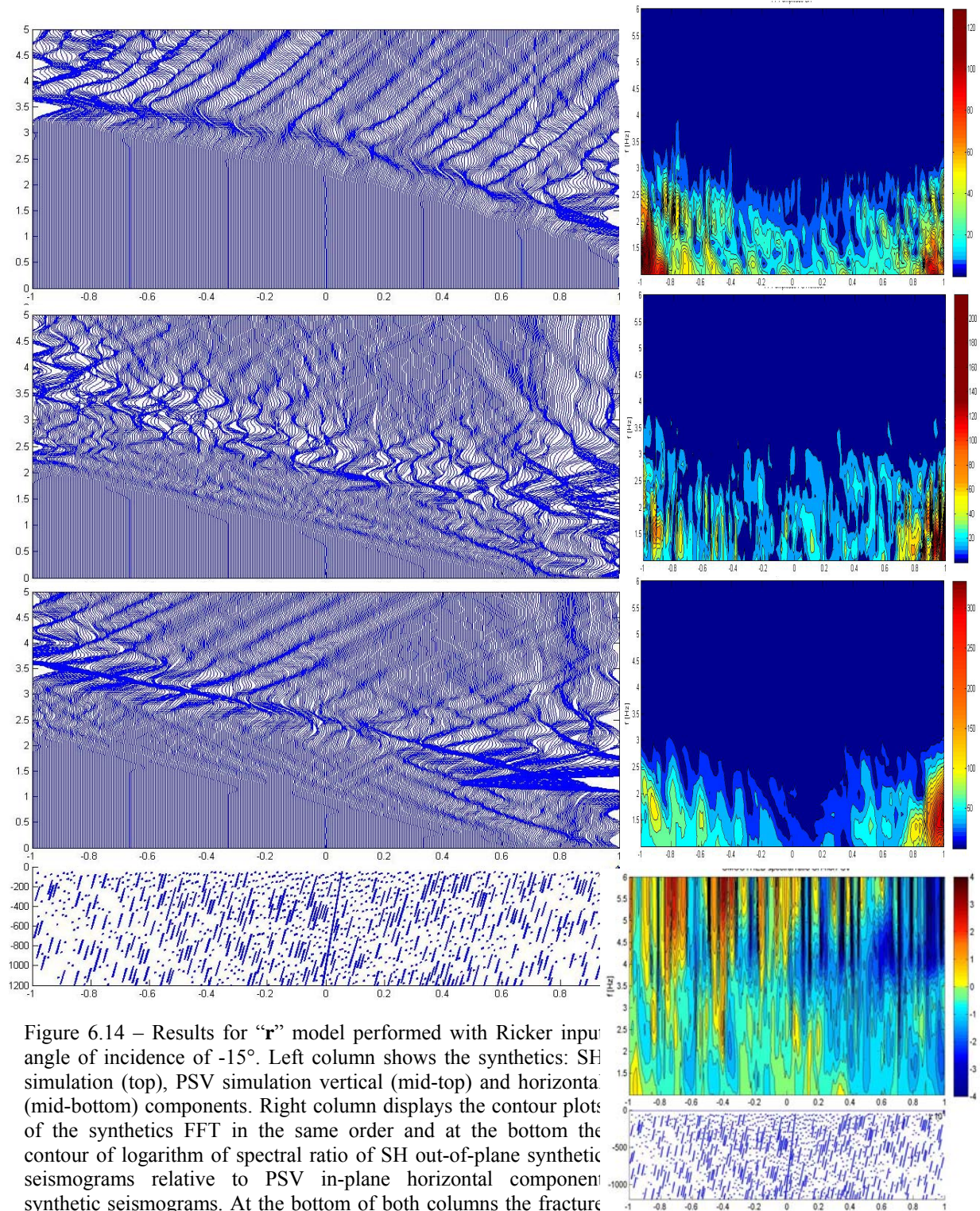


Figure 6.14 – Results for “r” model performed with Ricker input pulse with incidence angle of -15° . Left column shows the synthetics: SH simulation (top), PSV simulation vertical (mid-top) and horizontal (mid-bottom) components. Right column displays the contour plots of the synthetics FFT in the same order and at the bottom the contour of logarithm of spectral ratio of SH out-of-plane synthetic seismograms relative to PSV in-plane horizontal component synthetic seismograms. At the bottom of both columns the fracture distribution is displayed in the x and z (depth) references system. x values along the model have to be multiplied $\times 10^4$.

Figures 6.14 and 6.15 depict results of model “r” showing one 60° dip fault and two sets of fractures with dip respectively of 45 °and 5°. When the pulse is -15° incident, the spectral amplitude of the horizontal in-plane component is higher than the amplitude of the out-of-plane component one, almost everywhere along the profile and at frequencies lower than 3.5. The opposite behaviour occurs when the input is +15° incident.

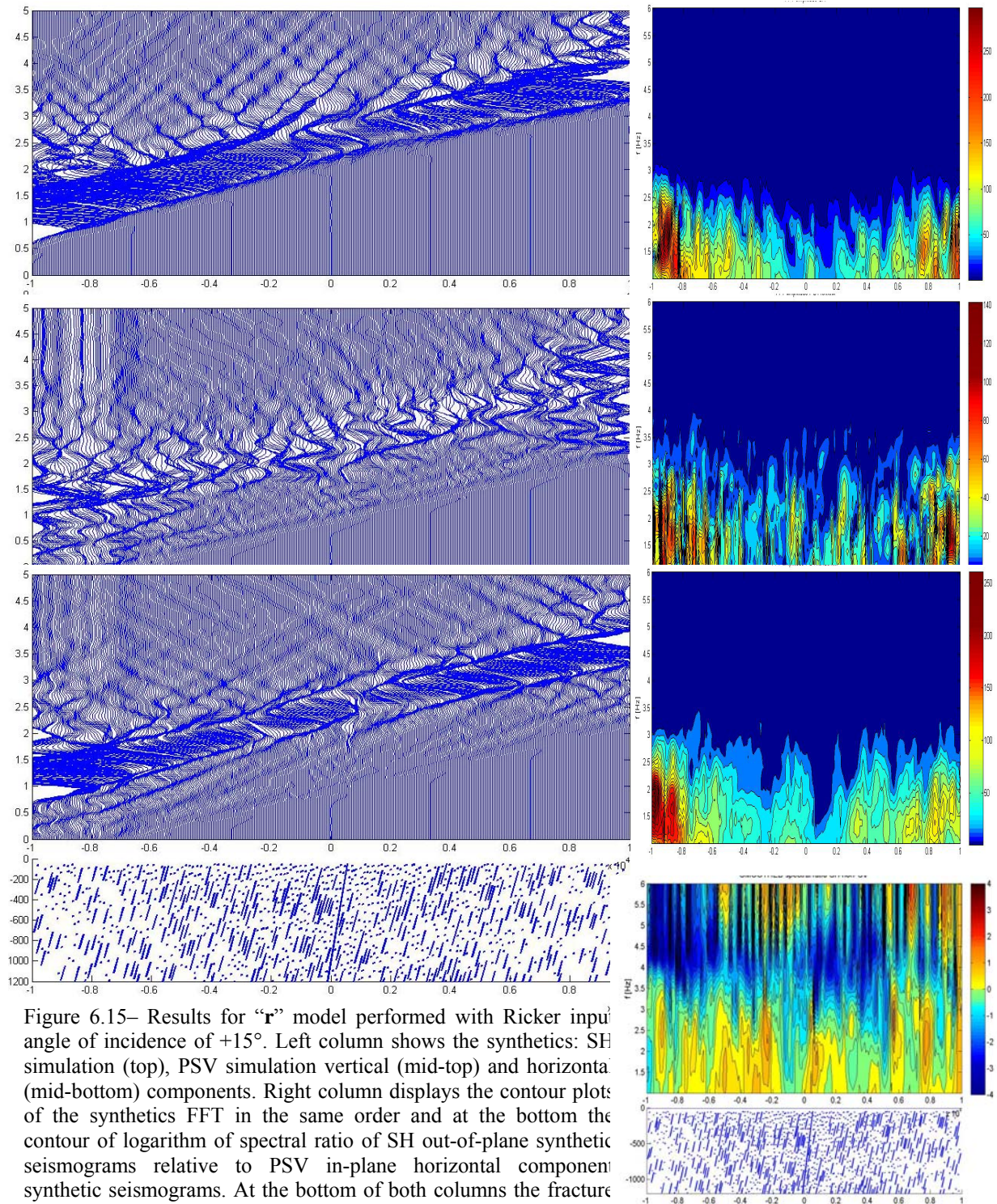


Figure 6.15– Results for “r” model performed with Ricker input angle of incidence of +15°. Left column shows the synthetics: SH simulation (top), PSV simulation vertical (mid-top) and horizontal (mid-bottom) components. Right column displays the contour plots of the synthetics FFT in the same order and at the bottom the contour of logarithm of spectral ratio of SH out-of-plane synthetic seismograms relative to PSV in-plane horizontal component synthetic seismograms. At the bottom of both columns the fracture distribution is displayed in the x and z (depth) references system. x values along the model have to be multiplied * 10⁴.

Results of model “s”, with a 60° dip fault and two sets of fractures with dip -75° and 15° are displayed in Figures 6.16 and 6.17. Here, the spectral amplitude of the horizontal in-plane component is higher than the amplitude of the out-of-plane component one when the pulse is $+15^\circ$ incident, everywhere along the profile and at frequencies lower than 4.5 Hz. As previously seen, the opposite happens with the other angle of incidence.

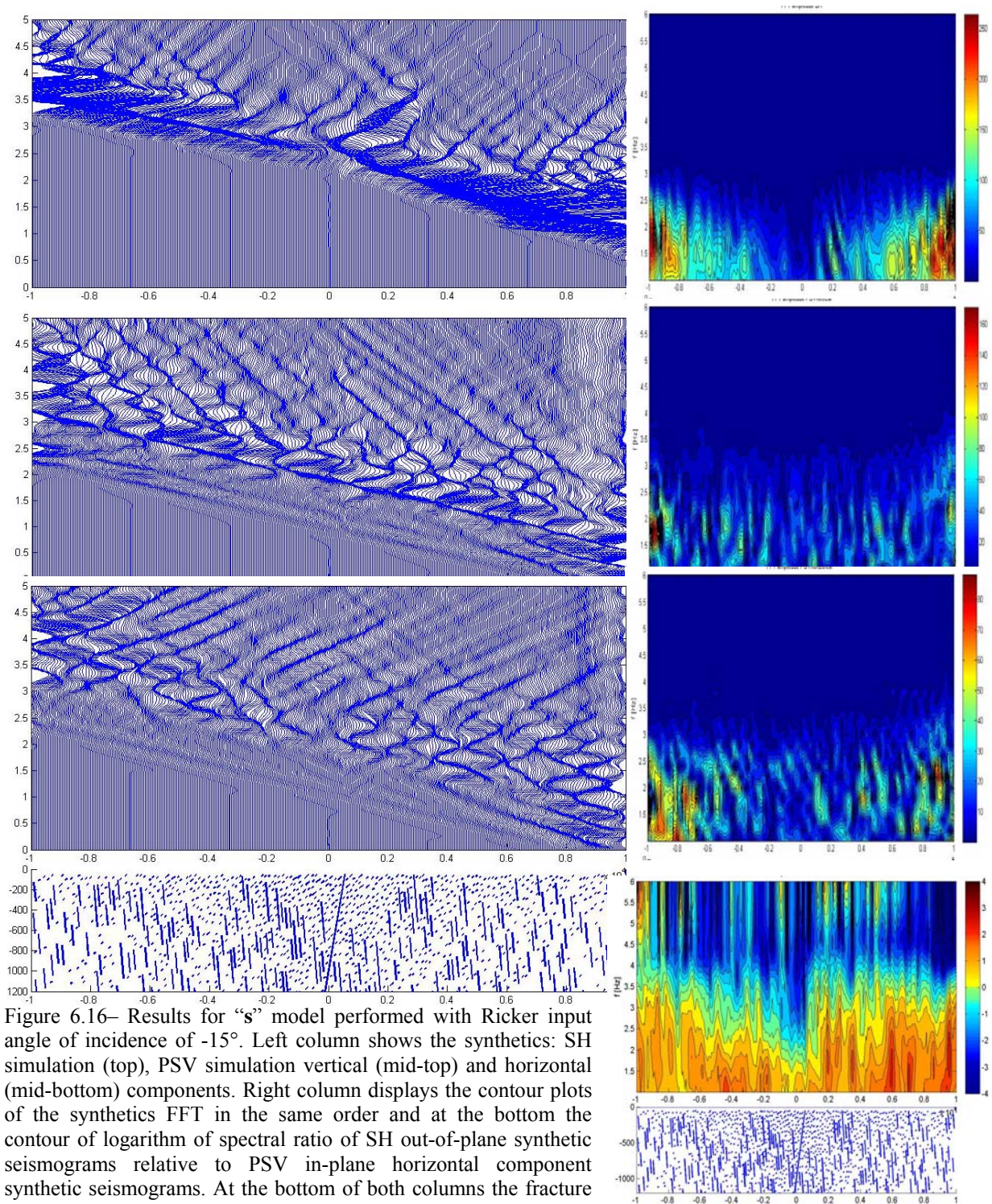


Figure 6.16– Results for “s” model performed with Ricker input angle of incidence of -15° . Left column shows the synthetics: SH simulation (top), PSV simulation vertical (mid-top) and horizontal (mid-bottom) components. Right column displays the contour plots of the synthetics FFT in the same order and at the bottom the contour of logarithm of spectral ratio of SH out-of-plane synthetic seismograms relative to PSV in-plane horizontal component synthetic seismograms. At the bottom of both columns the fracture distribution is displayed in the x and z (depth) references system. x values along the model have to be multiplied $\times 10^4$.

The pattern of the logarithmic spectral ratio between motion out-of-plane and motion in-plane is difficult to interpret on both models, with swings from negative to positive values uniformly along the profile and at changing frequencies. The logarithms of spectral ratios of the PSV horizontal component relative to the SH synthetics are shown in Figure 6.18, to provide a clearer way to evaluate differences between models with changes to the input angle of incidence.

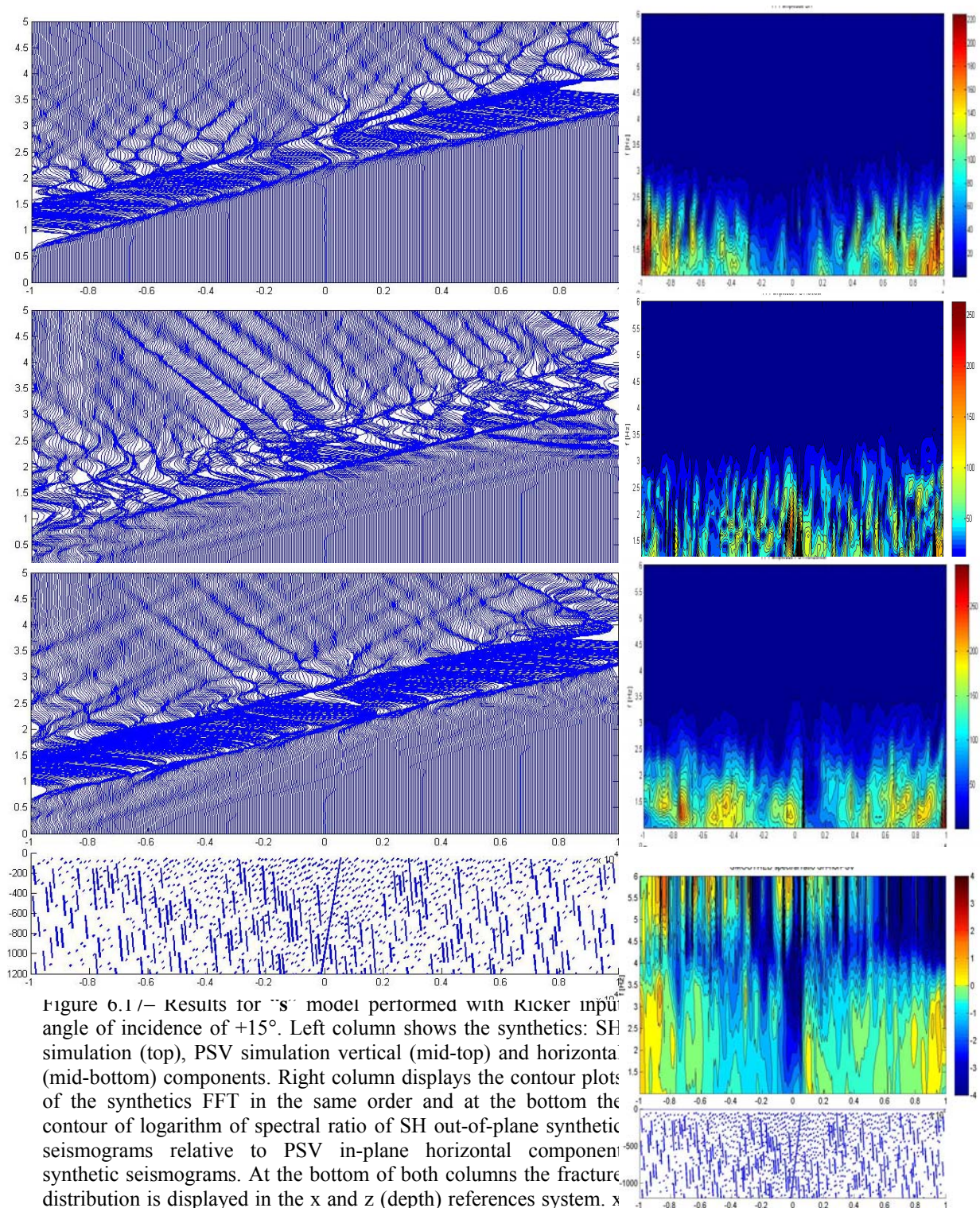


Figure 6.17— Results for “S” model performed with Kicker input angle of incidence of $+15^\circ$. Left column shows the synthetics: SH simulation (top), PSV simulation vertical (mid-top) and horizontal (mid-bottom) components. Right column displays the contour plots of the synthetics FFT in the same order and at the bottom the contour of logarithm of spectral ratio of SH out-of-plane synthetic seismograms relative to PSV in-plane horizontal component synthetic seismograms. At the bottom of both columns the fracture distribution is displayed in the x and z (depth) references system. x values along the model have to be multiplied $\times 10^4$.

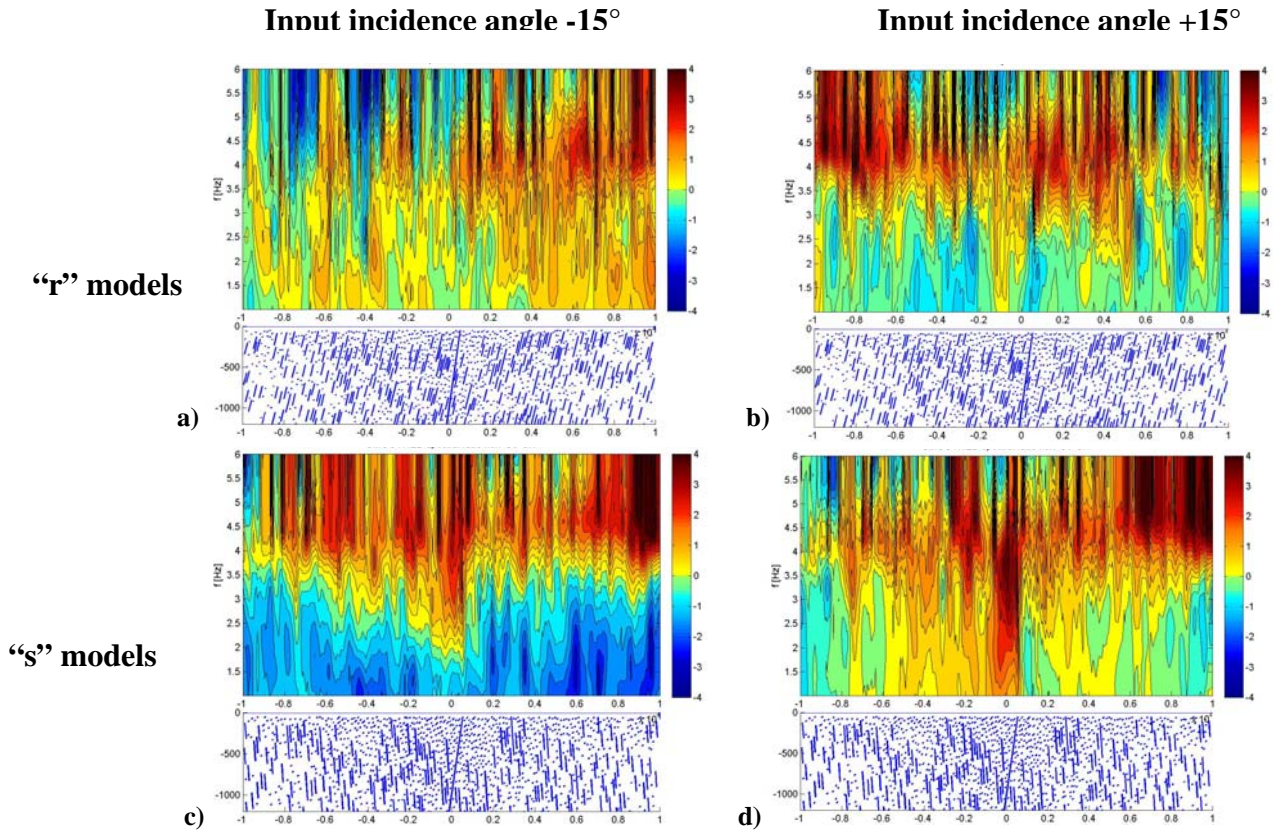


Figure 6.18 – Logarithms of spectral ratios of PSV in-plane horizontal component relative to SH out-of-plane simulation synthetics, for “r” and “s” models. (a and c) Ricker pulse with incidence angle of -15° ; (b and d) Ricker pulse with incidence angle of $+15^\circ$. x values along the model have to be multiplied $\times 10^4$.

Both “r” and “s” models show a high attenuation effect close to the fault on the in-plane horizontal component when the input incidence is $+15^\circ$. This is not evident on models performed with a -15° incident pulse probably because in this case the angle between fault dip and input propagation direction is higher, and the attenuation is similar for both in-plane and out-of-plane. Contrarily, when the pulse is input at $+15^\circ$ the attenuation is lower on SH because the angle between the fault dip and the input direction is lower. A similar consideration relates to the angle between the longer fracture set dip and the input incidence angle. The more they are parallel the lower is the attenuation on the out-of-plane component, and the lower is the PSV horizontal/SH ratio at frequencies lower than 3 Hz (Figures 6.15 and 6.16, cases b) and c) in Figure 6.18). At frequencies higher than 4Hz the in-plane horizontal component has higher amplitude than the out-of-plane one along most of the profile.

6.3 Conclusions

In order to study the effect of fluid-filled cracks on S waves propagation, several simulations were performed with out-of-plane (SH) and in-plane (PSV) motion.

The former is a simpler case because the polarisation is always parallel to the cracks and P waves are never generated. Therefore SH simulation provided an initial scheme to understand crack influence on S waves propagation. They revealed that fractures presence causes a strong attenuation that is higher with increasing the density, the homogeneity of orientations and the angle between input incidence and fractures dip.

The latter case is more complex as P and S waves are not separated. In PSV models, P waves can cross cracks that are perpendicular to the direction of propagation, while S waves can just diffract around them. For a crack with length comparable to or greater than the wavelength, at general angles of incidence the incident P and S waves will each result in four separate waves: the reflected P and S and the transmitted P and S waves, with the reflected S wave typically being much larger than the transmitted S wave.

To explore the differential attenuation between out-of-plane and in-plane components of motion, the spectral ratios between them were calculated. These showed a more pronounced attenuation effect on the in-plane horizontal component, particularly for simulated distributions with subvertical cracks, both with vertical and oblique input incidence. Only by adding two sets of oblique fractures in simulations performed with an oblique incident input, an inverse tendency was observed, with the in-plane component less attenuated. Even in this case the pattern is not clear and varies with changes in the angle of incidence, suggesting that it is the SH component which influences the ratio more strongly, as that suffers a differing attenuation level depending on the angle between the dip of the fractures and the input direction of propagation. In contrast, though the phenomena are more complex for S waves in PSV models, the dependence of attenuation level on angle of incidence is less strong.

Chapter 7

Conclusion

This thesis has investigated the polarization of ground motion. So far, this observation was often related to the radiation pattern produced by the seismic source, although some papers already indicated other possible causes. First Spudich et al. (1996) demonstrated the influence of topography on ground motion polarization on the Tazana hill, California. After the Loma Prieta earthquake Bonamassa & Vidale (1991) had already stressed the occurrence of directional resonances not related to source effects. Here, we study the problem from many points of view. First, specific experiments were designed and developed to collect new observations (on the hill of Cerreto Laziale and on the Hayward fault). Second, in addition to our own data, we have analyzed a large amount of already existing data: ambient vibrations recorded by peninsular stations of the INGV National Seismic Network, earthquakes recorded in previous experiments on the hills of Nocera Umbra and in fault zones (Hayward fault and Agri Valley fault). Third, we have applied different numerical modelling techniques to try an interpretation of observations in terms of physical models.

The first important conclusion is that polarization is much more recurrent than expected, and can be stably observed both on ambient noise and on earthquake recordings. The statistical study performed on the ambient noise of stations of the Italian seismic network, surprisingly demonstrates that polarization involves at least 30% of total stations. According to the Spudich et al. (1996) findings, in many of them polarization is oriented perpendicular to ridge axis due to scattering of seismic energy.

The study of data recorded on the Nocera Umbra Hill revealed a moderate amplification effect on earthquakes in the frequency band 2-4 Hz. Results of the numerical simulation performed in 2D approximation identifies this frequency band as related to the fundamental resonance frequency of the hill. Moreover, in this frequency band, the motion is polarized in a direction transversal to the hill major axis, independently of earthquake backazimuth. 2D numerical models show another peak at higher frequencies, that has been interpreted as the second higher resonance mode. Also experimental data show high frequency amplifications, although the match with theory is poorer. Finally these resonance modes are in agreement with results from 3D modeling performed by Ivo Oprsal (personal communication), leading to the conclusion that the 2D approximation is proper in this case and does not underestimate the amplification level.

Consistently to the Nocera Umbra Hill, on the Cerreto Laziale ridge the observed horizontal polarization of ground motion is transversal to the topography elongation. This is consistently found on ambient noise and on earthquakes, at frequencies between 1 and 5 Hz. Here, the application of a technique introduced by Frankel et al. (1991) allows to assess the direction from where wavetrains travel across the array, proving that the diffraction from the hill ridge controls the observed backazimuth distribution of ambient noise. On the contrary the earthquake waveforms show a predominant backazimuth more consistent with the source direction.

Both studies carried out on topographies demonstrate that seismic energy is diffracted by the ridge producing a polarization perpendicular to the hill elongation in a frequency band.

The correlation with topography is also investigated using seismic noise of stations of the Italian seismic network. Thanks to a dedicated software using digital elevation models (DEM), observed polarizations were correlated with topographical features (courtesy by Paola Vannoli). The result was that 60% of stations shows polarization angles within 70° to 90° from the ridge alignment.

The analysis across fault zones reveals innovative features. So far, polarization in these contexts has been related to the propagation of trapped waves in a direction parallel to the fault strike. First Rigano et al (2008) and Di Giulio et al. (2009) argued that the trapped wave model is not consistent with the observation of fault-transverse polarization. They hypothesized the occurrence of other effects, proposing a dependence on the orientation of fractures associated to the fault and to the local stress field.

Two study cases are here investigated, at a different scale: the Hayward fault and Agri Valley.

In the Hayward fault, the analysis of earthquakes shows marked differences between stations “off-fault”, hundreds of meters from the fault trace and station “on-fault”, at tens of meter. On the former stations each individual earthquake shows a different polarization, that is probably affected by seismic source and propagation path. On the contrary, the latter stations show a common and persistent polarization effect oriented in EW direction, independently of earthquake backazimuth. Two stations on fault often show two polarization effects in two different frequency bands: in the range 1-4 Hz a polarization oriented as the fault strike is observed while in the range 5-8 Hz a polarization EW. This is an important observation, demonstrating that the EW polarization can coexist with the already known, fault-parallel polarization of trapped waves, only occurring in different frequency intervals.

To explain the spatial distribution of the observed polarization, the brittle deformation pattern associated to the kinematics stress component is analytically computed using FRAP package (Salvini, 2002). The main expected cleavage is the synthetic one, that is oriented perpendicularly to the polarization direction observed at stations located very close to the fault trace. This led to the conclusion that polarization is perpendicular to synthetic cleavages produced the Kinematic stress component that are also favourably oriented from the regional stress field. This behaviour is opposite to what we would expect from the maximum velocity direction inferred from S-waves splitting, that is parallel to the maximum compressional stress component σ_1 . Anyway in

the Hayward fault is difficult to separate the influence of regional stress field to the kinematics component, and to identify which one plays a major role in the formation of the brittle deformation pattern in the damage zone at different distances.

Agri valley represents a simpler case to study the relations between polarization and either regional stress field and brittle deformation related to the kinematics component. Being a dip-slip context, the orientation of the kinematics deformation is close to the regional stress field. Polarization is studied on the same stations investigated by Pastori et al.(2009) and is compared to their results of S waves fast velocity directions inferred from S-wave splitting. Polarization was recognized to be very stable among earthquakes, independently of their focal mechanism and backazimuth. Most stations show a polarization perpendicular to S wave fast velocity and parallel to σ_3 orientation by Cucci et al. (2004). Polarization is even perpendicular to the azimuth of brittle deformation pattern modelled using FRAP package (Salvini, 2002).

The conclusion emerging from these applications is that although S waves propagate faster in a direction parallel to fluid filled microcracks (that are oriented parallel to the horizontal maximum compressional axis), the particle motion is polarized in a perpendicular direction. This perpendicular direction is observationally consistent to what found across the Hayward fault (Section 5.2).

In order to model the observed effect of fluid-filled cracks on S waves propagation, modeling of wave propagation in fractured media were developed in a partnership with Prof. A. John Haines (University of Cambridge, UK). In this approach, the normal components of traction and velocity along the fracture are continuous while the tangential traction is null.

Several simulations were performed with out-of-plane (SH) and in-plane (PSV) motion. SH simulations provide an initial scheme to understand crack influence on S waves propagation, revealing that fractures presence causes a strong attenuation that is higher with increasing the density, the homogeneity of orientations and the angle between input incidence and fractures dip.

In PSV models, P waves can cross cracks that are perpendicular to the direction of propagation, while S waves can just diffract around them.

The differential attenuation between out-of-plane and in-plane components of motion is explored calculating the spectral ratios between them. They often show a more pronounced attenuation effect on the in-plane horizontal component, particularly for simulated distributions with subvertical cracks. Only by adding two sets of oblique fractures with a fractal relation between spacing and length, an inverse tendency was observed, with the in-plane component less attenuated. Unfortunately in this case the pattern is not clear and varies with changes in the angle of incidence.

Models performed do not clearly reproduce the observed relation of polarization at 90° from the orientation of fluid-filled fractures. This is recognized also at the regional scale in the statistical study performed using the data of the Italian seismic network. The polarization mean directions of ambient noise, rotated by 90° result to be well correlated to lineament swarm domains (Wise et al.1985). Lineament swarm domains reflect stress state and tectonics at the regional scale, where topography and tectonic features are coaxial. Thus it joint observation done at detail on topography and in fault zones.

Acknowledgements

I am grateful to Francesco Salvini, for his precious suggestions, useful discussions and critical reading. Special thanks to John Haines and to Joe Fletcher for their advisements, precious comments and kindness during the two stages. I am grateful also to Paul Spudich for important suggestions and discussions. Thanks also to Larry Backer, to Russel Sell and to Chistopher Dietel for their help in fieldwork during the Hayward fault experiment, and to Paola Vannoli, Fabrizio Cara, Stefania Puccillo, Rocco Conigliano and Gaetano Riccio during Cerreto Laziale experiment. Thanks also to my husband Gianfranco and to my whole family for supporting me during all my studies.

References

- Amato, A., R. Azzara, C. Chiarabba, G.B. Cimini, M. Cocco, M. Di Bona, L. Margheriti, S. Mazza, F. Mele, G. Selvaggi, A. Basili, E. Boschi, F. Courboux, A. Deschamps, S. Gaffet, G. Bittarelli, L. Chiaraluce, D. Piccinini, M. Ripepe (1998). The 1997 Umbria-Marche, Italy, Earthquake Sequence: A First Look at the Main Shocks and Aftershocks, *Geophys. Res. Lett.* **25**, 2861-2864.
- Amato, A. & Montone, P. (1997). Present-day stress field and active tectonics in southern peninsular Italy. *Geophys. J. Int.*, **130**(2), 519–534.
- Andrews, D. J., D. H. Oppenheimer, Lienkaemper J. J. (1993). The Mission link between the Hayward and Calaveras Faults. *J. Geophys. Res.*, **98**, 12,083–12,095.
- Anooshehpour, A. & Brune, J. N. (1989). Foam rubber modelling of topographic and dam interaction effects at Pacoma Dam. *Bull. Seismol. Soc. Am.*, **79**, 1347-1360.
- Argus, D. F., & R. G. Gordon (2001). Present tectonic motion across the Coast Ranges and San Andreas fault system in central California. *Geol. Soc. Am. Bull.*, **113**, 1580– 1592.
- Aydin, A., Page, B.M., 1984. Diverse Pliocene–Quaternary tectonics in a transform environment, San Francisco Bay region, California. *Geol. Soc. Am. Bull.*, **95**, 1303– 1317.
- Bakun, W. H. (1999). Seismic activity of the San Francisco Bay region. *Bull. Seismol. Soc. Am.*, **89**, 764–784.
- Bannister, S. C., Husebye, E. S., Ruud, B.O. (1990). Teleseismic P coda analyzed by three component array technique. Deterministic location of the topographic P to Rg scattering near the NORESS array. *Bull. Seismol. Soc. Am.*, **80**, 1969-1986.
- Bard, P. Y..(1982). Diffracted waves and displacement field over two-dimensional topographies. *Geophys. J. R. Astron. Soc.*, **71**, 731-760.
- Bard, P.-Y. & B. E. Tucker (1985). Underground and ridge site effects: a comparison of observation and theory, *Bull. Seismol. Soc. Am.*, **75**, 905-922.
- Bard, P.-Y. & M. Bouchon (1985). The two-dimensional resonance of sediment-filled valleys, *Bull. Seismol. Soc. Am.*, **75**, 519-541.
- Ben-Zion, Y., & K. Aki (1990), Seismic radiation from an SH line source in a laterally heterogeneous planar fault zone, *Bull. Seismol. Soc. Am.*, **80**, 971– 994.
- Ben-Zion, Y., Z. Peng, D. Okaya, L. Seeber, J. G. Armbruster, N. Ozer, A. J. Michael, S. Baris, Aktar M. (2003). A shallow fault-zone structure illuminated by trapped waves in the Karadere-Duzce branch of the North Anatolian Fault, western Turkey, *Geophys. J. Int.*, **152**, 699 – 717.

- Barchi, M., Amato, A., Cippitelli, G., Merlini, S., Montone, P. (2007). Extensional tectonics and seismicity in the axial zone of the Southern Apennines. *Boll. Soc. Geol. It.*, Special Issue **7**, pp. 47–56.
- Benedetti, L., Tapponier, P., King, G.C.P., Piccardi, L. (1998). Surface rupture of the 1857 southern Italian earthquake. *Terra Nova. Eur. J. Geosci.*, **10(4)**, 206–210
- Bianco, F. & M. Castellano (1997). The anisotropic volume of Mt. Etna: Possible relationship with the stress-field. *Acta Vulcanol.*, **9(1/2)**, 31– 35.
- Bianco, F. & L. Zaccarelli (2009). A reappraisal of shear wave splitting parameters from Italian active volcanic area through a semiautomatic algorithm. *J. Seismol.*, **13(2)**, 253– 266.
- Bianco, F., M. Castellano, G. Milano, Vilardo, G. (1996). Shear-wave polarization alignment on the eastern flank of Mt. Etna volcano (Sicily, Italy), *Ann. Geofis.*, XXXIX, 2, 429– 443.
- Bianco, F., L. Scarfi, E. Del Pezzo, D. Patane`, D. (2006), Shear wave splitting changes associated with the 2001 volcanic eruption on Mt. Etna, *Geophys. J. Int.*, **167**, 959 – 967.
- Billi, A., Tiberti, M.M. (2009). Possible causes of arc development in the Apennines, central Italy. *Geol. Soc. Am. Bull.*, **121**;1409-1420
- Boness, N. L., & M. D. Zoback (2006). Mapping stress and structurally controlled crustal shear velocity anisotropy in California, *Geology*, **34(10)**, 825–828.
- Boore, D. M., V. M. Graizer, J. C. Tinsley, Shaka A.F. (2004). A study of possible ground-motion amplification at the Coyote Lake dam, California. *Bull. Seismol. Soc. Am.*, **94(4)**, 1327 – 1342.
- Boore, D.M. (1972). A note on the effect of simple topography on seismic SH waves. *Bull. Seismol. Soc. Am.*, **62**, 285-284
- Boore, D.M., Harmsen, S. C., Harding, S. T. (1981). Wave scattering from a steep change in surface topography. *Bull. Seismol. Soc. Am.*, **71**, 117-125.
- Boschi, E., Guidoboni, E., Ferrari, G., Mariotti, D., Valensise, G., Gasperini, P. (2000). Catalogue of strong Italian Earthquakes. *Ann. Geofis.*, 36, 237–243.
- Bouchon, M. (1973). Effect of topography on surface motion, *Bull. Seismol. Soc. Am.*, **63**, 615-632.
- Bouchon, M. & J.S. Barker (1996). Seismic response of a hill: The example of Tarzana, California, *Bull. Seismol. Soc. Am.*, **86**, 66-72.
- Burgmann, R., Arrowsmith, R., Dumitru, T., McLaughlin, R., 1994. Rise and fall of the southern Santa Cruz Mountains, California, from fission tracks, geomorphology and geodesy. *J. Geophys. Res.*, **99**, 20181– 20202.

- Burrato, P. & Valensise, G. (2008). Rise and fall of a hypothesized seismic gap: source complexity in the M_w 7.0 16 December 1857 Southern Italy earthquake. *Bull. seism. Soc. Am.*, **98**(1), 139–148
- Caine, J.S., Evans, J. P., Forster, C.B. (1996). Fault zone architecture and permeability structure. *Geology*, **24**, 1025–1028
- Calamita, F., G. Cello, G. Deiana, Paltrinieri, W. (1994). Structural styles, chronology rates of deformation, and time space relationships in the Umbria-Marche thrust system (central Apennines, Italy), *Tectonics*, **13**, 873–881.
- Cara, F. Di Giulio, G., Milana, G., Bordoni, P., Haines, J., Rovelli, A. (2010). On the Stability and Reproducibility of the Horizontal-to-Vertical Spectral Ratios on Ambient Noise: Case Study of Cavola, Northern Italy. *Bull. Seism. Soc. Am.*, in press.
- Caserta, A. (1998). A time domain finite-difference technique for oblique incidence of antiplane waves in heterogeneous dissipative media, *Annals of Geophysics*, **41**, 617– 631.
- Caserta A., F. Bellucci, G. Cultrera, S. Donati, F. Marra, G. Mele, B. Palombo, Rovelli A. (2000). Study of site effects in the area of Nocera Umbra (Central Italy) during the 1997 Umbria-Marche seismic sequence, *J. Seismology*, **4**, 555–565.
- Catalano, S., Monaco, C., Tortorici, L., Paltrinieri, W., Steel, N. (2004). Neogene-quaternary tectonic evolution of the Southern Apennines. *Tectonics*, **23**, TC2003, doi:10.1029/2003TC001512.
- Cavinato, G., & DeCelles, P.G. (1999). Extensional basins in tectonically bimodal central Apennines fold-thrust belt, Italy : Response to corner flow above a subducting slab in retrograde motion. *Geology*, **27**, 955–958. doi: 10.1130/0091-7613(1999)027<0955:EBITTB> 2.3.CO;2.
- Çelebi, M. (1987). Topographical and geological amplifications determined from strong-motion and aftershock records of the 3 March 1985 Chile earthquake, *Bull. Seismol. Soc. Am.*, **77**, 1147–1167.
- Cello, G., Gambini, R., Mazzoli, S., Read, A., Tondi, E. Zucconi, V. (2000). Fault zone characteristics and scaling properties of the Val d'Agri fault system (Southern Apennines, Italy), *J. Geod.*, **29**(3–5), 293– 307.
- Cello, G., Tondi, E., Van Dijk, J.P., Mattioni, L., Micarelli, L., Pinti (2003). Geometry, kinematics and scaling properties of faults and fractures as tools for modelling geofluid reservoirs; examples from the Apennines, Italy. *Geological Society, Special Publications*, 212, 7–22.
- Chavez-Garcia, F.J., L.R. Sanchez, Hatzfeld D. (1996). Topographic site effect and HVSR. A comparison between observation and theory, *Bull. Seismol. Soc. Am.*, **5**, 1725–1743.
- Clouser, R. H. & Langston C. A. (1995). Modeling observed P-Rg conversions from isolated topographic features near the NORESS array. *Bull. Seismol. Soc. Am.*, **85**, 859–873.

- Cochran, E. S., J. E. Vidale, Li, Y. (2003). Near-fault anisotropy following the Hector Mine earthquake. *J. Geophys. Res.*, **108**(B9), 2436, doi:10.1029/2002JB002352.
- Cochran, E. S., Y.-G. Li, Vidale, J. E. (2006). Anisotropy in the shallow crust observed around the San Andreas fault before and after the 2004 M 6.0 Parkfield earthquake. *Bull. Seismol. Soc. Am.*, **96**(4B), S364–S375, doi:10.1785/0120050804.
- Conda, L., Mariotti, G. (1986). Il bacino sabino: 2) Sedimentologia e stratigrafia della serie calcarea e marnoso-spongolitica (Paleogene–Miocene). *Mem. Soc. Geol. It.*, **35**, 33–47.
- Cormier, V. F., and Spudich, P. (1984). Amplification of Ground Motion and Waveform Complexities in Fault Zones: Examples from the San Andreas and Calaveras Faults. *G. J. Roy. Astr. Soc.* **79**, 135–152.
- Cucci, L., Pondrelli, S., Freopoli, A., Mariucci, M.T., Moro, M. (2004). Local pattern of stress field and seismogenic sources in Meandro Pergola basin and in Agri valley (Southern Italy). *Geophys. J. Int.*, **156**, 575–583.
- Cultrera, G., A. Rovelli, G. Mele, R. Azzara, A. Caserta, F. Marra (2003). Azimuth dependent amplification of weak and strong ground motions within a fault zone (Nocera Umbra, Central Italy), *J. Geophys. Res.*, **108** (B3), 2156, doi:10.1029/2002JB001929.
- Davis, L. L. & West L. R. (1973). Observed effects of topography on ground motion. *Bull. Seismol. Soc. Am.*, **63**, 283-298.
- Decandia, F.A., Lazzarotto, A., Liotta, D., Cernobori, L., Nicolich, R. (1998). The CROP 03 traverse: insights on post-collisional evolution of Northern Apennines. *Mem. Soc. Geol. It.*, **52**, 427–439.
- Deiana, G., Pasqualini, L., Salvucci, R., Stroppa, P. (1996). Il sistema di sovrascorrimenti dei Monti Reatini: analisi geometrica e cinematica. *Studi Geologici Camerti*, 1995/2, 199–206.
- Deiana, G., Mazzoli, S., Paltrinieri, W., Pierantoni, P.P., Romano, A. (2003). Struttura del fronte montuoso umbro-marchigiano-sabino. *Studi Geologici Camerti*, Nuova serie 1/2003, 15–36.
- Dell’Aversana, P. (2003). Integration loop of ‘global offset’ seismic, continuous profiling magnetotelluric and gravity data. *First break*, **21**, 32–41.
- Deschamps, A., F. Courboux, S. Gaffet, A. Lomax, J. Virieux, A. Amato, A. Azzara, B. Castello, C. Chiarabba, G.B. Cimini, M. Cocco, M. Di Bona, L. Margheriti, F. Mele, G. Selvaggi, L. Chiaraluce, D. Piccinini, M. Ripete (2000). Spatio-temporal distribution of seismic activity during the Umbria-Marche crisis, 1997, *J. Seismol.*, **4**, 377-386.
- Dewey, J.F., Helman, M.L., Turco, E., Hutton, D.H.W., Knott, S.D. (1989). Kinematics of the western Mediterranean. In: Coward, M.P., Dietrich, D., Park, R.G. (Eds.), *Alpine Tectonics Geological Society Special Publication* **45**, pp. 265–283.
- Di Bucci, D., Mazzoli, S. (2002). Active tectonics of the Northern Apennines and Adria geodynamics: new data and a discussion. *J. Geodyn.*, **34**, 687–707.

- Di Giulio, G., Cara, F., Rovelli, A., Lombardo, G., Rigano, R. (2009). Evidences for strong directional resonances in intensely deformed zones of the Pernicana fault, Mount Etna, Italy. *J. Geophys. Res.*, **114**, doi:10.1029/2009JB006393.
- Donati, S., F. Marra, A. Rovelli (2001). Damage and ground shaking in the town of Nocera Umbra during Umbria-Marche, central Italy, earthquakes: The special effect of a fault zone, *Bull. Seismol. Soc. Am.*, **91**, 511-519.
- England, R., Sabina, F. J., Herrera, I. (1980). Scattering of SH waves by surface cavities of arbitrary shape using boundary methods. *Phys. Earth Planet. Inter.*, **21**, 148-157.
- Faccenna, C., Piromallo, C., Crespo-Blanc, A., Jolivet, L. (2004). Lateral slab deformation and the origin of the western Mediterranean arcs. *Tectonics*, **23**, p. TC1012, doi: 10.1029/2002TC001488.
- Faulkner, D. R., M. Mitchell, D. Healy, Heap, M. J. (2006). Slip on weak faults by the rotation of regional stress in the fracture damage zone. *Nature*, **444**, 922–925, doi:10.1038/nature05353.
- Frankel, A., Hough, S., Friberg, P., Busby, R. (1991). Observation of Loma Prieta aftershocks from a dense array in Sunnyvale, California. *Bull. Seismol. Soc. Am.*, **5**, 1900-1922.
- Gaffet, S. & Bouchon, M. (1989). Effects of two-dimensional topographies using the wavenumber boundary integral element method in P-SV cases. *J. Acoust. Soc. Am.*, **85**, 2277-2283.
- Gans, C.R., Furlong, K.P. (2000). Fault creep and microseismicity on the Hayward fault, California: Implications for asperity size. *Geophys. Res. Lett.*, **30**, doi:10.1029/2003GL017904.
- Gasparini, C., Iannaccone, G., Scandone, P., Scarpa, R. (1982). Seismotectonics of the Calabrian Arc. *Tectonophysics*, **84**(2–4), 267–286.
- Geli L., P.-Y. Bard, B. Jullien (1988). The effect of topography on earthquakes ground motion: a review and new results. *Bull. Seismol. Soc. Am.*, **78**, 42-63.
- Ghisetti, F., and Vezzani, L. (1997). Interfering paths of deformation and development of arcs in the fold-and-thrust belt of the central Apennines. *Tectonics*, **16**, 523–536, doi: 10.1029/97TC00117.
- Gilbert, F & I.Knopoff, (1960). Seismic scattering from topography irregularities. *J. Geophys. Res.*, **65**, 3437-3444.
- Graymer, R. W., D. L. Jones, Brabb, E. E. (1995). Geologic map of the Hayward Fault zone, Contra Costa, Alameda, and Santa Clara Counties, California: A digital database, U.S. Geol. Surv. Open File Rep., 95–597.

- Graymer, R.W., Ponce, D.A., Jachens, R.C., Simpson, R.W., Phelps, G.A., Wentworth C.M (2005). Three-dimensional geologic map of the Hayward fault, northern California: Correlation of rock units with variations in seismicity, creep rate, and fault dip. *Geology*, **33**, 521-524
- Graymer, R. W., A. M. Sarna-Wojcicki, J. P. Walker, R. J. McLaughlin, Fleck, R.J. (2002). Controls on timing and amount of right-lateral offset on the East Bay fault system, San Francisco Bay region, California. *Geol. Soc. Am. Bull.*, **114**, 1471– 1479.
- Greenfield, R. J. (1971). Short-period P wave generation by Raileigh wave scattering at Novaya Zembya. *J. Geophys. Res.*, **76**, 7988-8002.
- Griffith D.W. & Bollinger G. A. (1979). The effect of Appalachian mountain topography on seismic waves. *Bull. Seismol. Soc. Am.*, **69**, 1081-1105.
- Gupta, I. N., Lynnes, C. S., McElfresh, T. W., Wagner, R. A. (1990). F-k analysis of NORESS array and single station data to identify sources of near-receiver and near-source scattering . *Bull. Seismol. Soc. Am.*, **80**, 2227-2241
- Hardebeck, J. L., A. J. Michael, Brocher, T. M. (2004). Seismic velocity structure and seismotectonics of the Hayward fault system, East San Francisco Bay, California. *Eos Trans. AGU*, **85(47)**, Fall Meet. Suppl., Abstract S34A-05.
- Hartzell, S. H., Carver, D. L., King, K. W. (1994). Initial investigation of site and topographic effects at Robinwood ridge, California. *Bull. Seismol. Soc. Am.*, **84**, 1336-1349.
- Huang, B. S., Teng, T.-L., Yeh, Y. T. (1995). Numerical Modeling of Fault-zone Trapped Waves: Acoustic Case. *Bull. Seismol. Soc. Am.* **85**, 1711–1717.
- Hudson J.A. (1967). Scattered surface waves from a surface obstacle. *Geophys. J.R. Astron. Soc.*, **13**, 441-458.
- Hunstad, I., Selvaggi, G., D’agostino, N., England, P., Clarke, P., Pierozzi, M. (2003). Geodetic strain in peninsular Italy between 1875 and 2001. *Geophys. Res. Lett.*, **30(4)**, 1181, doi:10.1029/2002GL016447.
- Hough, S. E., Ben-Zion, Y., Leary, P. C. (1994). Fault-zone Waves Observed at the Southern Joshua Tree Earthquake Rupture zone. *Bull. Seismol. Soc. Am.* **8**, 761–767.
- Igel, H., G. Jahnke, Ben-Zion, Y. (2002). Numerical simulation of fault zone trapped waves: Accuracy and 3-D effects. *Pure Appl. Geophys.*, **159**, 2067–2083, doi:10.1007/s00024-002-8724-9.
- Ilan, A. & Bond, L. J. (1981). Interaction of a compressional impulse with a slot normal to the surface of an elastic half-space, II. *Geophys. J. R. Astron. Soc.*, **65**, 75-90.
- Jahnke, J., H. Igel, Ben-Zion, Y. (2002). 3D calculations of fault zone guided waves in various irregular structures. *Geophys. J. Int.*, **151**, 416–426, doi:10.1046/j.1365-246X.2002.01784.x.

- Jurkevics A. (1988). Polarization analysis of three component array data, *Bull. Seismol. Soc. Am.*, **78**, 1725-1743.
- Kawase, H. (1988). Time domain response of a semicircular canyon for incident SV, P and Raileigh waves calculated by the discrete wavenumber boundary element method. *Bull. Seismol. Soc. Am.*, **78**, 1415-1437.
- Kawase H. & K. Aki (1990). Topography effect at the critical SV-wave incidence: possible explanation of damage pattern by the Whittier Narrows, California, earthquake of 1 October 1987, *Bull. Seismol. Soc. Am.*, **80**, 1-22.
- Kelson, K. I. & G. D. Simpson (1995). Late Quaternary deformation of the southern East Bay Hills, Alameda County, CA. *AAPG Bull.*, **79**, 590.
- Key, F.A. (1967). Signal generation noise recorded at the Eskalemuir seismometer array station. *Bull. Seismol. Soc. Am.*, **57**, 27-37.
- Klein, E. (2008). Perfectly matched layer boundary conditions in two numerical methods for seismic wave calculation. *PhD thesis*, Cambridge University, UK.
- Kurita, T., Annaka, T., Takahashi, S., Shimada, M., Suehiro, T. (2003). Effect of Irregular Topography on Strong Ground Motion Amplification. *Transation of the 17th international Conference on Structural Mechanics in Reactor Technology (SMiRT 17) Prague, Czech Republic*.
- La Rocca, M., D. Galluzzo, G. Saccorotti, S. Tinti, G. B. Cimini, Del Pezzo, E. (2004). Seismic signals associated with landslides and with a tsunami at Stromboli volcano, Italy, *Bull. Seismol. Soc. Am.*, **94**(5), 1850–1867, doi:10.1785/012003238.
- Lanucara P., M.P. Busico, A. Caserta, B. Firmani (2004). Numerical modeling of the ground motion: a parallel approach for finite element methods, Proceedings of the 7th Conference on Applied and Industrial Mathematics in Italy, Venice, Italy, 487-495.
- Lawson, A. C., The earthquake of 1868 in A. C. Lawson, ed., The California earthquake of April 18, 1906, Report of the State Earthquake Investigation Commission (Volume I), Carnegie Institution of Washington Publication No. **87**, 434-448, 1908.
- Le Brun, B., D. Hatzfeld, P.-Y. Bard (1999). Experimental study of the ground-motion on a large scale topographic hill a Kitherion (Greece), *J. Seismology*, **3**, 1-15.
- Lewis, M. A., Z. Peng, Y. Ben-Zion, Vernon, F. L. (2005). Shallow seismic trapping structure in the San Jacinto fault zone near Anza, California. *Geophys. J. Int.*, **162**, 867 – 881, doi:10.1111/j.1365-246X.2005.02684.x.
- Li, Y. G., P. C. Leary, K. Aki, Malin, P. (1990). Seismic trapped modes in the Oroville and San Andreas fault zones. *Science*, **249**, 763– 765, doi:10.1126/science.249.4970.763.
- Li, Y. G. & J. E. Vidale (1996). Low-velocity fault-zone guided waves: Numerical investigations of trapping efficiency, *Bull. Seismol. Soc. Am.*, **86**, 371–378.

- Lienkaemper, J. J., G. Borchardt, Lisowski, M. (1991). Historic creep rate and potential for seismic slip along the Hayward fault, California. *J. Geophys. Res.*, **96**, 18,261-18,283.
- Lienkaemper, J. J., J. S. Galehouse, Simpson, R. W. (2001). Long-term monitoring of creep rate along the Hayward Fault and evidence for a lasting creep response to 1989 Loma Prieta earthquake. *Geophys. Res. Lett.*, **28**, 2265– 2268.
- Lienkaemper, J. J. (1992). Map of recently active traces of the Hayward fault, Alameda and Contra Costa Counties, California, scale 1:24,000, U.S. Geol. Surv. Misc. Field Stud. Map MF-2196, 13 p.
- Mabee B. S., Hardcastle, K., Wise, D.U (1994). A Method of Collecting and Analyzing Lineaments for Regional-Scale Fractured-Bedrock Aquifer Studies. *Ground Water*, **32-6**, 885-894.
- Malinverno, A., & Ryan, W.B.F. (1986). Extension in the Tyrrhenian Sea and shortening in the Apennines as result of arc migration driven by sinking of the lithosphere. *Tectonics*, **5**, 227–254. doi: 10.1029/TC005i002p00227
- Manaker, D. M., A. J. Michael, Burgmann, R. (2005). Subsurface structure and kinematics of the Calaveras-Hayward fault stepover from three-dimensional Vp and seismicity, San Francisco Bay region, California. *Bull. Seismol. Soc. Am.*, **95**, 446– 470.
- Marra F., R. Azzara, F. Bellucci, A. Caserta, G. Cultrera, B. Mele, B. Palombo, A. Rovelli, E. Boschi (2000). Large amplification of ground motion at rock sites within a fault zone in Nocera Umbra (central Italy), *J. Seismology*, **4**, 543-554.
- Maschio, L., Ferranti, L., Burrato, P. (2005). Active extension in Val d’Agri area, Southern Apennines, Italy; implications for the geometry of the seismogenic belt. *Geophys. J. Int.*, **162**(2), 591–609.
- Mazzoli, S. et al.(2000). Time and space variability of thin skinned and thick skinned thrust tectonics in the Apennines (Italy). *Rendiconti Lincei Scienze Fisiche e Naturali*, **IX**, 5–39.
- Mazzoli, S. & Helman, M. (1994). Neogene patterns of relative plate motion for Africa–Europe: some implications for recent central Mediterranean tectonics. *Geologische Rundschau*, **83**, 464–468.
- Mazzoli, S., Deiana, G., Galdenzi, S., Cello, G. (2002). Miocene fault controlled sedimentation and thrust propagation in the previously faulted external zones of the Umbria–Marche Apennines, Italy. EGU Stephan Mueller Special Publication Series 1, 195–209.
- Mazzoli, S., Pierantoni, P.P., Borraccini, F., Paltrinieri, W., Deiana, G. (2005). Geometry, segmentation pattern and displacement variations along a major Apennine thrust zone, central Italy. *Journal of Structural Geology*, **27**, 1940–1953

- Menardi Noguera, A. & Rea, G. (2000). Deep structure of the Campanian-Lucanian Arc (Southern Apennine, Italy). *Tectonophysics*, **324**(4), 239–265.
- Michael, A. J. & Y. Ben-Zion (1998). Inverting fault zone trapped waves with genetic algorithm. *Eos Trans. AGU*, **79**(45), Fall Meet. Suppl., F584.
- Michelini, A., D. Spallarossa, M. Cattaneo, A. Govoni, Montanari, A. (2000). The 1997 Umbria-Marche (Italy) earthquake sequence: tomographic images obtained from data of the GNDT-SSN temporary network, *J. Seismology*, **4**, 415-433.
- Michetti, A.M., Serva, L., Vittori, E. (2000). ITHACA (Italian hazard from Capable Faulting), a database of active capable faults of the Italian onshore territory. *Database onCD-ROM. Internal report of ANPA-Agenzia Nazionale Protezione Ambiente*, Roma.
- Moczo, P., A. Rovelli, P. Labák, L. Malagnini (1995). Seismic response of the geologic structure underlying the Roman Colosseum and a 2-D resonance of a sediment valley, *Annals of Geophysics*, **38**, 939-956.
- Nakamura, Y. (1989). A method for dynamic characteristics estimation of subsurface using microtremors on the ground surface, *Quarterly Rept. RTRI, Jpn.*, **30**, 25-33.
- Ohtsuky, A & Harumi, K. (1983). Effect of topography and subsurface inhomogeneities on seismic SV waves. *Earthquake Eng. Struct. Dyn.*, **11**, 441-462.
- Oppenheimer, D. H., I. G. Wong, Klein, F.W. (1993). The seismicity of the Hayward fault, California. *Calif. Div. Mines Geol. Spec. Publ.*, **113**, 91– 100.
- Paolucci, R. (2002). Amplification of earthquake round motion by steep topographic irregularities, *Earthquake Engng Struct. Dyn.*, **31**, 1831-1853.
- Parotto, M. & Praturlon, A. (1975). Geological summary of the Central Apennines. In: Structural Model of Italy. Quaderni de ‘La Ricerca Scientifica’, CNR, **90**, pp. 257–311.
- Parsons, T., R. Sliter, E. L. Geist, R. C. Jachens, B. E. Jaffe, A. Foxgrover, P. E. Hart, McCarthy, J. (2003). Structure and Mechanics of the Hayward-Rodgers Creek fault step-over, San Francisco Bay, California. *Bull. Seismol. Soc. Am.*, **93**, 2187– 2200.
- Pastori, M., Piccinini, D., Margheriti, L., Improta, L., Valoroso, L., Chiaraluce, L., Chiarabba, C. (2009). Stress aligned cracks in the upper crust of the Val d’Agri region as revealed by shear wave splitting. *J. Geophys. Res.*, **179**, 601–614
- Patacca, E., Scandone, P., Di Luzio, E., Cavinato, G.P., Parotto, M. (2008). Structural architecture of the central Apennines: Interpretation of the CROP 11 seismic profile from the Adriatic coast to the orographic divide. *Tectonics*, **27**., p. TC3006, doi: 10.1029/ 2005TC001917.
- Pedersen, H.A., B. Le Brun, D. Hatzfeld, M. Campillo, P.-Y. Bard (1994). Ground-motion amplitude across ridges, *Bull. Seismol. Soc. Am.*, **84**, 1786-1800.

- Pedersen, H.A., F. J. Sánchez-Sesma, M. Campillo (1994). Three-dimensional scattering by two-dimensional topographies, *Bull. Seismol. Soc. Am.*, **84**, 1169-1183.
- Pierantoni, P.P., Deiana, G., Romano, A., Paltrinieri, W., Borraccini, Mazzoli, S. (2005). Geometrie strutturali lungo la thrust zone del fronte montuoso umbro-marchigiano-sabino. *Bollettino della Società Geologica Italiana*, **124**, 395–411.
- Pierantoni, P.P., Deiana, G., Romano, A., Paltrinieri, W., Borraccini, F., Mazzoli, S. (2005). Geometrie strutturali lungo la thrust zone del fronte montuoso umbro-marchigiano-sabino = Structural geometries along the thrust zone of the Umbria-Marche-Sabina mountain front. *Bollettino della Società Geologica Italiana*, **2**, 395-411.
- Ponce, D. A., G. A. Phelps, R. W. Graymer, R. C. Jachens, R. W. Simpson, Wentworth, C.M. (2003). Geophysical anomalies and seismicity suggest a connection between the Hayward and Calaveras faults, eastern San Francisco Bay Area, northern California. *Eos Trans. AGU*, *84(46)*, *Fall Meet. Suppl.*, Abstract T11D-0425.
- Pondrelli, S., Salimbeni, S., Ekstrom, G., Morelli, A., Gasparini, P., Vannucci, G. (2006). The Italian CMT dataset from 1977 to the present. *Phys. Earth planet. Inter.*, **159(3–4)**, 286–303.
- Ponti, D. J. & R.E. Wells (1991). Off-fault ground ruptures in the Santa Cruz Mountains, California: Ridge-top spreading versus tectonic extension during the 1989 Loma Prieta earthquake, *Bull. Seismol. Soc. Am.*, **81**, 1480-1510.
- Provost, A.-S. & Houston (2003). Stress orientations in northern and central California: Evidence for the evolution of frictional strength along the San Andreas plate boundary system. *J. Geophys. Res.*, **108(B3)**, 2175, doi:10.1029/2001JB001123.
- Rigano, R., Cara, F., Lombardo, G., Rovelli, A. (2008). Evidence for ground motion polarization on fault zones of Mount Etna volcano. *J. Geophys. Res.*, **113**, B10306, doi:10.1029/2007JB005574.
- Rosenbaum, G., & Lister, G.S. (2004). Formation of arcuate orogenic belts in the western Mediterranean region, in Sussman, A.J., and Weil, A.B., eds., *Orogenic Curvature: Integrating Paleomagnetic and Structural Analyses*. *Geol. Soc. Am. Special Paper* **383**, 41–56.
- Rovelli, A., Caserta, A., Marra, F., Ruggiero, V. (2002). Can seismic waves be trapped inside an inactive fault zone? The case study of Nocera Umbra, central Italy, *Bull. Seismol. Soc. Am.*, **92**, 2217-2232.
- Royden, L., Patacca, E., Scandone, P.(1987). Segmentation and configuration of subducted lithosphere in Italy: An important control on thrust-belt and foredeep-basin evolution. *Geology*, **15**, 714–717, doi: 10.1130/0091-7613(1987)15<714:SACOSL>2.0.CO;2.
- Sabina, F. J. & Willis, J. R. (1975). Scattering of SH waves by a rough half-space of arbitrarily slope. *Geophys. J. R. Astron. Soc.*, **42**, 685-703.
- Salvini F. (2002). Daisy 3, the Structural Data Integrated Analyzer.

Salvini, F. (2002) -FRAP 3

Salvini, F. & Vittori, E. (1982). Analisi strutturale della linea Olevano–Antrodoco–Posta (‘Ancona–Anzio’ Auct.): metodologia di studio delle deformazioni fragili e presentazione del tratto meridionale. *Mem. Soc. Geol. It.*, **24**, 335–337.

Sánchez-Sesma, F. J. (1990). Elementary solutions for response of a wedge-shaped medium to incident *SH* and *SV* waves, *Bull. Seismol. Soc. Am.*, **80**, 737-742.

Sanchez-Sesma, F.J. (1983). Diffraction of elastic waves by three dimensional surface irregularities. *Bull. Seismol. Soc. Am.*, **73**, 1621-1636.

Sanchez-Sesma, F.J. & Campillo, M. (1991). Diffraction of P, SV, and Rayleigh waves by topographic features: A boundary integral formulation. *Bull. Seismol. Soc. Am.*, **81**, 2234-2253.

Sanchez-Sesma, F.J. & Rosenblueth, E. (1979). Ground motion at calyons of arbitrarily shape under incident *SH* waves. *Earthquake Eng. Struct. Dyn.*, **7**, 441-450.

Santoni D., Giuffrida, C., Ruggiero, V., Caserta, A., Lanucara, P. (2004). Web user-friendly interface to produce input data for numerical simulations of seismic wave propagation, EGS-AGU-EUG Joint Assembly, Nice, France (poster).

Savage, J. C. & M. Lisowski (1993). Inferred depth of creep on the Hayward fault, central California. *J. Geophys. Res.*, **98**, 787– 793.

Schmidt, D. A. , Burgmann, R., Nadeau, R.M. (2005). Distribution of aseismic slip rate on the Hayward fault inferred from seismic and geodetic data. *J. Geophys. Res.*, **110**, doi:10.1029/2004JB003397.

Serpelloni, E., Anzidei, M., Baldi, P., Casula, G., Galvani, A. (2005). Crustal velocity and strain-rate fields in Italy and surrounding regions; new results from the analysis of permanent and non-permanent GPS networks. *Geophys. J. Int.*, **161(3)**, 861–880.

Shah, A., Wong, K. C., Datta, S. K. (1982). Diffraction of plane *SH* waves in half-space. *Earthquake Eng. Struct. Dyn.*, **10**, 519-528.

Shakal, A., Huang, M., Darragh, R., Cao, T, Sherburne, R., Malhotra, P., Cramer, C., Sydon, R., Grazer, V., Maldonado, G., Peterson, C., Wampole, J. (1994) CSMIP strong motion records from the Northridge California earthquake of 17 January 1994, Rep OSMS 94-07, Calif. Div. of Mines and Geol., Sacramento.

Shiner, P., Beccacini, A., Mazzoli, S. (2004). Thin-skinned versus thick skinned structural models for Apulian carbonate reservoirs; constraints from the Val d’Agri fields, S Apennines, Italy. *Mar. Petrol. Geol.*, **121(7)**, 805–827.

Sills, L. (1978). Scattering of horizontally polarized shear waves by surface irregularities. *Geophys. J. R. Astron. Soc.*, **54**, 319-348.

- Simpson, R. W., R. W. Graymer, R. C. Jachens, D. A. Ponce, Wentworth, C. M. (2004). Cross-sections and maps showing double-difference relocated earthquakes from 1984 – 2000 along the Hayward and Calaveras faults, California. U.S. Geol. Surv. Open File Rep., 04– 1083, 91 pp. (Available at <http://pubs.usgs.gov/of/2004/1083/>.)
- Speranza, F., Chiappini, M. (2002). Thick-skinned tectonics in the external Apennines, Italy: new evidence from magnetic anomaly analysis. *J. Geophys. Res.*, **B11**, 2290. doi:10.1029/2000JB000027.
- Spudich P, M. Hellweg, H.K. Lee (1996) Directional topographic site response at Tarzana observed in aftershocks of the 1994 Northridge California earthquake: Implications for mainshocks motions, *Bull. Seismol. Soc. Am.*, **86**, 193-208.
- Spudich, P & Xu, L. (2003). Documentation of software package ISOSYN: Isochrone integration programs for earthquake ground motion calculations, CD accompanying IASPEI *Handbook of Earthquake and Engineering Seismology*, 72 pp.
- Takemiya, H., Fujiwara, A. (1994). SH-wave scattering and propagation analyses at irregular sites by time domain BEM. *Bull. Seismol. Soc. Am.*, **84**, 1442-1455.
- Tirelli, V. (2002). Studio strutturale delle zone di faglia presso Nocera Umbra (PG) e loro influenza sugli effetti di sito dell'evento sismico Settembre 1997. Thesis, Department of Geology, University Roma3, Rome, Italy, pp. 112 (in Italian).
- Trice, R., 1999. Application of borehole image logs in constructing 3D static models of productive fracture network in the Apulian Platform, Southern Apennines, in *Borehole imaging: applications and case histories*, Vol. 159, pp. 156–176, eds Lovell, M.A., Williamson, G. & Harvey, P.K., Geological Society, London, Special Publications, doi:10.1144/GSL.SP.1999.159.01.08.
- Trifunac, M. D. (1973). Scattering of plane SH waves by a semi-cylindrical canyon. *Earthquake Eng. Srtuc. Dyn.*, **1**, 267-281.
- Umeda, Y., Kuroiso, A., Ito, K., Saeki, T. (1986). High accelerations in the epicentral area of the Western Nagana Prefecture, Japan earthquake of 1984. *J. Seismol. Soc. Jpn.*, **39**, 217-228.
- Unruh, J.R. & Sawyer, T.L. (1995). Late Cenozoic growth of the Mt. Diablo fold and thrust belt, central Contra Costa County, California and implications for transpressional deformation of the northern diablo range. Pacific Section Convention, American Association of Petroleum Geologists and Society of Economic Paleontologists and Mineralogists, **47**.
- Valensise, G. & Pantosti, D. (2001). Database of potential sources for earthquakes larger than M 5.5 in Italy. *Annali di Geofisica*, **44**, 180.
- Valoroso, L., Improta, L., Chiaraluce, L., Di Stefano, R., Ferranti, L., Govoni, A., Chiarabba, C. (2009). Active faults and induced seismicity in the Val d'Agri area (Southern Apennines, Italy). *Geophys. J. Int.*, **178**(1), 488–502.

- Yu, E. & P. Segall (1996). Slip in the 1868 Hayward earthquake from the analysis of historical triangulation data. *J. Geophys. Res.*, **101**, 16,101–16,118.
- Wagner, G. S., Langston, C. A. (1992). Body to surface wave scattered energy in teleseismic coda observed at the NORESS seismic array. *Bull. Seismol. Soc. Am.*, **82**, 2126-2138.
- Waldhauser, F. & W. L. Ellsworth (2002). Fault structure and mechanics of the Hayward Fault, California, from double-difference earthquake locations. *J. Geophys. Res.*, **107**(B3), 2054, doi:10.1029/2000JB000084.
- Wakabayashi, J. (1999). Distribution of displacement on, and evolution of, a young transform fault system: the northern San Andreas fault system, California. *Tectonics*, **18**, 1245– 1274.
- Wakabayashia, J., Hengeshb, J.V., Sawyerc, T.L. (2004). Four-dimensional transform fault processes: progressive evolution of step-overs and bends. *Tectonophysics*, **392**, 279– 301
- Williams, P. L. (1992). Geologic record of southern Hayward Fault earthquakes, in Proceedings of the Second Conference on Earthquake Hazards in the Eastern San Francisco Bay Area, edited by G. Borchardt et al.. *Spec. Publ. Calif. Div. Mines Geol.*, **113**, 171– 179.
- Williams, R.A., Simpson, R.W., Jachens, R.C., Stephenson, W.J., Odum, J.K., Ponce, D.A. (2005). Seismic reflection evidence for a northeast-dipping Hayward fault near Fremont, California: Implications for seismic hazard. *J. Geophys. Res.*, **114**, doi:10.1029/2005GL023113.
- Wise, D.U. (1983). Lineamentship and the practise of linear geo-art. *Geol. Soc. Am. Bull.*, **94**, 1379.
- Wise, D.U., Funicello, R., Parotto, M., Salvini, F (1985). Topographic lineaments swarms: clues to their origin from domain analysis of Italy, *Geol. Soc. Am. Bull.*, **96**, 952-967.
- Working Group on California Earthquake Probabilities (WGCEP). Earthquake probabilities in the San Francisco Bay region: 2000 to 2030—Asummary of findings, U.S. Geol. Surv. Open File Rep., 99– 517, 1999.
- Wong, I. G. & M. A. Hemphill-Haley (1992). Seismicity and faulting near the Hayward and Mission Faults, in Proceedings of the Second Conference on Earthquake Hazards in the Eastern San Francisco Bay Area, edited by G. Borchardt et al., *Spec. Publ. Calif. Div. Mines Geol.*, **113**, 207– 215.
- Wong, H.L. (1982). Effect of surface topography on the diffraction of P, SV, and Rayleigh waves. *Bull. Seismol. Soc. Am.*, **72**, 1167-1183.
- Wong, H.L. & Jennings, P. C. (1975). Effect of canyon topography on strong ground motion. *Bull. Seismol. Soc. Am.*, **65**, 1239-1257.